



HAL
open science

Experimental characterization and phenomenological modeling of knock occurrence in turbocharged spark-ignition engines

Georges El Hajj

► **To cite this version:**

Georges El Hajj. Experimental characterization and phenomenological modeling of knock occurrence in turbocharged spark-ignition engines. Mechanics [physics]. École centrale de Nantes, 2022. English. NNT : 2022ECDN0001 . tel-03722278

HAL Id: tel-03722278

<https://theses.hal.science/tel-03722278>

Submitted on 13 Jul 2022

HAL is a multi-disciplinary open access archive for the deposit and dissemination of scientific research documents, whether they are published or not. The documents may come from teaching and research institutions in France or abroad, or from public or private research centers.

L'archive ouverte pluridisciplinaire **HAL**, est destinée au dépôt et à la diffusion de documents scientifiques de niveau recherche, publiés ou non, émanant des établissements d'enseignement et de recherche français ou étrangers, des laboratoires publics ou privés.

THESE DE DOCTORAT DE

L'ÉCOLE CENTRALE DE NANTES

ÉCOLE DOCTORALE N° 602
Sciences pour l'Ingénieur
Spécialité : Energétique-Thermique-Combustion

Par :

Georges EL HAJJ

Caractérisation expérimentale et modélisation phénoménologique de l'apparition du cliquetis dans les moteurs à allumage commandé suralimentés

Thèse présentée et soutenue à Nantes, le 13 janvier 2022
**Unité de recherche : UMR 6598, Laboratoire de recherche en Hydrodynamique Energétique et
Environnement Atmosphérique (LHEEA)**

Rapporteurs avant soutenance :

Christine ROUSSELLE
Alan KEROMNES

Professeur des universités, Université d'Orléans
Maître de conférences HDR, Université de Limoges

Composition du Jury :

Président :	Jérôme BELLETTRE	Professeur des universités, Université de Nantes
Examineur :	Alessio DULBECCO	Ingénieur de Recherche, IFP Energies Nouvelles, Rueil-Malmaison
Dir. de thèse :	Alain MAIBOOM	Professeur des universités, École Centrale de Nantes
Co-dir. de thèse :	Xavier TAUZIA	Professeur des universités, École Centrale de Nantes
Invité :	Olivier DAVODET	Expert Modélisation numérique, Stellantis, Poissy

Acknowledgment

Les travaux de recherche présentés dans ce manuscrit ont été réalisés dans le cadre du partenariat entre l'équipe D2SE (Décarbonation et Dépollution des Systèmes Energétiques) de Centrale Nantes et l'entreprise Stellantis, groupe automobile issu de la fusion entre le groupe PSA et Fiat Chrysler Automobiles.

Je tiens tout d'abord à exprimer ma gratitude à mon directeur de thèse, Alain Maiboom, pour la qualité de son encadrement, ses conseils et sa grande disponibilité. Je remercie chaleureusement mon co-directeur, Xavier Tauzia, pour avoir assisté Alain dans mon encadrement et pour sa vision complémentaire. L'expertise scientifique et technique d'Alain et de Xavier ainsi que leurs qualités humaines ont joué un rôle important dans la réussite de ma thèse de doctorat. Je les remercie pour la confiance qu'ils m'avaient accordée.

J'adresse mes sincères remerciements à toute l'équipe du partenariat et du pôle technique de D2SE qui a contribué à la réussite de mes travaux, notamment au niveau de la réalisation des essais expérimentaux et de l'élaboration du modèle numérique. Merci à Yann Le Moual, François Prevost, Camille Cuisinier, Patrick Pannier, Gaël Enée, Arnaud Mucherie, Alexis Bazin, Rémy Moreau, Jérôme Houstin et Léo Arsène.

Je tiens à remercier Olivier Davodet et Thomas Payet-Burin de l'entreprise Stellantis pour leur expertise et leur suivi régulier tout au long de mes travaux de thèse.

Je tiens à remercier les membres du jury qui se sont toutes et tous déplacé·e·s le jour de la soutenance malgré ce contexte inédit de crise sanitaire. Un grand merci à Jérôme Bellettre d'avoir présidé le jury, Christine Rousselle et Alan Kéromnès d'avoir évalué mon travail en tant que rapporteur·e·s et Alessio Dulbecco d'avoir examiné mon travail en détail.

Je remercie tou·te·s mes ami·e·s pour tous les moments agréables que j'ai passés avec eux, pour tous les voyages, les aventures, les petits-breaks et les escapades. Muchas gracias por estos recuerdos! Thank you for the shared moments! Je remercie également tou·te·s mes collègues de l'équipe D2SE pour l'ambiance exceptionnelle dans nos locaux.

Et enfin, je remercie mes parents et mon frère, pour leur amour et leur soutien tout au long de mes années d'études et d'être présents à côté de moi.

Table of Content

Introduction	1
1. Literature review.....	5
1.1. Review of combustion in spark ignition engine:	7
1.1.1. Laminar premixed flame and flame characteristics.....	8
1.1.2. Turbulent premixed flames.....	12
1.1.3. Combustion instabilities	13
1.1.4. Non-dimensional numbers and Borghi-Peters Diagram.....	14
1.2. Fundamentals of knock.....	18
1.2.1. Knock: definition and sources	19
1.2.2. Different types of observed knock.....	21
1.2.3. Knock consequences	23
1.2.4. Knock suppression methods	25
1.2.5. Impact of fuel on knock.....	35
1.3. Conclusion of the literature review.....	36
2. Experimental Setup and Numerical tools.....	39
2.1. Presentation of the engine test bench.....	41
2.2. Preliminary Campaign	47
2.2.1. Performance tests.....	48
2.2.2. Preliminary combustion tests.....	49
2.3. Numerical tools.....	73
2.3.1. Complete engine model	75
2.3.2. Combustion model	78
2.3.3. Calibration of a predictive combustion model.....	90
2.4. Conclusion on the experimental setup and numerical tools	106
3. Experimental Results.....	109
3.1. Presentation of the knock tests	111
3.2. Knock indicator	113
3.2.1. Definition of a knock indicator	113
3.2.2. Repeatability Tests.....	117
3.2.3. Cylinder choice.....	119
3.3. Impact of Knock on engine behavior	125

3.3.1.	Knock index evolution with valves timings sweeps.....	125
3.3.2.	Conclusion of knock impact on engine behavior.....	134
3.4.	Impact of injection strategies on knock occurrence.....	135
3.4.1.	Impact of injection timing during intake stroke on knock occurrence.....	137
3.4.2.	Impact of injection timing during compression stroke on knock occurrence.....	141
3.4.3.	Impact of injected fuel ratio in a double injection on knock occurrence.....	143
3.4.4.	Impact of injected fuel ratio in a triple injection on knock occurrence.....	146
3.4.5.	Conclusion of injection law strategies impact on knock occurrence.....	150
3.5.	Impact of intake air temperature on knock occurrence.....	151
3.5.1.	Knock index evolution with intake air temperature sweeps.....	152
3.5.2.	Conclusion of intake air temperature impact on knock occurrence.....	160
3.6.	Impact of coolant and lubricant oil temperatures on knock occurrence.....	161
3.6.1.	Knock index evolution with coolant and oil temperatures sweep.....	162
3.6.2.	Conclusion of coolant and oil temperatures impact on knock occurrence.....	167
3.7.	Conclusion on the experimental results.....	168
4.	Knock modeling and simulations.....	171
4.1.	Review of knock models.....	173
4.2.	Knock modeling and calibrations.....	181
4.2.1.	Calibration procedure of knock models based on the crank angle at knock onset.	184
4.2.2.	Implementation of knock detection on a Kinetics Fit model.....	193
4.3.	Simulation results on complete engine model.....	201
4.3.1.	Knock model sensitivity of valves timings on knock prediction.....	202
4.3.2.	Knock model sensitivity of injection strategies on knock prediction.....	205
4.3.3.	Knock model sensitivity of intake air temperature on knock prediction.....	208
4.3.4.	Knock model sensitivity of coolant and oil temperature on knock prediction.....	211
4.4.	Sensitivity study for perspectives.....	213
4.4.1.	Impact of heat transfer coefficient.....	213
4.4.2.	Impact of the burn rate.....	217
4.5.	Conclusion of knock modeling and simulations.....	220
5.	Conclusions and Perspectives.....	223
	References.....	229

Abbreviations

Latin letters

Letter	Unit	Signification
A	m^2	Area
$ABDC$		After bottom dead center
$ATDC$		After top dead center
CAD		Crank angle degree
D_3		Fractal exponent
Da		Damköhler number
D_m	m^2/s	Mass (species) diffusion
D_{th}	m^2/s	Thermal diffusion
EVC	CAD	Exhaust valves closing
Exp		Experimental
K	J	Mean flow kinetic energy
k	J	Turbulent flow kinetic energy
Ka		Karlovitz number
KI		Knock index
$KLSA$		Knock limit spark advance
$IMPO$		Integral of modulus of pressure oscillation
IVO	CAD	Intake valves opening
IVC	CAD	Intake valves closing
L	m	Markstein length
Le		Lewis number
L_T	m	Integral length scale
m	kg	Mass
M	kg/mol	Molar mass
Ma		Markstein number
$MAPO$	bar	Maximum amplitude of pressure oscillation
N	rpm	Engine speed
NTC		Negative Temperature Coefficient
N_{tumble}		Turbulent tumble number
p	bar	Pressure
Q	J	Heat
R	$J/kg.K$	Perfect gas constant
Re		Reynolds number
R_d	m	Flame radius
s_b	m/s	Absolute flame velocity
s_L	m/s	Laminar flame velocity
s_R	m/s	Propagation flame velocity

s_T	m/s	Turbulent flame velocity
SA	CAD	Spark advance
SOI	CAD	Start of Injection
t	s	time
T	K	Temperature
u	m/s	Flow velocity
u'	m/s	Turbulent intensity
V	m^3	Volume
v	m^3/kg	Specific volume
Y		Mass fraction
Ze		Zeldovich number

Greek letters

Letter	Unit	Signification
δ_L	m	Laminar flame thickness
δ_p	m	Thickness of preheat zone
δ_r	m	Thickness of reaction zone
η		Efficiency
θ	deg	Crank angle
κ	s^{-1}	Flame stretch
λ	$W/m.K$	Thermal conductivity
λ_T	m	Taylor length
ν	m^2/s	Kinematic viscosity
$\bar{\epsilon}$		Flame wrinkling
ρ	kg/m^3	Density
φ		Fuel-to-air equivalence ratio
τ		Ignition delay

Subscripts

air	Air
b	Burned gases
Cyl	cylinder
i	Inlet
ko	Knock onset
o	Lubricant oil
u	Unburned gases
w	Coolant water

List of figures

Figure 1-1: laminar premixed flame front [1].....	8
Figure 1-2: flame and gases velocities[1].....	9
Figure 1-3: turbulent kinetic energy cascade[1].....	12
Figure 1-4: Sketch of thermo-diffusive instabilities[1].....	13
Figure 1-5: Borghi-Peters diagram of turbulent premixed combustion [19].....	15
Figure 1-6: Peters-Borghi diagram for SI engine combustion [20].....	16
Figure 1-7: wrinkled turbulent flame [21].....	16
Figure 1-8: in-cylinder pressure, the pressure oscillation, the heat release rate, and the unburned gas temperature of a knocking case[22].....	20
Figure 1-9: comparison of a normal combustion cycle, a knocking cycle and a super knock cycle [26].....	21
Figure 1-10: spatial distribution of pre-ignition origins[36].....	22
Figure 1-11: mechanism for auto-ignition of oil droplet from piston crevice[22].....	22
Figure 1-12: examples of component damage from knocking combustion: piston melt (top left), cylinder bore scuffing(top right), gasket leakage (bottom left), cylinder head erosion (bottom right)[21].....	23
Figure 1-13: Pressure, heat release and MFB traces of the iEGR cases. [51].....	27
Figure 1-14 : In-cylinder pressure, heat release and MFB traces of the studied cases.[51].....	27
Figure 1-15: experimental results of a stratified stoichiometric mixture (SSM) and homogeneous stoichiometric mixture (HSM) from knock suppression[57].....	28
Figure 1-16 Schematic of the two zones formed [57].....	28
Figure 1-17 Super knock frequency, Fuel consumption and Exhaust temperature vs SOI1 (EOI2=170° CA ATDC, ROI2=0.3) [62].....	29
Figure 1-18: Comparison of triple-pulse injection strategies for varying DOIs Case 1 (33:33:33) versus Case 2: (50:25:25) versus Case 3 (50:40:10) for common SOIs [64].....	30
Figure 1-19: configuration of direct high pressure air injection [66].....	31
Figure 1-20: Torque vs Ignition timing for reference and first configuration [66].....	32
Figure 2-1: Engine configuration.....	42
Figure 2-2: measuring spark plug flush-mounted on the engine test bench.....	42
Figure 2-3: Horiba Mexa One gas analyzer.....	44
Figure 2-4: cylinder head, thermocouples implementation.....	45
Figure 2-5: engine bloc thermocouples implementation.....	46
Figure 2-6: in-cylinder pressures and burn rates for fuel-to-air equivalence ratio sweep at fixed spark advance (a & c) and for spark advances sweep at fixed fuel-to-air equivalence ratio (b & d) for 2000x1000 mbar.....	50
Figure 2-7: in-cylinder pressures and burn rates for fuel-to-air equivalence ratio sweep at fixed spark advance (a & c) and for spark advances sweep at fixed fuel-to-air equivalence ratio (b & d) for 4000x1000 mbar.....	51
Figure 2-8: Oil+ Coolant power of 2000x1700 mbar-R1,R2&R3 at different coolant and oil temperature levels (each division represents 0.5kW).....	52

Figure 2-9: Coolant power of 2000x1700 mbar -R1,R2&R3 at different coolant and oil temperature levels (each division represents 1kW).....	53
Figure 2-10: Oil power of 2000x1700 mbar -R1,R2&R3 at different coolant and oil temperature levels (each division represents 1kW).....	53
Figure 2-11: thermocouples positions.....	54
Figure 2-12: Head temperature of 2000x1700 mbar -R1,R2&R3 at different coolant and oil temperature levels (each division represents 10°C).....	54
Figure 2-13: Upper block temperature of 2000x1700 mbar -R1,R2&R3 at different coolant and oil temperature levels (each division represents 10°C).....	55
Figure 2-14: Bottom block temperature of 2000x1700 mbar -R1,R2&R3 at different coolant and oil temperature levels (each division represents 10°C).....	55
Figure 2-15: mass flow rate and matrix of oil and coolant temperature sweep of OP1-R1 (each division is 2mg/str).....	57
Figure 2-16: : in-cylinder pressures (a&b) and burn rates (c&d) of 2000x700 mbar in R1&R3 at different coolant and oil temperature levels.....	58
Figure 2-17: in-cylinder pressures (a&b) and burn rates (c&d) of 2000x700 mbar-R1&R3 at different coolant and oil temperature levels.....	60
Figure 2-18: in-cylinder pressures (a&b) and burn rates (c&d) of 2000x1000 mbar-R1&R3 at different coolant and oil temperature levels.....	61
Figure 2-19: in-cylinder pressures (a&b) and burn rates (c&d) of 2000x1700 mbar-R1&R3 at different coolant and oil temperature levels.....	63
Figure 2-20: in-cylinder pressure (a) and burn rate (b) of 2000x1700 mbar-R1&R3 at different coolant and oil temperature levels.....	64
Figure 2-21: in-cylinder pressures (a&b) and burn rates (c&d) of 2000x1000 mbar-R1&R2 at different coolant and oil temperature levels.....	65
Figure 2-22: Intake and exhaust valves timings at 1550x1400 mbar	67
Figure 2-23: incylinder pressures (top) and burn rates (bottom) for the valves timings sweep considered for 1550x1400 mbar.....	68
Figure 2-24: residuals in function of valves overlapping for all camshaftstimings at 1550x1400 mbar.....	69
Figure 2-25: Intake and exhaust valves timings considered at 1550x900 mbar.....	70
Figure 2-26: in-cylinder pressures (top) and burn rates (bottom) for the considered valves timings at 1550x900 mbar.....	70
Figure 2-27: residuals in function of valves overlapping for all camshaftstimings at 1550x900 mbar.....	72
Figure 2-28: Overview of the complete engine model.....	74
Figure 2-29: intake line upstream the compressor.....	75
Figure 2-30: conversion on the compressor inlet duct into 10 GT-Power components.....	76
Figure 2-31 :Eddy burn-up combustion scheme[20].....	78
Figure 2-32 : difference between simulation and experimental results regarding the burn rate at different engine speeds from part load to wide open throttle [85]	81
Figure 2-33:fractal combustion model scheme[20].....	82

Figure 2-34: Comparison between the 3D simulation and the CFM-1D model developed by IFP[91].....	86
Figure 2-35: points used for the optimization process of SITurb-1.....	93
Figure 2-36: evolution of the SITurb-1 parameters in function of the number of cases considered	94
Figure 2-37: measured vs predicted for SITurb-1 CA50 within [-3,3] CAD range	95
Figure 2-38: measured vs predicted for SITurb-1 CA1075 within [-3,3] CAD range.....	95
Figure 2-39: measured vs predicted for SITurb-1 IMEP within [-5%,5%] range	96
Figure 2-40: measured vs predicted for SITurb-1 maximum pressure within [-5,5] bar range	96
Figure 2-41: points used for the optimization process of SITurb-2.....	98
Figure 2-42: zoom on the points used for the optimization process of SITurb-2.....	99
Figure 2-43: experimental vs SITurb prediction of in-cylinder pressures (a&b) and burn rates (c&d) for 2 operating points at 1550 rpm	100
Figure 2-44: experimental vs SITurb prediction of in-cylinder pressures (a&b) and burn rates (c&d) for 2 operating points at 2000 rpm	101
Figure 2-45: experimental vs SITurb prediction of in-cylinder pressures (a&b) and burn rates (c&d) for 2 operating points at 2500 rpm	102
Figure 2-46: measured vs predicted for SITurb-2 CA50 within [-3,3] CAD range	103
Figure 2-47: measured vs predicted for SITurb-2 CA1075 within [-3,3] CAD range.....	103
Figure 2-48: measured vs predicted for SITurb-2 maximum pressure within [-5,5] bar range....	104
Figure 2-49: measured vs predicted for SITurb-2 crank angle at maximum pressure within [-3,3] CAD range.....	104
Figure 2-50: measured vs predicted for SITurb-2 IMEP within [-5%,5%] range	105
Figure 3-1: representation of DKl indicator of Breccq, the illustration is limited to the MAPO value in the y-axis and to window length in the x-axis [103].....	114
Figure 3-2: knock index evolution with the threshold at 1550x1500mbar	116
Figure 3-3: repeatability tests required to compute the accuracy of the knock index.....	117
Figure 3-4: in-cylinder pressure traces for some cycles for the cylinder 1 (a), cylinder 2 (b&c) and cylinder 3 (d) at 2000x1700 mbar with 4 CAD of spark advance increase.....	119
Figure 3-5: in-cylinder pressure traces for 4 cycles (a, b, c & d) for the cylinder 1, cylinder 2 and cylinder 3 at 2000x1700 mbar with 4 CAD of spark advance increase.....	120
Figure 3-6: knock index versus spark advance increase for the three cylinders at 2000x1700 mbar	121
Figure 3-7: cylinder liner average temperatures for the three cylinders.....	122
Figure 3-8: cylinder temperature zones.....	123
Figure 3-9: example of the knock index evolution with different strategies adopted.....	123
Figure 3-10: overlapping valves timing for 1550x1500 mbar (a) with a zoom on the overlap (b) 125	
Figure 3-11: not overlapping valves timing for 1550x1500 mbar (a) with a zoom on the overlap (b)	126
Figure 3-12: Knock index evolution with spark advance at 1550x1500 mbar	127
Figure 3-13: percentage of residuals confined inside the cylinder at 1550x1500 mbar	128
Figure 3-14: unburned gas temperature at 1550x1500 mbar.....	129
Figure 3-15: CO concentrations at 1550x1500 mbar	130

Figure 3-16: IMEP evolution with spark advance at 1550x1500 mbar	130
Figure 3-17: Knock index evolution with spark advance at 2000x1700 mbar	131
Figure 3-18: percentage of residuals confined inside the cylinder at 2000x1700 mbar	132
Figure 3-19: Knock index evolution with spark advance at 2500x1700 mbar	132
Figure 3-20: in-cylinder mass at 2500x1700 mbar.....	133
Figure 3-21: valves timings and injection timings for the single injection strategie at 1550x1500 mbar.....	137
Figure 3-22: Knock index evolution with injection timing sweep during the intake stroke at 1550x1500 mbar	138
Figure 3-23: in-cylinder pressure (a) and burn rate (b) evolution with injection timing sweep during the intake stroke at 1550x1500 mbar and at 0 spark advance increase	138
Figure 3-24: Knock index evolution with injection timing sweep during the intake stroke at 2000x1700 mbar	139
Figure 3-25: Knock index evolution with injection timing sweep during the intake stroke at 2500x1700 mbar	140
Figure 3-26: Knock index evolution with injection timing sweep during the compression stroke at 1550x1500 mbar	141
Figure 3-27: in-cylinder pressure (a) and burn rate (b) evolution with injection timing sweep during the compression stroke at 1550x1500 mbar and at 0 spark advance increase.....	141
Figure 3-28: knock intensity for homogeneous stoichiometrix mixture (HSM) and stratified mixture as studied by Bai et al. [57].....	142
Figure 3-29: valves timings and injection timings for the double injection strategy at 1550x1500 mbar.....	143
Figure 3-30: Knock index evolution with injection ratios sweep in a double injection strategy at 1550x1500 mbar	144
Figure 3-31: in-cylinder pressure evolution with injected fuel ratio sweep in a double injection at 1550x1500 mbar and at 0 spark advance increase.....	144
Figure 3-32: Knock index evolution with injection ratios sweep in a double injection strategy at 2000x1700 mbar	145
Figure 3-33: valves timings and injection timings for the triple injection strategy at 1550x1500 mbar.....	146
Figure 3-34: Knock index evolution with injection ratios sweep in a triple injection strategy at 1550x1500 mbar	147
Figure 3-35: in-cylinder pressure evolution with injected fuel ratio sweep in a double and triple injection strategies at 1550x1500 mbar and at 0 spark advance increase	148
Figure 3-36: valves timings and injection timings for the double injection strategy at 2000x1700 mbar.....	148
Figure 3-37: Knock index evolution with injection ratios sweep in a triple injection strategy at 2000x1700 mbar	149
Figure 3-38: knock index evolution with spark advance increase for intake air temperatures sweep at 1550x1500 mbar	152
Figure 3-39: maximum unburned zone temperature.....	153

Figure 3-40: in-cylinder pressure (a) and burn rate (b) evolution with intake air temperature sweeps at 1550x1500 mbar overlapping and at 0 spark advance increase.....	153
Figure 3-41: knock index evolution with spark advance increase for intake air temperatures sweep at 1550x1500 mbar for both overlapping and not overlapping settings.....	154
Figure 3-42: in-cylinder pressure (a) and burn rate (b) evolution with intake air temperature sweeps at 1550x1500 mbar and at 0 spark advance increase	154
Figure 3-43: Mass of air trapped at 1550x1500 mbar with overlap	155
Figure 3-44: torque at 1550x1500 mbar.....	156
Figure 3-45: knock index evolution with spark advance increase for intake air temperatures sweep at 2500x1700 mbar for both overlapping and not overlapping settings.....	157
Figure 3-46: in-cylinder pressure (a) and burn rate (b) evolution with intake air temperature sweeps at 2500x1700 mbar and at 0 spark advance increase	157
Figure 3-47: in-cylinder air mass for intake air temperatures sweep at 2500x1700 mbar for both overlapping and not overlapping settings.....	158
Figure 3-48: in-cylinder air mass for intake air temperatures sweep at 2500x1700 mbar for iso mass settings.....	158
Figure 3-49: knock index evolution with spark advance increase for intake air temperatures sweep at 2500x1700 mbar for both overlapping and not overlapping and iso mass settings	159
Figure 3-50: in-cylinder pressure (a) and burn rate (b) evolution with intake air temperature sweeps at 2500x1700 mbar and at 0 spark advance increase for both overlap and isomass settings	159
Figure 3-51: knock index evolution with spark advance increase for coolant and oil temperatures sweep at 1550x1500 mbar.....	162
Figure 3-52: in-cylinder pressure (a) and burn rates (b) of the 5 settings of coolant and oil temperatures at 0 spark advance increase for 1550x1500 mbar	163
Figure 3-53: knock index evolution with spark advance increase for coolant and oil temperatures sweep at 2500x1700 mbar.....	164
Figure 3-54: knock index evolution with spark advance increase for coolant and oil temperatures sweep at iso mass conditions at 2500x1700 mbar.....	165
Figure 3-55: n-cylinder pressure (a) and burn rates (b) of the 5 settings of coolant and oil temperatures at 0 spark advance increase for 2500x1700 mbar.....	166
Figure 4-1: the correlation between knock onset and engine speed according to Shu et al.[101]	174
Figure 4-2: schematic showing the NTC behavior and typical temperature histories of low-temperature, NTC and high-temperature auto-ignition regimes [129].....	177
Figure 4-3: Comparison between detailed chemical kinetic calculations (line) and combined global expressions (dash-dot) for the ignition delays of stoichiometric n-heptane/air mixture under 10 (red) and 20 (blue) atm [129].....	178
Figure 4-4: Developing detonation peninsula on plot of ξ against ε [28] [137].....	179
Figure 4-5: Comparison between estimated and experimental knock onset crank angles by Beccari et al. [141].....	181
Figure 4-6: predicted vs experimental crank angle at knock onset [46].....	182
Figure 4-7: Measured versus simulated knock angle for 3000 rpm and Stoichiometric, rich and lean conditions [124].....	182

Figure 4-8: Experimental knock onset vs. predicted knock onset time for different predictive knock models [121].....	183
Figure 4-9: experimental crank angle at knock onset	187
Figure 4-10: crank angle at knock onset variation with spark advance increase.....	188
Figure 4-11: number of knocking cycles evolution with spark advance increase	189
Figure 4-12: experimental vs predicted crank angle at knock onset for 1550x1500 mbar overlapping case for the different spark advances (calibration points).....	190
Figure 4-13: experimental vs predicted crank angle at knock onset for 1550x1500 mbar not overlapping case for the different spark advances (validation points).....	190
Figure 4-14: knock probability for 1550x1500 mbar	191
Figure 4-15: optimization designs obtained at the end of the calibration procedure.....	195
Figure 4-16: knock probability for the various design obtained on the new calibration procedure at 1550x1500 mbar overlapping (calibration points)	196
Figure 4-17: crank at knock onset for the various design obtained on the new calibration procedure at 1550x1500 mbar overlapping (calibration points).....	196
Figure 4-18: knock probability for the various design obtained on the new calibration procedure at 1550x1500 mbar no overlapping (validation points).....	197
Figure 4-19: crank at knock onset for the various design obtained on the new calibration procedure at 1550x1500 mbar no overlapping (validation points)	198
Figure 4-20: knock probability for the various design obtained on the new calibration procedure at 2000x1700 mbar overlapping (calibration points)	198
Figure 4-21: knock probability for the various design obtained on the new calibration procedure at 2500x1700 mbar overlapping (calibration points)	199
Figure 4-22: knock probability for the various design obtained on the new calibration procedure at 2000x1700 mbar no overlapping (validation points).....	199
Figure 4-23: knock probability for the various design obtained on the new calibration procedure at 2500x1700 mbar no overlapping (validation points).....	200
Figure 4-24: experimental vs predicted knock index for both overlapping and not overlapping case at 1550x1500 mbar	202
Figure 4-25: experimental vs predicted knock index for both overlapping and not overlapping case at 2000x1700 mbar	203
Figure 4-26: experimental vs predicted knock index for both overlapping and not overlapping case at 2500x1700 mbar	204
Figure 4-27: experimental vs predicted knock index for the injection timing of a single injection for 1550x1500 mbar	205
Figure 4-28: knock probability predictions for single injection strategy at 1550x1500 mbar	206
Figure 4-29: experimental vs predicted knock index for the injection timing of a single injection for 2000x1700mbar	206
Figure 4-30: knock probability predictions for single injection strategy at 2000x1700 mbar	207
Figure 4-31: experimental vs predicted knock index for intake air temperatures variations for 1550x1500 mbar	208
Figure 4-32: knock probability predictions for intake air temperature sweeps at 1550x1500 mbar	208

Figure 4-33: experimental vs predicted knock index for intake air temperatures variations at iso mass for 2500x1700 mbar	209
Figure 4-34: knock probability predictions for intake air temperature sweeps at 2500x1700 mbar	210
Figure 4-35: experimental vs predicted knock index for coolant and oil temperatures variations for 1550x1500 mbar	211
Figure 4-36: knock probability predictions for coolant and oil temperature sweeps at 1550x1500 mbar.....	212
Figure 4-37: experimental vs predicted air mass trapped in function of the heat transfer multiplier	213
Figure 4-38: experimental vs SITurb prediction of in-cylinder pressures (a&b) and burn rates (c&d) for 2 operating points at 1550 rpm with the sensitivity of heat transfer multiplier	214
Figure 4-39: experimental vs SITurb prediction of in-cylinder pressures (a&b) and burn rates (c&d) for 2 operating points at 2000 rpm with the sensitivity of heat transfer multiplier	215
Figure 4-40: experimental vs SITurb prediction of in-cylinder pressures (a&b) and burn rates (c&d) for 2 operating points at 2500 rpm with the sensitivity of heat transfer multiplier	215
Figure 4-41: knock probability predictions with 1550x1500 overlapping with heat transfer multiplier sweep	216
Figure 4-42: knock probability predictions with 1550x1500 no overlapping with heat transfer multiplier sweep.....	216
Figure 4-43: knock probability predictions at 1550x1500 overlapping with both SITurb and experimental burn rate imposed	217
Figure 4-44: crank angle at knock onset predictions at 1550x1500 overlapping with both SITurb and experimental burn rate imposed	217
Figure 4-45: knock probability predictions at 1550x1500 no overlapping with both SITurb and experimental burn rate imposed	218
Figure 4-46: crank angle at knock onset predictions at 1550x1500 no overlapping with both SITurb and experimental burn rate imposed.....	218

List of tables

Table 2-1: Engine Specifications.....	41
Table 2-2: Types, ranges and accuracies of the sensors implemented on the engine bench.....	43
Table 2-3: technical data for the measuring spark plug 6115C.....	44
Table 2-4: Exhaust component analyzer range.....	45
Table 2-5: coolant and oil temperature sweep for 2000x700 mbar-R1	56
Table 2-6: 2000x700 mbar in R1 settings.....	58
Table 2-7: 2000x700 mbar R3 settings	59
Table 2-8: 2000x1000 mbar in R1 settings	60
Table 2-9: 2000x1700 mabr in R1 settings	62
Table 2-10: 2000x1700 mbar in R3 settings.....	63
Table 2-11: 2000x1000 mbar in R2 settings.....	65
Table 2-12: valves timings sweep considered at 1550 rpm and $P_{adm}=1400$ mbar	67
Table 2-13: camshafts timings considered for 1550 rpm x 900 mbar	69
Table 2-14: values of the calibrated parameters of the SITurb-1 model	94
Table 2-15: values of the calibrated parameters of the SITurb-1 and SITurb-2 models.....	99
Table 3-1: list of the operating points used and their corresponding calibrated spark advance...	115
Table 3-2: simulation of 12 consecutive cycles and their corresponding MAPO values.....	117
Table 3-3: Operating points specifications.....	125
Table 3-4: coolant and oil temperatures sweep at 1550x1500 mbar.....	162
Table 3-5: coolant and oil temperatures sweep at 2500x1700 mbar.....	163
Table 3-6: coolant and oil temperatures sweep at 2500x1700 mbar while maintaining the in-cylinder mass constant.....	164
Table 4-1: summary of the some models and their correlation.....	175
Table 4-2: values of the Kinetics Fit model constant	176
Table 4-3: overview of the operating points with the different spark advances increase used for calibration in blue frames and the spark advances increase used for validation in orange frames	186
Table 4-4: multipliers values obtained for both Douaud&Eyzat and Kinetics Fit models at the end of the calibration procedure	186
Table 4-5: overview of the operating points with the different spark advances increase used for calibration in blue frames	193
Table 4-6: experimental "knock probability" and "crank angle on knock onset" values.....	194
Table 4-7: functions values of the best designs	195

Introduction

In the field of automotive propulsion, regulations are getting more and more restrictive. They initially focused on the pollutant emissions such as nitrogen oxides or particles, and for several years now, they have focused on greenhouse gas emissions, with a growing desire on the part of states to eliminate direct emissions of CO₂ from the vehicle fleet. We are also witnessing a gradual electrification of the vehicle fleet (100% electric or plug-in hybrid vehicles). Nonetheless, two reasons require to continue developing spark-ignition engines: in the short and medium term, the spark-ignition engines, alone or hybrid, will still be marketed during the transitional phase of ramp-up of 100% electric vehicles; in the longer term, the development and use of synthetic fuels may make it possible to decarbonize spark-ignition engines which can then retain a place for certain applications.

Regarding spark-ignition internal combustion engines, various technologies have been introduced to reduce their consumption and CO₂ emissions. Among these, downsizing which consists in reducing the displacement while maintaining the same level of performance thanks to the use of turbocharging. More generally, the search for good thermodynamic efficiency often leads to the use of high pressures and temperatures during the cycle, in particular during combustion. Spark ignition engines then run into the problem of auto-ignition or knock.

Knock is an abnormal combustion triggered at high engine loads and can lead to engine failure. Knock is the name attributed to the audible sound that is heard due to the in-cylinder pressure oscillations as a result of the end-gas auto-ignition.

Thereafter, several technologies have been implemented on spark ignition engines to reduce or delay knock such as variable timing systems (intake and / or exhaust), direct fuel injection, exhaust gas recirculation, water injection, or the variable compression ratio. Nevertheless, we often remain dependent on a trade-off between efficiency and the occurrence of knock which leads to a suboptimal spark advance.

Moreover, these technologies have led to a very significant increase in the complexity of engines, and therefore of their design and development. This makes it increasingly necessary to use numerical simulation (3D CFD or OD-1D) to perform these tasks by performing a reasonable number of experimental tests. It is in this context that a partnership was created between Ecole Centrale Nantes and Stellantis entitled in French "vers une conception 100% numérique des chaînes de traction" which translates in English to "towards a 100% numerical design of powertrains". The objective is to design models and calibration methodologies for the design and development of powertrains. The thesis presented in this manuscript was carried out in the frame of this partnership. It relates more specifically to the experimental characterization and the development of a methodology for

calibrating a model for predicting the onset of knocking, intended to be used in the engine pre-calibration phase.

Even if many works on knock exist in the literature, there is no exhaustive database, to our knowledge, with the same definition of the occurrence of knock, presenting the impact of the various engine control parameters on knock. There is not either a database on the physical parameters of influence such as the air filling, the equivalence ratio of the trapped mixture, the wall temperatures, the combustion rate, or the residual gas rate. This is why the first objective of this thesis is to constitute such a database.

Concerning the knock modeling, there is also a large number of models, but the calibration procedure is generally not very detailed and the validation is partial. The second objective of the thesis is to provide a complete procedure for modeling the occurrence of knocking combustion on a turbocharged spark-ignition engine.

Also, this thesis manuscript is composed of five chapters whose contents are as follows:

The first chapter is a review of the literature on combustion development and knock fundamentals. General concepts of combustion such as flame characteristics, turbulence and non-dimensional numbers are introduced and the fundamentals of knocking are presented along with the consequences and methods of knocking suppression.

The second chapter first presents the experimental setup used in the context of this thesis. Subsequently, an experimental campaign focusing on the characterization of the various engine control parameters on combustion is presented. This is a necessary step before the experimental study on the occurrence of knock, as it is closely related to the rate of combustion (heat release). Finally, the general numerical tools are described (complete engine model and combustion model); in particular, a calibration procedure for a OD combustion model (heat release) is presented.

The third chapter deals with the experimental analysis of the occurrence of the knock, in particular the impact of the various engine control parameters such as: parameters relating to camshaft timings, the temperature of the intake air, the profile of fuel injection into the combustion chamber, coolant and oil temperatures.

The fourth chapter deals with the implementation of a methodology for calibrating a knock model from the literature. First, a bibliographic review of knocking models is presented. Then a calibration methodology based on the experimental tests presented in the previous chapter is developed. A comparison between calculations and experiments is then carried out.

Finally, the fifth chapter is a general conclusion of the thesis manuscript and includes perspectives for future work.

Dans le domaine de la propulsion automobile, les réglementations sont toujours plus contraignantes. Si elles ont d'abord porté essentiellement sur les émissions de polluants tels que oxydes d'azote ou particules, elles portent depuis plusieurs années sur les émissions de gaz à effet de serre, avec une volonté croissante des états à supprimer à terme les émissions directes de CO₂ du parc automobile. On assiste aussi à une électrification progressive du parc automobile (véhicules 100% électriques ou hybrides rechargeables). Deux raisons nécessitent néanmoins de continuer de développer des moteurs thermiques à allumage commandé : à court et moyen termes, le moteur thermique à allumage commandé, seul ou hybridé, sera encore commercialisé pendant la phase transitoire de montée en charge des véhicules 100% électriques ; à plus long terme, le développement et l'usage de carburants de synthèse permettront peut-être de décarboner les moteurs thermiques qui pourront alors garder une place pour certaines applications.

S'agissant des moteurs thermiques à allumage commandé, pour réduire leur consommation et leurs émissions de CO₂, différentes technologies ont été apportées. Parmi celles-ci, le downsizing consiste à réduire la cylindrée tout en maintenant un même niveau de performance grâce au recours à la suralimentation. Plus généralement, la recherche d'un bon rendement thermodynamique conduit souvent à mettre en œuvre des fortes pressions et températures au cours du cycle, notamment pendant la combustion. Les moteurs à allumage commandé se heurtent alors au problème d'autoallumage ou cliquetis.

Le cliquetis est une combustion anormale déclenchée à de fortes charges pouvant être destructrice. C'est le nom attribué au bruit métallique et aigu découlant des oscillations de la pression dans le cylindre à l'issue de l'auto-allumage des gaz frais. Plusieurs technologies ont été mises en œuvre sur les moteurs à allumage commandé pour réduire ou retarder le cliquetis comme les systèmes de distribution variable (admission et/ou échappement), l'injection directe de carburant, la recirculation des gaz d'échappement, l'injection d'eau, ou encore le taux de compression variable. Néanmoins, on reste souvent tributaire d'un compromis entre rendement et apparition du cliquetis qui conduit à une avance à l'allumage non optimale.

Ces technologies ont conduit à une complexification très importante des moteurs, et donc de leur conception et de leur mise au point. Cela rend de plus en plus nécessaire le recours à la simulation numérique (CFD 3D ou OD-1D) pour réaliser ces tâches en réalisant un nombre de tests expérimentaux raisonnable. C'est dans ce contexte qu'a été créé un partenariat entre l'Ecole Centrale Nantes et Stellantis intitulé « vers une conception 100% numérique des chaînes de traction ». L'objectif est de concevoir des modèles et méthodologies de calibration des modèles pour la conception et la mise au point des chaînes de traction. Le travail de thèse présenté dans ce mémoire a été réalisé dans le cadre de ce partenariat et porte plus spécifiquement sur la caractérisation expérimentale et la mise au point d'une méthodologie de calibration d'un modèle de prédiction d'apparition du cliquetis, destiné à être utilisé en phase de pré-calibration du moteur.

Même si de nombreux travaux portant sur le cliquetis existent dans la littérature, il n'existe à notre connaissance de base de données exhaustives, présentant, avec une même définition de l'apparition de cliquetis, l'impact des différents paramètres de contrôle moteur sur l'apparition de cliquetis, mais également sur les paramètres physiques d'influence tels que le remplissage en air, la richesse du mélange enfermé, les températures de parois, le taux de combustion, ou encore le taux de gaz résiduels. C'est pourquoi le premier objectif de cette thèse est de constituer une telle base de données.

Concernant la modélisation du cliquetis, il existe également un grand nombre de modèles, mais la procédure de calibration est en générale peu détaillée et la validation partielle. Le deuxième objectif de la thèse est de proposer une procédure complète de modélisation de l'apparition du cliquetis sur un moteur à allumage commandé suralimenté.

Aussi, ce manuscrit de thèse est composé des cinq chapitres dont les contenus sont les suivants:

Le premier chapitre est une revue de la littérature sur le développement de la combustion et les fondamentaux du cliquetis. Des concepts généraux de combustion tels que les caractéristiques de la flamme, la turbulence et les nombres non dimensionnels sont introduits et les principes fondamentaux du cliquetis sont présentés ainsi que les conséquences et les méthodes de suppression du cliquetis.

Le deuxième chapitre présente dans un premier temps le dispositif expérimental utilisé dans le cadre de cette thèse. Par la suite, une campagne expérimentale portant sur la caractérisation des différents paramètres de contrôle moteur sur la combustion est présentée. Il s'agit d'une étape nécessaire avant l'étude expérimentale portant sur l'apparition du cliquetis, dans la mesure où celui-ci est étroitement lié à la vitesse de combustion (dégagement de chaleur). Enfin, les outils numériques généraux sont décrits (modèle complet du moteur et modèle de combustion); une procédure de calibration d'un modèle OD de combustion (dégagement de chaleur) est notamment présentée.

Le troisième chapitre porte sur l'analyse expérimentale de l'apparition du cliquetis, en particulier l'impact des différents paramètres de contrôle moteur tels que: paramètres relatifs à la distribution, la température de l'air d'admission, le profil d'injection de carburant dans la chambre de combustion, les températures du liquide de refroidissement et de l'huile.

Le quatrième chapitre porte sur la mise en place d'une méthodologie de calibration d'un modèle de cliquetis issu de la littérature. Dans un premier temps, une revue bibliographique de modèles de cliquetis est présentée. Puis une méthodologie de calibration s'appuyant sur les essais expérimentaux présentés au chapitre précédent est développée; une comparaison calculs-expériences est ensuite menée.

Enfin, le cinquième chapitre est une conclusion générale du manuscrit de thèse et comprend des perspectives pour des travaux futurs.

1. Literature review

This chapter constitutes a first literature survey. As the appearance of knock is partially linked to the combustion development, it is first necessary to recall the general concepts relating to premixed combustion in spark ignition engines, as well as certain characteristics of the flame, turbulence and non-dimensional numbers.

In a second part, we present the phenomenology of the knocking combustion, its consequences, as well as the means to delay its appearance.

Note that the bibliographic study will be completed in Chapter 2 with the presentation of phenomenological models of combustion in spark ignition engines, and in Chapter 4 with the presentation of knock detection models.

Ce chapitre constitue une première étude bibliographique. L'apparition du cliquetis étant liée pour partie au déroulement de la combustion, il convient dans un premier temps de rappeler les concepts généraux relatifs à la combustion de type pré-mélange dans les moteurs à allumage commandé, ainsi que certaines caractéristiques de la flamme, la turbulence et les nombres non dimensionnels.

Dans une seconde partie, on présente la phénoménologie du cliquetis, ses conséquences, ainsi que les moyens pour repousser son apparition.

A noter que l'étude bibliographique sera complétée au chapitre 2 avec la présentation des modèles phénoménologiques de combustion dans les moteurs à allumage commandé, et au chapitre 4 avec la présentation des modèles de détection de cliquetis.

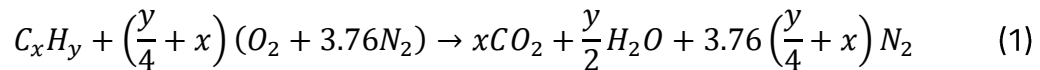
1.1. Review of combustion in spark ignition engine:

The combustion process is the power part of the engine operating cycle. It is the working stroke of a four-stroke internal combustion engine where all the energy of the fuel ignited with the presence of air, is released in a very short time. The produced high temperatures, high pressures and burned gases expand within the combustion chamber walls and transfer work into the piston. When the spark plug discharges, the combustion process starts with an ignition of the premixed fuel, air and residual burned gases. A small flame kernel starts to develop and then grows into a turbulent flame and propagates across the combustion chamber. It then extinguishes near the chamber walls. This unsteadily growing flame is confined within the specific geometry of the combustion chamber and the piston. In this section, some general concepts on combustion development will be reviewed: laminar and turbulent premixed flames will be presented along with some of the flame characteristics. Combustion instabilities will be later on introduced in that section followed by a definition of some non-dimensional numbers that are employed to characterize the flame.

1.1.1. Laminar premixed flame and flame characteristics

When a fuel/air mixture ignites, in other terms, when the mixture temperature becomes higher than the ignition temperature, a chemical combustion reaction starts. Heat is released during such a reaction, part of it diffuses towards the fresh gases which will be consumed by a combustion flame. This flame leaves behind it products of the combustion.

The global chemical reaction for this combustion process of a hydrocarbon under stoichiometric conditions is presented as the following:



According to the theory of Mallard and Le Châtelier 1883, the fresh gases and the burnt gases are separated by a region formed of 2 zones: the reaction zone and the preheat zone as it can be seen in the figure 1-1:

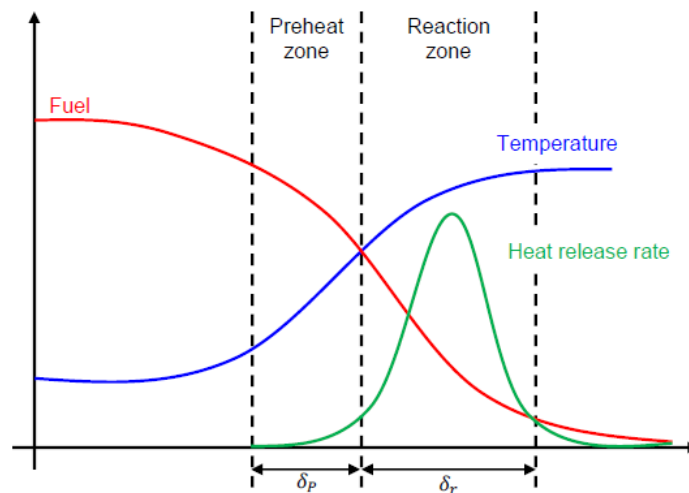


Figure 1-1: laminar premixed flame front [1]

In the preheat zone, the heat flux coming from the burned gases increase the temperature of the nearest fresh gases up to a certain thickness δ_p . The heat diffusion is dominant in this zone, however, some minor chemical reactions could take place. In the reaction zone, chemical reactions are enchainned over a thickness δ_r mass and heat diffusions occur and generate heat towards the fresh gases. The peak of the heat release is located in this zone which is as well called the flame front [1]

1.1.1.1. Flame Speed:

The flame front propagates in the direction of the fresh gases. The flame speed can be defined in several ways. The definition that was retained is the one provided by Poinso et Veynante [2]:

The laminar flame speed s_L : it is a global magnitude which is associated to the speed of consumption of fresh gases in the case of a planar flame.

The absolute velocity s_b : this magnitude corresponds to the flame front normal velocity in a fixed coordinate system and it is called as well the flame propagation velocity.

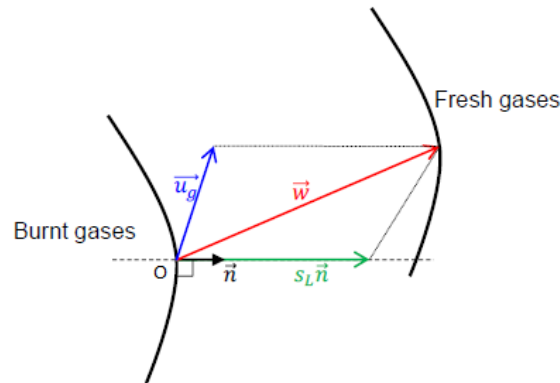


Figure 1-2: flame and gases velocities[1]

In figure 1-2, let's consider a point O located on the flame front. \vec{n} is the vector normal to the flame front directed towards the fresh gases. \vec{w} is the displacement velocity of the flame front with respect to a fixed coordinate system. \vec{u}_g represents the velocity of the fresh gases in front of the flame front. The laminar flame speed s_L is by definition normal to the flame front. Thus the following vector relation can be deduced:

$$\vec{w} = s_L \vec{n} + \vec{u}_g \quad (2)$$

In a planar or spherical flame, \vec{u}_g and \vec{w} are collinear with \vec{n} . In this particular case, the flame propagation velocity $s_b = \vec{w} \cdot \vec{n}$ and so it is directly the sum of the laminar flame speed s_L (or speed of consumption of fresh gases) and the fresh gases velocity u_g .

$$s_b = s_L + u_g \quad (3)$$

1.1.1.2. Flame thickness

The laminar flame thickness is an important parameter in the characterization of laminar flames. Many definitions can be found in the literature [3], however we will present the following:

According to Zeldovich [4], the laminar flame thickness δ_L^0 is defined as the ratio between the thermal diffusivity D_{th} and the unstretched laminar flame speed s_L^0

$$\delta_L^0 = \frac{D_{th}}{s_L^0} = \frac{\lambda_u}{c_{p,u} \rho_u s_L^0} \quad (4)$$

As it can be seen the thermal diffusivity is a function of the thermal conductivity of the fresh gases λ_u , the heat capacity of the fresh gases $c_{p,u}$ and the density of the fresh gases ρ_u .

Poinsot and Veynante explained that in practice this flame thickness is very small [2]. For his definition of flame thickness, Blint [5] takes into account the temperatures of the fresh gases T_u and the burnt gases T_b :

$$\delta_L = 2\delta_L^0 \left(\frac{T_b}{T_u} \right)^{0.7} \quad (5)$$

Spalding defined the flame thickness as the following:

$$\delta_L = \frac{T_b - T_u}{(|\vec{grad}T|)_{max}} \quad (6)$$

Blint's definition is considered as the most representative of the flame thickness for the numerical simulation purposes, however it requires the computation of the final temperature T_b which is not usually easy to compute experimentally. The Spalding definition is the closest to the experimental results, however it requires the complete temperature profile. Zeldovich definition lies on the assumption of the equilibrium between the thermal and the molecular diffusions [6]

The above defined flame thickness is considered to be equal to the preheat zone thickness δ_p and the reaction zone thickness δ_r .

1.1.1.3. Flame stretch

The concept of flame stretch has been highlighted since the middle of the 20th century thanks to the works of Karlovitz [7] and Markstein [8]. The flame stretch represents the rate of increase of the flame surface in function of the time according the following definition given by Williams [9]:

$$\kappa = \frac{1}{A} \frac{dA}{dt} \quad (7)$$

Two physical phenomena influence the flame front stretch: the velocity gradient in front of the flame and the curvature of the flame front itself. In the particular case of a spherical flame, the flame curvature only contributes to the flame stretch which is therefore written in function of the flame radius R_f . s_b is the flame propagation velocity as the radius change.

$$\kappa = \frac{1}{A} \frac{dA}{dt} = \frac{2}{R_f} \frac{dR_f}{dt} = \frac{2s_b}{R_f} \quad (8)$$

Under the assumption of constant pressure combustion, the flame stretch of a spherical flame is defined in function of the laminar speed s_L [1]

$$\kappa = \frac{1}{A} \frac{dA}{dt} = \frac{2}{R_f} \frac{dR_f}{dt} = \frac{2s_b}{R_f} = \frac{2}{R_f} \frac{\rho_u}{\rho_b} s_L \quad (9)$$

In the literature, it was pointed out that the flame stretch has an impact on the laminar flame velocity. We will present these relationships in the following [10][11]:

A Markstein number for the fresh gases Ma_u , is defined as the ratio of the Markstein length for the fresh gases L_u to the flame thickness δ_L^0 :

$$Ma_u = \frac{L_u}{\delta_L^0} \quad (10)$$

A linear relationship between the un-stretched and the stretched laminar velocity is assumed [10][12]

$$s_L = s_L^0 - L_u \kappa \quad (11)$$

A Markstein number for the burnt gases Ma_b , is defined as the ratio of the Markstein length for the burnt gases L_b to the flame thickness δ_L^0 :

$$Ma_b = \frac{L_b}{\delta_L^0} \quad (12)$$

L_b is calculated using the Zeldovich number Ze . The Zeldovich number is a function of the activation energy of the fuel-air mixture E , the perfect gas constant R , the fresh gas temperature T_u and the burnt gas temperature T_b [11]

$$Ze = \frac{E}{RT_b^2} (T_b - T_u) \quad (13)$$

$$L_b \approx \frac{Ze}{2} \left(1 - \frac{1}{Le}\right) \delta_L^0 \quad (14)$$

1.1.1.4. Impact of fuel

Aleiferis et al. conducted a study of combustion of gasoline, iso-octane, methane, ethanol and butanol fuels in direct-injection spark-ignition engine. They examined various key operating conditions : stoichiometric ($\phi = 1$) and lean ($\phi = 0.83$) settings, 20° and 90° engine coolant temperature; and they fixed the engine speed to 1500 rpm and the intake pressure to 0.5 bar [13].

Aleiferis et al. reported that flame growth ($\phi = 1$) was fastest for ethanol, followed by butanol, gasoline and isooctane with similar trends for 20° and 90°. When compared to at a fixed flame radii, methane had the fastest flame speed. Butanol burning velocity was slower than ethanol's burning velocity by 8% and faster than gasoline's by 5%. They also analyzed the mixture transport properties for all the fuels and suggested that methane and the alcohols might fall within the transition region of "corrugated flame" to "thin reaction zone" combustion regimes associated with partially "thickened flame fronts". Fuels whose flames propagate faster showed some lower Markstein number.

1.1.2. Turbulent premixed flames

A turbulent phenomenon is characterized by a presence of some eddies of different sizes that are responsible for the fluctuation of the velocities, heat transfer and mass diffusion in the turbulent flow.

This spectrum in figure 1-3 has regions of specific physical processes whose characteristic length scale is well defined:

Energy production region where the eddies are the largest and they contain the greatest part of turbulent kinetic energy and have a large fluctuation. The associated length scale is the integral length scale L_T and it represents the size of such eddies

Energy transfer region where the energy transfer from the big structures to the small structures happens. The associated length scale is the Taylor microscale λ_T [14]

$$\lambda_T = \sqrt{15 \frac{L_T \nu}{u'}} \quad (15)$$

ν is the kinematic viscosity and u' is the turbulent velocity field or the turbulent intensity.

Energy dissipation region where the eddies frequencies is the biggest and they dissipate the turbulent kinetic energy. The eddies have a small length and the associated length scale is the Kolmogorov length scale [14]

$$\eta_k = L_T \left(\frac{u' L_T}{\nu} \right)^{0.75} \quad (16)$$

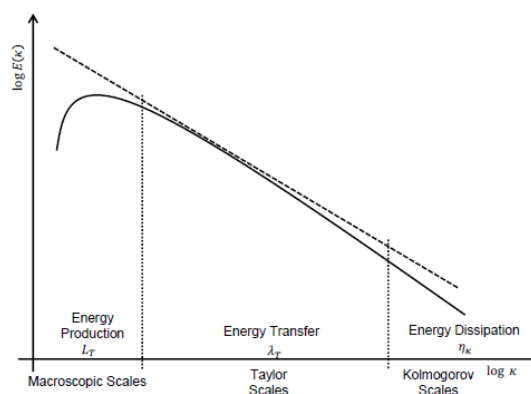


Figure 1-3: turbulent kinetic energy cascade[1]

In combustion modeling, an estimation of the turbulent intensity u' and the integral length scale L_T is needed. In a homogeneous and isotropic turbulence:

$$u' = \sqrt{\frac{2}{3} k} \quad (17)$$

1.1.3. Combustion instabilities

Various instabilities such as gravitational, hydrodynamic and thermo diffusive might influence the flame dynamics during its propagation. They affect the homogeneities of the molecular and thermal diffusions which lead to local perturbations of the equilibrium between the heat diffusion and the species diffusion. Perturbations of the laminar flame may appear and might result in a deformation of the flame front or an abnormal displacement.

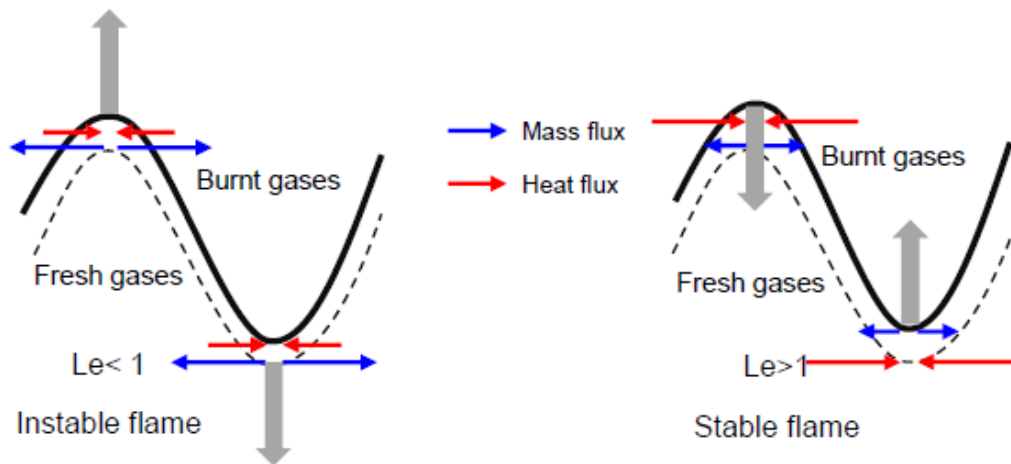


Figure 1-4: Sketch of thermo-diffusive instabilities[1]

1.1.3.1. Thermo-diffusive instabilities:

They are also known as Rayleigh-Taylor instabilities, are provoked by the competition of the heat flux and the species flux on a flame front. This could either lead to a flame stabilization or to more flame wrinkling.

The Lewis number Le characterizes this competition:

$$Le = \frac{D_{th}}{D_m} \quad (18)$$

Where D_{th} is the thermal diffusivity and D_m is the molecular or species diffusivity.

If the species diffusivity is higher than the heat diffusivity, which means $Le < 1$, when the flame front is convex towards the fresh gases, the concentration of species fluxes lead to an increase in the local velocity s_L that becomes higher than s_L^0 . Thus the flame front will locally displace towards the fresh gases, thus increasing the wrinkling. When the flame front is convex towards the burnt gases, the flame velocity s_L becomes less than s_L^0 and the flame front will displace locally towards the burned gases. This globally increases the flame wrinkling. [2]

Following a similar analysis in the case of thermal diffusivity higher than the molecular diffusivity ($Le > 1$), the flame is stable, the flame surface decreases since the wrinkling tends to decrease.

1.1.4. Non-dimensional numbers and Borghi-Peters Diagram

The non-dimensional numbers that are used to characterize the turbulent flames are:

The turbulent Reynolds number: it describes the competition between the inertial forces (destabilizing events) and the viscous forces (stabilizing events). High Reynolds numbers means large fluctuations [15] [16]

$$Re_t = \frac{u' L_T}{\nu} = \frac{u' L_T}{s_L \delta_L} \quad (19)$$

The Damköhler number which is the ratio of the turbulent time scale to the chemical time scale. It correlates the time for turbulent mixing with the time of the completion of chemical reactions. A high Damköhler number describes a combustion whose limiting factor is the mixing process and where the reaction happens quickly. Whereas, low Damköhler numbers describes combustions where the chemical kinetics are the limiting factors and the mixing rates are high. They are known by "well-stirred reactors" [17]

$$Da = \frac{\tau_T}{\tau_{ch}} = \frac{\left(\frac{L_T}{u'}\right)}{\left(\frac{\delta_L}{s_L}\right)} \quad (20)$$

The Karlovitz number which is the ratio of the chemical time scale to the Kolmogorov time scale. It compares the thickness of the region in which the chemical reactions take place with the Kolmogorov length scale. [7] [16]

$$Ka = \frac{\tau_{ch}}{\tau_K} \quad (21)$$

Under the assumption of homogeneous and isotropic turbulence, the number becomes [16].

$$Ka = \left(\frac{L_T}{\delta_L}\right)^{-0.5} \left(\frac{u'}{s_L}\right)^{1.5} \quad (22)$$

These non-dimensional numbers allows to classify the turbulent flames according their flame front structure into different regimes of turbulent combustion. By the comparison of the characteristic turbulent time scale and the chemical time scale, the different physical and chemical phenomena controlling the flame can be described. A better understanding of the phenomenology of the combustion and the flame structure lead to a more physical combustion modeling. The different regimes of turbulent combustion are presented in the Borghi-Peters diagram such as the figure 1-5 and 1-6 [18] [16].

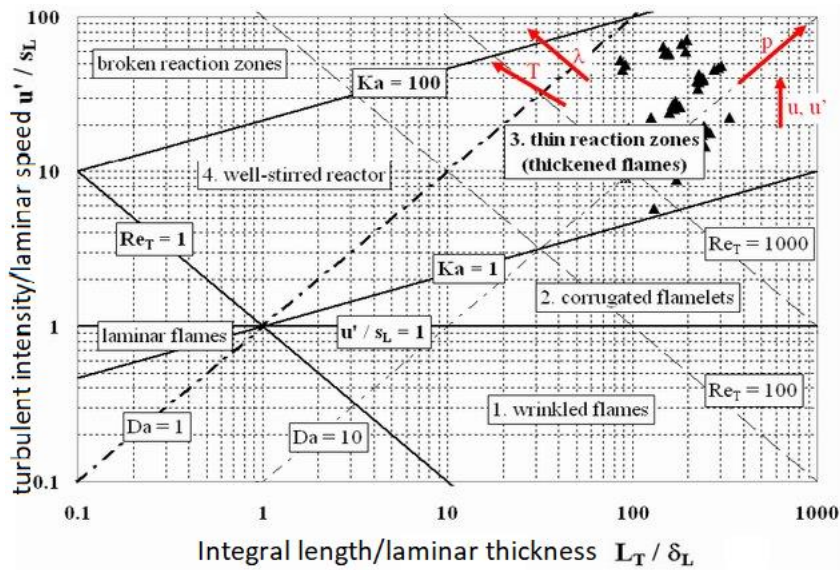


Figure 1-5: Borghi-Peters diagram of turbulent premixed combustion [19]

In the Borghi-Peters diagram, the ratio of the turbulent intensity over the laminar speed (u'/s_L) is plotted against the ratio of the integral length over the laminar thickness (L_T/δ_L).

1.1.4.1. The flamelets regime:

This regime is defined for $Re_t > 1$ and $Ka < 1$. It is characterized by chemical time scales lesser than the Kolmogorov time scales. This implies that the chemical kinetics of the flame are rapid in front of the flow turbulence thus a natural deformation of the flame front can be observed. 2 cases of the flamelets regime can be defined where the turbulent flames can locally have all the characteristics of the laminar flames.

The wrinkled flamelet regime where $u' < s_L$, the mechanism of laminar propagation is stronger than the corrugations of the flame front. The turbulent flame front is only wrinkled without causing any interactions between the different small flamelets formed on the flame front. The flame thickness is not modified.

The corrugated flamelets regime where $u' > s_L$, the corrugation mechanism is strong. The eddies of the turbulent flow have enough energy to modify the flame front. Interactions between local flame fronts are possible, pockets of fresh gases may detach from the continuous front to appear in the burned gases and pockets of burned gases may appear as well in the fresh gases.

The flamelet regime is then an assembly of different flames having locally the characteristics of the laminar flames. The turbulence affects then the surface of the flame whereas the flame front is still considered infinitely thin. The premixed turbulent combustion in the flamelets regimes can be modeled then by the principals of the laminar

flamelets considering the interaction between the flame front and the turbulence is of kinematic nature [1] [15] [16] [18]

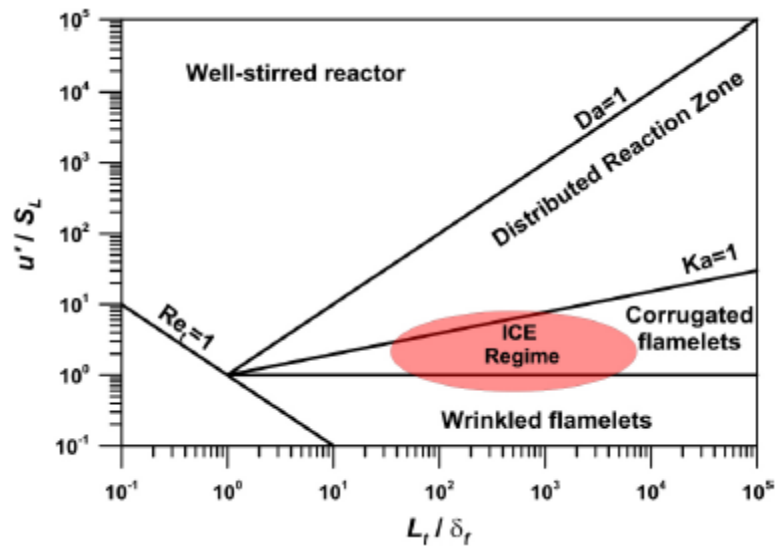


Figure 1-6: Peters-Borghi diagram for SI engine combustion [20]

1.1.4.2. Propagation of the flame:

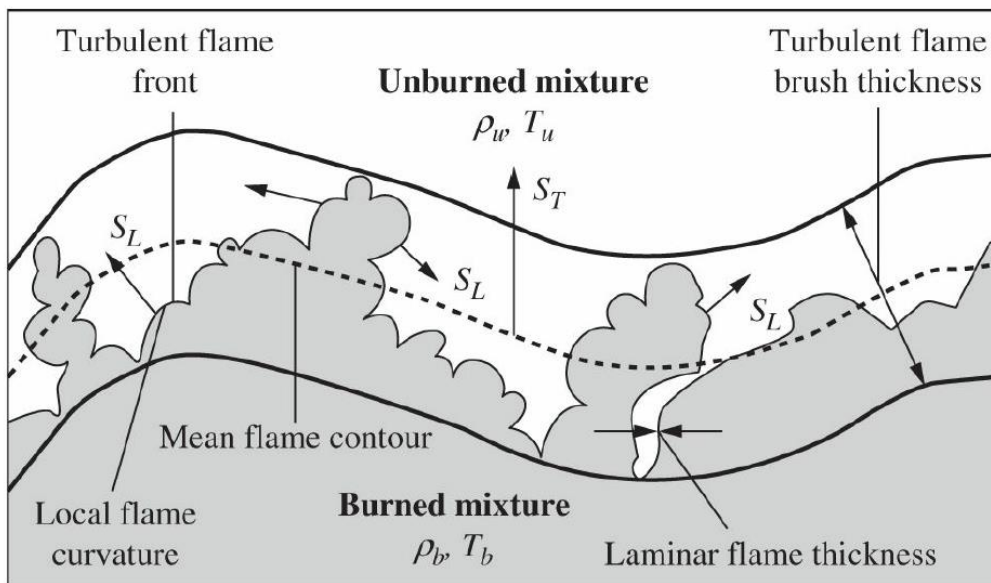


Figure 1-7: wrinkled turbulent flame [21]

The combustion process starts with the discharge of the spark plug that generates a high temperature kernel. This is the initial quasi-laminar highly stretched flame kernel that grows and transits to a turbulent flame distorted by the flow. The flame is then fully-developed and its front is wrinkled by the turbulence. The flame propagates throughout the combustion chamber and the greatest part of the energy is released. When the flame comes in contact with the chamber walls, it extinguishes.

The combustion process compresses the unburned mixture ahead of the flame and displaces it towards the chamber walls. The burned elements are also compressed and displaced towards the spark plug [21].

As it can be seen in figure 1-7, a wrinkled and turbulent flame is examined. Flames in spark-ignition engines are placed in the flamelets regimes. The contour of this turbulent flame front shows wrinkles and corrugations at various length scales.

A_T is the turbulent flame surface and it is the total surface of the contour.

A_L is the contour of a fictitious mean flame surface which is considered spherical in OD modeling.

Both the flame front contour (side of the fresh gases and the burned gases) define the turbulent flame thickness δ_T . The turbulent flame speed, s_T , is the flame propagation speed in the fresh gases.

This turbulent flame can be regarded as many flame elements of the reaction zone which have a laminar flame thickness δ_L and propagates towards the fresh gases with a laminar flame speed s_L .

The wrinkling factor, \mathcal{E} , is the ratio of the turbulent to laminar flame speed or the ratio of turbulent to mean flame surface. It diminishes during the extinguishment mechanism due the flow boundary layer, heat losses towards the cold walls and the confinement of the flame by the walls [17]

$$\mathcal{E} = \frac{s_T}{s_L} = \frac{A_T}{A_L} \quad (23)$$

Then, the burning mass rate can be written as:

$$\frac{dm_b}{dt} = \rho_u A_T s_L = \rho_u A_L s_T = \rho_u A_L s_L \mathcal{E} \quad (24)$$

1.2. Fundamentals of knock

Knock, an abnormal combustion, is a spontaneous ignition of the charge rapidly releasing chemical energy after spark discharge. It is usually accompanied by pressure fluctuations and an audible sound and might lead to engine failure.

Knocking combustion in internal combustion engine is major concern in automotive industry and it represent the hub of this PhD thesis. In order to characterize the knocking combustion in a stock turbocharged spark-ignition automotive internal combustion engine and to model knock apparition on a complete engine model knock fundamentals will be elaborated in this section. Different types of observed knock and knock sources will be reviewed, knock consequences will be then presented and some methods to suppress knock will be examined later on.

1.2.1. Knock: definition and sources

Knock and surface (or localized) ignitions are the two major phenomena of the abnormal combustions provided that they can cause the engine failure and they limit the engine operation[21].

Knock is defined as the name of the noise which is transmitted through the engine structure when a spontaneous ignition of the end-gas ahead of the propagating flame occurs. When this abnormal combustion process takes place, there is usually an extremely rapid release of chemical energy in the end-gas, causing very high local pressures and the propagation of pressure waves of high amplitude across the combustion chamber.

Surface(or localized) ignition is a spontaneous ignition of the mixture initiated by a hot spot on the combustion chamber walls (overheated valve, spark plug, carbon, and floating deposits, oil droplets) rather than the normal spark discharge. It can occur before the occurrence of the spark (preignition) or after (post ignition).

Following both knock and surface ignition, a flame develops and starts to propagate across the combustion chamber. These spontaneous ignition phenomena are governed by the temperature and pressure history of the end gas, thus the combustion phasing and development. Taking into consideration that knock phenomena vary substantially from cycle to cycle, when auto-ignition occurs repeatedly during a series of combustion events, the phenomenon is called spark-knock: this spark-knock is controllable by the spark advance: advancing the spark discharge increases the knock intensity and occurrence and delaying the spark discharge decreases the appearance of knock[21].

Knock in spark-ignited engines arises from the auto-ignition of the unburned end-gas ahead of the propagating flame. A knocking combustion process has thus two stages: a flame propagation induced by the spark discharge and a pressure oscillation caused by the end-gas autoignition. In the following figure 1-8, the in-cylinder pressure, the pressure oscillation, the heat release rate, and the unburned gas temperature of a knocking case are presented.

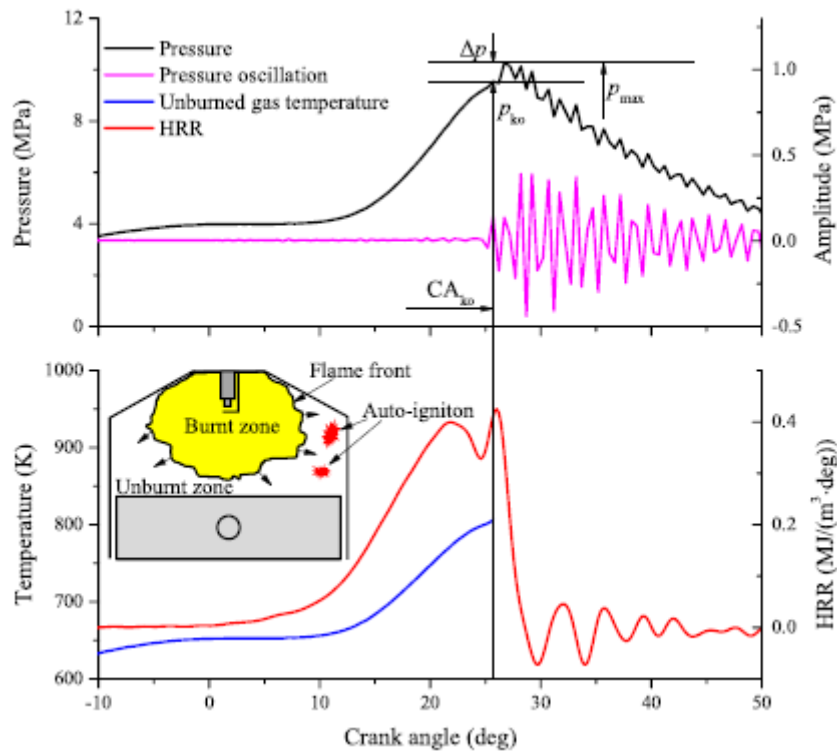


Figure 1-8: in-cylinder pressure, the pressure oscillation, the heat release rate, and the unburned gas temperature of a knocking case[22]

CA_{ko} is the crank angle degree at knock onset and P_{ko} is the pressure value at knock onset. The spark triggered flame propagates from the ignition timing to the CA_{ko} and the pressure reaches the value of P_{ko}. In the auto-ignition stage, the pressure increases substantially reaching a peak value of P_{max} and starts to oscillate with decaying amplitude. The heat release rate increases during the first combustion stage and then starts to drop due to the piston downward movement and the heat transfer. The heat release rate starts to increase again in the auto-ignition stage and then drops and oscillates in a decaying way. The unburned gas temperature rises stably in the combustion phases due to the compression heating of the burned gases. At CA_{ko}, the temperature and pressure of the unburned end gases reach a critical level causing their auto-ignition. A pressure wave then propagates in the combustion chamber, reflecting back and forth from the walls causing the pressure oscillations [22].

1.2.2. Different types of observed knock

Recently, the need to reduce fuel consumption and increase specific power has led to the development of high boosted spark-ignited gasoline engines. At high loads and low engine speeds, this development was challenged by the apparition of a new mode of engine knock, the super knock[23]. Super knock was also termed sporadic preignition [21], unwanted preignition, mega knock [24], low-speed pre-ignition[25], deto-knock [26], stochastic preignition [27], developing detonation [28] and subsequent front propagation [29]. A single super knock event can severely damage the engine instantaneously due to the high-pressure peak and the associated pressure oscillations being developed [22]. These super knock events have little or no direct relationship with the engine control parameters (intake temperatures, air-to-fuel equivalence ratio, and spark advance). Thus applying knock suppression methods such as delaying spark timing or charge cooling are effective to suppress super knock making it a major obstacle for improving the boost level of turbocharged spark-ignited gasoline engines[22].

In-cylinder pressures and heat release rates of a normal combustion cycle, a knocking cycle (denoted conventional knock), and super knock are shown in the figure 1-9.

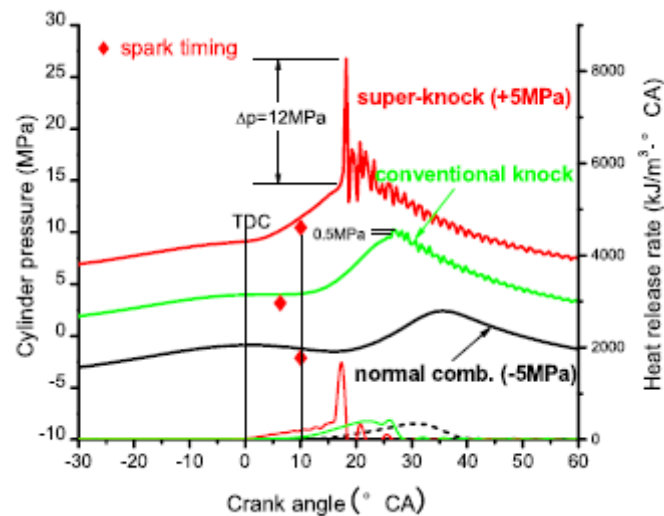


Figure 1-9: comparison of a normal combustion cycle, a knocking cycle and a super knock cycle [26]

Since super knock is a severe engine knock triggered by a sporadically pre-ignition. The causes of the pre-ignition can be divided into structured hot spots such as the valves and the spark plug, and unstructured hot spots such as oil droplets, gasoline/oil mixing [26] [24] [25] [30] and floating deposits [31] [32] in the combustion chamber as it can be seen in figure 1-10. These hot spots increase the local temperature and cause auto-ignition. In addition, gas-phase auto-ignition [33],[34], fuel properties [31] are also causes of pre-ignition apparition. Optimizing the combustion chamber design can help to avoid pre-ignition caused by structured hot spots.[22] The pre-ignition that develops into a super-

knock is not a homogeneous gas combustion process: pre-ignition occurs via an obvious flame kernel growth and a flame propagation [35] [31].

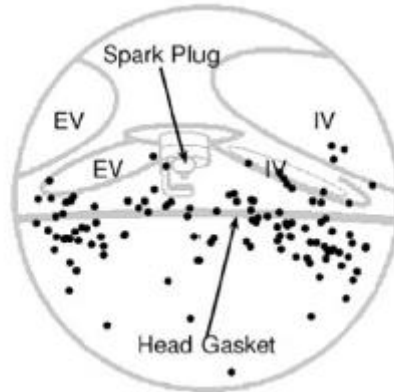


Figure 1-10: spatial distribution of pre-ignition origins[36]

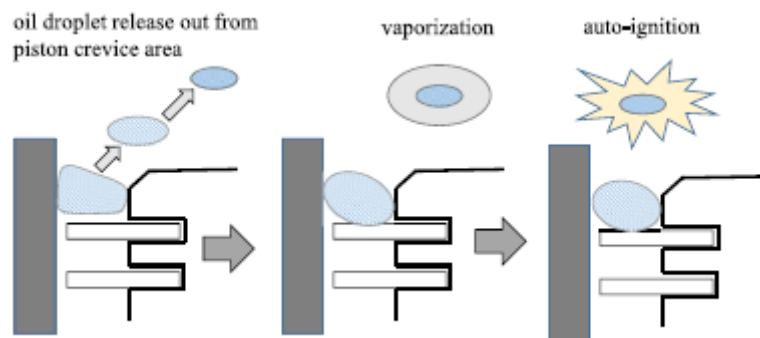


Figure 1-11: mechanism for auto-ignition of oil droplet from piston crevice[22]

As it can be seen in figure 1-11, when oil droplets enter the combustion chamber, it could become a hot spot because some of its formulation components (detergent, antioxidant, corrosion inhibitor etc.) may have a shorter ignition delay and subsequently could auto-ignite [22].

1.2.3. Knock consequences

When knock occurs in spark-ignited gasoline engines, high-frequency pressure oscillations are observed. This phenomenon can be damaging to the engine in different ways [21]

- Piston crown melting
- Piston ring sticking
- Cylinder bore scuffing
- Piston ring-land cracking
- Cylinder head gasket leakage
- Cylinder head erosion

In the figure 1-12, typical damages caused by knock are presented.

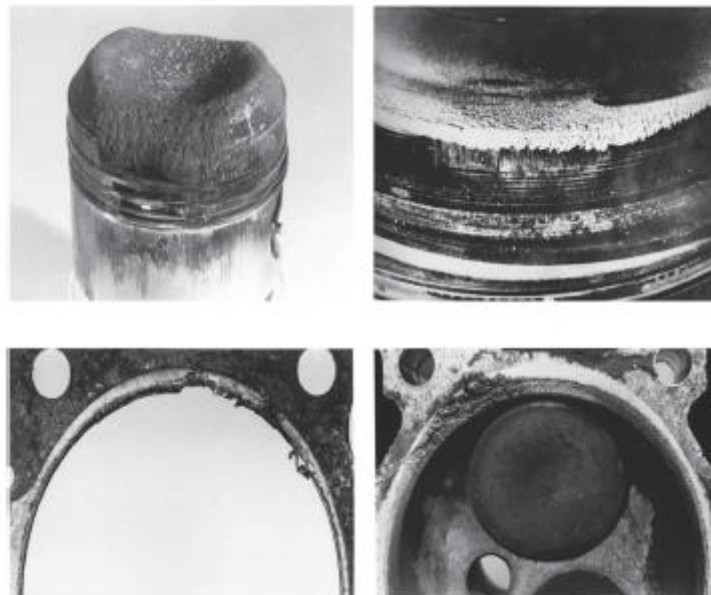


Figure 1-12: examples of component damage from knocking combustion: piston melt (top left), cylinder bore scuffing (top right), gasket leakage (bottom left), cylinder head erosion (bottom right)[21]

Knocking combustion is observed in three modes and it is the consequence of the auto ignition of what we call an exothermic center. Exothermic centers are “easier to ignition regions” in the end gas whose composition (fuel vapor, air and residuals) lead to a shorter induction time (required time to trigger the oxidation chemistry) or in other terms faster auto-ignition delay. These shorter induction times are caused by local inhomogeneities and variations in the thermodynamic states and the mode of the observed knock is dependant on the size and the concentrations of these exothermic centers [21].

The three modes are [21]

- Deflagration which causes small pressure fluctuation and in this mode, the flame propagates in a way similar to the flame caused by the spark plug and it is caused by a small exothermic center.
- Thermal explosion: it is characterized by larger exothermic centers. It causes some light damage and pressure oscillations are moderate.
- Developing detonation which is the most violent and it rarely occurs. It is caused by medium-sized exothermic centers and it generates large pressure oscillations which might cause some significant damage.

1.2.4. Knock suppression methods

Knock is a competition between the spark triggered flame in the engine and the auto-ignition of the end gas. Thus, to avoid knock, the time for the flame propagation τ_1 should be less than the time of the auto-ignition τ_2 [21].

1.2.4.1. Delaying spark timing

The most effective method to avoid knock is delaying spark timing as it reduces simultaneously the end gas temperature and pressure which prolongs the ignition delay τ_2 . Excessive spark timing delay leads to un-optimized combustions accompanied by lower mean temperatures and pressures in the combustion chamber which deteriorates engine performance and efficiency [37] [38] [39]

1.2.4.2. Fuel enrichment

Fuel characteristics play a role in controlling engine knock, thus improving octane number helps to suppress knock. This can be achieved by introducing antiknock additives like ethers and alcohols which increase the end-gas ignition delay τ_2 [22].

Enriching the mixture increases the effect of charge cooling, decreases the air-fuel mixture temperature thus prolonging the end-gas ignition delay which helps to suppress the knock. Nevertheless, fuel enrichment increases the emissions of HC and CO and reduces the fuel economy [22].

Duchaussoy et al. [40] studied the effect of dilution on knock suppression, combustion phasing and emissions. When increasing the fuel enrichment, the combustion and energy release were faster. The excess fuel acts as a diluent and cools the mixture because of fuel vaporization. Enrichment reduced the knock and increased the IMEP however it degrades the indicated efficiency.

Singh et al. [41] conducted experiments on a single cylinder engine equipped with both port fuel injection and direct injection. The enrichment was done through direct injection. As Enrichment increases, knock can be suppressed as the charge cooling effect start to dominate. However, a compromise is needed between increased knock from lower quantities of fuel injection before the spark and misfires from too much fuel enrichment as the flame is quenched. They also noticed that Injecting excess fuel directly onto the flame is a better strategy but it could lead to pre-ignition events at boosted conditions. In fact fuel impinge in the liner and oil-fuel droplets are formed leading to pre-ignition events that could happen earlier and earlier in the cycle leading to much catastrophic engine failure.

1.2.4.3. Exhaust gas recirculation

Exhaust gas recirculation has been regarded as an effective knock suppressing method in advanced spark-ignition engines by many authors[38] [42] [43] [44] [45] [46] [47] [48] [49] [50]. The addition of cooled exhaust gas recycle EGR can help to dilute the mixture and limits its temperature rise and therefore the autoignition time is increased so that the knock would be suppressed and high compression ratio and boosting level can be reached [21].

Duchaussoy [40] compared lean burn and EGR and found that the combustion phasing was very different. As the mixture got leaner, the combustion slowed too much when compared to EGR. Both lean condition and EGR suppressed knock and reduced the turbine inlet temperature. However, the efficiency dropped under lean condition whereas the indicated efficiency increased when EGR was used. When EGR surpassed a certain amount, the combustion slowed down and efficiency dropped too. Hence, a trade-off between efficiency and knock suppression should be defined for the amount of EGR

Xie et al demonstrated that higher external exhaust gas recirculation rate slows down the early flame development, which is responsible for the higher cyclic fluctuation of combustion[51]. Xie et al. also studied the effects of internal and external gas recirculation at iso-recirculated gas conditions. It was demonstrated that a moderate increase in the internal exhaust gas recirculation rate from 9.8% to 13%, initial flame kernel formation is faster. This is beneficial to the combustion by accelerating the early flame development, advancing the combustion timing, and stabilizing the combustion. However, With the internal exhaust gas recirculation rate further increased to 19.6%, the mean expansion speed of the flame front decreases, resulting in a retarded early flame development and a slower heat release, which leads to severe deterioration in the combustion stability [51]. This can be observed in figures 1-13 and 1-14.

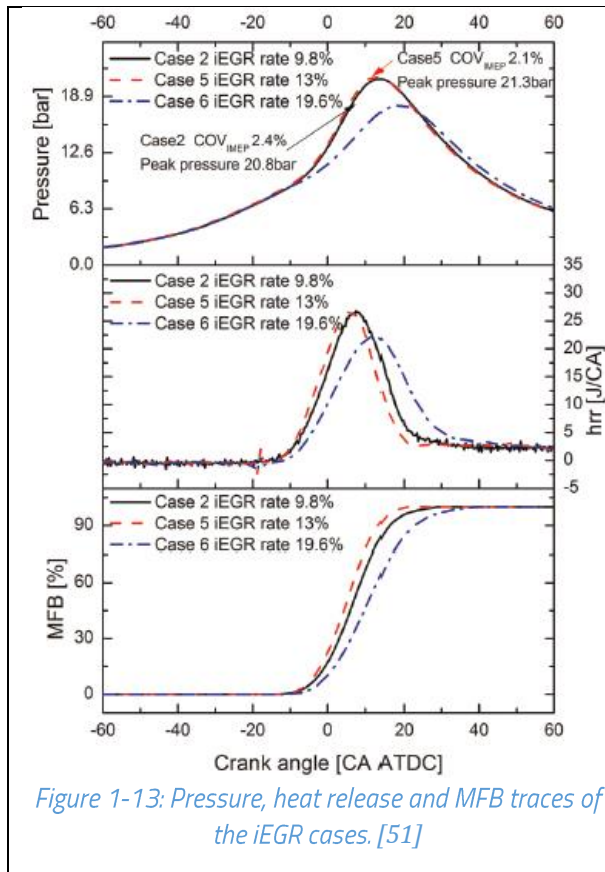


Figure 1-13: Pressure, heat release and MFB traces of the iEGR cases. [51]

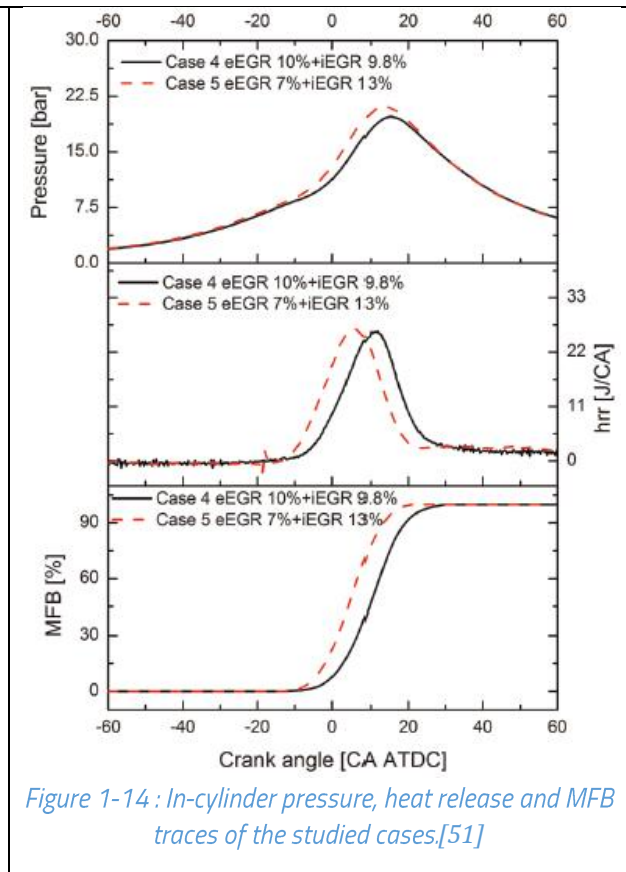


Figure 1-14: In-cylinder pressure, heat release and MFB traces of the studied cases.[51]

Potteau et al. [52] conducted experiments on a 2L turbo charged spark ignition engine and two EGR circuits : a Low pressure EGR (LP-EGR) circuit and a High pressure EGR (HP-EGR) circuit. They observed that both LP and HP EGR reduced the in-cylinder temperature suppressing the knock and allowed the spark to be advanced. Both circuits also reduced the BSFC. But HP-EGR could not be used at lower engine speeds as there is not enough gas going to the turbine. HP-EGR was feasible at higher RPMs while LP-EGR was feasible at both low and high RPMs. Teodosio et al. [53] also conducted experiments and simulations to observe the effects of LP-EGR on fuel consumption, knock suppression and turbine inlet temperature. They found that as EGR increases, the turbine inlet temperature decreases, BSFC is reduced and knock is suppressed.

Kumano et al. [54] integrated both HP-EGR and LP-EGR in the same engine. There was tiny or no noticeable difference in knock margin and they observed that the amount of spark advance possible with HP-EGR and LP-EGR were almost the same. However, the amount of exhaust that can be sent to the intake was more in case of LP-EGR than HP-EGR leading to higher torque gains in the LP-EGR case.

1.2.4.4. Mixture Stratification

Mixture stratification is generally achieved through multiple injection strategy where total mass of the fuel is injected at different times in different amounts. A stratified mixture is an alternative approach to delay or suppress knock and it is achieved through direct injection [55] [56] [57] [58] [38] [59] [60] [61]. In fact, Fuel directly injected in the cylinder lower the mixture temperature due to the cooling effects associated with fuel evaporation.

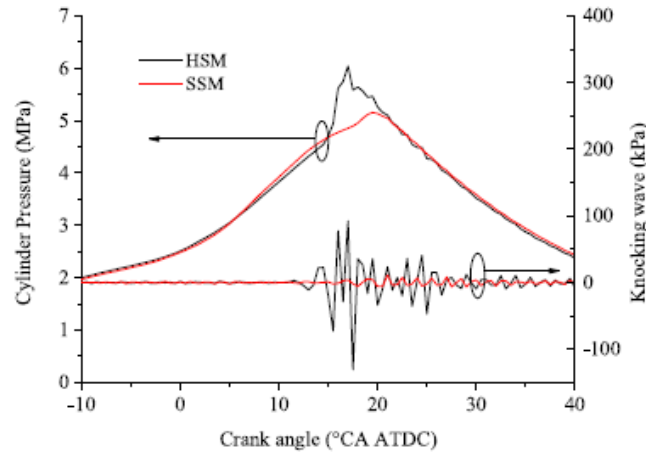


Figure 1-15: experimental results of a stratified stoichiometric mixture (SSM) and homogeneous stoichiometric mixture (HSM) from knock suppression[57]

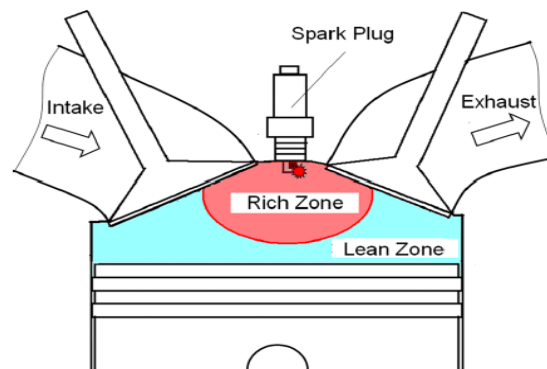


Figure 1-16 Schematic of the two zones formed [57]

Bai et al. [57] tested the concept of two zone homogeneity. In the figure 1-16, the first injection created a lean zone near the cylinder walls and a late second injection created a rich zone around the spark plug for an overall global stoichiometric mixture. When the spark is initiated, the flame velocity increases due to the rich mixture near the plug. However, the combined lean mixture near the walls and the cooling effect of the second injection, the end gas mixture will not reach auto-ignition condition before the arrival of the spark induced flame. The experiments showed that a lean zone with a stoichiometric ratio of 0.8 and rich zone with a stoichiometric ratio of 1.2 resulted in the best knock suppression as it can be

seen on the cylinder pressure curves and knock waves in figure 1-15. Also, they observed that late second injection led to inhomogeneity as there is not enough time for the fuel to mix. As, the mass of fuel in the second injection increased, the zone near the spark plug became richer leading to incomplete combustion and reduction in combustion efficiency. Hence, a trade off should be found between the second injection timing and the quantity of injected fuel.

Bai et al. also compared the knock suppression abilities of Homogenous Stoichiometric Mixture (HSM) and Stratified Stoichiometric Mixture (SSM). SSM suppressed the knock significantly better than HSM. [57].

Wang et al. [62] did experiments on a turbo charged gasoline direct injection engine with double injection in the intake stroke to prevent super knock. They found that a single injection would not suppress super knock no matter the injection timing.

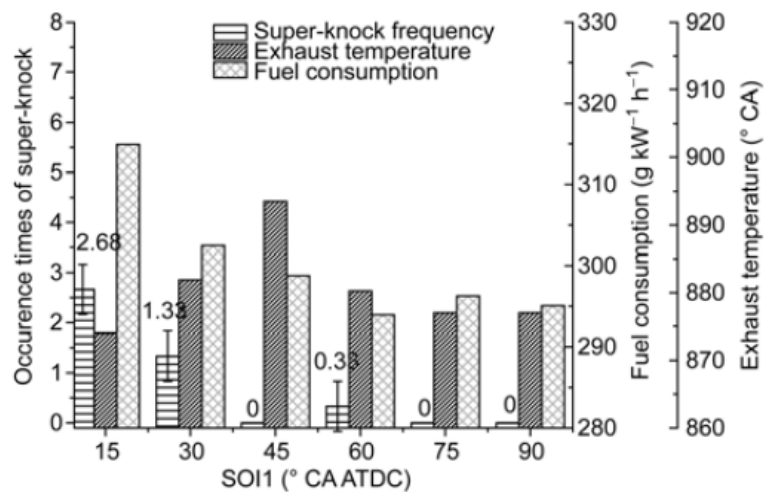


Figure 1-17 Super knock frequency, Fuel consumption and Exhaust temperature vs SOI1 (EOI2=170° CA ATDC, ROI2=0.3)[62]

They concluded that a double injection strategy with SOI1 in the middle of the intake stroke and EOI2 at the end of the intake stroke with mass ratio of second injection of 0.3 is the best strategy to suppress knock effectively. In addition to this, the NO_x, HC and soot emissions were also low when compared to other combinations of the above-mentioned parameters [62]. Their results are plotted in figure 1-17.

Zhou et al. [63] tested the effect of retarding the injection timing to suppress knock. The experiments were carried out on a single cylinder engine. They observed the knock percentage decreased from 60% to 10% and knock intensity decreased as the injection timing is delayed. However, the combustion stability was affected and cycle to cycle variations increased. To counter this, they increased the inlet air temperature. This resulted in a much stable combustion and also reduction in cycle-to-cycle variation.

Singh et al. [64] carried out an extensive campaign double and triple injection strategies, varying fuel injection pressure, injection duration and fuel injected ratios. They found out that knock index can be kept low in a single injection strategy only if the injection timing is retarded. However, this led to a decrease in IMEP. In order to stop the decrease in IMEP, the intake pressure had to be increased but it was compensated by an increase of CoV of IMEP. With double injection, as the injection timing of the second pulse is retarded, the knock index decreased due to the cooling effect of the late injection. The later the second injection from the first, the better the knock suppression. This came at a cost of decrease in IMEP. When the injection duration of the second pulse was more than the first, the knock index was reduced. They also concluded that increasing the duration of second pulse which increases the mass of fuel injected, leads to more cooling inside the cylinder. But very high durations of second pulse resulted in decrease in IMEP. With triple injection, as the second pulse is injected close to the top dead center and third pulse as late as possible, the knock index reduced. All of these knock reducing strategies were compensated by a decrease in IMEP.

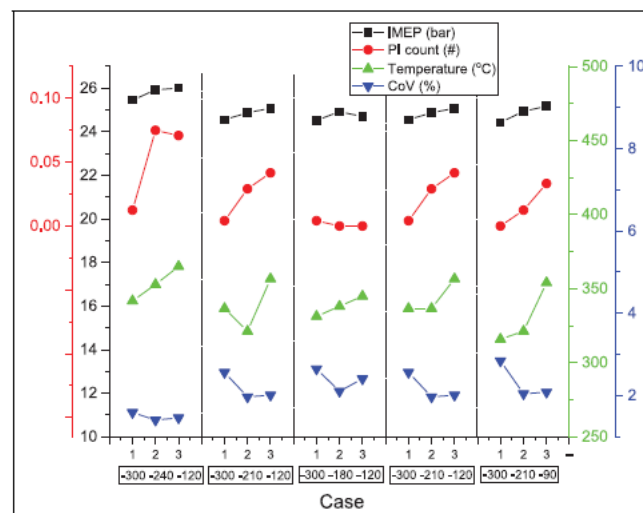


Figure 1-18: Comparison of triple-pulse injection strategies for varying DOIs Case 1 (33:33:33) versus Case 2: (50:25:25) versus Case 3 (50:40:10) for common SOIs [64]

Singh et al. also found an optimized combination without compromising IMEP, it is a triple injection with the first injection at 300 CA BTDC, second injection at 180 CA BTDC and third injection at 120 CA BTDC and fuel ratios of 50%, 25%, 25% respectively for an operating point at 2000 rpm and 2100 mbar of intake pressure. They also tested the effect of fuel injection pressure and saw that higher pressure did increase IMEP but also the knock index. More fuel was required to get zero pre-ignitions. Hence, it was concluded that higher injection pressure had more disadvantages and it was better to operate at lower injection pressures. They also observed that IMEP, CoV of IMEP and knock intensity have a linear relationship with in-cylinder temperature. These results are presented in figure 1-18

1.2.4.5. Enhancing turbulence

Turbulence is another approach to suppress knock. Increasing the in-cylinder turbulence leads to faster combustion flame development thus faster combustions and fewer tendencies to knock.

Luisi et al. [65] tested early and late intake valve closing impact on knock. In their preliminary testing, they noticed that the EIVC was reducing the turbulence inside the cylinder leading to low flame speed and uneven mixing. Turbulence is important for knock suppression as high turbulence increases flame velocity thereby consuming the end gas before it auto-ignites. LIVC resulted in lower charge temperatures, increase in efficiency and reduction in BSFC. Closing the intake valve late allows some of the mixture heated by the walls to escape thereby leaving cooler mixture inside. But, extreme LIVC cannot be used to lower engine speeds as the turbo charger will not be provided enough air flow. At lower engine speeds, the LIVC is limited by the turbocharger.

On their behalf, Hirooka et al. [66] studied the effect of turbulence on flame speed, burn rate and knock suppression by injecting high-pressure air directly into the combustion chamber while modifying injection timing and the arrangement and the quantity of injector nozzles. This configuration as it can be seen in figure 1-19 generates highly turbulent in-cylinder flow. Their simulation results showed that a faster burn rate will allow to reach the MBT timing before the knock limit. Their optimized solution was a single injector with two nozzles injecting air in the opposite direction to each other. This configuration had all the advantages of increasing the burn rate and reducing the interval between the knock limit and MBT timing without the complexity.

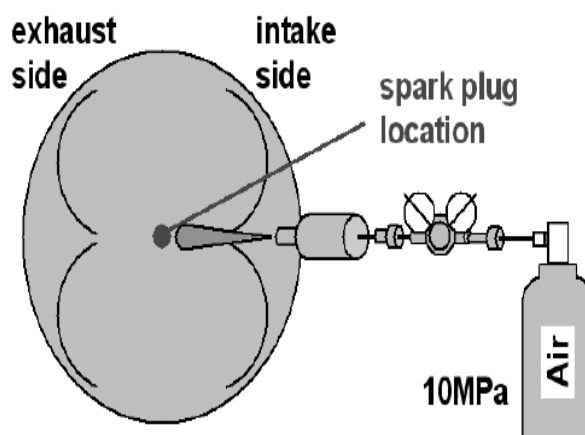


Figure 1-19: configuration of direct high pressure air injection [66]

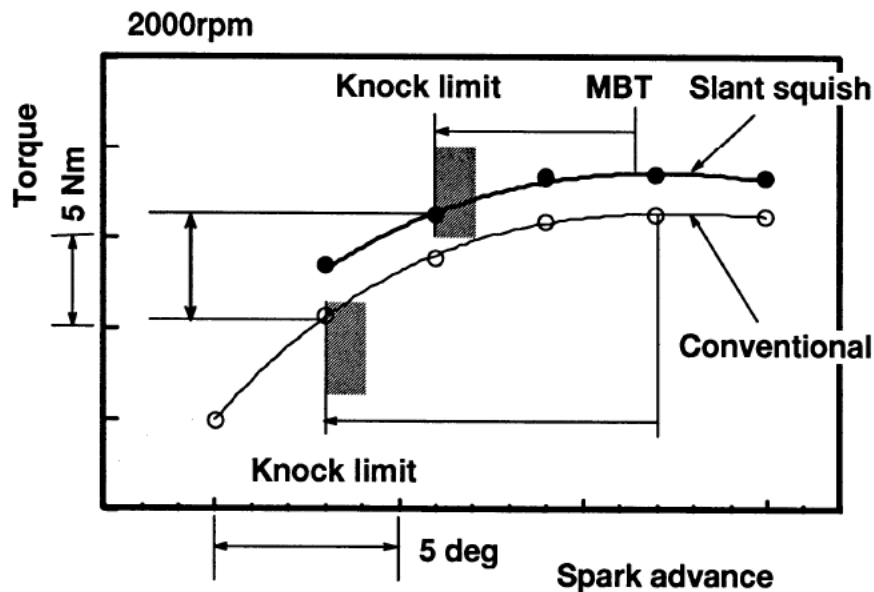


Figure 1-20: Torque vs Ignition timing for reference and first configuration [66]

Ueda et al. [67] experimented with different intake port designs to increase turbulence inside the cylinder. They tested a slant squish area. The cylinder in a normal squish configuration will be straight whereas in the slant squish configuration, the cylinder head was slant. They observed 10 CAD of increase in spark advance, 10 Nm increase in torque, 20 g/kWh decrease in BSFC and 10% increase in volumetric efficiency as in figure 1-20.

1.2.4.6. Engine thermal management

As it was stated, knock appears when the end-gas temperature and pressure reach a critical condition, thus cooling of the end-gas temperature is an alternative approach to delay and suppress knock as it plays an important role in engine knock as expected by Livengood-Wu correlation[68]. This can be achieved by directly cooling the fresh charge or by cooling the combustion chamber walls or changing the coolant flow patterns to improve the distribution of wall temperatures [69]. Nevertheless, this could decrease the thermal efficiency as the heat transfer is increased, thus an optimized solution is to cool down the upper portion of the exhaust side bore [42]

Asif et al.[70] tested the effects of coolant flow rate and its temperature on knocking. They observed that both the coolant flow rate and temperature did not have much effect on the knocking suppression. They attributed this mainly to their narrow range of coolant temperatures [90°C-100°C] and flow rates [20.6-25.8] l/min chosen for the tests. They also tested effect of valve overlap on knock. The higher valve overlap resulted in increase in spark advance. When valve overlap increases the scavenging is enhanced, the in-cylinder charge temperature decreases leading to knock suppression.

Takahashi et al. [71] used a computational fluid dynamic solver to predict the parts of the cylinder responsible for the heat transfer from the surface to the mixture. They observed

that in the intake stroke and compression stroke, the cylinder liner transferred heat to the fresh mixture at a high rate than other surfaces like cylinder head or the piston. This was mainly due to the large surface area of cylinder liner.

Cho et al.[72] studied the effect of coolant flow and temperatures making the head and the liner coolants independent of each other and they observed that cooling both the head and the liner simultaneously allowed a greater increase in spark advance, increase in load limit expansion and decrease in BSFC when compared to only the head cooling or only the liner cooling. Cho et al. [73] also studied effects of cylinder wall temperatures and heat transfer between the cylinder and the fresh mixture. As the coolant temperature reduced, the knock limit spark advance can be advanced more. With cooling of both the cylinder and the cylinder head, they were able to advance the knock limited spark advance (KLSA) and increase the load limit. Lower coolant temperatures reduce the cylinder temperature and also the difference in temperatures between the cylinder and the fresh mixture. Lesser the temperature difference, lesser will be heat transfer between the cylinder and mixture. In fact, when the mixture gets compressed, it gets heated up and heat transfer reverses its direction as the mixture will be at a higher temperature than the cylinder walls. This timing where the heat transfer reverses is called Inversion timing. The inversion timing depends on the charge temperature at the beginning of the compression stroke. They found that intake port was responsible for the highest amount of heat transfer to the charge. This heat transfer decreases as the engine speed increased due to lack of time of the heat transfer to take place. This explains partially why higher engine speeds are less prone to knock.

Intake air temperature impact on knock apparition was not directly studied, however, some authors studied air influences on engines performance and some of their results can be correlated to knock. Abdullah et al. [74] studied the effect of inlet air temperature on fuel consumption and emissions at different engine speeds. The cooling of the inlet air reduced the in-cylinder temperature as the incoming mixture was at a lower temperature. Such low charge temperatures results in increased ignition delay and burn durations delaying auto-ignition events of end gas.

1.2.4.7. Combined strategies

In the above mentioned knock suppressing methods, it was observed that the adoption of a single strategy might have some drawbacks. It could be a decrease in IMEP, an increase in BSFC, increase in emissions etc. To overcome these disadvantages and still suppress knock, multiple strategies can be integrated simultaneously on to a single engine. The objective of this combination is to increase the knock suppression and to counter the drawbacks [75] [76]. Zhou et al. [77] integrated EGR with split injection and tested its effects on knock on a Spark Assisted Compression Ignition (SACI) engine. They observed that i-EGR, e-EGR and IT controlled the combustion and the transition from SI to CI. When NVO was high, i-EGR was high which increased the in-cylinder temperature. The transition

occurred early and knocking was observed. It's the same trend when IT is advanced excessively. When both i-EGR and e-EGR was used, the knock was delayed significantly with increase in e-EGR as the in-cylinder temperature decreased. As result, any drop in engine performance can be gained back by advancing IT. Split injection with both e-EGR and i-EGR showed the best knock suppression and increase in performance. Split injection and e-EGR reduced the in-cylinder temperatures thereby suppressing the knock. Liu et al. [78] also combined e-EGR and split injection with a SACI engine with a mixture stratification. They observed that after reaching a certain EGR rate, any further increase in EGR did not result in increase in spark advance.

1.2.4.8. Other strategies

The above-mentioned strategies are widely used to delay or suppress knock apparition. However, there are some strategies which do suppress knock but are either complicated to use or expensive. For example, dual fuel injection where a gas like ethanol or methanol is injected along with the main fuel to suppress knock. Liu et al. [79] investigated the effects of methanol injection on a SI engine. The addition of methanol increases the ignition delay of the entire mixture due to its high-octane number thereby suppressing the knock. Also, as the methanol is highly oxygenated and due to methanol's high latent heat, the peak pressure increased and the load limit was expanded. Hence, with a proper blend of methanol and gasoline, authors were able to achieve knock suppression as well as expansion of load limit. Zhuang et al. [80] studied the effect of ethanol injection on knock suppression. With the ethanol injection, the knock was suppressed and advance in spark timing was achieved. As the inlet air pressure was increased, the mass of ethanol injected was increased in order to suppress knock. This resulted in increase in IMEP, thermal efficiency and increase in load expansion. However ethanol injection has a drawback on emission, as ethanol mass increased, the CO, HC and NO emissions increased.

Water injection is also an effective way to suppress knock like in Zhu et al. studies [81]. In a SI engine, the water injection slowed down the flame propagation and allowed the advance in spark timing. They also observed that the HC and CO emissions reduced. But these characteristics are dependent on air-fuel equivalence ratio. In a downsized SI engine, the water injection not only reduced the in-cylinder temperature but also the turbine inlet temperature. However, water injection strategies present cost and packaging problems and do not offer additional knock suppress when compared to other techniques. One of the best study on that subject was achieved by Bozza et al. [82] and they found that the best BSFC improvements are obtained in operating points at low and medium speeds of 2100, 2500 and 3300 rpm with a water ratio of 20 to 30% of the fuel quantity.

1.2.5. Impact of fuel on knock

Hydrocarbons compounds vary in their capacity to resist knock apparition and that depends on the molecular size and the structure of the compounds. This tendency to knock is characterized by the critical compression ratio [21]. The critical compression ratio is the one at which under specific operating conditions, the fuel compound will undergo knock. As an example, increasing the length of the carbon chain increases the knocking tendency while compacting the chain by incorporating a side chain delays knock apparition for paraffins. For Olefins, introducing a double bond decreases the tendency to knock and Napthenes have significantly an anti-knock effect. Introducing double bonds to Napthenes and aromatics increases the anti-knock effect [83].

In general, practical fuel are blends of a lot of individual hydrocarbons compounds and a practical method to measure the knock resistance is important. This knock resistance is characterized by the octane number. The higher the octane number (ON), the higher the resistance and this characterization is performed in a given engine under specific operating conditions. Fuels blends behavior and resistance to knock are compared to blends of isooctane (ON=100) and n-heptane (ON=0). Isooctane is regarded as highly resistant to knock and n-heptane as non-resistant to knock. The fuel octane number is thus determined by the blend of isooctane and n-heptane that matches the fuel's resistance to knock under the same operating conditions. For example a fuel ON of 90 resists knock in the same manner as a blend of 90% of isooctance and 10% of n-heptane [21].

1.3. Conclusion of the literature review

The literature study described the knock onset phenomenon. Knocking combustion is a complex phenomenon of abnormal combustion that is strongly influenced by engine characteristics, thermodynamic conditions, and engine control parameters. The onset or not of the knock and its intensity depend on a competition between the speed of flame propagation triggered by the spark plug, and the auto-ignition of the fresh gases upstream the flame front.

The parameters influencing the onset of knock are therefore multiple and several methods have been proposed in the literature to delay its onset, suppress it or reduce its intensity. However, most of these methods are usually accompanied by a degradation in efficiency or engine performance.

Numerous studies on knocking are described in the literature. They have been conducted most often on research engines or single-cylinder engines and generally focus on one or two parameters of influence. During this literature study, it was not possible to find a complete experimental database presenting, with the same definition of the appearance of knock, the impact of the various control parameters on the onset of knock, but also on the physical parameters of influence such as the air filling, the equivalence ratio of the trapped mixture, the wall temperatures, the combustion rate, or the residual gas rate.

This is why, in the following chapters such a database will be built.

L'étude de la littérature a permis de décrire la phénoménologie de l'apparition du cliquetis. Le cliquetis est un phénomène complexe de combustion anormale qui est fortement influencé par les caractéristiques du moteur, les conditions thermodynamiques, et les paramètres de contrôle du moteur. L'apparition ou non du cliquetis et son intensité dépendent d'une compétition entre la vitesse de propagation de flamme déclenchée par la bougie d'allumage, et l'auto-allumage des gaz frais en amont du front de flamme.

Les paramètres influençant l'apparition du cliquetis sont donc multiples et plusieurs méthodes ont été proposées dans la littérature pour retarder l'apparition de cliquetis, la supprimer ou réduire son intensité. Cependant, la plupart de ces méthodes sont généralement accompagnées d'une dégradation du rendement ou des performances du moteur.

De nombreuses études sur le cliquetis sont décrites dans la littérature. Elles ont été menées le plus souvent sur des moteurs de recherche ou monocylindre et se focalisent généralement sur un ou deux paramètres d'influence. Au cours de cette étude bibliographique, il n'a pu être trouvé de base de données expérimentales complète, présentant, avec une même définition de l'apparition de cliquetis, l'impact des différents paramètres de contrôle moteur sur l'apparition de cliquetis, mais également sur les paramètres physiques d'influence tels que le remplissage en air, la richesse du mélange enfermé, les températures de parois, le taux de combustion, ou encore le taux de gaz résiduels.

C'est pourquoi, dans les chapitres suivants, on constituera une telle base de données.

2. Experimental Setup and Numerical tools

In this chapter, the experimental setup that has been used for this thesis is first presented. A preliminary measurement campaign is then described; it includes the general characterization of the engine, in particular the combustion in the absence of knocking and the influence of the various engine control parameters. In a third section, the numerical engine simulation tools are detailed. They serve both to further analyze the experimental results, and as the basis for the complete simulation of the engine. A particular emphasis is placed on the choice of the combustion model, and a calibration procedure is proposed.

Dans ce chapitre, le montage expérimental qui a été mis en place et exploité dans le cadre de cette thèse est tout d'abord présenté. Une campagne de mesure préliminaire est ensuite décrite ; elle regroupe la caractérisation générale du moteur, notamment de la combustion en l'absence de cliquetis et l'influence des différents paramètres de contrôle moteur. Dans une troisième section, les outils numériques de simulation moteur sont détaillés. Ils servent à la fois à analyser plus en détails les mesures expérimentales, et servent de base à la simulation complète du moteur de l'étude. L'accent est notamment porté sur le choix du modèle de combustion, et une procédure de calibration de ce dernier est proposée.

2.1. Presentation of the engine test bench

In the frame of the industrial partnership between Ecole Centrale de Nantes and Stellantis, all of the experiments were conducted on a three-cylinder 1.2 L Euro 6.1 turbocharged spark-ignition internal combustion engine equipped with an intercooler and a three-way catalyst. The turbine is equipped with a waste-gate. The engine configuration is presented in figure 2-1 and main engine specifications are listed in table 2-1.

Number of cylinders	3
Number of valves per cylinder	4
Bore	75 mm
Stroke	90 mm
Displacement	1.2 L
Air System	Turbocharged, fixed geometry, waste gate
Injection system	Direct injection, gasoline, up to 3 injections
Compression ratio	10.2:1

Table 2-1: Engine Specifications

It is an automotive engine that equips several passengers' cars. The advantages of using such a stock engine for the experiments are to assess the problems that are encountered in real-life cars and to adapt the corresponding solutions. Moreover, with the numerical analysis, a complete engine model can thus be calibrated using measures obtained from this engine bench. A series-engine does not allow a detailed analysis of the combustion development with optical diagnosis and the apparition of abnormal combustion such as the knock, but it helps to understand the phenomena by a system approach and to study the impact of several control parameters in conditions very close to real life.

The engine test bench is equipped with an open electronic control unit provided by Stellantis. The access to the control unit allows the modification of engine parameters such as the valves timing, the injection strategies, the spark advance, etc.

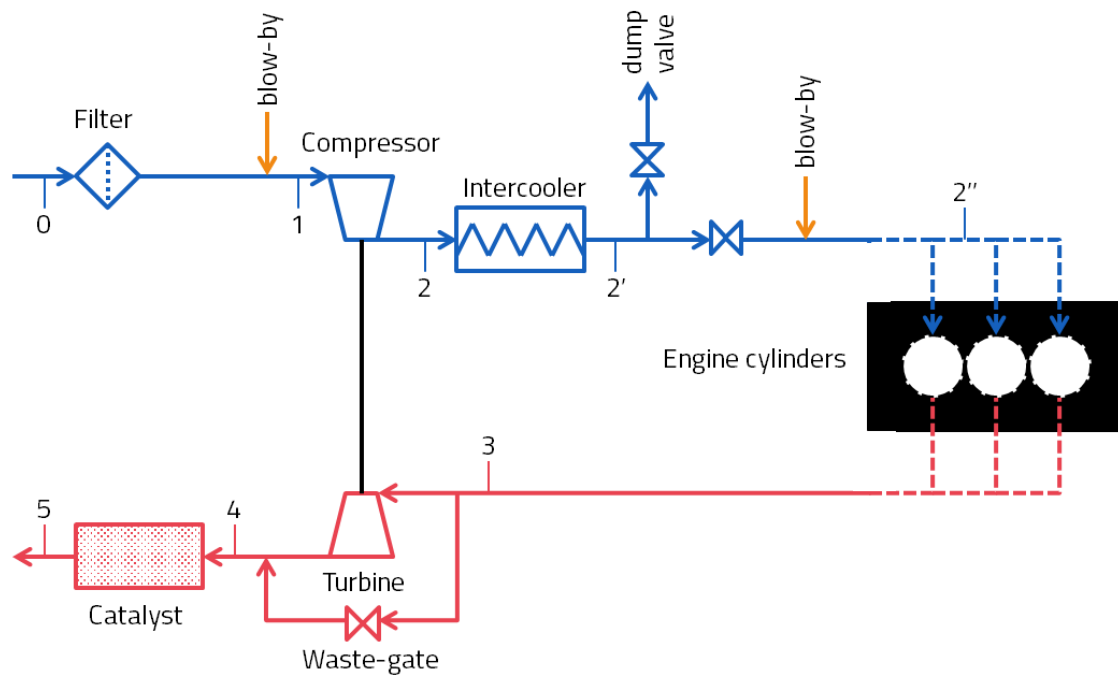


Figure 2-1: Engine configuration

Temperatures and pressures are measured all along with the intake air loop and the exhaust path. In-cylinder pressures are measured through instrumented sparks, Kistler 6115C. Temperatures sensors are also implemented all over the cylinder block and the cylinder head to measure the wall temperature at several points of the engine (head, liner, and piston). Turbocharger speed is measured using a Micro-epsilon sensor and the relative humidity as well as the atmospheric conditions are also reported from the engine cell. Fuel consumption is measured using an AVL 733 fuel balance with a 0-150 kg/h range. All the details regarding sensors type, range and accuracy are listed in table 2-2.

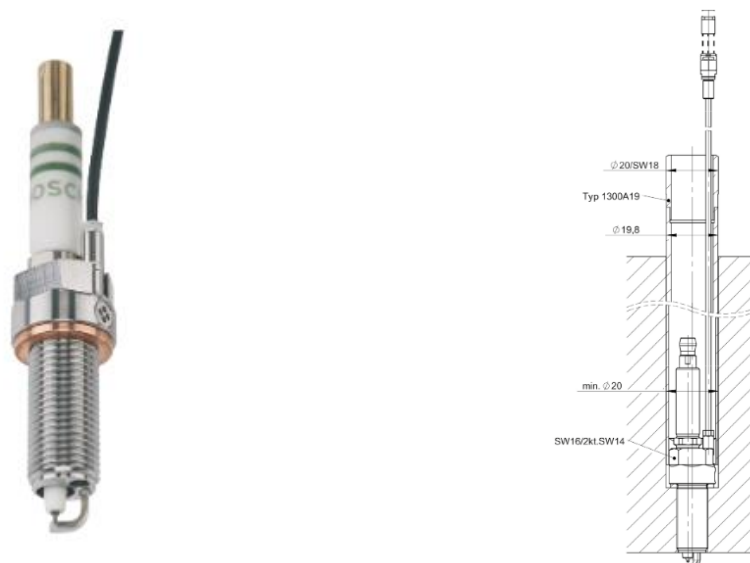


Figure 2-2: measuring spark plug flush-mounted on the engine test bench

	Sensor type	Range	Accuracy
Temperature – air loop	T-type thermocouple	-185 – 300 °C	+/-0,1 °C
Temperature – exhaust	N-type thermocouple	0 – 1150 °C	+/- 2.2C
Temperature : coolant, lubricant, metal thermometry	T-type thermocouple	-185 – 300 °C	+/-0,1 °C
P0	First Sensor, HCX		Linearity: +- 0,25% FSO
P1	First Sensor, HCX	0 - 100 mbar	Linearity: +- 0,25% FSO
P2	First Sensor, HCX	0 – 2,5 bar relative	Linearity: +- 0,25% FSO
P2'	First Sensor, HCX	0 – 2,5 bar relative	Linearity: +- 0,25% FSO
P2'' > 1bar abs.	First Sensor, HCX	0 – 1 bar relative (depression)	Linearity: +- 0,25% FSO
P2'' < 1 bar abs.	First Sensor, HCX	0 – 2,5 bar relative	Linearity: +- 0,25% FSO
P3	First Sensor	0 – 5 bar relative	Linearity: +- 0,2% FSO
P4	First Sensor	0 – 3 bar relative	Linearity: +- 0,2% FSO
P5	First Sensor	0 – 5 bar relative	Linearity: +- 0,2% FSO
PEAEPOMP, PEASMOT	First Sensor	0 – 3 bar relative	Linearity: +- 0,2% FSO
PHUETURB	First Sensor	0 – 5 bar relative	Linearity: +- 0,2% FSO
dP2, dP2', dP2'', dP3	Kistler, type 4049 DS Water cooled	0 – 5 bar abs.	< +- 0,3 % FSO
dP4, dP5	Kistler, type 4049 DS Water cooled	0 – 10 bar abs.	< +- 0,3 % FSO
Fuel consumption	AVL 733 fuel balance	0 – 150 kg/h	≤ 0.12% (acc. to DIN 1319)
Turbocharger speed	Micro-epsilon, DS1	0 – 400 krpm	Linearity: +- 0,2% FSO
Engine torque	HBM	0-1000 Nm	
Relative humidity test cell	VAISALA	0 – 100%	
Cylinder pressure	Sensor: Kistler 6115C Charge amplifier: MMF M72 A1	Detailed in table 3	Detailed in table 3

Table 2-2: Types, ranges and accuracies of the sensors implemented on the engine bench

The measuring spark plug (see figure 2-2) is very suitable for measurements at high engine speeds, or for knock detection applications. The measuring spark plug Type 6115C is

flush-mounted and it enables cylinder pressure measurement without requiring a separate measuring bore. The technical data for the measuring spark plug are listed in table 2-3.

Technical Data

Measuring range	bar	0 ... 200
Calibrated partial ranges 200 °C	bar	0 ... 50
		0 ... 100
		0 ... 150
Overload	bar	250
Sensitivity at 200 °C	pC/bar	≈-10
Natural frequency	kHz	>120
Natural frequency (acoustic)	kHz	≈65
Linearity, all ranges (at 23 °C)	%FSO	<±0,5
Sensor operating temperature range	°C	-20 ... 350
Cable operating temperature range	°C	-20 ... 250
Thermal sensitivity shift	%	<±1
Acceleration sensitivity	mbar/g	<0,001
Thermal shock error		
(at 1 500 min 1/min, IMEP = 9 bar)		
Δp (short-term drift)	bar	<±0,6
ΔIMEP	%	<±3
Δp _{max}	%	<±1,5
Spark plug insulation resistance (at 23 °C)		
between central electrode and spark plug body at 1 000 V		
	MΩ	>100

Table 2-3: technical data for the measuring spark plug 6115C

A Horiba Mexa One gas (figure 2-3) analyzer is used to measure the CO, CO₂, and O₂ concentrations on dry gases and NO_x, THC, and CH₄ concentrations on raw gases. Exhaust gases are analyzed before entering the three-way catalyst.

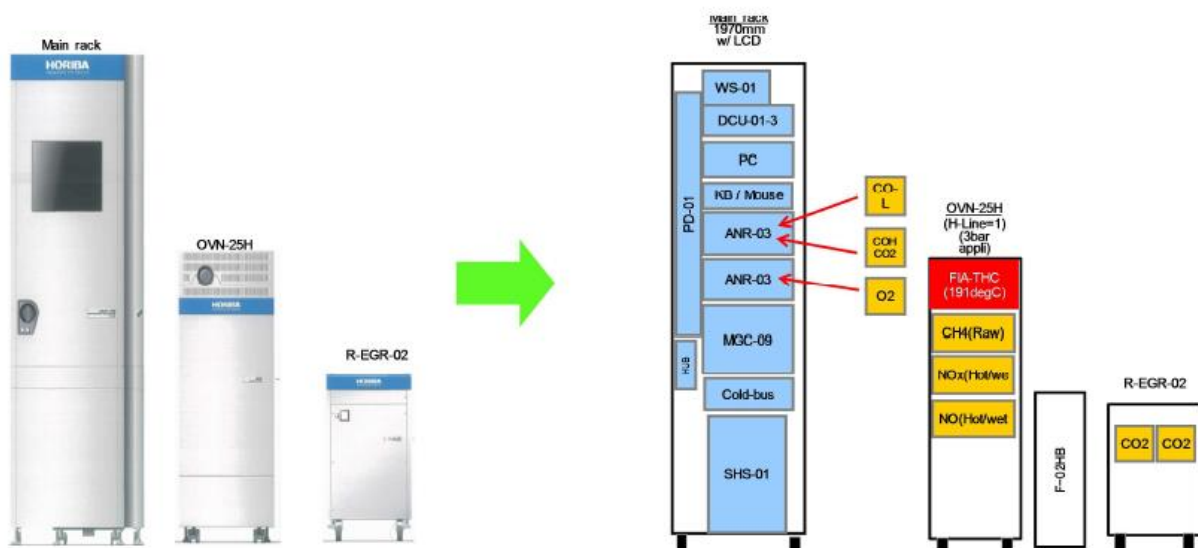


Figure 2-3: Horiba Mexa One gas analyzer

The analyzer range for each of the exhaust gases are listed in table 2-4.

Rack	Analyzer	Component	Analyzer Range
ANR03	AIA-01	CO(L)	0 - 50 - 5.000 ppm
	AIA-03	CO(H)	0 - 0,5 - 12%
		CO2	0 - 0,5 - 20%
ANR03	MPA-01	O2	0 - 1 - 25%
OVN 25-H	FIA-02H-ND	THC	0 - 50 - 1.000 ppmC
			0 - 2.000 - 60.000 ppmC
		CH4	0 - 50 - 1.000 ppm
			0 - 2.000 - 25.000 ppmC
	CLA-02OV	NO, NOx, NO2	0 - 10 - 1.000 ppm
			0 - 2.000 - 10.000 ppm
EGR-02	AIA-32	CO2	0 - 0,5 - 20 %
	AIA-32	CO2	0 - 0,5 - 20 %

Table 2-4: Exhaust component analyzer range

As stated earlier, engine bloc and cylinders head were both instrumented with thermocouples according to the CAD plans in figures 2-4 and 2-5.

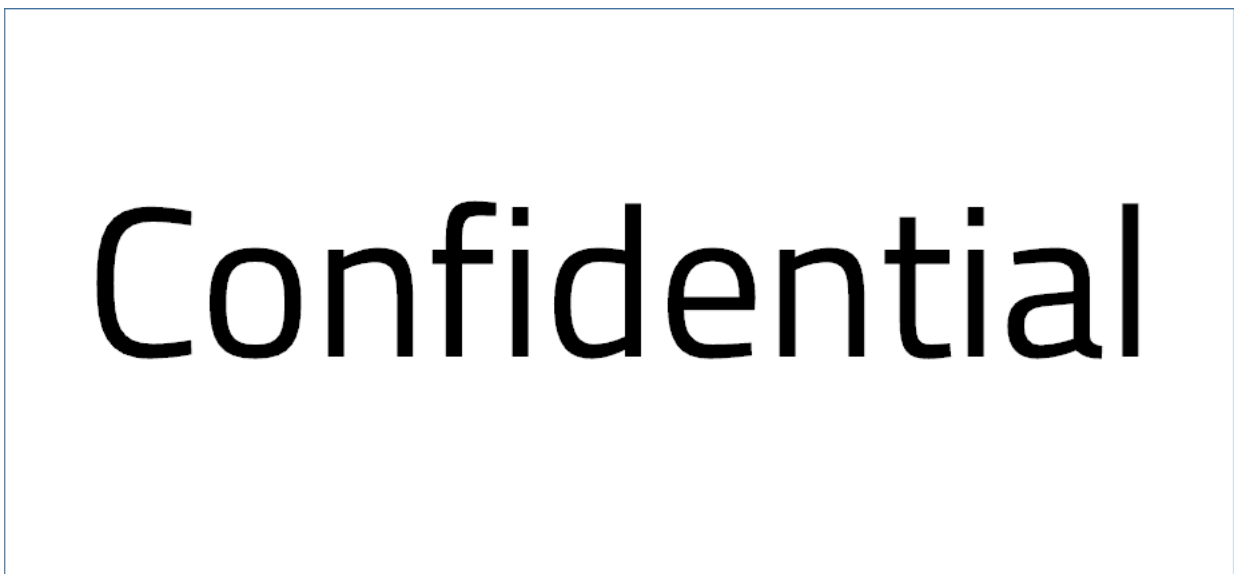


Figure 2-4: cylinder head, thermocouples implementation

Temperature sensors that were implemented on the engine bench are indicated by red circles on both the cylinders head and engine bloc CADs. The sensors were used since it was accessible to implement them on the engine and they could provide interesting information on the temperature gradient of the engine bloc.



Figure 2-5: engine bloc thermocouples implementation

All the sensors signals are connected to a NI "National Instrument" data acquisition plug-in board. A "LabVIEW" data acquisition system is used to measure, monitor and store the signals. All the measurements for all the aforementioned sensors in this section are stabilized before saving the data and the in-cylinder pressures are recorded for 250 cycles. 250 cycles is the maximum number of cycles that can be stored using this acquisition system.

The bench that was presented was used for 3 types of tests.

- A- Performance tests
- B- Preliminary combustion tests
- C- Knock tests

The benefits of having an engine bench are to assess the problems the way they are encountered in a series engine equipped to a passengers car and to develop a complete engine model that will be able to predict the knock apparition. The variety of the tests will help in a first place to understand the combustion development in order to present a proper explanation for the different phenomena observed specially at the knock level and to calibrate combustion and knock models in a second place.

2.2. Preliminary Campaign

In this section, the preliminary tests campaign is presented. This campaign groups the performance tests that were performed. In a second place, a specific preliminary combustion campaign is presented and the effect of control parameters on engine behavior is also explained. These tests put in evidence the influence of some parameters on combustion development as an impact could be established with the knock apparition.

Dans cette section, la campagne d'essais préliminaires est présentée. Cette campagne regroupe les tests de performances qui ont été effectués. Dans un second temps, une campagne de combustion préliminaire spécifique est présentée et l'effet des paramètres de contrôle sur le comportement du moteur est également expliqué. Ces tests ont mis en évidence l'influence de certains paramètres sur le développement de la combustion puisqu'un impact a pu être établi avec l'apparition du cliquetis.

2.2.1. Performance tests

Performance tests are operating points all over the engine performance map at engine speed going from 1050 rpm until 5800 rpm and a load step of 100 mbar of admission pressure until the full load. To perform these tests, coolant temperature is regulated at 85°C except for the naturally aspirated operating points from 2500 rpm till 5800 rpm where it is regulated at 105°C. Oil temperature is regulated at 90°C and the intake temperatures regulations increase from 25°C to 45°C with the load increase. These regulated values reproduce the best the real life engine conditions and they are repeatable. The engine parameters are strictly controlled by the engine control unit. All data are recorded after stabilization. The stabilization criterion is the thermal stabilization which consists of achieving an average value of each temperature sensor that fluctuates within $\pm 2^\circ\text{C}$ over the past 250 cycles. The objectives of these tests are:

- Generate performance maps that cover the whole operating range of the engine.
- Develop the engine model: multipliers all over the engine sub-models (models that constitute the whole engine model) have to be tuned using experimental results.
- Calibrate a combustion model: as it will be discussed in the third section “Numerical tools” of this chapter, a combustion model is calibrated using the experimental results.

The performance maps thus group 298 operating points. Some of them will be picked to perform models calibration.

2.2.2. Preliminary combustion tests

The preliminary tests are combustion tests that were performed to characterize the development of the combustion and the behavior of the engine. They are separated into three different types of tests:

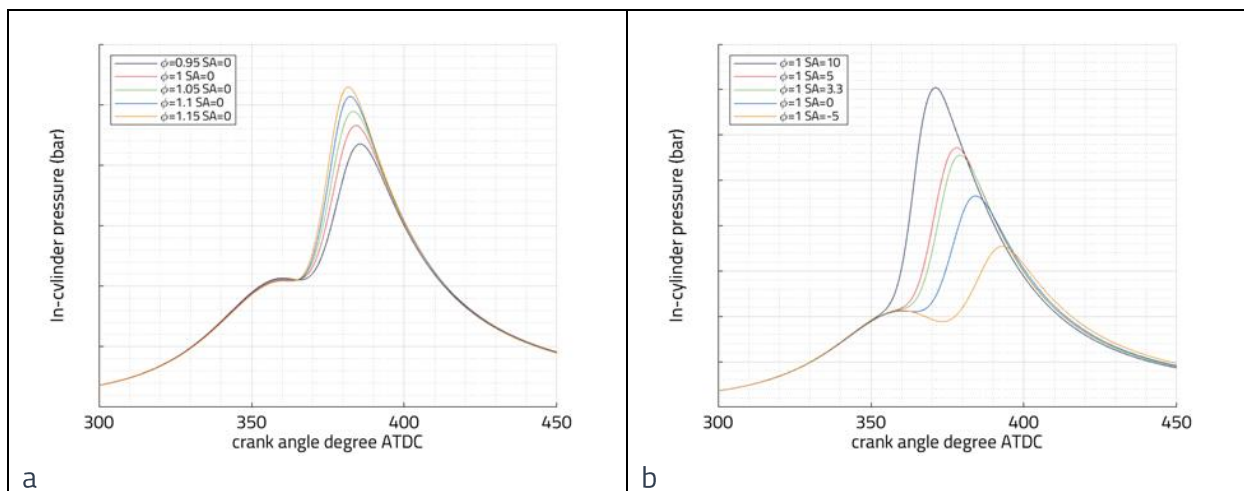
1. Fuel-to-air equivalence ratio and spark timing sweeps
2. Coolant and oil temperatures sweeps
3. Valves timings sweeps

The previously mentioned tests were performed on several operating points: each operating point is referred to by engine speed (rpm) x admission pressure (mbar).

A lot of preliminary tests were performed on the engine bench, they do not represent the hub of this PhD Thesis which is the knock characterization but they are related to knock as they represent control parameters that impact knock occurrence. A selection is made and will be presented to understand the combustion development under modified parameters.

2.2.2.1. Fuel-to-air equivalence ratio and spark advance sweeps

First, fuel-to-air equivalence ratios and spark timings were swept. The in-cylinder pressures were plotted while varying the fuel-to-equivalence ratio at fixed spark advance in the first place, and while varying the spark advance at fixed fuel-to-air equivalence ratio in figures 2-6 and 2-7.



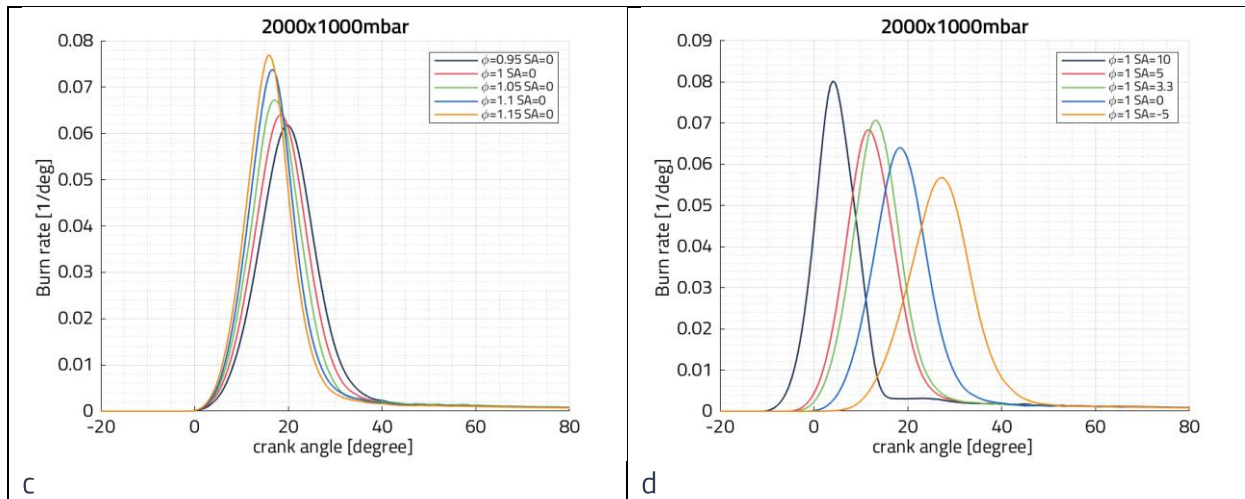
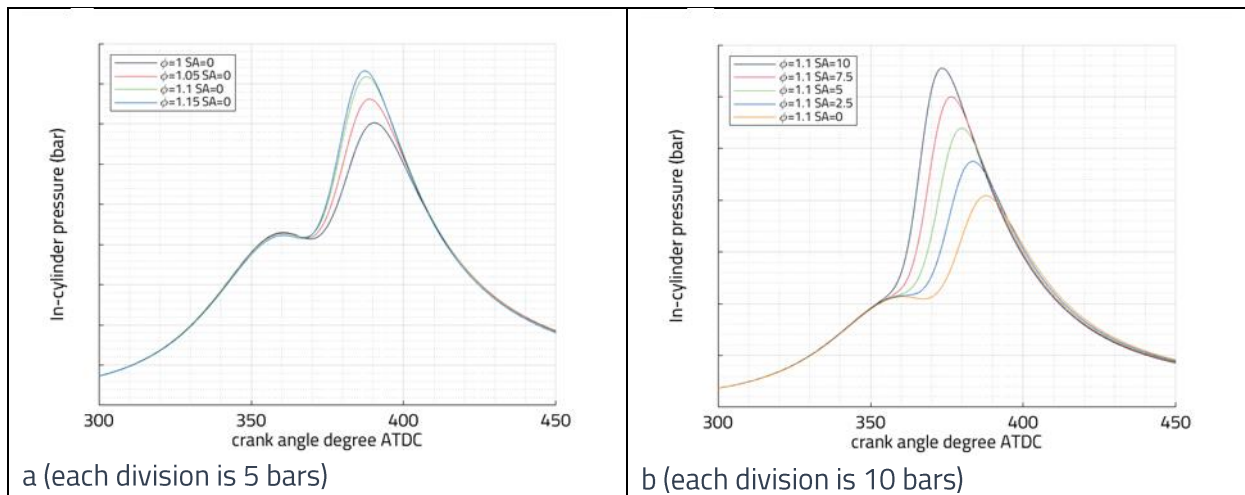


Figure 2-6: in-cylinder pressures (each division 10 bars) and burn rates for fuel-to-air equivalence ratio sweep at fixed spark advance (a & c) and for spark advances sweep at fixed fuel-to-air equivalence ratio (b & d) for 2000x1000 mbar

As the fuel-to-air equivalence ratio is increased, the peak of the in-cylinder pressure is also increased for a constant spark advance (a difference of +10 bar is obtained between the 2 extreme values of fuel-to-air equivalence ratio 0.95 and 1.15).

At fixed fuel-to-air equivalence ratio, as the spark advance was decreased, the start of the combustion was then delayed resulting in a lower in-cylinder peak pressure and shifted to the right.



a (each division is 5 bars)

b (each division is 10 bars)

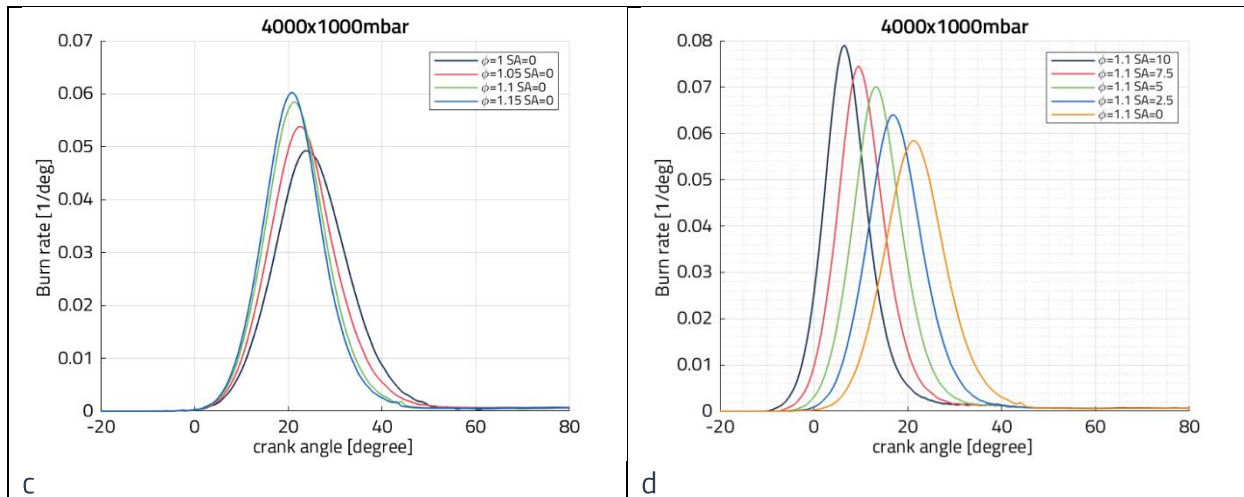


Figure 2-7: in-cylinder pressures and burn rates for fuel-to-air equivalence ratio sweep at fixed spark advance (a & c) and for spark advances sweep at fixed fuel-to-air equivalence ratio (b & d) for 4000x1000 mbar

The same behavior was observed for the different operating points. The combustion development is faster when the mixture is richer. CA50 decreased from 21 CAD till 16 CAD and the burn duration CA1075 decreased from 13 CAD till 10 CAD for 2000x1000 mbar as the equivalence ratio increased from 0.95 till 1.15. The maximum rate of pressure rise also increased from 2.06 bar/CAD till 3.35 bar/CAD as mixture gets richer. Besides, as spark timing was delayed, the combustion development is degraded. At 4000x1000 mbar for example, the burn duration CA1075 increased from 10 CAD till 14 CAD as spark advance decreased 10 CAD. The maximum rate of pressure rise decreased from 4.56 bar/CAD till 1.75 bar/CAD. CA50 also increased from 7 CAD till 22 CAD as spark advance decreased from 10 CAD till 0 CAD, however, the reason behind that increase is at first place related to the delayed combustion development and in second place to the decreased burn rate: 10 CAD of spark advance decrease increased the CA50 by 15 CAD.

This preliminary study is very interesting to understand the combustion development. As it was seen in the literature review, both fuel-to-air equivalence ratio and spark advance are important parameters that affect the knock occurrence. Richer mixture increase the spark-induced flame speed which consumes the end-gas before it auto-ignites. On another hand, increasing the spark advance increases the knock apparition.

2.2.2.2. Coolant and oil temperatures sweep

Subsequently, coolant and oil temperatures were swept. The tests are performed according to 3 different research modes:

Research Mode 1 (R1): the admission pressure and the spark advance are maintained fixed

Research Mode 2 (R2): the admission pressure is varied to maintain the air mass flow rate constant as the oil or coolant temperature is being swept. The spark advance is also fixed.

Research Mode 3 (R3): the admission pressure is fixed but the spark advance is varied to maintain the CA50 constant as oil and coolant temperatures are being swept.

First, coolant and oil temperatures sweep will be studied on the thermal behavior of the engine. For that purpose one operating point will be considered which at 2000 rpm and 1000 mbar of intake pressure.

For that purpose, Coolant and oil power will be plotted in figure 2-8, 2-9 and 2-10 as the coolant temperature is decreasing for two different levels of oil temperatures.

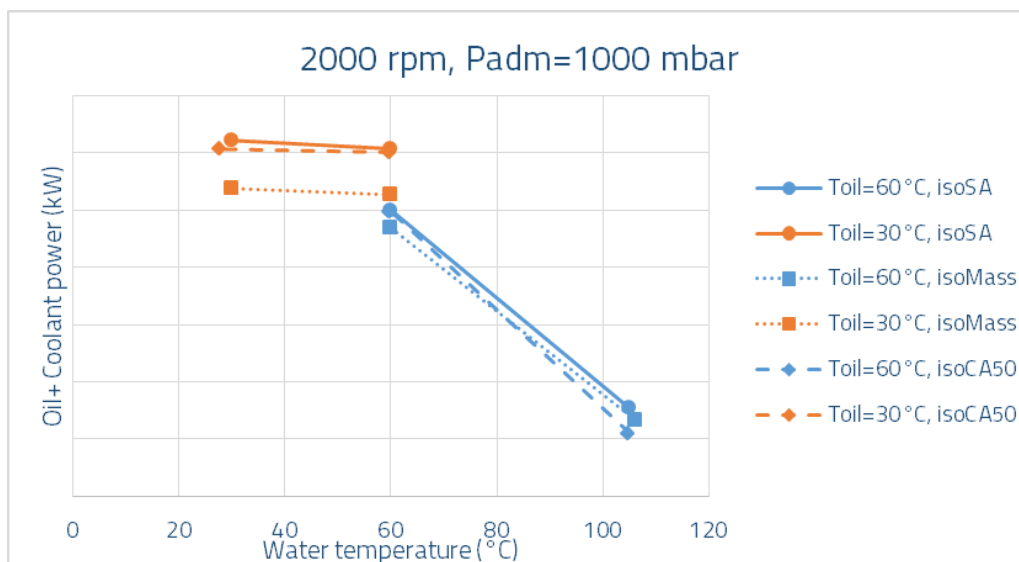


Figure 2-8: Oil+ Coolant power of 2000x1700 mbar-R1,R2&R3 at different coolant and oil temperature levels (each division represents 0.5kW)

The total power (Oil+ Coolant) tends to increase as coolant and oil are cooled. Colder walls imply higher convective exchange.

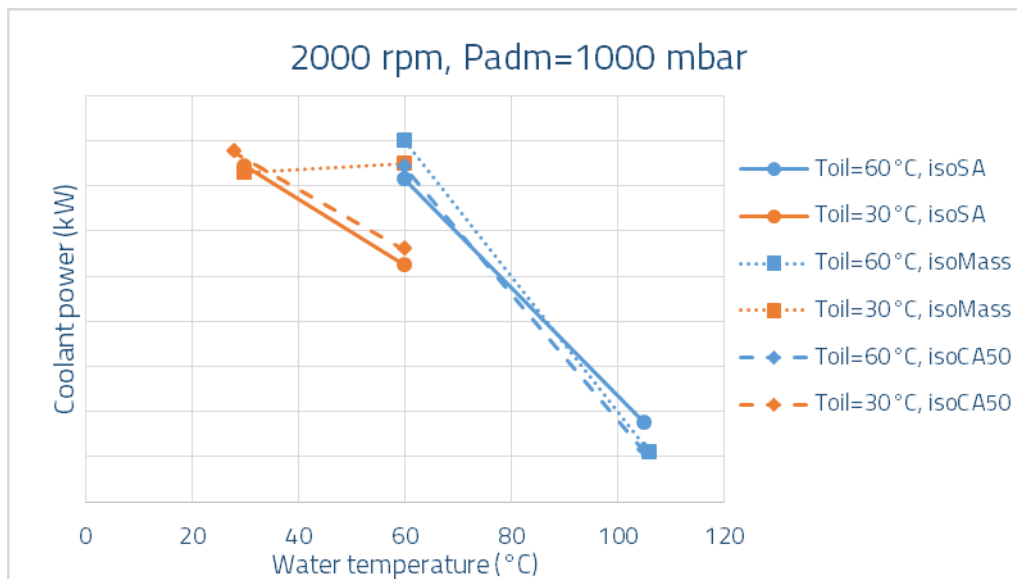


Figure 2-9: Coolant power of 2000x1700 mbar -R1,R2&R3 at different coolant and oil temperature levels (each division represents 1kW)

Coolant power evolution is similar than total power: tends to increase as coolant is cooled meanwhile oil temperature is kept at 60°C. We notice that coolant power decrease if oil temperature is decreased when water temperature stays at 60°C. A part of heat flux goes in oil instead of water as we can see on the following figure 2-10.

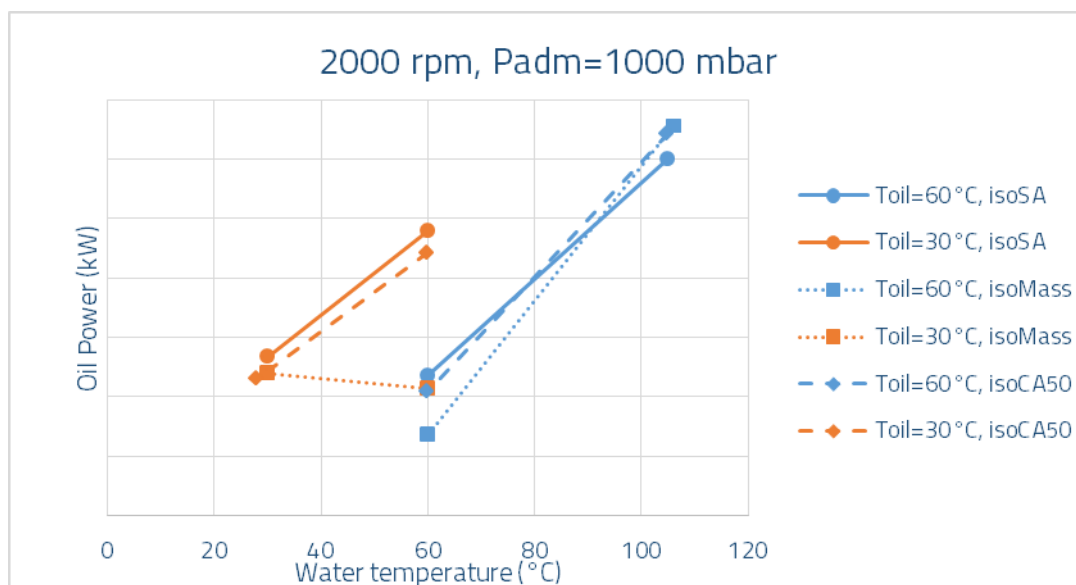


Figure 2-10: Oil power of 2000x1700 mbar -R1,R2&R3 at different coolant and oil temperature levels (each division represents 1kW)

The oil power evolves at the opposite of the coolant power. As the coolant temperature increases the oil power increases. As we can see on figures 2-12, 2-13, 2-14 wall temperatures depend mainly on water temperature. Thus exchanges between oil and wall increase with water temperature. Moreover, colder oil may lead to increased friction which is dissipated into oil and thus increases oil power.

Temperatures sensors are implemented all over the cylinder block and the cylinder head to measure the wall temperature at several points of the engine (head, liner) to study their evolution as the coolant or oil temperatures are modified according to the figure 2-11.

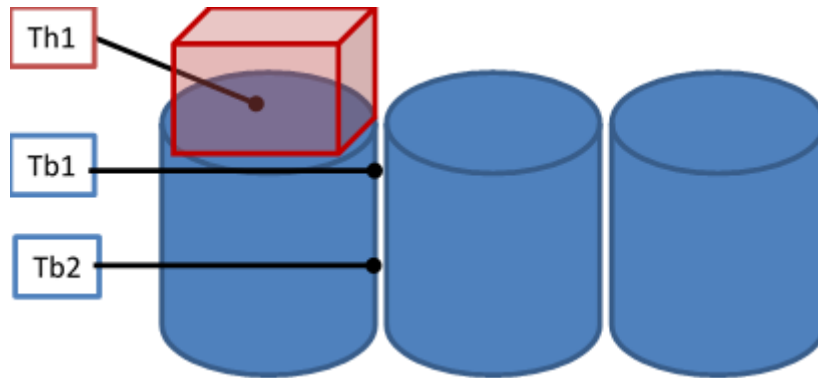


Figure 2-11: thermocouples positions

The temperature distributions of the block are:

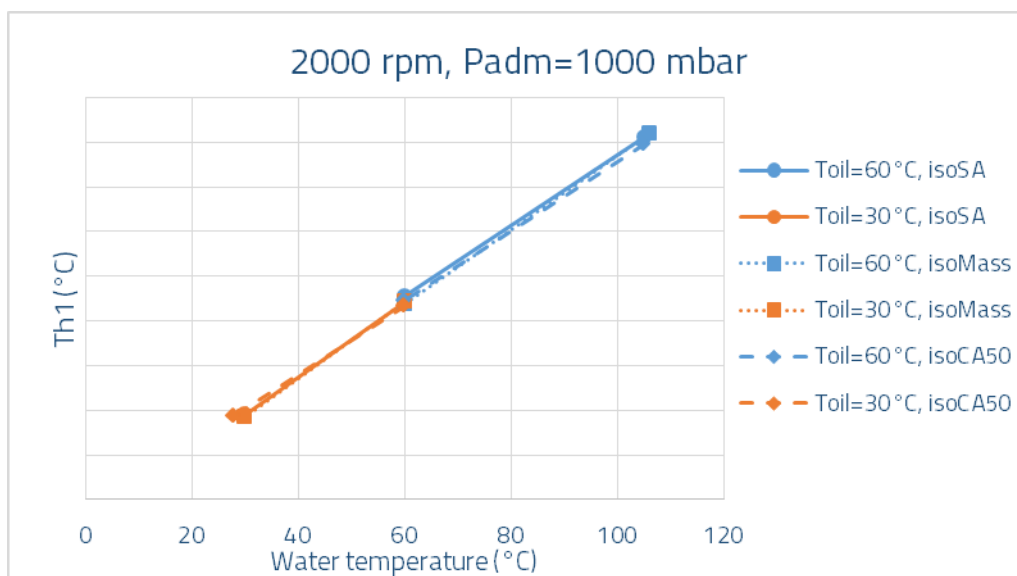


Figure 2-12: Head temperature of 2000x1700 mbar -R1,R2&R3 at different coolant and oil temperature levels (each division represents 10°C)

As it can be seen in figure 2-12, head temperature is linked with water temperature: tends to increase as water temperature increase without impact of the oil temperature.

Head temperature impact the volumetric efficiency, that is why water temperature impacts on in-cylinder mass as it will be seen on the effect of coolant temperature on in-cylinder mass.

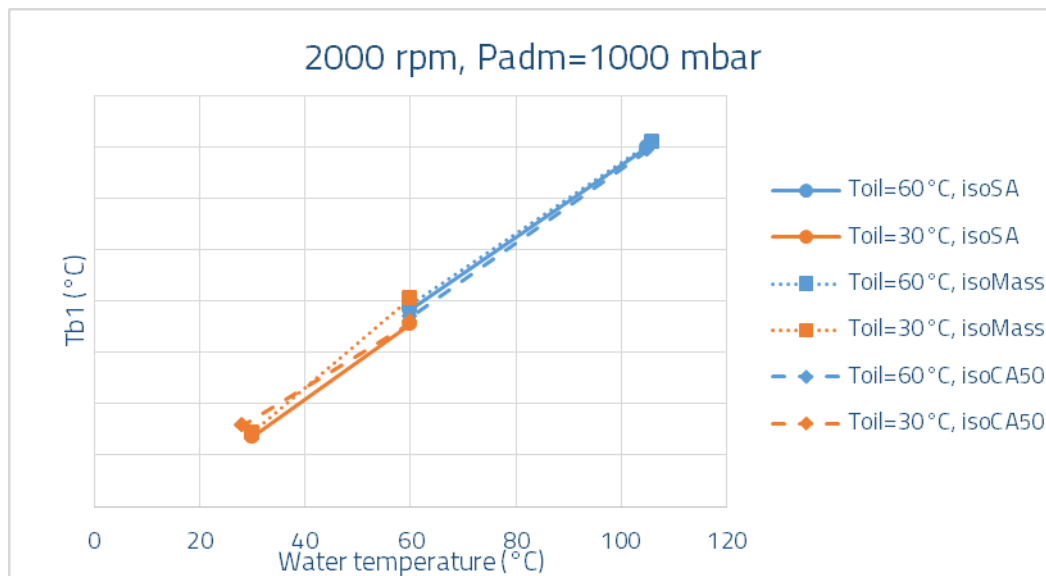


Figure 2-13: Upper block temperature of 2000x1700 mbar -R1,R2&R3 at different coolant and oil temperature levels (each division represents 10 °C)

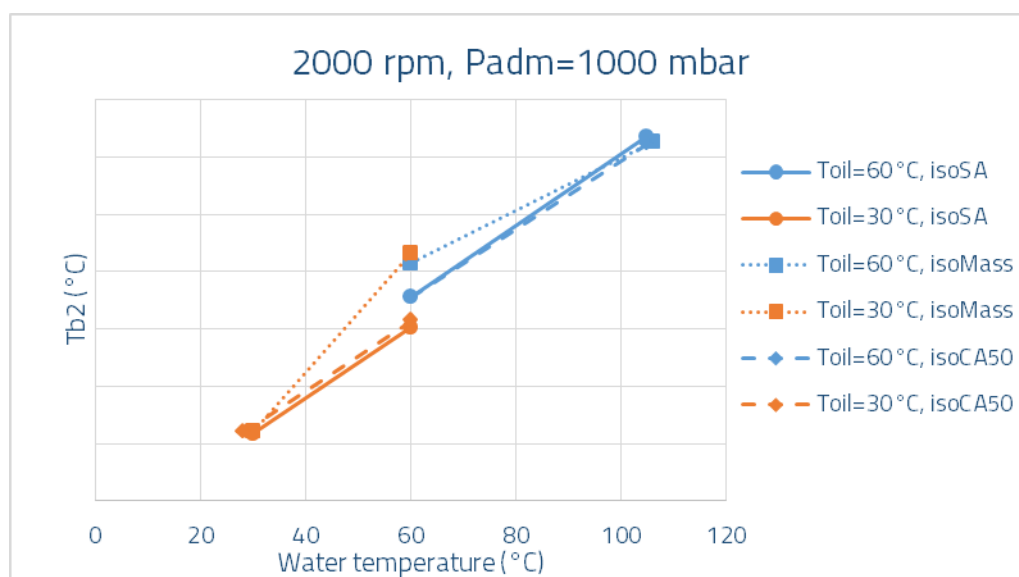


Figure 2-14: Bottom block temperature of 2000x1700 mbar -R1,R2&R3 at different coolant and oil temperature levels (each division represents 10 °C)

As seen in figure 2-13 and 2-14, block temperature are mainly linked with water temperature as well. Bottom temperatures are colder since combustion takes place in the upper part. We can notice that isoMass Research Mode lead to higher block temperature (especially Tb2) on OP2 at Twater=60°C. This is coherent with the difference noticed on oil power, lower heat transfer leads to higher temperature. The bottom part of the block is affected by the oil temperature. Indeed we notice a difference of approximately 5 °C on Tb2 when oil is shifted from 60 to 30°C while water is kept at 60°C. Oil below the piston exchanges with both cylinder wall and piston.

Oil temperature and oil jet nozzle may impact piston temperature and combustion [84]. The piston was not instrumented, it is thus impossible to investigate this axe but these effects should be kept in mind.

In a second place, the effect of coolant temperature will be studied on in-cylinder mass.

The volumetric efficiency in the cylinder is affected by the intake system heat transfer and by the in-cylinder heat transfer [21]

The heat transfer to the incoming mixture in the intake manifold and port and within the cylinder walls decreases its density. The volumetric efficiency can be formulated as a function of the mass flow rate according to Heywood:

$$\eta_v = \frac{2\dot{m}_a}{\rho_{a,0}V_dN}$$

The heat flux is generally conducted through the chamber walls and then convected from the wall to the coolant. The temperature of the coolant thus plays a major role in the in-cylinder mass and on the airflow rate.

In the case of our study, coolant and oil temperatures were varied for the different considered operating points. First, we will start with the operating point at 2000 rpm and 700 mbar of intake pressure. The matrix of coolant and oil temperature are presented in the table 2-5

2000 x700 mbar		
T coolant	T oil	Test no.
°C	°C	
103	90	1
103	60	2
60	60	3
60	30	4
30	30	5

Table 2-5: coolant and oil temperature sweep for 2000x700 mbar-R1

As coolant and oil temperatures were swept, the admission pressure was maintained constant at 700 mbar , the spark advance and the intake temperature are constant as well.

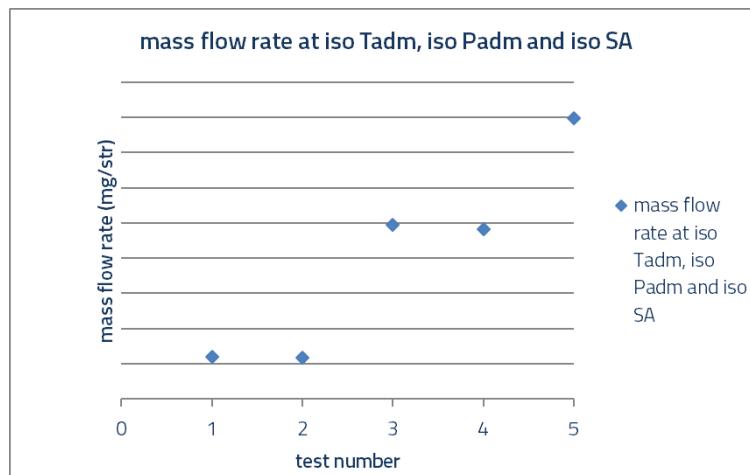


Figure 2-15: mass flow rate and matrix of oil and coolant temperature sweep of OP1-R1 (each division is 2mg/str)

The x-axis represents the different tests as they were numbered in the test matrix. Between test 1 and test 2, the coolant temperature was kept constant at 103° and oil temperature was decreased from 90° to 60°. No significant difference between the mass flow rates was obtained. However, between tests 2 and 3, oil temperature was kept constant at 60° and coolant temperature decreased from 103° to 60°. A significant increase in the mass flow rate was achieved and thus volumetric efficiency was enhanced. This indicates that the coolant temperature has a higher impact on the volumetric efficiency than oil temperature. The same can be concluded for a couple of tests 3&4 and 4&5. On this operating point, the coolant temperature impacted the flow rate of the incoming air. The effect of oil temperature is not significant. The coolant temperature directly affects the in-cylinder charge within the chamber walls as it was seen in the evolution of the head and block temperatures in figures 2-12, 2-13 and 2-14

In the following, the coolant and oil temperatures effect will be studied on the combustion. In the following figures, two sets of in-cylinder pressure and burn rate are plotted on the same graph. The first set represents two different levels of oil and coolant temperatures at the same spark advance and they are labeled by "isoSA" (iso spark advance). The second set represents the same levels of oil and coolant temperatures at the same CA50 and they are labeled "isoCA50".

The settings for the operating point 2000x700 mbar are presented in the table 2-6.

2000x700 mbar					
Tadm	Padm	SA	T coolant	T oil	CA50
°C	mb	°vil	°C	°C	
23	700	23,8	103	90	8,47
			103	60	9,19
			60	60	11,07
			60	30	11,26
			30	30	12,60

Table 2-6: 2000x700 mbar in R1 settings

The in-cylinder pressure traces and the burn rate are plotted in the figure 2-16.

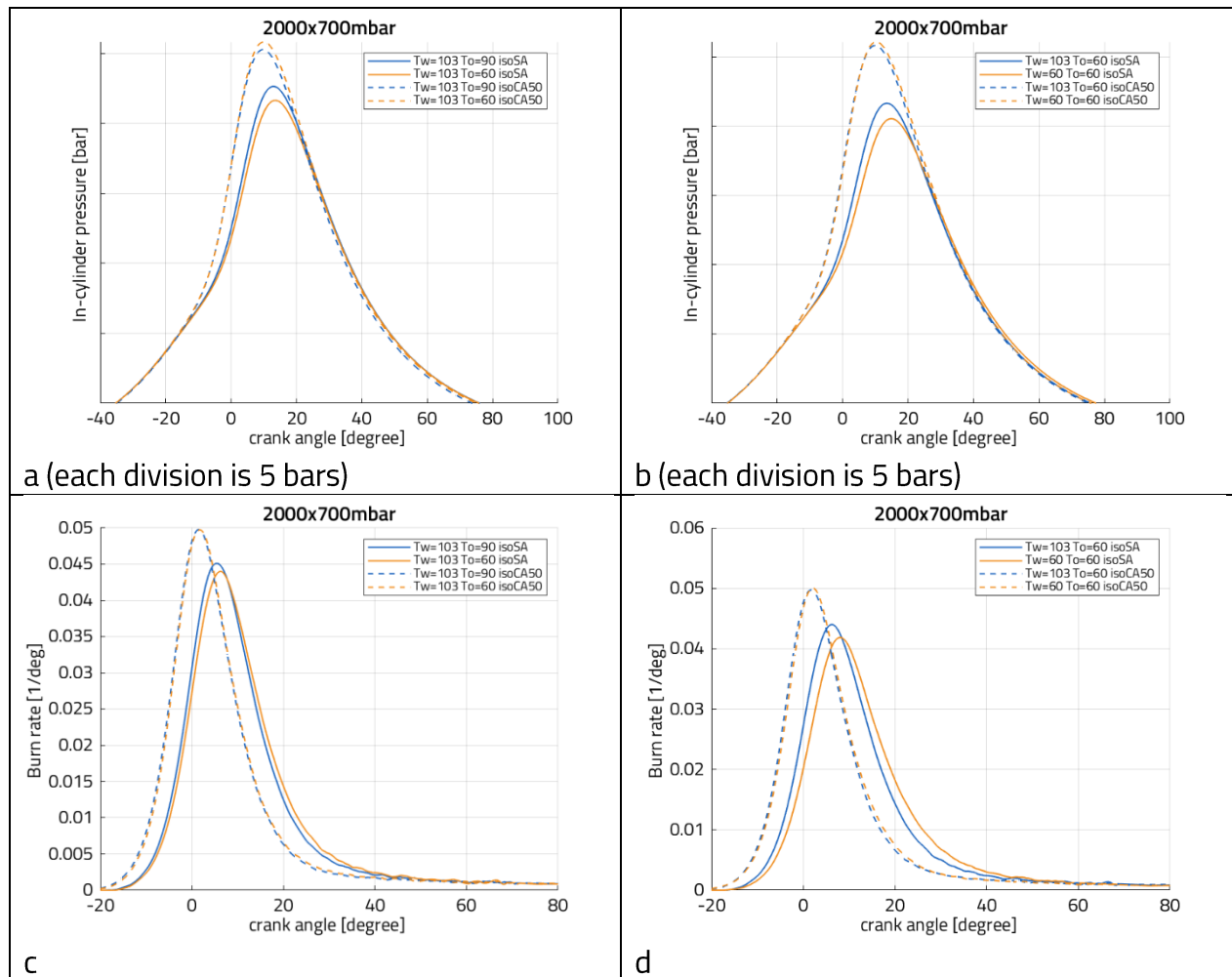


Figure 2-16: in-cylinder pressures (a&b) and burn rates (c&d) of 2000x700 mbar in R1&R3 at different coolant and oil temperature levels

At low load, the decrease of coolant or oil temperature led to a decrease in the burn rate. The effect was more evident when coolant temperature was decreased for fixed oil temperature. Decreasing coolant temperature leads to colder cylinder walls, a higher heat exchange rate is obtained between the intake charge and the walls, which affects the initiation of the combustion which starts a little bit delayed. This can be explained by a slower flame development under cooler conditions. This can be observed on the normalized burn rates: as temperatures decrease, the burn rate starts a little bit delayed with a less steep slope. This is also projected on the in-cylinder pressure traces: after the compression stroke, the combustion starts a bit later than hotter settings, reaching lower pressure peaks. In both cases, the coolant temperature has a higher impact than the oil temperature where the delay in the combustion initiation is clearer. This can be explained by the higher heat exchange that can be obtained when the coolant temperature is decreased.

Based on that, the first effect of coolant and oil temperature decrease can be formulated: Cooler cylinder walls tend to decrease the burn rate thus delaying the combustion initiation leading to lower engine performance.

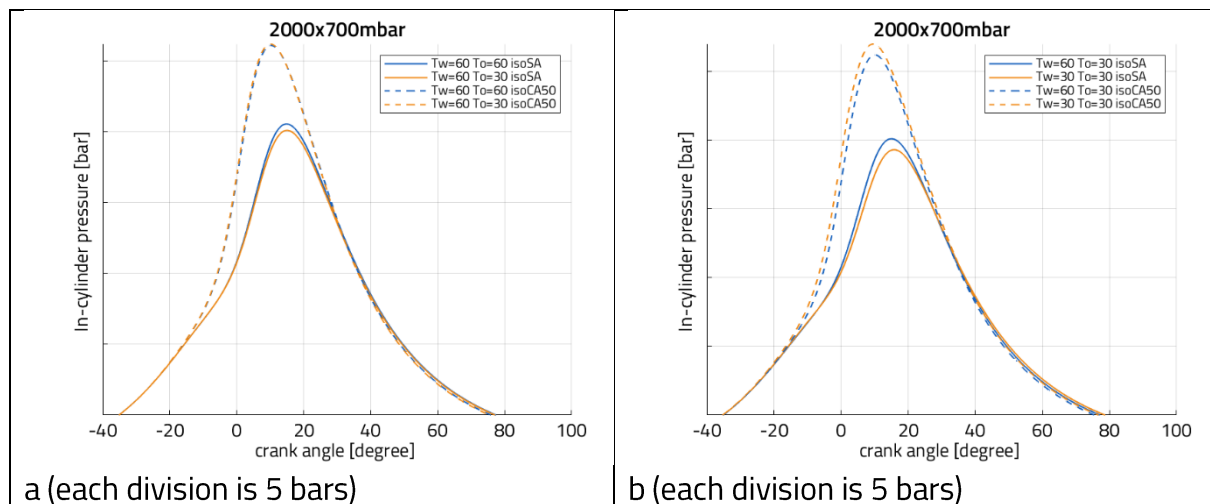
On another hand, when the CA50 was maintained constant, we can see in the pictures above that the combustion is almost the same as coolant or oil temperatures were modified. In fact, to maintain a constant CA50, the spark advance was modified according to the table 2-7

2000x700 mbar						
Tadm	Padm	CA 50 set point	T coolant	T oil	CA50 exp	SA
°C	mb	°vil	°C	°C	dV	dV
23	700	3,9	103	90	3,67	31,13
			103	60	3,95	29,25
			60	60	4,25	32,51
			60	30	3,81	33,75
			30	30	4,49	40,20

Table 2-7: 2000x700 mbar R3 settings

At this operating point and at fixed spark advance, the combustion was degraded as cylinder walls were cooled down. To compromise this effect, in the second set of experiments, the spark advance was increased and the CA50 was maintained constant.

A further decrease in coolant and oil temperatures is also performed and presented in the figure 2-17:



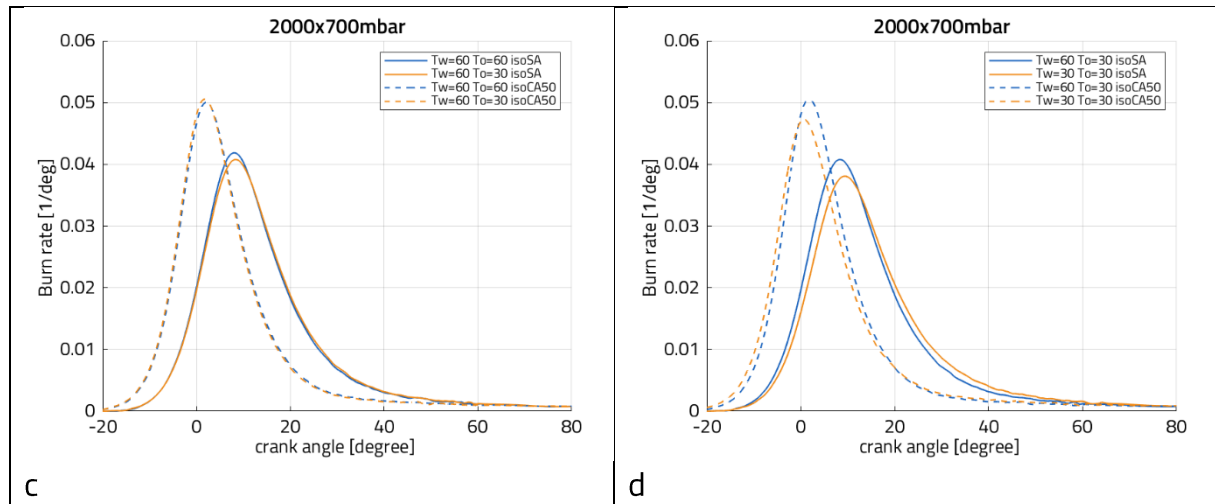


Figure 2-17: in-cylinder pressures (a&b) and burn rates (c&d) of 2000x700 mbar-R1&R3 at different coolant and oil temperature levels

Nevertheless, a further decrease in oil temperature on this operating point had very little effect on the combustion behavior in that case. However, a higher impact of cold walls was observed again when the coolant temperature was further decreased. In that case, it can be seen the burn rate was decreased and the delayed start of the combustion. These observations are consistent with the literature approaching the combustion development under cold start [78]

Here as well, in the second set of experiments, the spark advance was increased to maintain a constant CA50. This also compromised to degradation of the combustion due to cold walls and thus the combustion development was the same.

The settings for the operating point 2000x1000 mbar are presented in the table 2-8:

2000x1000 mbar					
Tadm	Padm	SA	T coolant	T oil	CA50
°C	mb	°vil	°C	°C	
25	1000	3,3	105	90	15,17
			105	60	14,01
			60	60	13,67
			60	30	13,86
			30	30	15,22

Table 2-8: 2000x1000 mbar in R1 settings

The coolant and oil temperature sweep for this operating point is presented in figure 2-18

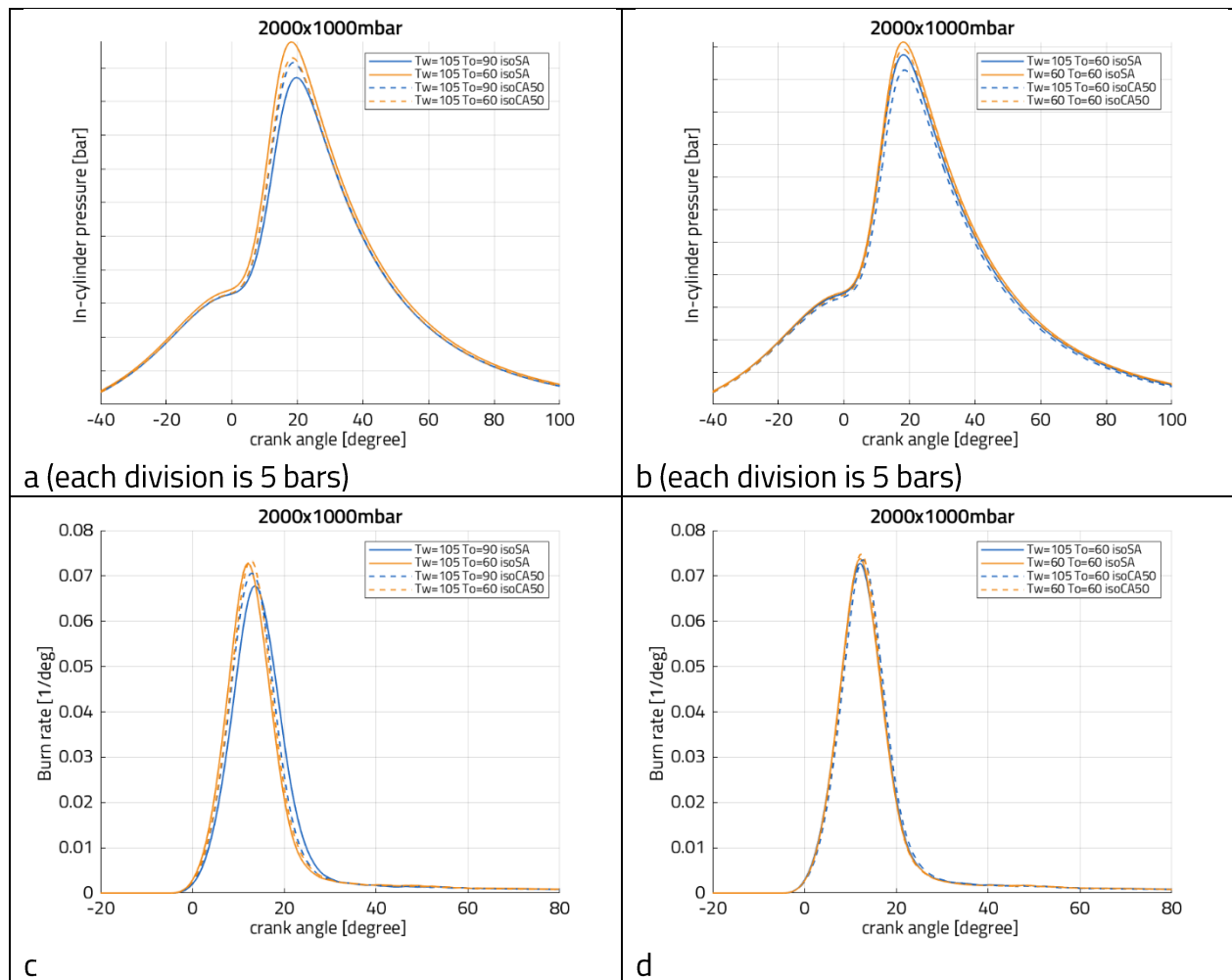


Figure 2-18: in-cylinder pressures (a&b) and burn rates (c&d) of 2000x1000 mbar-R1&R3 at different coolant and oil temperature levels

At medium load, a different phenomenon was observed when the oil temperature has been decreased by 30° in the first case. The cooler oil temperature affected the heat exchange in the cylinder head in a different manner. The density of the admitted air was increased, the charge mass that was confined inside the cylinder was increased as well. In fact, the air flow rate was increased from 405 to 425 mg/stroke. This leads to an increase in the burn rate as it can be seen in burn rate traces. The flame initiated by the spark propagated quicker than the hotter setting leading to faster consumption of air and fuel mixture and a higher pressure peak. The same phenomenon was observed in the second case where the coolant temperature was decreased from 105° till 60° but with a lower influence on the combustion behavior.

The second effect of cooler walls can then be formulated: lower engine walls temperature can increase the density of the intake charge, thus increasing the confined mass in the cylinder which leads to an increase in the burn rate.

As for the set of experiments where the CA50 was maintained constant, on this operating point, the spark advance was not modified between the different tests when the oil and

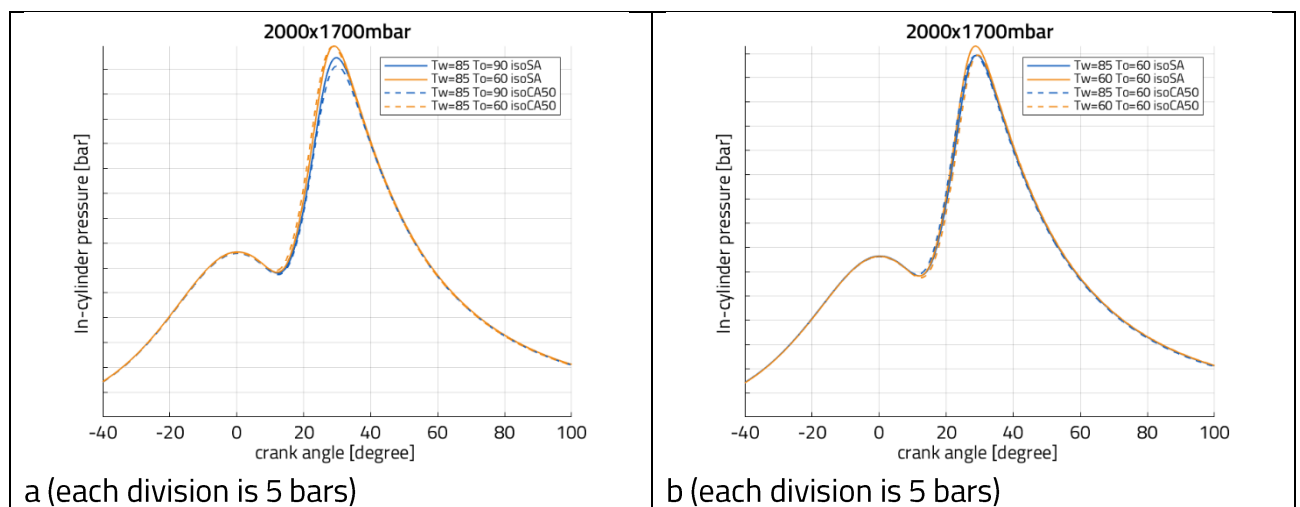
coolant temperatures were swept. In the first case where the oil temperature was decreased from 90°C to 60°C, little or no impact on burn rate and combustion development was observed although this oil temperature change increased the burn rate at the constant spark advance test. However, when the coolant temperature was decreased from 105°C to 60°C, the same behavior was reproduced in the case of fixed spark advance and fixed CA50. This can be explained by the fact that in constant spark advance tests, the CA50 was not modified, so when we tried to fix the CA50, we were not confronted with a modification of the spark advance either. This has led to reproduce the same combustion behavior.

The coolant and oil temperature sweep for 2000x1700 mbar is presented in the table 2-9:

2000x1700 mbar					
Tadm	Padm	SA	T coolant	T oil	CA50
°C	mb	°vil	°C	°C	
35	1700	-7,3	85	90	24,97
			85	60	24,58
			60	60	24,22
			60	35	24,27
			40	35	24,32

Table 2-9: 2000x1700 mabr in R1 settings

The pressure traces are presented in the figure 2-19:



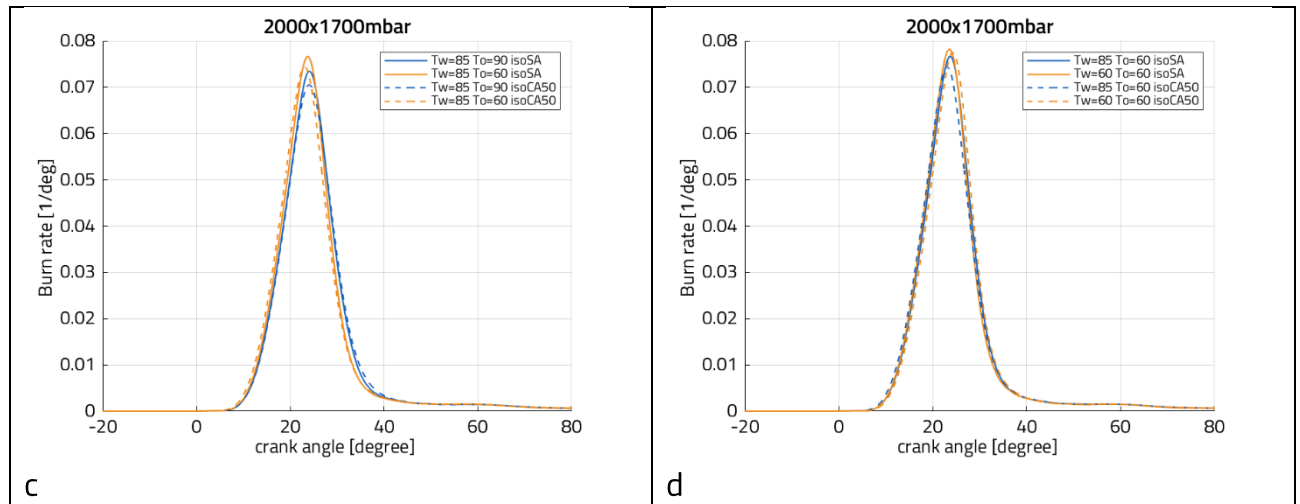


Figure 2-19: in-cylinder pressures (a&b) and burn rates (c&d) of 2000x1700 mbar-R1&R3 at different coolant and oil temperature levels

At high load of 1700 mbar, the second effect of cooler walls was also observed in the first case when the oil temperature was decreased as the in-cylinder charge increased leading to a rapid burn rate. In addition, this effect was also observed in the second case where the coolant temperature is decreased but with a lower impact than oil temperature decrease. In the IsoCA50 tests, the same behavior as the iso spark advance test was reproduced. This is since when the spark advance was fixed, the CA50 was almost constant in the different tests, then when we intended to fix the CA50, the spark advance was also maintained for the different tests. This can be seen in the table 2-10:

2000x1700 mbar						
Tadm	Padm	CA 50 Set point	T coolant	T oil	CA50 exp	SA
°C	mb	°vil	°C	°C		
35	1700	25,2	85	90	24,64	-7,34
			85	60	24,38	-7,19
			60	60	25,04	-7,54
			60	36	25,05	-7,50
			38	33	25,78	-7,88

Table 2-10: 2000x1700 mbar in R3 settings

The in-cylinder pressure traces and the burn rates are presented in the figure 2-20.

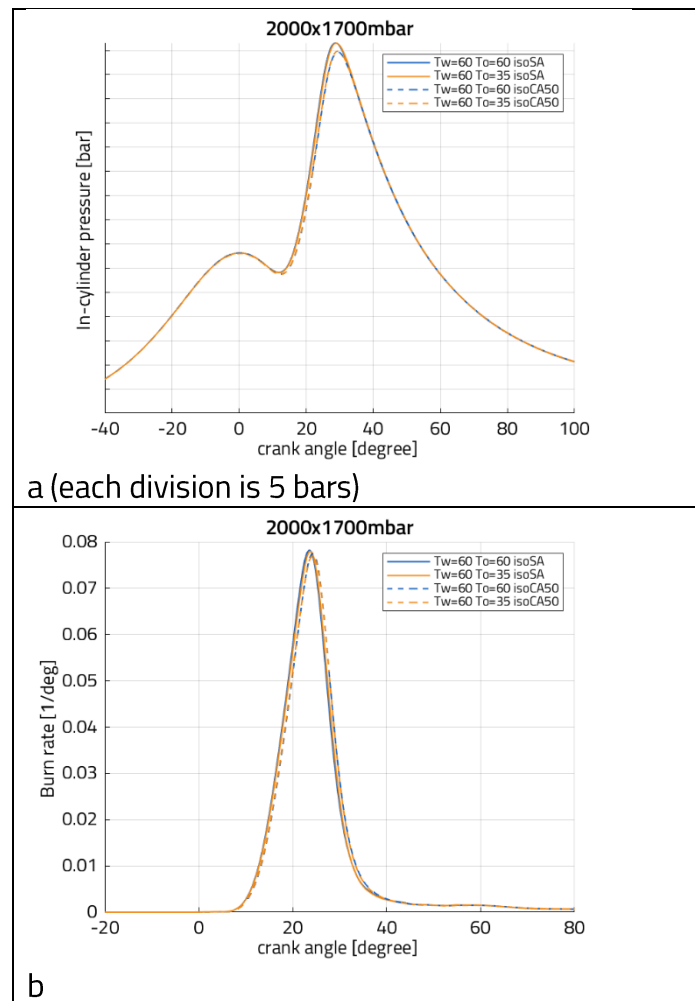


Figure 2-20: in-cylinder pressure (a) and burn rate (b) of 2000x1700 mbar-R1&R3 at different coolant and oil temperature levels

However, the previously mentioned effects of cool cylinder walls seem to be compensated in the third case as the combustion is developed similarly. This is applied for the test at iso spark advance and iso CA50.

As we saw in the previous paragraphs, when the admission pressure was maintained constant and the oil or coolant temperature was decreasing, the air mass flow rate increased. The walls of the cylinders and the intake components affected the volumetric efficiency. In this paragraph, and for the different operating points, the admission pressure was modified on the engine bench to fall on the same air mass flow rate when the oil or coolant temperature was decreasing. In the following figures, two sets of in-cylinder pressure and burn rate are plotted on the same graph. The first set represents two different levels of oil and coolant temperatures at the same spark advance and they are labeled by "isoSA" (iso spark advance). The second set represents the same levels of oil and coolant temperatures while varying the admission pressure to fall on the same air mass flow rate "isoMass"

The coolant and oil temperature sweep for this operating point is presented in the table 2-11

2000x1000 mbar						
Tadm	Padm	SA	T coolant	T oil	CA50	Test #
°C	mb	°vil	°C	°C		
25	1035	3,3	105	90	14,22	1
	1031		105	60	13,70	2
	1001		60	60	14,28	3
	1002		60	30	14,13	4
	975		30	30	15,02	5

Table 2-11: 2000x1000 mbar in R2 settings

The in-cylinder pressure traces are presented in the figure 2-21.

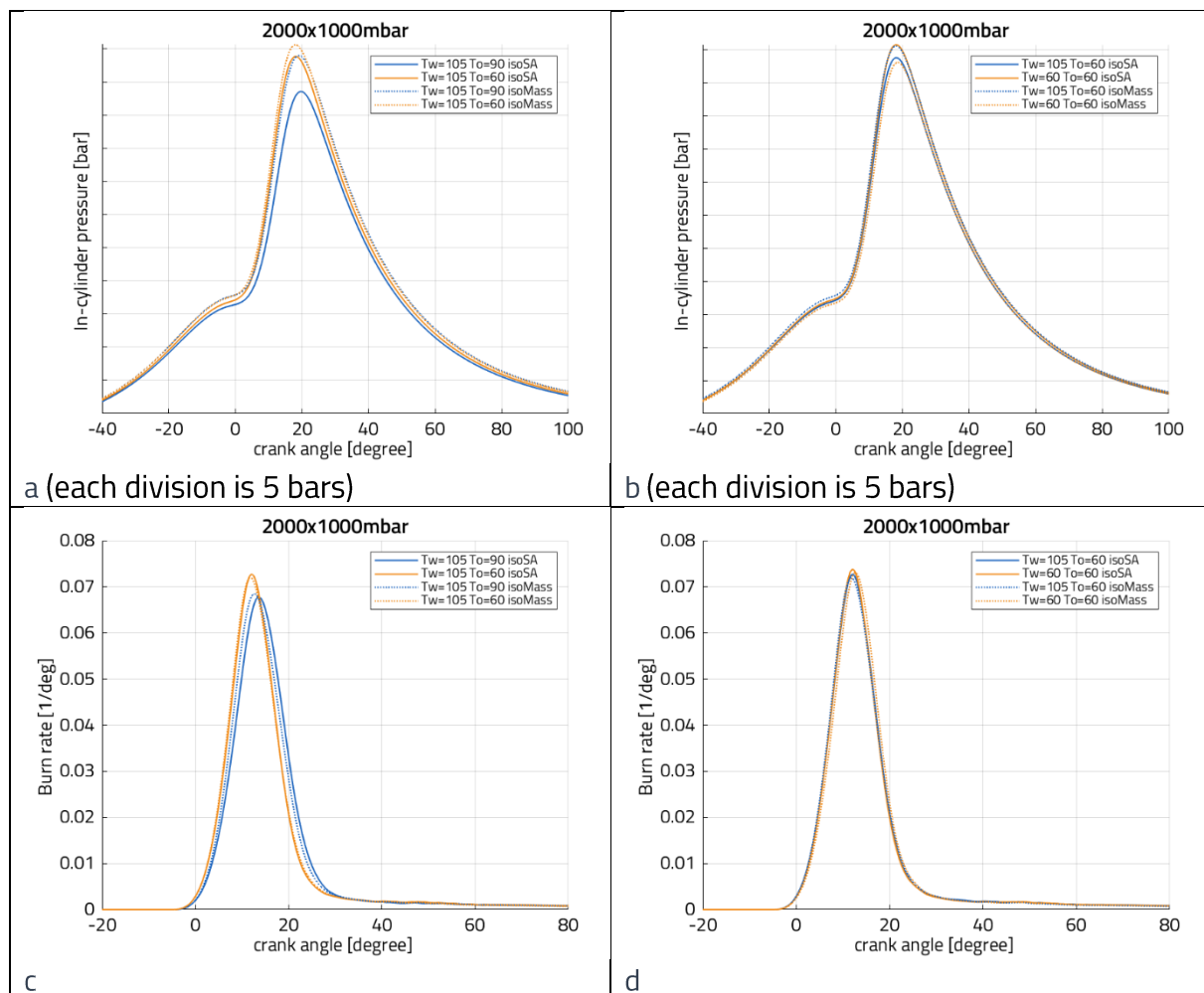


Figure 2-21: in-cylinder pressures (a&b) and burn rates (c&d) of 2000x1000 mbar-R1&R2 at different coolant and oil temperature levels

In the first case where the oil temperature was decreased from 90°C to 60°C, the admission pressure was not modified a lot to maintain a constant air mass flow rate. However, the burn rate was affected, as it was faster in that case. However, when the coolant temperature was decreased, the volumetric efficiency was affected, the admission

pressure had to be modified. The resulting air flow rate was a little bit lower than the rest of the cases, this was also identified at the end of the compression stroke. The pressure at the end of the compression was lower, the combustion developed at almost the same burn rate but since it started at lower pressure, it reached a lower peak as well.

This coolant and oil temperatures sweep puts in evidence that both fluids affect the combustion development. It is thus interesting to see the engine behavior under knocking conditions and to understand how the spark-induced combustion will develop vis-à-vis the end-gas while modifying these coolant temperatures. The impact of coolant and oil temperatures on knock apparition will be analyzed in details in the chapter 3 of this PhD Thesis "Experimental results".

2.2.2.3. Valves timings sweep

Furthermore, the camshaft timing sweep was performed on the engine at 1550 rpm and for different admission pressure. It should be noted that the cases that are going to be presented for each operating point, represent the extreme cases of intake and exhaust valve timing variations.

The different combinations of IVO and EVC considered for 1550 rpm x1400 mbar are presented in table 2-12. Volumetric efficiency is calculated based on the air mass flow past the intake valves and the residuals are calculated at the combustion start by the measured pressure analysis by GT Power.

Intake Valve Opening (CAD ATDC)	Exhaust Valve Closing (CAD ATDC)	Case	Volumetric Efficiency	Residuals (%)	valve overlap (CAD)	Center of valve overlap (CAD ATDC)	Spark Timing (CAD)
-30	-14	1	1,32	1,1	15,683	-22,19	6
-30	0	2	1,46	0,3	30,013	-15,03	6
16	-0	3	1,15	2,0	-15,82	7,8288	3
16	36	4	1,23	1,0	20,161	25,855	3

Table 2-12: valves timings sweep considered at 1550 rpm and P_{adm}=1400 mbar

The camshafts timings are clearly displayed in the figure 2-22

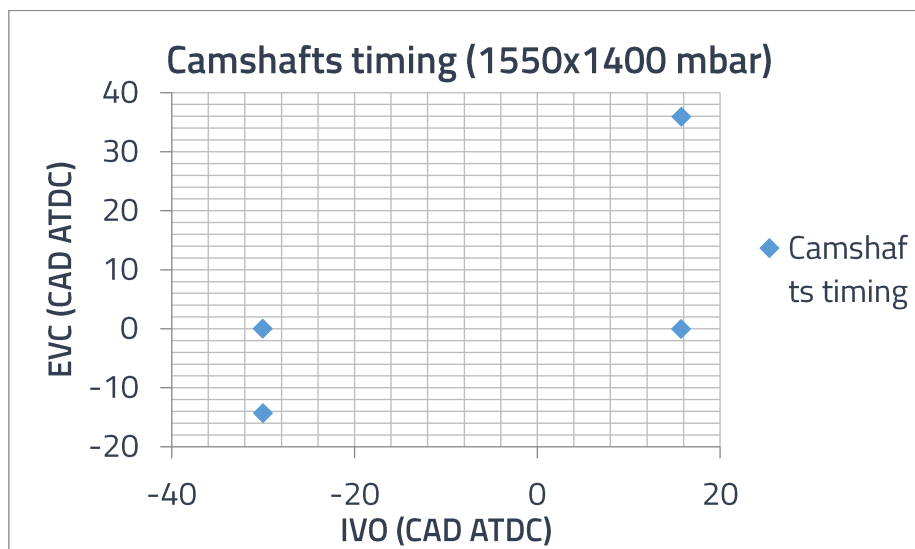


Figure 2-22: Intake and exhaust valves timings at 1550x1400 mbar

The combustion development is studied in the in-cylinder pressure and burn rates curves in figure 2-23.

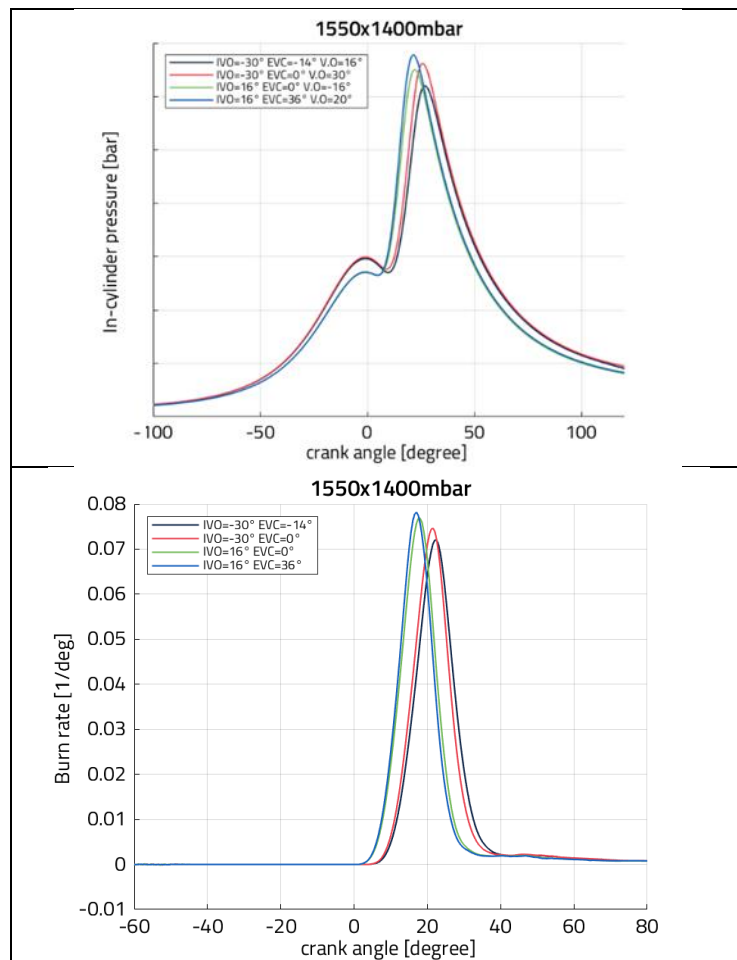


Figure 2-23: incylinder pressures (top, each division is 10 bars) and burn rates (bottom) for the valves timings sweep considered for 1550x1400 mbar

In the first 2 cases, IVO was kept constant and this led to the same compression behavior of the in-cylinder charge. However, the differences of the EVC lead to different combustion behaviors. In #2, higher valve overlapping between the intake and exhaust valves than #1 led to a lower residual rate, a faster combustion process, higher pressure-peak, higher gross IMEP, higher mass flow rate and lower fuel-to-air equivalence (global: at the exhaust) ratio and lower ISFC.

The same can be deduced for #3 & #4 for the compression stroke.

Valves overlapping occurred for #4 ATDC and valves do not overlap for #3.

Between cases 1&2 and 3&4, intake valve opens later for 3&4, allowing less air to be induced to the cylinder. To compensate for the high compression pressure, spark timing was delayed for 1&2 contributing to a relatively lower pressure.

Burn rate for #3 & #4, are shifted to left. This is due to the earlier spark timing when compared to #1&2. Lesser residuals (#2 compared to #1 and #4 compared to #3) lead to a relatively faster combustion, thus higher burn rate (a little bit).

Since only the extreme cases were previously studied, the residuals will be then plotted in function of the valves overlapping for all the camshafts timings that were tested for 1550x1400 mbar in figure 2-24.

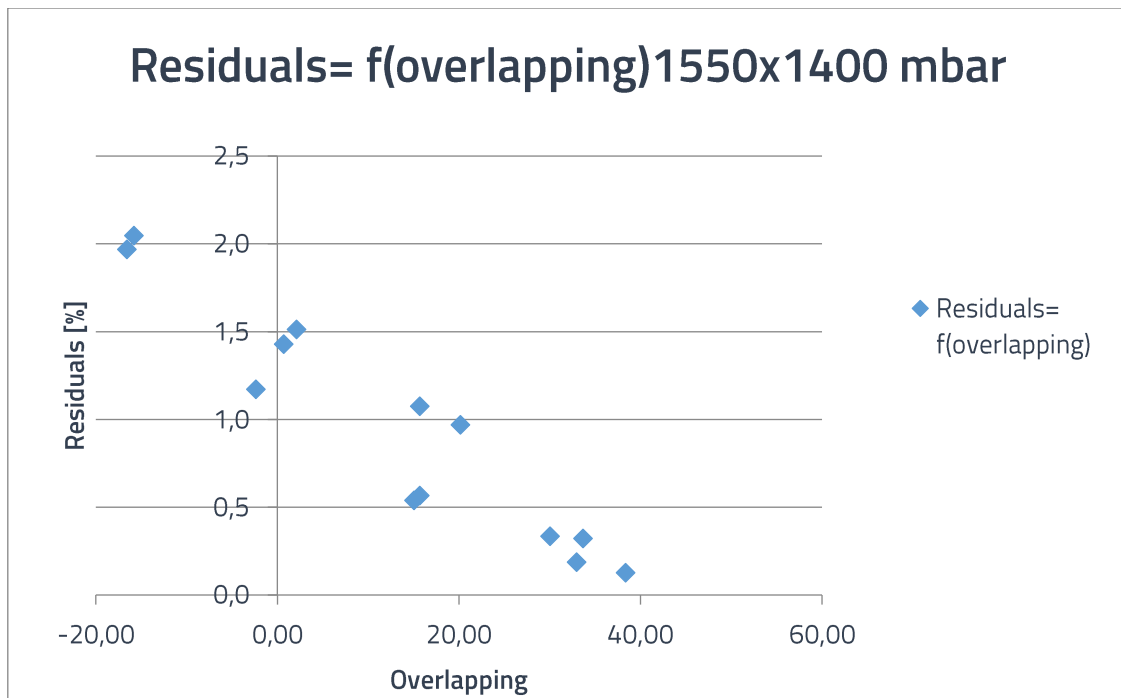


Figure 2-24: residuals in function of valves overlapping for all camshaftstimings at 1550x1400 mbar

As it can be seen, on this operating point, the valves overlapping leads to the scavenging thus decreasing the quantity of residuals confined inside the cylinder. On the contrary, reducing the valves overlap, increases the quantity of residuals inside the cylinder.

Another operating point will be also studied but this time in the naturally aspirated region. The considered point is 1550x900 mbar. The extreme cases of IVO and EVC are displayed in table 2-13.

Intake Valve Opening (CAD ATDC)	Exhaust Valve Closing (CAD ATDC)	Case	Volumetric Efficiency	Residuals (%)	valve overlap (CAD)	Center of valve overlap (CAD)	Spark Timing (CAD)
-30	-15	1	0,62	11,7	14,895	-22,45	-8,615
-30	36	2	0,41	30,2	65,71	2,9656	-20,26
40	-15	3	0,59	4,8	-54,96	12,553	-11,48
40	36	4	0,52	10,8	-4,18	37,941	-17,28

Table 2-13: camshafts timings considered for 1550 rpm x 900 mbar

The intake and exhaust valves timings are better displayed in figure 2-25

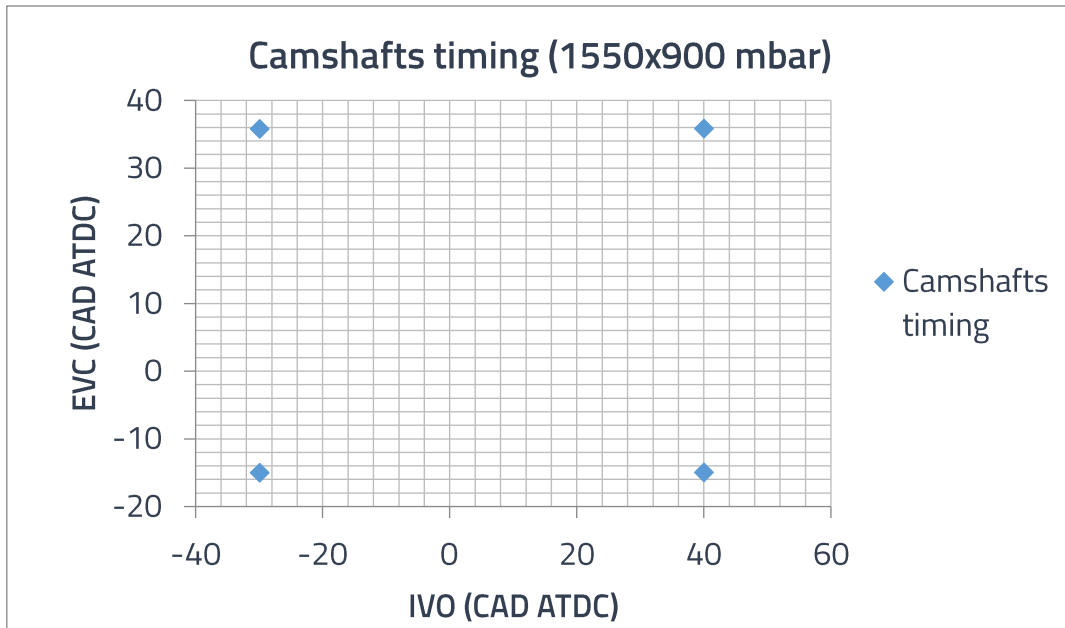


Figure 2-25: Intake and exhaust valves timings considered at 1550x900 mbar

In order to better understand the combustion for the considered valves timings, in-cylinder pressures and burn rates are plotted in the figure 2-26.

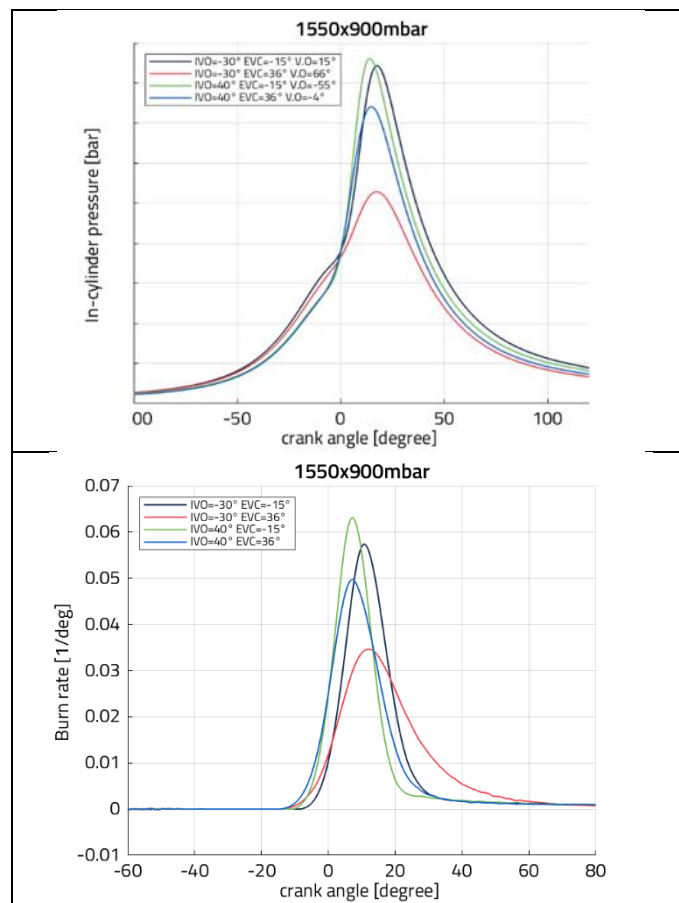


Figure 2-26: in-cylinder pressures (top, each division is 5 bars) and burn rates (bottom) for the considered valves timings at 1550x900 mbar

In the last 2 cases, IVO was kept constant and this led to the same compression behavior of the in-cylinder charge. As for the first 2 cases, a lower compression pressure was obtained for #2 due to the late closing of the exhaust valves after bottom dead center leading to re-aspiration of the burned gases

Overlapping the valves in this operating point contributes to higher rate of iGR thus slower combustion (case #2). Case #3 (no overlapping at all), combustion is the fastest and the in-cylinder pressure reaches the highest peak.

In an atmospheric operating point, overlapping exhaust and intake valves lead to the re-aspiration of the burned gases from the exhaust back to the chamber or even the intake manifold. Higher residuals rate lead to worse combustion (#2)

Even though, no overlapping occurred in #3&4, residuals are found in the chamber due to trapped at the end of the exhaust. In #4, the increased residual content is due to the late closing of the exhaust valves after bottom dead center leading to re-aspiration of the burned gases.

Burn rate profiles are in accordance with in-cylinder pressure: valves overlapping lead to higher fraction of residuals and thus slower combustion and lower burn rates #2. The #3 has a faster burn due to the higher in-cylinder pressure at the end of the compression stroke.

Since only the extreme cases were previously studied, the residuals will be then plotted in function of the valves overlapping for all the camshafts timings that were tested for 1550x900 mbar in figure 2-27.

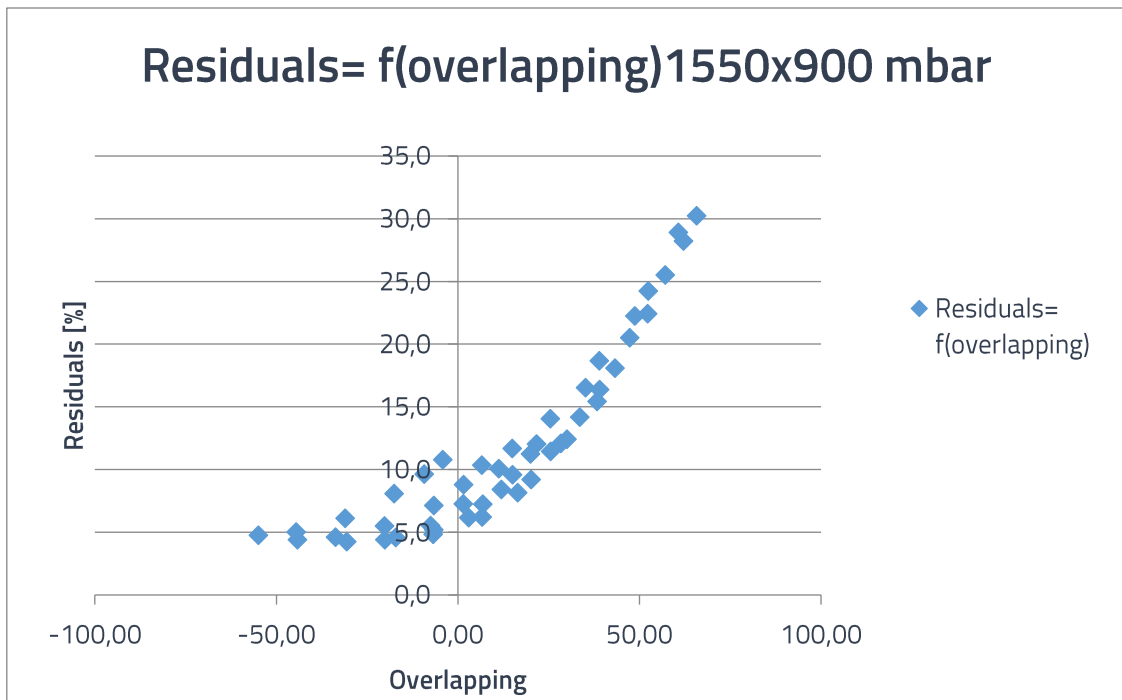


Figure 2-27: residuals in function of valves overlapping for all camshaftstimings at 1550x900 mbar

With atmospheric operating points, the opposite phenomenon is obtained: overlapping valves leads to higher residuals rate in the cylinder. The engine behavior is not the same when an atmospheric or a turbocharged operating point is considered.

Valves timings sweep put in evidence that the combustion development is once again affected. In fact, residuals play sometimes a huge role in the combustion process. It is thus interesting to study the engine behavior under knocking conditions and to understand how the spark-induced combustion will develop vis-à-vis the end-gas while modifying the valves timings. The impact of valves timings on knock apparition will be analyzed in details in the chapter 3 of this PhD Thesis "Experimental results". It is also coupled to the impact of intake air temperature on knock.

2.3. Numerical tools

In this section, the numerical tools that were employed in this PhD thesis are presented and they are the GT-POWER engine simulation software and the different models that were utilized including a predictive combustion model.

GT-POWER is an engine performance simulation used to predict basic performance quantities such as power, torque, airflow, volumetric efficiency, fuel consumption, etc. It also includes physical models for extending the predictions: cylinder and tailpipe-out emissions, in-cylinder and pipe/manifold structure temperature, measured cylinder pressure analysis, combustion development, etc. A complete engine model was collaboratively developed with research engineers in the frame of the industrial partnership between Ecole Centrale de Nantes and Stellantis as it can be seen in the figure 2-28.

This engine model will be used in the frame of this PhD Thesis for 2 purposes:

1. To help with the analysis of the experimental results obtained at the test bench specially at the level of the knock tests. The model can help to provide additional data such the combustion chamber wall temperature, the composition of the in-cylinder mixture, the temperature of the unburned and the burned gases inside the cylinder as well as the flame speeds.
2. To improve a phenomenological knock model and to test its capacity when implemented in the complete engine model to predict the knock apparition when varying engine control parameters. The knock modeling and the simulations results will be presented in a separate chapter in this PhD Thesis.

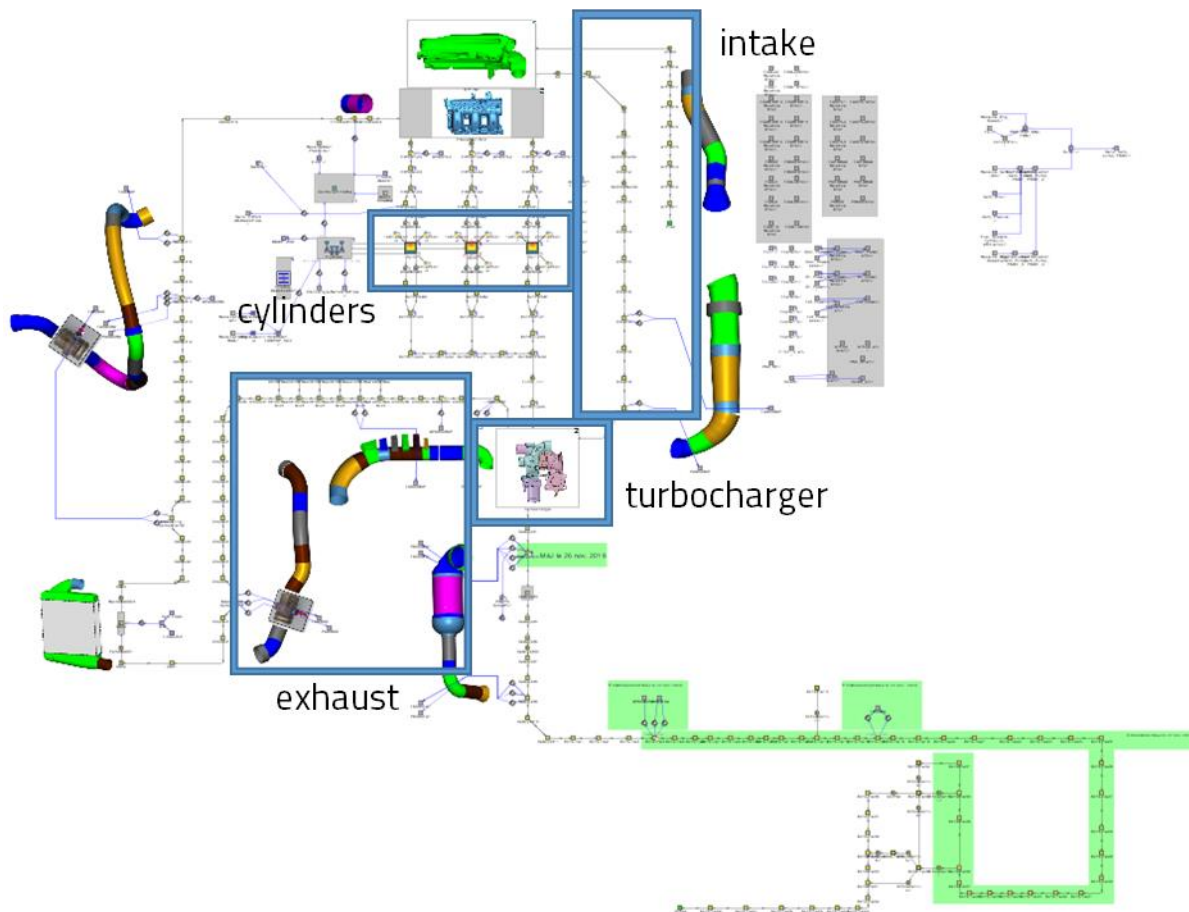


Figure 2-28: Overview of the complete engine model

In the following part, an overview of the engine model construction will be presented in the part 2.3.1 and then a survey on the combustion models will be elaborated in part 2.3.2 followed by a choice of a model and a calibration.

It should be noted that combustion modeling represents a preliminary task in knock modeling as a combustion model must be defined in the cylinder before proceeding with a knock model.

2.3.1. Complete engine model

The engine model is designed to target the inlet pressure of each operating point. The intake pressure regulation was achieved by 2 means:

1. In the atmospheric area, the admission pressure at each engine speed is regulated by adjusting the throttle angle position.
2. In the turbocharged area and since the throttle is fully opened, the admission pressure is regulated by the waste gate position.

The regulation of the admission pressure at all of the engine speeds by either the waste gate or the throttle position permits to reach the required loads. Throttle position and waste gate position are not directly used as inputs for the engine model because the actual position is not necessarily known very accurately.

Air loop parts were converted to GT-Power components using a GT-Power software Spaceclaim and GEM3D. CAD plans are processed in Spaceclaim to remove useless parts and keep those that compose the wetted surfaces and GEM3D cut the different parts obtained into GT-Power components. As an example, the intake line as it can be seen in the figure 2-29, can be divided into 3 parts:

1. The Duct between the atmosphere and the filter
2. The air filter
3. The duct between the air filter and the compressor inlet

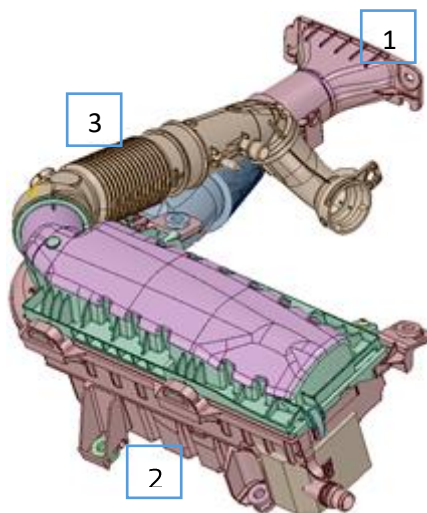


Figure 2-29: intake line upstream the compressor

The duct between the air filter and the compressor inlet can then be converted into 10 GT-Power components to respect the total length, the bends and the changing areas as it can be seen in the figure 2-30.

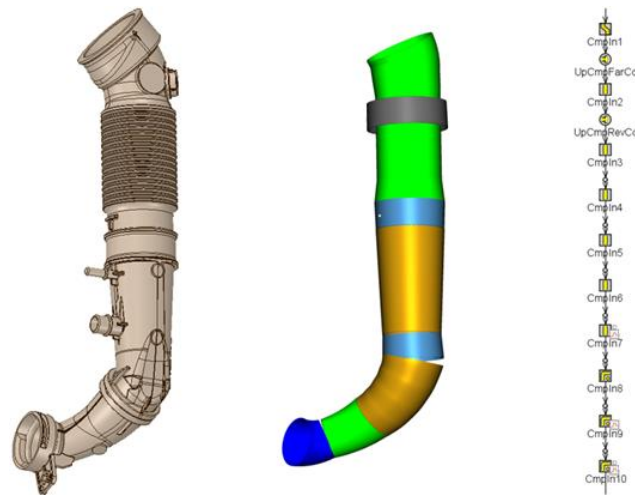


Figure 2-30: conversion on the compressor inlet duct into 10 GT-Power components

Discharge and friction multipliers are also implied and tuned to fit the pressure drop of the experimental results.

This procedure is applied to all of the air loop and exhaust line components of the engine. The tuning of all of the multipliers and coefficients is performed using operating points from the performance tests that were previously presented.

Compressor and turbine were each modeled separately. The compressor was modeled to meet three purposes:

1. Reproduce the experimental temperature at the compressor outlet
2. Reproduce the experimental air flow rate
3. Reproduce the experimental compression ratio

In the atmospheric area, and since the load is regulated by the throttle, the compressor speed is thus regulated with the waste gate to reach experimental compression ratio.

The turbine is modeled to meet two purposes

1. Reproduce the experimental turbine expansion ratio
2. Reproduce the experimental turbine outlet temperature

In the turbocharged area and since the load is regulated by the waste gate, a flow split is added to the turbine inlet representing the waste gate. The waste gate diameter is then regulated to target the experimental expansion ratio.

As for the cylinder head, forward and reverse discharge coefficients were also tuned to match the experimental head pressure drop at the level of the pipes and the valves.

In order to accurately predict the combustion development and the knock occurrence, the combustion chamber dimensions, spark and valves locations are also provided. Thus in the cylinder object, a combustion model should be first defined and calibrated.

A review of the available combustion models in the literature will be presented in section 2.3.2, at the end of this section, a model will be selected, calibrated and then validated. Nevertheless, the main objective on the numerical side of this PhD thesis is to predict the knock occurrence on a complete engine model. Thus, after tuning the combustion model, a knock model will be defined and calibrated as well. Everything related to knock modeling are presented in details in a separate chapter of this PhD Thesis "Knock modeling and simulations"

2.3.2. Combustion model

An overview of the different combustion models available in the literature is presented and then a one of these models will be chosen, and calibrated using engine performance tests.

2.3.2.1. Eddy burn-up model

The eddy burn-up model consists of separating the combustion into 2 zones. As seen in figure 2-31, a fresh gases zone and a burned gases zone and they are both separated by the flame front. In this model, it is assumed that the fresh gas eddies are entrained in a spherical flame front and burn in a characteristic time.

The fresh gases have a density ρ_u , are entrained at velocity equal to the summation of the turbulent s_T and the laminar speed s_L . The rate of the entrained mass is:

$$\frac{dm_e}{dt} = \rho_u A_L (s_L + s_T) \quad (25)$$

This entrained mass is burned in a characteristic time τ_b

$$\frac{dm_b}{dt} = \frac{m_e - m_b}{\tau_b} \quad (26)$$

However, an exponential term has been added to the burned mass rate as stated by [21] in [1]:

$$\frac{dm_b}{dt} = \frac{m_e - m_b}{\tau_b} \exp\left(C_{tw} \frac{t_{wall} - t}{\tau_b}\right) \quad (27)$$

$$\tau_b = C_{\tau_b} \frac{L_T}{s_L} \quad (28)$$

t_{wall} is the time when the flame reaches the wall and t is the time from the beginning of the combustion. C_{tw} and C_{τ_b} are coefficients to adapt the model to different operating points of the engines. Some models consider the Taylor microscale for the computation of the characteristic time instead of the integral length scale such as [85].

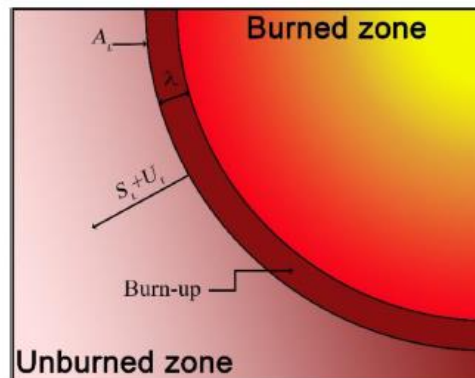


Figure 2-31 :Eddy burn-up combustion scheme[20]

As for the computation of the turbulent velocity (as said in [86])

$$s_T = Da^{0.25} u' A_{sT} \sqrt{1 + \frac{\tau_t}{t} \left(\exp\left(-\frac{t}{\tau_t}\right) - 1 \right)} \quad (29)$$

$$\tau_t = C_{\tau_t} \frac{L_T}{u'} \quad (30)$$

This equation is reported to well describe the freely propagating flame as well as the early flame kernel development [1]. A_{sT} and C_{τ_t} are calibrating coefficients.

Laminar flame velocity:

The laminar flame speed is an important parameter for the combustion modeling. The empirical correlations that were proposed in the literature are the following [1] [87] [88]:

$$s_L = s_L^0(\varphi) \left(\frac{T_u}{T_0}\right)^\alpha \left(\frac{p}{p_0}\right)^\beta (1 - 2.06X_{RGB}^b) \quad (31)$$

$$s_L^0 = B_m + B_\varphi(\varphi - \varphi_0)^2 \quad (32)$$

For isooctane:

$$s_L^0 = B_m + B_\varphi(\varphi - \varphi_0)^2 = 0.263 - 0.847(\varphi - 1.13)^2 \quad (33)$$

$$\alpha = 2.18 - 0.847(\varphi - 1) \quad (34)$$

$$\beta = -0.16 + 0.22(\varphi - 1) \quad (35)$$

Standard condition: $p_0=1$ atm and $T_0=298$ K. T_u is the fresh gas temperature, p is the cylinder pressure and X_{RGB} is the residual burned gases fraction. α and β are the calculated exponents as a function of air-to-fuel equivalence ratio φ and characteristic of the fuel. $b=0.733$ is the dilution exponent multiplier for the RGB fraction influence on the laminar speed.

The integral length scale :

The integral length scale L_T of aerodynamic turbumence is also an essential parameter for the combustion modeling. It is imposed by the geometry of the combustion chamber and modeled in function of the combustion chamber volume [1] [89]

$$L_T = C_{L_T} V^{1/3} \quad (36)$$

2.3.2.2. FKFS model

FKFS model is based on the Eddy burn-up model where the flame propagation takes place in hemisphere. The combustion chamber is divided into two zones: burned and unburned zone separated by the flame front. The spark plug in the simulation must not be set in the exact center of the combustion chamber. The hemispherical propagation of the flame first increases until it reaches the walls where it extinguishes [85].

$$\frac{dm_e}{dt} = \rho_u A_L (s_L + s_T) \quad (37)$$

$$\frac{dm_b}{dt} = \frac{m_e - m_b}{\tau_b} \quad (38)$$

$$\tau_b = \frac{\lambda_T}{s_L} \quad (39)$$

$$\lambda_T = \sqrt{15 \frac{L_T \nu}{u'}} \quad (40)$$

$$L_T = \left(\frac{6}{\pi} V\right)^{1/3} \quad (41)$$

$$s_L = s_L^0(\varphi) \left(\frac{T_u}{298 \text{ K}}\right)^\alpha \left(\frac{p}{1 \text{ bar}}\right)^\beta (1 - 2.06 X_{RGB}^b) \quad (42)$$

$$s_L^0 = 0.305 - 0.549(\varphi - 1.21)^2 \quad (43)$$

$$\alpha = 2.18 - 0.8(\varphi - 1) \quad (44)$$

$$\beta = -0.16 + 0.22(\varphi - 1) \quad (45)$$

A FKFS model was calibrated by M. Grill et al. [85] and the simulation process was compared to the measured results. It was concluded that the reproduction of the burn rate was very good where only few deviations were showed up at high load. In addition, a very realistic pressure trace was also achieved. This could be seen in the following figure 2-32:

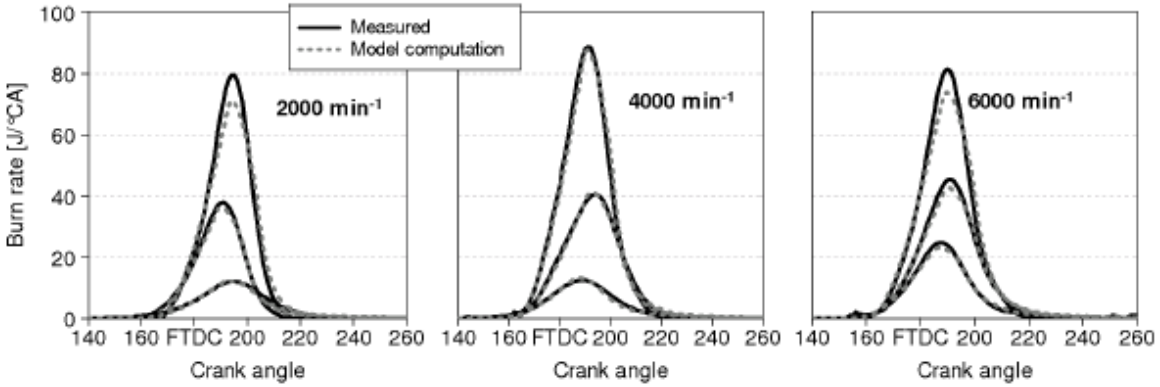


Figure 2-32 : difference between simulation and experimental results regarding the burn rate at different engine speeds from part load to wide open throttle [85]

2.3.2.3. Fractal model

In this approach, the flame is wrinkled by the aerodynamic turbulence. The wrinkle of the flame is supposed to have a self-similar development (figure 2-33) [89].

The wrinkling factor and the burning mass rates are defined

$$\mathcal{E} = \frac{S_T}{s_L} = \frac{A_T}{A_L} \quad (46)$$

$$\frac{dm_b}{dt} = \rho_u A_L s_L \mathcal{E} \quad (47)$$

The laminar flame surface A_L corresponds to the spherical flame surface.

In the fractal model, the wrinkling phenomenon can be represented by a fractal dimension D_3 for a range of length scales going from L_{min} to L_{max} so [90]:

$$\mathcal{E} = \left(\frac{L_{max}}{L_{min}} \right)^{D_3 - 2} \quad (48)$$

D_3 is a function of the turbulent flow behavior. L_{min} is the Kolmogorov scale. L_{max} is a function of the flame radius R_f through a calibrating coefficient C_R .

$$D_3 = \frac{2.35u' + 2.05s_L}{u' + s_L} \quad (49)$$

$$L_{min} = \eta_k = L_T \left(\frac{u' L_T}{\nu} \right)^{0.75} \quad (50)$$

$$L_{max} = C_R R_f \quad (51)$$

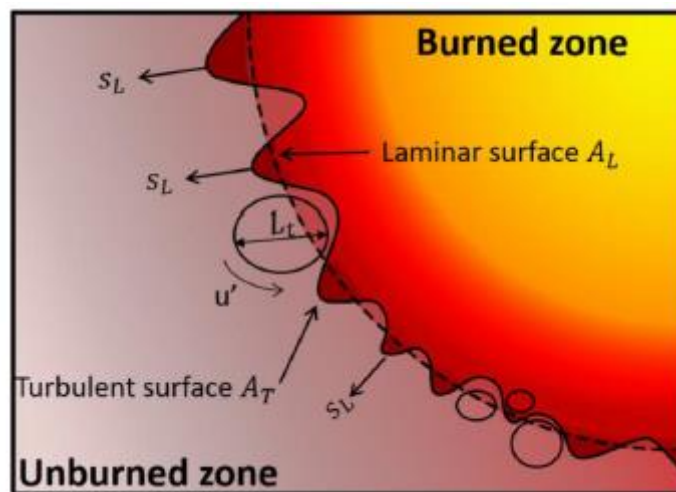


Figure 2-33:fractal combustion model scheme[20]

2.3.2.4. CFM 1D Model

The CFM-1D, Coherent Flame Model, is based on the 3D gasoline combustion model ECFM developed by Colin et al. at IFP. In this model, the combustion chamber is divided into 2 zones: a burned gases and an unburned gases zone separated by a premixed turbulent flame. The model was validated comparing 1D and 3D results on steady state operating engine. The CFM is adapted to the flamelet regime for premixed combustions and is based on the following hypothesis [91]:

Homogeneity of the mixture

Mixture of perfect gases

Mixture of 3 gas: fresh air, fuel vapor and burned gases

Stoichiometric combustion

Cylindrical combustion chamber

No space dependency of the different variables

The pressure is supposed to be homogeneous $p = p_u = p_b$

In the CFM-1D, it is assumed that the flame is an infinitely thin layer separating the burned and the unburned zone. Using the mass conservation through the flame front gives the burned mass fraction or what is called by the progress variable \tilde{c} :

$$\tilde{c} = \frac{m_b}{m} = 1 - \frac{m_u}{m} \quad (52)$$

The basis of the CFM is to describe the fuel consumption taking into account the flame surface and the laminar speed.

$$\frac{dm_f}{dt} = \rho_u A_T s_L Y_f^u \quad (53)$$

Y_f^u is the fuel mass fraction in the unburned mixture, ρ_u density of unburned mixture.

$$Y_f^u = \frac{m_f}{m_u} \quad (54)$$

The laminar flame speed is calculated using the Metghalchi and Keck correlation [88]

$$s_L = s_L^0(\varphi) \left(\frac{T_u}{T_0}\right)^\alpha \left(\frac{p}{p_0}\right)^\beta (1 - 2.1X_{RGB}) \quad (55)$$

$$s_L^0 = B_m + B_\varphi(\varphi - \varphi_0)^2 \quad (56)$$

$$\alpha = 2.18 - 0.8(\varphi - 1) \quad (57)$$

$$\beta = -0.16 + 0.22(\varphi - 1) \quad (58)$$

B_m and B_φ and φ_0 are defined by Metghalchi and keck for a standard gasoline [88]

The flame surface is defined by:

$$A_T = A_{geo} \mathcal{E} C_{fw} \quad (59)$$

C_{fw} is calibrating coefficient to model the flame-wall interaction.

A_{geo} is the geometrical surface of the flame and it is computed knowing the burned mixture volume V_b under the hypothesis of a spherical flame:

$$A_{geo} = 4\pi r_{geo}^2 \quad (60)$$

$$r_{geo} = \sqrt[3]{\frac{3V_b}{4\pi}} \quad (61)$$

$$V_b = V - V_u \quad (62)$$

V is the combustion chamber volume defined by the crankshaft motion, engine speed, stroke and connecting rod. V_u is the unburned mixture volume defined by:

$$V_u = \frac{m_u r_u T_u}{p} \quad (63)$$

With r_u and T_u the perfect gas constant and the unburned mixture temperature respectively.

When the flame diameter reaches the stroke value, the flame becomes a cylinder:

$$A_{geo} = 2\pi r_{geo} S \quad (64)$$

$$r_{geo} = \sqrt{\frac{V_b}{\pi S}} \quad (65)$$

S is the stroke: distance between the piston and the cylinder head.

The evolution of the flame is assumed to be laminar until its radius reaches a characteristic value of r_0 when the flame is wrinkled by turbulence. The wrinkling factor \mathcal{E} is then:

$$\mathcal{E} = \begin{cases} 1, & r_{geo} < r_0 \\ 1 - \min\left(1, \frac{r_{geo} - r_0}{r_0}\right) \cdot \mathcal{E}_{eq}, & r_{geo} > r_0 \end{cases} \quad (66)$$

\mathcal{E}_{eq} is defined by:

$$\mathcal{E}_{eq} = 1 + \frac{S_T}{S_L} = 1 + \frac{2\sqrt{E \cdot \nu_T}}{S_L} \quad (67)$$

$$\nu_T = 0.09 \frac{k^2}{\varepsilon} \quad (68)$$

$$E = \alpha \frac{u'}{L_T} \quad (69)$$

$$k = \frac{3}{2} u'^2 \quad (70)$$

$$\varepsilon = 0.42 \frac{k^{3/2}}{L_T} \quad (71)$$

ν_T is the turbulent viscosity, u' is the turbulent intensity, L_T is the integral length scale, k is the turbulent kinetic energy at a dissipation rate ε .

The turbulent kinetic energy k is correlated to the dissipated kinetic energy $E_{c,diss}$ and the kinetic energy E_c [92]:

$$k = C_{turb} \frac{E_{c,diss}}{m} \quad (72)$$

$$\frac{dE_{c,diss}}{dt} = \frac{dE_c}{dt} - C_{diss} E_{c,diss} \quad (73)$$

The evolution of this kinetic energy varies in function of the kinetic energy of the motions of the swirl and the tumble, the spray injection and the effects of the squish:

$$\frac{dE_c}{dt} = \frac{dE_{c,swirl}}{dt} + \frac{dE_{c,tumble}}{dt} + \frac{dE_{c,spray}}{dt} + \frac{dE_{c,squish}}{dt} \quad (74)$$

All of preceding kinetic energies are neglected except of the tumble whose evolution in spark ignition engines is the main generator of kinetic energy. Considering a solid rotation of the mixture [91]

$$E_c = \frac{1}{2} \cdot J \cdot \omega_{tumble}^2 = \frac{1}{2} \cdot J \cdot N_{tumble} \cdot \omega_e^2 \quad (75)$$

$$J = \frac{1}{2} \cdot m \cdot \left(\frac{\Delta l}{2}\right)^2 \quad (76)$$

ω_e is the engine angular velocity, N_{tumble} is the tumble number

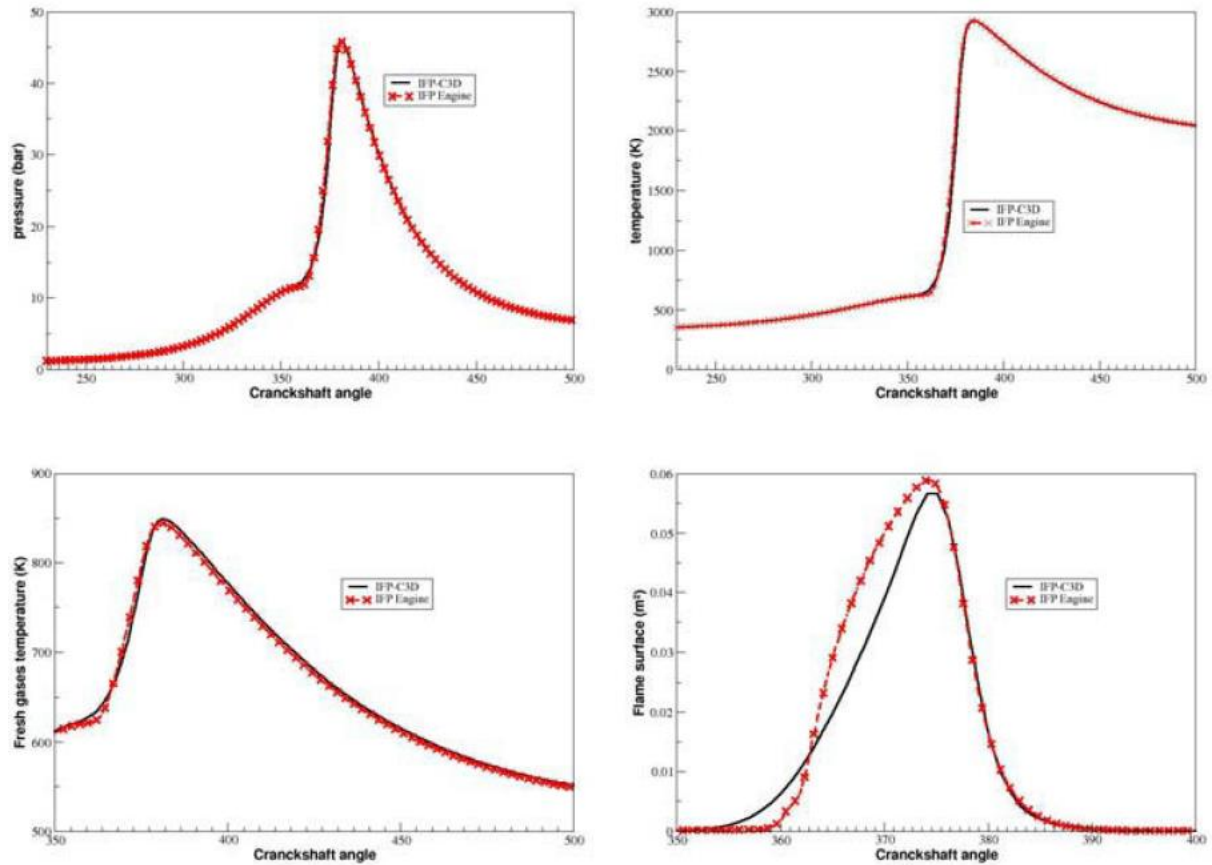


Figure 2-34: Comparison between the 3D simulation and the CFM-1D model developed by IFP[91]

In figure 2-34, the 3D calculation are plotted in black solid lines whereas the CFM-1D model is plotted in red-dotted lines. Some differences of 0.1% were found in the high-pressure loop IMEP. The evolution of burned fuel fraction, unburned gases temperature in CFM-1D are in good agreement with the 3D computations [91]

2.3.2.5. SI-Turb

The SI-Turb is the spark ignition turbulent flame model developed by GT Power. It is based on the Eddy burn-up model and it predicts the burn rate for homogeneous charge in spark-ignition engines taking into account the cylinder's geometry, the spark location and timing, air motion and fuel properties [93] [94] [95]

The fresh gases have a density ρ_u , are entrained at velocity equal to the summation of the turbulent s_T and the laminar speed s_L as described by equation (1) and (2)

This entrained mass is burned in a characteristic time τ_b

$$\tau_b = \frac{\lambda_T}{s_L} \quad (77)$$

λ_T is the Taylor microscale

$$s_T = u' C_{TFS} \left(1 - \frac{1}{1 + C_{FKG} \frac{R_f^2}{L_T^2}} \right) \quad (58)$$

$$\lambda_T = \frac{C_{TLS} L_T}{\sqrt{Re_t}} \quad (78)$$

$$Re_t = \frac{\rho_u u' L_T}{\mu_u} \quad (79)$$

$$s_L = (B_m + B_\varphi (\varphi - \varphi_0)^2) \left(\frac{T_u}{T_0} \right)^\alpha \left(\frac{p}{p_0} \right)^\beta f(Dilution) \quad (80)$$

$$f(Dilution) = 1 - 0.75 * C_{DE} * (1 - (1 - 0.75 * C_{DE} * X_{RGB})^7) \quad (81)$$

u' is the turbulent intensity, R_f is the flame radius, L_T is the integral length scale, Re_t is the turbulent Reynolds number, μ_u is the fresh zone dynamic viscosity, φ is the fuel-air equivalence ratio. T_u is the fresh gas temperature, p is the cylinder pressure and X_{RGB} is the residual burned gases fraction. $p_0=1$ atm and $T_0=298$ K (standard conditions).

For the laminar speed s_L and for the gasoline used as the fuel:

$B_m = 0.35$ m/s and represents the maximum laminar speed

$B_\varphi = -0.549$ m/s and represents the laminar speed roll-off value

$\varphi_0 = 1.1$ and represents the equivalence ratio at maximum speed

$\alpha = 2.4 - 0.271\varphi^{3.51}$ and represents the temperature exponent

$\beta = -0.357 + 0.14\phi^{2.77}$ and represents the pressure exponent.

In these modeling equations, 4 calibrating factors are used:

1. C_{FKG} : Flame kernel growth multiplier FKGM which adjusts the initial growth rate of the flame kernel
2. C_{TFS} : Turbulent flame speed multiplier TFSm
3. C_{TLS} : Taylor length scale multiplier TLSm

C_{TFS} and C_{TLS} both adjust the effects of turbulent intensity and length scale

4. C_{DE} : Dilution exponent multiplier DEM which adjusts the effect of dilution

2.3.2.6. Model selection

All of the previously mentioned combustion models are interesting and they proved to be beneficial in the prediction of the combustion development and combustion parameters. They all showed some similar performance in the prediction of the combustion development. However, SITurb was selected since it is already coded in the software GT. Nevertheless, the SITurb combustion model was calibrated on the model using experimental results from the performance maps in order to accurately predict the combustion behavior. In the following part, the calibration of the SITurb will be elaborated in details.

2.3.3. Calibration of a predictive combustion model

These aforementioned multipliers in the predictive combustion SITurb need to be calibrated. The calibration requires a set of experimental operating points taken from the performance tests that were presented earlier in this PhD manuscript and it was done in 2 steps:

1. An in-cylinder pressure analysis
2. An optimization procedure

The calibration procedure was inspired by the manuals of the GT-Suite engine performance provided by Gamma Technologies but it was improved in order to better predict combustion behavior and consequently the knock apparition[96].

To perform an in-cylinder pressure analysis, the complete engine model is used without a combustion model, experimental operating points must be defined and some measured data are required to perform the analysis and they include:

- Crank angle resolved instantaneous cylinder pressure
- Air flow and fuel flow rates
- Spark Timing
- Engine pollutant emissions (unburned hydrocarbon and CO)

At the start of each cycle the burn rate is calculated using the trapped conditions within the cylinder along with the measured in-cylinder pressure trace and this calculated burn rate is then imposed during the next cycle to calculate the in-cylinder pressure. These cycles are repeated until the convergence is reached. As a result of the in-cylinder pressure analysis, volumetric efficiency, trapping ratio, residual fraction, in-cylinder turbulence and wall initial temperature are computed.

The resulting data from the in-cylinder analysis are used to perform the optimization procedure. For that purpose, a model has to be setup. All parts, but the cylinder, cranktrain and injector connected to the cylinder are deleted. Also, The SITurb predictive combustion model has to be defined at that stage. The model will only perform a closed volume pressure analysis, i.e. no gas-exchange is included. The model will provide a comparison of cylinder pressure and burn rate between the measurement and the predictive combustion model.

The initialization is done at three different locations in the cylinder:

An cylinder initial state object has been created. It initializes the cylinder using Volumetric Efficiency, Trapping Ratio, Fuel at IVC and Residual Fraction. Volumetric efficiency, fuel mass at IVC, trapping ratio and residual fraction are results available from the in-cylinder pressure analysis created in the previous step.

The cylinder wall temperatures are set using the results from the in-cylinder pressure analysis.

Furthermore, the 'SITurb' model has to be specified as Combustion Object. It requires the combustion chamber geometry which is specified using the head and piston STL files. Also, the spark plug location is specified here.

The aforementioned four parameters are used for the calibration:

- Flame kernel growth multiplier FKGM: multiplier used to scale the calculated value of the growth rate of the flame kernel and it influences the ignition delay.

$$s_T = u' \cdot TFSm \left(1 - \frac{1}{1 + FKGM \frac{R_f^2}{L_T^2}} \right) \quad (58)$$

- Dilution exponent multiplier Dem: multiplier used to scale the effect of dilution (residuals and EGR) on the laminar flame speed

$$f(Dilution) = 1 - 0.75 * DEm * (1 - (1 - 0.75 * C_{DE} * X_{RGB})^7) \quad (82)$$

- Turbulent flame speed multiplier TFSm: multiplier used to scale the calculated turbulent flame speed and it influences the overall duration of combustion.
- Taylor length scale multiplier TLSm: multiplier used to scale the calculated value of the "Taylor microscale" of turbulence.

$$\lambda_T = \frac{TLSm \cdot L_T}{\sqrt{Re_t}} \quad (59)$$

An optimization runs to find the single set of model constants that will provide the best possible match to a wide variety of operating points. This best match may be defined in terms of matching measured and predicted burn rate, cylinder pressure, IMEP, emissions, etc. It was chosen to find the best match of measured and predicted burn rates, by running a genetic algorithm that gives the lowest value of the "Improved Burn Rate RMS Error " averaged over all operating points.

The Improved Burned Rate RMS Error (Measured vs Predicted) is defined by the following formula:

$$parmserr2br = \sqrt{\frac{\int_{t_0}^{t_f} (LHV_{pred} \cdot BR_{pred} - BR_{meas})^2 dt}{t_f - t_0}}$$

BR_{pred} : Combustion burn rate calculated from predicted pressure (normalized by total fuel)

BR_{meas} : Combustion burn rate calculated from measured pressure (normalized by total fuel)

t_f : Time at end of integration. This is the time at which the measured 90% burn point is reached relative to the total burned fuel. The integration is stopped at measured 90% fuel burned to avoid inclusion of long "tails" that may include excessive noise from the measured pressure measurement.

t_0 : Time at beginning of integration. This will correspond to the start of combustion specified in the EngBurnRate object.

The Improved Burn Rate Root Mean Squared Error (RMS Error) is a calculation of the error between the predicted combustion burn rate and measured combustion burn rate over the time period between the specified start of combustion and measured 90% burn angle and also is weighted by the LHV multiplier of the predicted analysis in order to match the energy content of the measured exhaust gases. This value is provided to facilitate automated optimization of predictive combustion models as it provides a single value that characterizes the quality of fit between the predicted and measured burn rate curves. The value may be minimized over many different operating points (a larger value represents higher deviation between the two curves).

The whole calibration procedure wouldn't have been possible without some experimental results.

2.3.3.1. 1st calibration using experimental data from the whole engine performance map: SITurb-1

In a first place a calibration was performed using experimental data results from the whole engine performance map. 30 operating points from the 298 points were chosen across all the region as it can be seen in figure 2-35. They are marked in green. Points highlighted in white are operating points that were performed on the bench but were not used for calibration. They were however used with the calibration points to validate the results. Points highlighted in grey are operating points that could not be performed due to the engine configuration limitations.

Rad Ind	1050	1200	1350	1550	1750	2000	2500	3000	3500	4000	4500	5000	5500	5800
0,5														
1			█			█			█				█	
2														
3				█				█				█		
4										█				
5		█												
6														█
7	█											█		
8							█			█				
9				█										
10														
11									█					
12						█							█	
13											█			
14					█									
15			█				█							
16										█		█		
17														
18														
19			█											
20								█		█				
21					█									
22						█								
23														
24								█						
25														

Figure 2-35: points used for the optimization process of SITurb-1

The number of points used for the calibration was based on a preliminary sensitivity study. In this study several calibration procedures were performed under the same conditions with the only differences of the number of the operating points used for the calibration. At the end of each calibration, the values of the obtained calibrated multipliers (FKGm, DEm, TFSm and TLSm) were plotted with respect the number of operating points considered in figure 2-36.

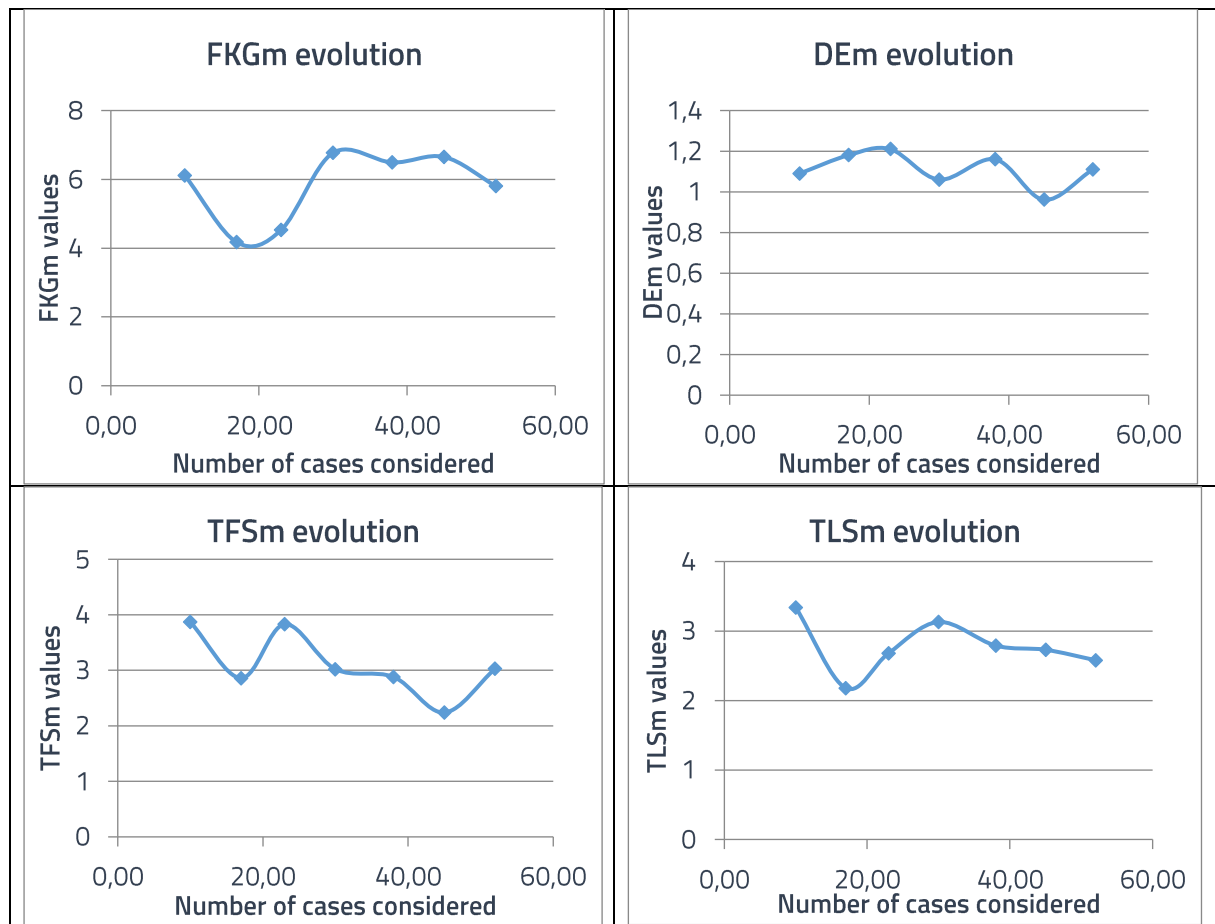


Figure 2-36: evolution of the SITurb-1 parameters in function of the number of cases considered

These graphs show that starting 30 cases considered, the value of the parameters don't fluctuate a lot. However, in order define a number for the cases to be considered, these parameters obtained from the different calibrations were exported to the model and tested on all the other cases that weren't used for calibration. Note that the 10 cases considered in the first calibration were re-considered in the 17 cases calibration that were also used in 23 cases calibration and accordingly to the 52 cases. Taking into account the energy and time consumption when running an optimization procedure, considering 30 operating points represent a good trade-off.

For the calibration of the SITurb-1, the obtained values of multipliers are presented in table 2-14:

	SITurb-1
FKGm	6.9677477
DEm	1.2420095
TFSm	3.2782295
TLSm	2.5839753

Table 2-14: values of the calibrated parameters of the SITurb-1 model

Some of the combustion parameters will only be displayed in figures 2-37 to 2-40. Some measured versus predicted combustion parameters are plotted on the same graph to evaluate to capacity of the SITurb-1 combustion model.



Figure 2-37: measured vs predicted for SITurb-1 CA50 within [-3,3] CAD range

247 out of 298 points are within the range ± 3 CAD

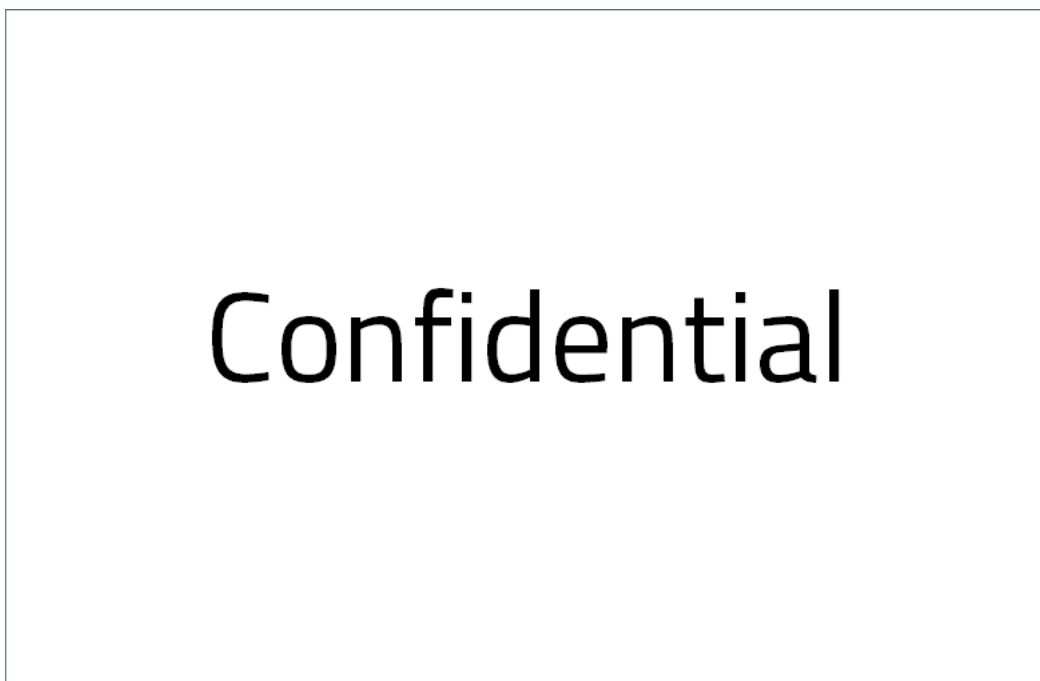


Figure 2-38: measured vs predicted for SITurb-1 CA1075 within [-3,3] CAD range

206 out of 298 points are within the range ± 3 CAD



Figure 2-39: measured vs predicted for SITurb-1 IMEP within [-5%,5%] range

234 out of 298 points are within the range $\pm 5\%$

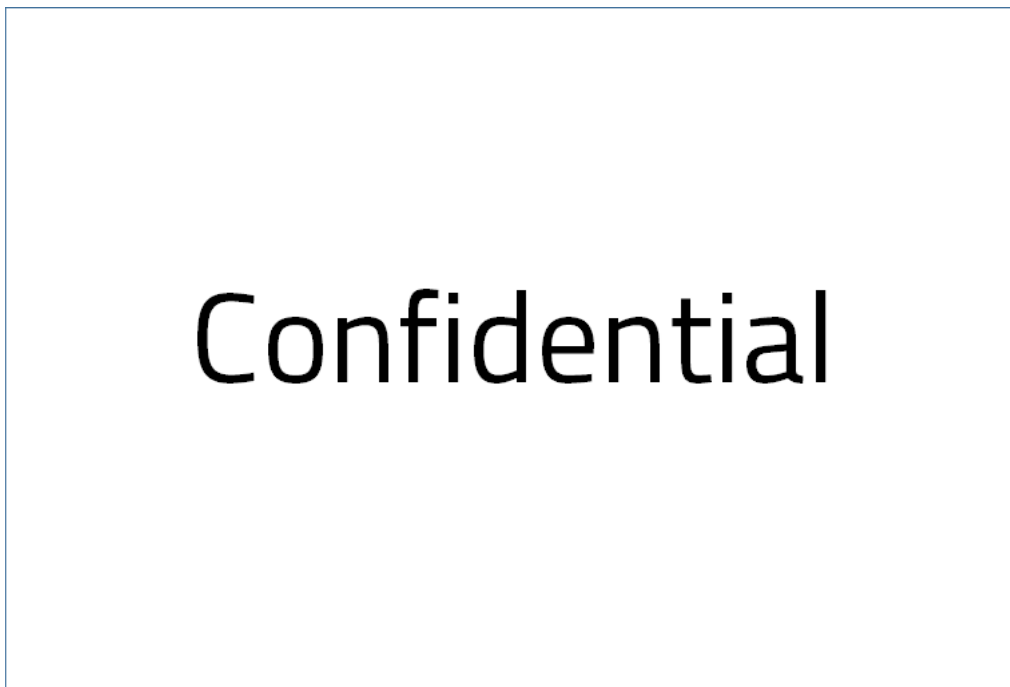


Figure 2-40: measured vs predicted for SITurb-1 maximum pressure within [-5,5] bar range

227 out of 298 points are within the range ± 5 bar

It should be noted that SITurb is mainly designed to operate in homogeneous conditions. However, for engine speeds between 1200 and 2000 rpm and when the intake pressure exceeds 1100 mbar, the injection strategy on the engine-bench is a triple injection. A triple

injection with a late third injection leads to charge stratification and could impact the accuracy of the predicted results when compared to experimental results. Moreover, knock is the main concern and as it was seen in the literature review, the knock apparition is mainly restricted to the low engine speed and high load regions. It is then interesting to calibrate the SITurb on the complete engine model only in the region where knock apparition is the most probable.

2.3.3.2. 2nd calibration using experimental data from the knock region in the engine performance map: SITurb-2

As stated earlier, SITurb is designed to predict combustion development and calculate combustion parameters for a homogeneous charge. On the engine bench, and more specifically between 1200 rpm and 2000 rpm, the engine control unit requests a triple injection for the operating points whose admission pressure exceed 1100 mbar. This strategy was modified to a single injection in that region and the performance tests were repeated under that homogeneous conditions. They represent in total 68 operating points. Coolant temperature was regulated at 85°C and oil temperature at 90°C. The objective of performing these tests in this region is to use them later on for the combustion model calibration.

15 out of 68 operating points were picked from the low speed high load region of the maps as it can be seen in figure 2-41. They are highlighted in blue.

rad Indr	1050	1200	1350	1550	1750	2000	2500	3000	3500	4000	4500	5000	5500	5800
0,5														
1			█			█			█				█	
2														
3				█				█			█			
4									█					
5		█												
6														█
7	█											█		
8							█			█				
9				█										
10														
11										█				
12				█	█	█	█						█	
13											█			
14					█									
15			█				█							
16				█	█	█	█			█		█		
17				█										
18					█									
19			█		█		█							
20				█	█	█		█		█				
21					█									
22						█								
23					█	█	█							
24								█						
25														

Figure 2-41: points used for the optimization process of SITurb-2

In order to better visualize the engine region which is the most prone to knock, a zoom is made and it represents 68 operating points in total, from which 15 operating points were picked for the calibration as it is seen in figure 2-42.

Points highlighted in white are operating points that were performed on the bench but were not used for calibration. They were however used with the calibration points to validate the results. Points highlighted in grey (load index 16 and beyond) are operating points that could not be performed due to the engine configuration limitations.

Load Index	1050	1200	1350	1550	1750	2000	2500
0.5							
1							
2							
3							
4							
5							
6							
7							
8							
9							
10							
11							
12							
13							
14							
15							
16							
17							
18							
19							
20							
21							
22							
23							
24							
25							

Figure 2-42: zoom on the points used for the optimization process of SITurb-2

The obtained calibrated parameters of SITurb-2 are presented in table 2-15 and compared to those of SITurb-1

	SITurb-1	SITurb-2
FKGm	6.9677477	6.489617
DEm	1.2420095	1.1927402
TFSm	3.2782295	3.9478
TLSm	2.5839753	2.8323846

Table 2-15: values of the calibrated parameters of the SITurb-1 and SITurb-2 models

As it can be observed, the calibration procedure impacted the optimized values of the SITurb parameters.

First, a comparison of experimental versus predicted by SITurb in-cylinder pressures and burn rates are plotted on the same graph for some of 68 operating points in figure 2-43 to 2-45. At 1550 rpm:

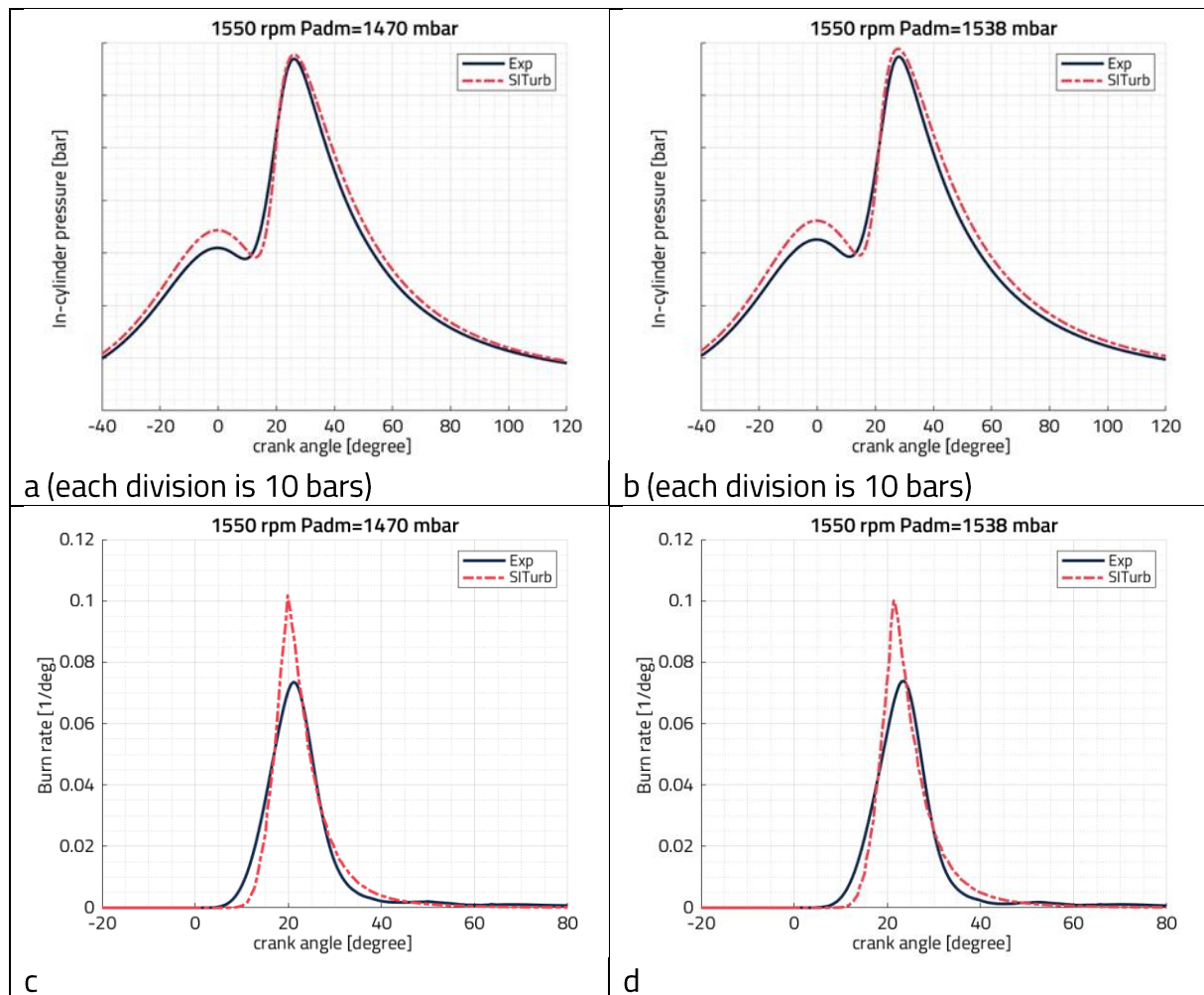


Figure 2-43: experimental vs SiTurb prediction of in-cylinder pressures (a&b) and burn rates (c&d) for 2 operating points at 1550 rpm

The SiTurb capacity to predict the in-cylinder pressure and burn rates are satisfactory for 1550 rpm. No discrepancies are observed in the early stage of the combustion development and even after the maximum pressure peak and till the end of the combustion phase. Such prediction is so important for the upcoming modeling of the knock in chapter 4. It should be noted that the trapped charge is overestimated using the model as it can be seen that the pressure at the end of the compression stroke is higher for the model than the experiments. This is due to complete engine model configuration which is designed to target the intake pressure values along with the heat transfer model. Such discrepancies are not linked to the SiTurb combustion model. However, the calibrated SiTurb model compensate this overestimation by an ignition delay. The ignition delay can be observed on the burn rate curves and it is around 5 CAD.

In-cylinder pressures and burn rates comparison are also presented for two more engine speeds 2000 rpm and 2500 rpm.

At 2000 rpm:

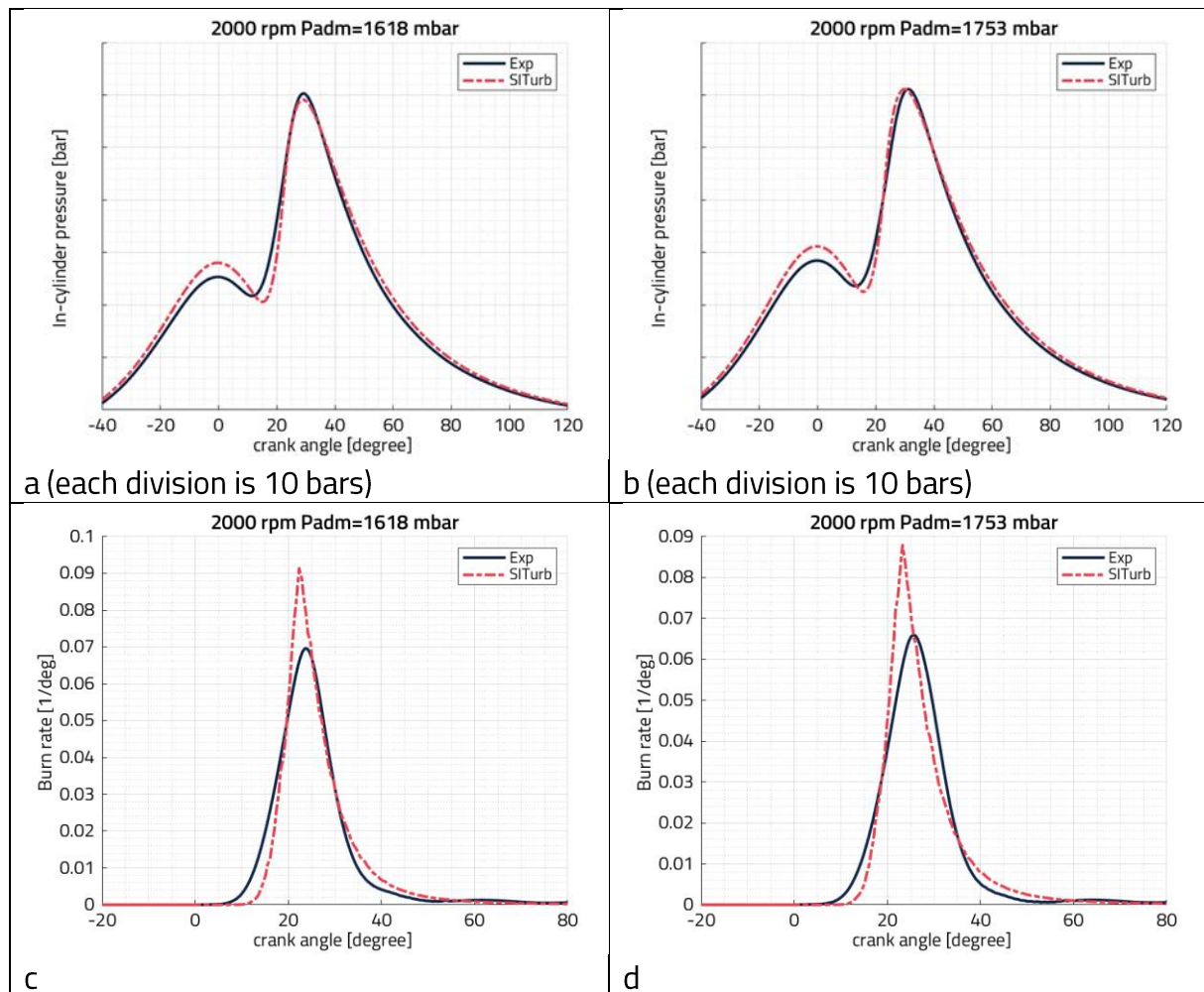


Figure 2-44: experimental vs SI-Turb prediction of in-cylinder pressures (a&b) and burn rates (c&d) for 2 operating points at 2000 rpm

Satisfactory results are also obtained for the two operating at 2000 rpm when experimental and predicted in-cylinder pressures and burn rates are compared. However, and as it was also seen on the operating points at 1550 rpm, the engine model overestimates a little bit the end of compression pressure. This overestimation was compensated by SI-Turb model by a little bit of ignition delay when compared to the experimental results. Either way, this overestimation and compensation are not expected interfere later on the knock prediction capacity of the knock model.

At 2500 rpm:

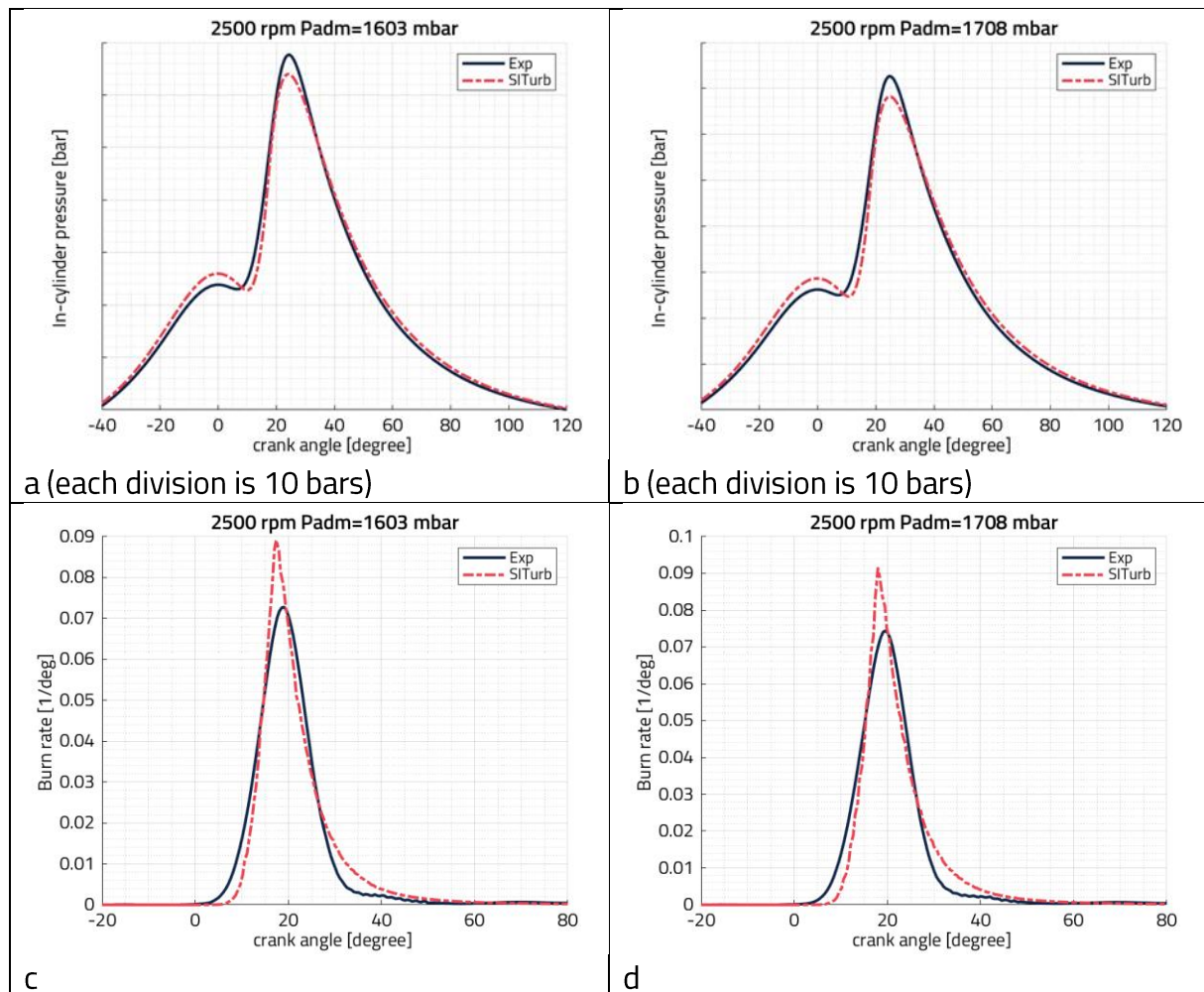


Figure 2-45: experimental vs SITurb prediction of in-cylinder pressures (a&b) and burn rates (c&d) for 2 operating points at 2500 rpm

The same behavior of the SITurb model is also obtained for these two operating points at 2500 rpm with one difference that peak pressure was a little bit underestimated by SITurb. This underestimation could impact a little bit the knock prediction later on in chapter 4 as the knock occurrence is influenced by the pressure of the end-gas and the knock apparition might be predicted delayed as pressure decreases. Even so, knock is more probable to appear at engine speeds of 1550 rpm and 2000 rpm than 2500 rpm.

In fact, the choice of these 6 operating points, two at each engine speed, was made on purpose. These 6 operating points from the engine performance maps surround the 3 operating points that were chosen to perform engine knock tests.

Moreover, some measured versus predicted combustion parameters are also plotted on the same graph to evaluate to capacity of the SITurb combustion model taking into account the validation points. They are presented in figures 2-46 to 2-50.



Confidential

Figure 2-46: measured vs predicted for SITurb-2 CA50 within [-3,3] CAD range

The CA50 is very well predicted by SITurb. 66 out of 68 operating points fall within the +/- 3 CAD range



Confidential

Figure 2-47: measured vs predicted for SITurb-2 CA1075 within [-3,3] CAD range

The CA1075 is also very well predicted by SITurb. 67 out of 68 operating points fall within the +/- 3 CAD range.



Figure 2-48: measured vs predicted for SITurb-2 maximum pressure within [-5,5] bar range

65 out of 68 operating points fall within the [-5,5] bar range. These points refer to the highest loaded points at 2500 rpm for which the in-cylinder pressure is underestimated by the mpde.



Figure 2-49: measured vs predicted for SITurb-2 crank angle at maximum pressure within [-3,3] CAD range

The crank angle at maximum pressure is very well predicted by the SITurb combustion models. Along with the previously mentioned parameters, the SITurb capacities are good

enough to ensure a good prediction of the combustion development which will later on impact the knock predictions. 67 out of 68 operating points fall within the +/- 3 CAD range.



Figure 2-50: measured vs predicted for SITurb-2 IMEP within [-5%,5%] range

The engine performance is very well predicted by the model. 67 out of 68 operating points fall within the [-5%,5%].

To conclude, SITurb offers a very good prediction for the combustion development, the in-cylinder pressure, the burn rates as well as the combustion parameters. Such capacity of the SITurb wouldn't have been possible without a complete engine model that is capable of calculating as accurate as possible the in-cylinder compositions. This is very important for the knock modeling as knock occurrence is highly influenced by the combustion progress as well as the in-cylinder composition. As it was stated, combustion modeling represent a preliminary task in this PhD thesis since the knock modeling is the main task on the numerical side. Knock modeling is presented in details in the chapter 4 "knock modeling and simulation".

2.4. Conclusion on the experimental setup and numerical tools

A turbocharged 3-cylinder stock engine was instrumented. The instrumentation includes in particular instantaneous pressure and temperature measurements over the entire air loop, instantaneous pressure measurements in the combustion chamber, wall temperatures at various locations in the combustion chamber.

An experimental campaign made it possible to characterize the impact of various engine control parameters on the development of the combustion, such as spark advance, air-to-fuel equivalence ratio, coolant and oil temperatures and for different control strategies (constant intake pressure versus constant trapped air mass, fixed spark advance versus fixed CA50).

The complete engine model has been briefly described: regarding the combustion, a bibliographic study was carried out on the main OD phenomenological models and led to the choice of the "SI Turb" model implemented in the GT POWER environment. A calibration procedure for it has been described, making it possible to find the main characteristics such as the CA50, the combustion duration, the maximum in-cylinder pressure, or the IMEP over the entire engine operating range. It was also deemed necessary, for the present study of knock in areas at low speeds and high loads, to carry out a specific calibration of the model.

Un moteur de série 3-cylindres suralimenté a été instrumenté. L'instrumentation comprend notamment des mesures de pression instantanée et de températures sur l'ensemble de la chaîne d'air, des mesures de pressions instantanées dans la chambre de combustion, des températures de parois à différents endroits de la chambre de combustion.

Une campagne expérimentale a permis de caractériser l'impact de différents paramètres de contrôle moteur sur le déroulement de la combustion, tels que l'avance à l'allumage, la richesse, les températures de liquide de refroidissement et d'huile, ceci pour différentes stratégies de contrôle (iso pression d'admission versus iso masse d'air enfermée, iso avance à allumage versus iso CA50).

Le modèle complet du moteur a été décrit sommairement ; s'agissant de la combustion, une étude bibliographique a été menée sur les principaux modèles phénoménologiques OD et a conduit à retenir le modèle « SI Turb » implémenté dans l'environnement GT POWER. Une procédure de calibration de celui-ci a été décrite, permettant de retrouver les principales caractéristiques telles que le CA50, la durée de combustion, la pression maximale dans le cylindre, ou la PMI sur l'ensemble du champ de fonctionnement moteur. Il a été en outre jugé nécessaire, pour la présente étude du cliquetis dans les zones à faibles régimes et fortes charges, de réaliser une calibration spécifique du modèle.

3. Experimental Results

This third chapter deals with the experimental analysis of the knock:

First, a general presentation of the tests is given.

In a second part, after reviewing the literature, a knock indicator is selected and tested, particularly in terms of repeatability.

In a third part, studies of the influence on the occurrence of knock are carried out for various engine control parameters, such as the valves timing (intake and exhaust), the profile of fuel injection in the combustion chamber (number of injections, quantities injected, and phasing of each injection), the intake temperature, and the temperatures of the coolant and the lubricating oil.

Ce troisième chapitre porte sur l'analyse expérimentale de l'apparition du cliquetis.

Dans un premier temps, une présentation générale des essais est effectuée.

Dans une seconde partie, après passage en revue de la littérature, un indicateur de cliquetis est retenu et testé, notamment en termes de répétabilité.

Dans une troisième partie, des études d'influence sur l'apparition du cliquetis sont menées pour différents paramètres de contrôle moteur, tels que le calage de la distribution (admission et échappement), le profil d'injection de carburant dans la chambre de combustion (nombre d'injections, quantités injectées, et phasages de chaque injection), la température d'admission, et les températures de liquide de refroidissement et de l'huile de lubrification.

3.1. Presentation of the knock tests

Knock tests represent the hub of this PhD Thesis. They were performed to study the impact of the knock limit on engine performance and to characterize the influence of engine control parameters on knock apparition. The tests that were performed are the following:

1. Impact of knock on engine behavior and performance under 2 valves settings: valves overlapping and valves not overlapping since varying the valves timings impacted the residuals trapped. As it was seen in chapter 2, such variations impacted the combustion development which might subsequently impact the knock apparition
2. Impact of intake air temperature on knock apparition: knock occurrence is related to the end-gas auto-ignition conditions including its temperature. Since variations in end-gas temperatures influence the knock apparition, the intake-air temperature will be varied and its impact on end-gas temperature and knock apparition will be assessed.
3. Impact of injection strategies on knock apparition. Injections strategies influence the homogeneity of the charge and since cool gasoline is evaporated, it also influence the thermodynamic state of the mixture which consequently can impact the knock apparition.
4. Impact of coolant and lubrication oil temperatures on knock apparition: as it was seen in the previous chapter, coolant and oil temperature impact the combustion development which might in turn influence the knock occurrence.

The first set of tests will be later used to improve the knock prediction capacities of a complete engine model. The other sets of tests will be used to study the capacity of the model to predict the modification of control parameters.

Each of the previously mentioned tests are performed on 3 operating points representing 3 engines speeds:

1. 1550 rpm and an intake pressure of 1500 mbar. This operating point is referred to by 1550x1500mbar
2. 2000 rpm and an intake pressure of 1700 mbar. This operating point is referred to by 2000x1700mbar
3. 2500 rpm and an intake pressure of 1700 mbar. This operating point is referred to by 2500x1700mbar

These operating points were picked in the low engine speed area and the highly loaded which is the area the most prone to knock.

In order to better understand the knock apparition under different control parameters, a knock indicator must be defined. This indicator should be capable to compare different

strategies in order to conclude on the engine behavior, combustion development and knock occurrence under modified parameters.

3.2. Knock indicator

3.2.1. Definition of a knock indicator

In order to compare the different engine settings and their impact on knock occurrence, it is important to define a knock indicator. The knock index that will be implemented in this PhD thesis is elaborated in this section.

Several methods were proposed in the literature to quantify the knock. They are mainly based on the in-cylinder pressure signal.

The maximum amplitude of pressure oscillation (*MAPO*): is one of the most widely used methods of knock quantification [97] [98] [99] [100] [101]

$$MAPO = \max(|\tilde{p}|_{\theta_0}^{\theta_0+w})$$

\tilde{p} as the bandpass filtered pressure signal, θ_0 as the crank angle at the beginning of the knock interval and w is the duration of the knock window.

The integral of the modulus of the pressure oscillation (*IMPO*): it was introduced by Arrigoni [102] and defined as:

$$IMPO = \frac{1}{T_c} \int_0^{T_a} |p_{hp}| dt$$

T_c : period for 1 engine cycle

T_a : time corresponding to 70° ca after the peak pressure

p_{hp} : the high pass filtered cylinder pressure measured by a flush-mounted transducer

Arrigoni used a high pass filter of 5 kHz. He also averaged the *IMPO* value of 2 seconds to take into account the cycle by cycle variations. However other authors included all of the considered cycles as in the work of Brecq[103]

$$IMPO = \frac{1}{N} \sum_1^N \int_{ST}^{ST+w} |\tilde{p}| d\theta$$

$$MAPO = \frac{1}{N} \sum_1^N \max(|\tilde{p}|_{ST}^{ST+w})$$

Where N represents the number of computed cycles, ST the spark timing in crank angle degrees, \tilde{p} the filtered pressure and w the with of the computational window

He also used a bandpass filter for the in-cylinder pressure signal (4-20 kHz) and calculated the *IMPO* from the spark timing up to 60° CA after the spark.

Brecq used the *IMPO* and *MAPO* to define his dimensionless indicator *DKI* [103]:

$$DKI = \frac{IMPO}{MAPO \times w}$$

While *IMPO* is the surface under the filtered pressure signal and *MAPO* × *w* is the surface of the computational window as illustrated in the figure 3-1 which represents the multiplication of the *MAPO* value by the window length, the *DKI* represents the “weight” of *IMPO* within the computational window.

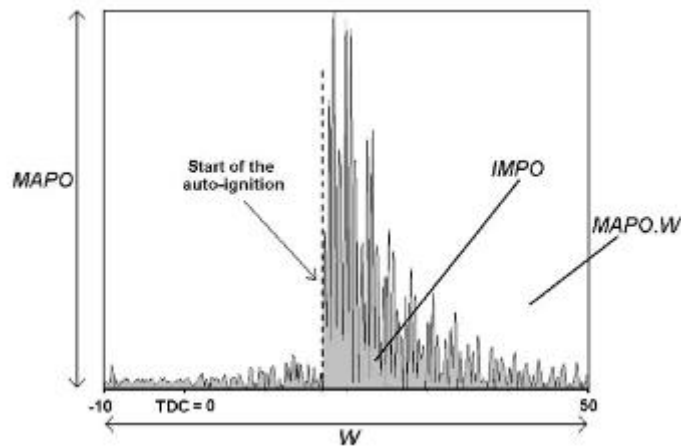


Figure 3-1: representation of *DKI* indicator of Brecq, the illustration is limited to the *MAPO* value in the y-axis and to window length in the x-axis [103]

Logarithmic knock index:

It uses the average energy of the filtered pressure signal to describe knock intensity. This is appropriate given that the pressure oscillations are made up of several frequencies [104]. The average energy of a signal in the time domain is given by:

$$Average\ Energy = \frac{1}{N} \sum_{n=1}^N \tilde{p}^2(n)$$

The advantage of using the average energy method is its equivalence in the frequency domain and in the time domain [105]. The complexity of the Fourier analysis in the frequency domain and the risk of spectral spreading makes it easier to evaluate the LKI value in the time domain as an ‘average energy’ calculation of the filtered pressure data. The LKI is calculated as the following : *C* is a constant.

$$KI = \ln(C \times Average\ Energy)$$

$$LKI = \ln\left(C \frac{\sum_{n=1}^N \tilde{p}^2(n)}{N}\right)$$

All of the mentioned indicators are interesting and they are useful to define a knock intensity of any operating point under any setting. However, this knock intensity cannot be compared unless the spark advance is constant for the different settings for every operating point. It is then necessary to plot the evolution of the knock indicator with several spark advances for every engine setting in order to compare them. In order to select a knock index for the study, the previously mentioned indicators were adapted to the results obtained on the bench and tested as the following.

For each engine setting, 3 tests are at least performed. The first one is with the value of the stock calibration of the engine and it corresponds to 0 CAD of spark advance increase. The second value is an intermediate spark advance increase and the third value is the maximum spark advance increase. In the figures of knock index versus spark advance increase, the x-axis represents the spark advance increases and it corresponds to the additional spark advance that was added to the calibrated spark advance value in order to induce knock. The calibrated spark advance is fixed for every operating point and for all the tests performed on that operating point (impact of knock on engine performance, impact of intake temperature, impact of injections strategies and impact of coolant and oil temperature). The calibrated spark advance for each operating point is presented in table 3-1.

Operating point	1550 rpm x 1500 mbar	2000 rpm x 1700 mbar	2500 rpm x 1700 mbar
Calibrated spark advance [CAD ATDC]	-6.75	-6.75	-3
Spark timing [CAD ATDC]	6.75	6.75	3

Table 3-1: list of the operating points used and their corresponding calibrated spark advance

The in-cylinder pressure traces are recorded for 250 cycles, and for each cycle, a value is saved every 0.36 CAD. In order to calculate the knock index, the following procedure is performed for each cycle.

1. The in-cylinder pressure is filtered between 3 kHz and 10 kHz.
2. The filtered signal is windowed for 72 CAD starting from the spark timing
3. The maximum value of the windowed signal within each cycle is retained as $MAPO_{cycle}$. This value corresponds to the maximum amplitude of pressure oscillation as it was described.

If this value $MAPO_{cycle}$ exceeds a threshold, it will be considered in the calculation of the knock index. If this value does not exceed the threshold, a value of 0 will be affected to $MAPO_{cycle}$. The evaluation of the threshold will be presented later on in this section.

The knock index is then calculated based on the following formula:

$$KI_{MAPO} = \frac{\sum_1^N MAPO_{cycle}}{N_{cycles}}$$

Where $N_{cycles} = 250$, the total number of cycles considered.

The threshold value was chosen as the lowest value that maintain the KI_{MAPO} value at 0 for the calibrated spark advance. The objective of fixing a threshold is to eliminate all sources of noise in the signal that are not related to knock. First a value of 0.1 was chosen for the threshold and a step of 0.1 is applied until the $KI_{MAPO}=0$ for every operating point.

From a threshold of 0.6 bar and above and for all the operating points, the knock index value at 0 spark advance increase is 0 as it can be seen in the figure 3-2 for 1550x1500 mbar.

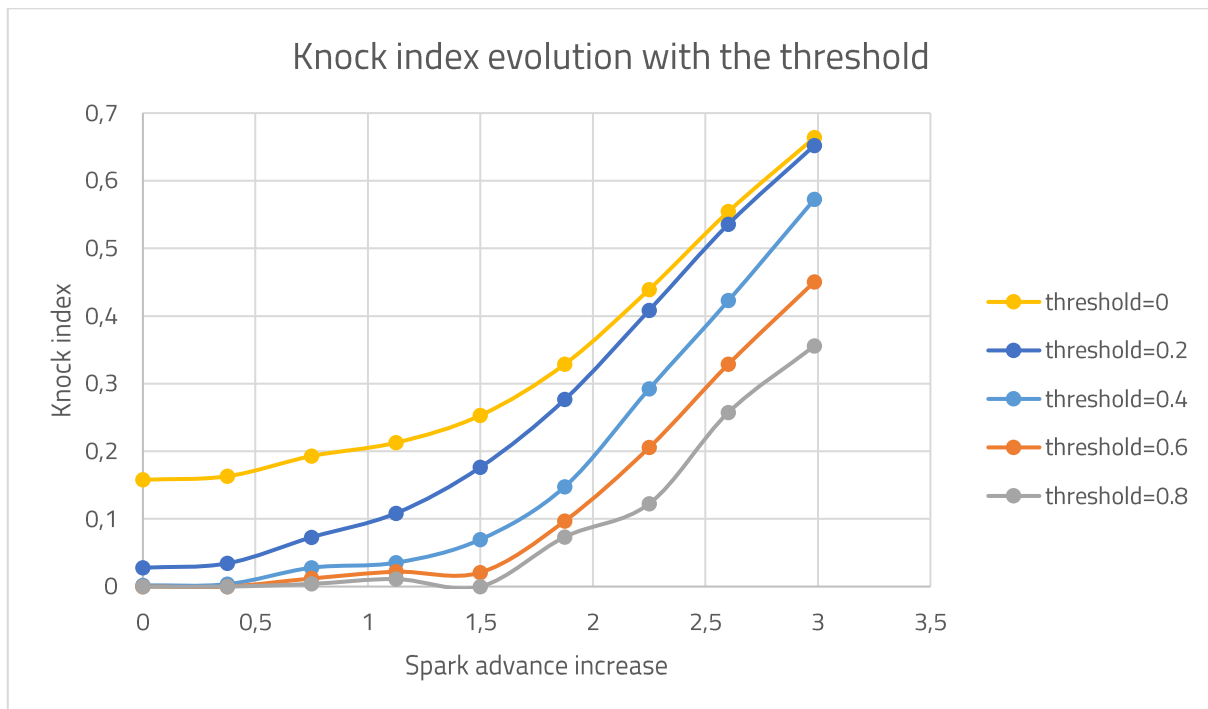


Figure 3-2: knock index evolution with the threshold at 1550x1500mbar

In the following parts of this PhD thesis, the use of the terms knock index or simply “KI” refers to the KI_{MAPO} .

3.2.2. Repeatability Tests

Some repeatability tests were performed in order to compute the uncertainties of the defined knock index as it can be seen in figure 3-3. The tests were performed at 1550 rpm and intake pressure of 1500 mbar and intake temperature of 30°C. The first and the last tests are separated by a 10-day period.

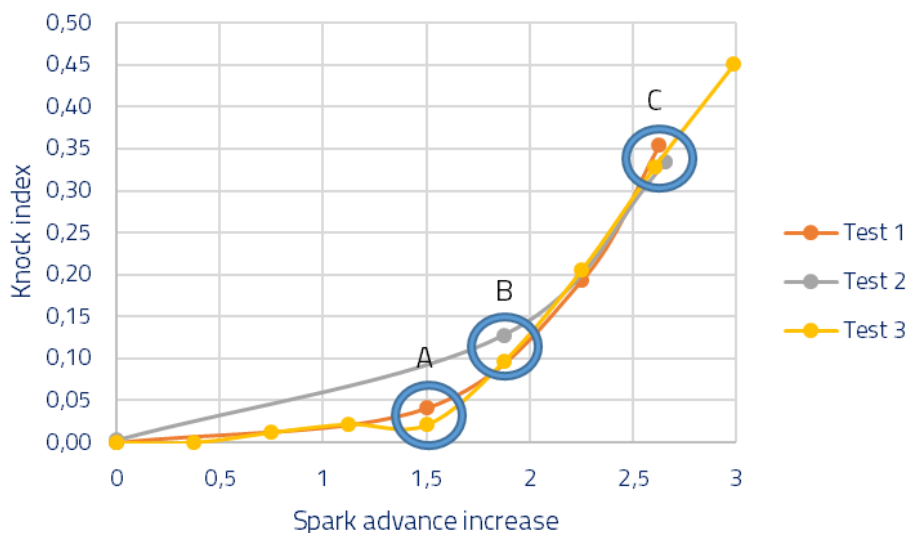


Figure 3-3: repeatability tests required to compute the accuracy of the knock index

At location "A", the differences on the knock index between test 1 and test 3 are about 0.02

At location "B", the differences on the knock index between test 2 and test 1&3 are about 0.03

At location "C", the differences on the knock index between the tests are about 0.02.

The observed differences on the knock index are small and the related uncertainty is ± 0.015 . In fact, this uncertainty in the measurement was reduced after the implementation of the threshold, which removes all the noise that is not related to knocking events in the filtered pressure signal. However, this small uncertainty could be due to the data acquisition: on the engine bench, 250 cycles are recorded but they are not necessarily consecutive cycles, the acquisition system might skip some intermediate cycles but at the end of the measurement, it will store 250 cycles. Some of the skipped cycles could be some significant knocking cycles and their omission could impact a little bit the resulting knocking index of the operating point. To be clear let's consider a series of 12 consecutive cycles and their corresponding MAPO values in the table 3-2.

Cycle	1	2	3	4	5	6	7	8	9	10	11	12
MAPO	0.5	0.4	0.6	0.65	0.5	0.7	0.45	0.35	0.4	0.4	0.65	0.6

Table 3-2: simulation of 12 consecutive cycles and their corresponding MAPO values

If the acquisition system stores cycles 1, 2, 5, 8 and 12, the average MAPO value is 0.47

If the acquisition system stores cycles 1, 4, 6, 9 and 10 the average MAPO value is 0.53

If the acquisition system stores cycles 2, 5, 7, 11 and 12 the average MAPO value is 0.52

As it can be seen in the previous simulations, the averaged MAPO values can vary a little bit depending on the stored cycles.

Nevertheless, on the first part of the test 2 curve (grey), a significant difference is observed between the test 2 and both test 1 & 3. In fact, on this part, no operating points with the corresponding spark advance increase were stored and the curve simply joins the points at 0 CAD and 1.875 CAD of spark advance increase. This is not restrictive for the rest of the study and the comparison of the different strategies in this chapter since the operating points are performed with a smaller step in spark advance increase.

3.2.3. Cylinder choice

Testing knock on a stock internal combustion engine gives the opportunity to study the impact of the knock on each of the cylinders. This was done on the operating point at 2000 rpm, intake pressure of 1700 mbar and intake temperature at 35°C.

First let's start with a global visualization of some in-cylinder pressures for 5 cycles of the 3 cylinders in figure 3-4. The plot for cylinder 2 was presented twice in figure 3-4b and 3-4c in order to be used for comparison for cylinders 1 and 3.

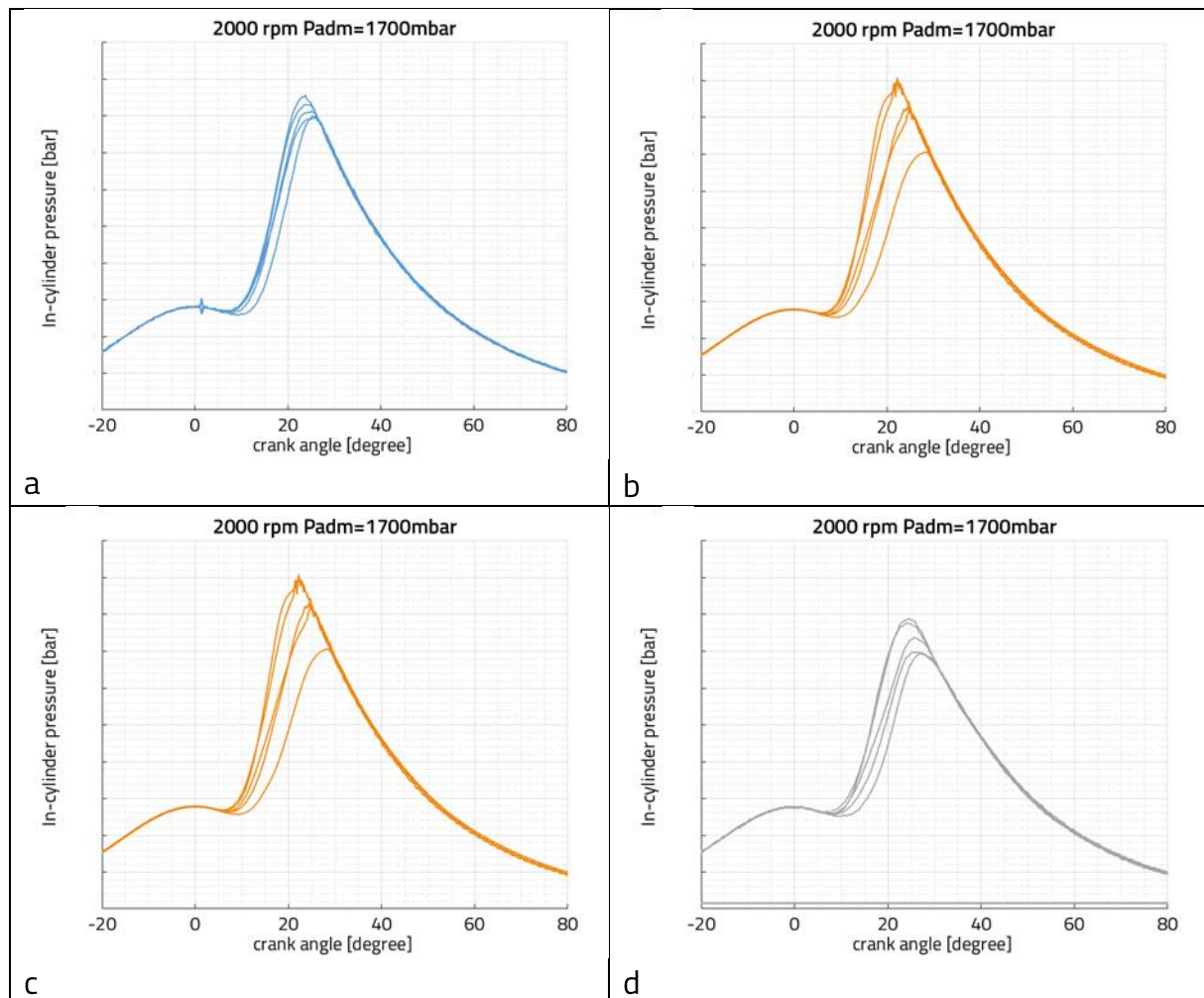


Figure 3-4: in-cylinder pressure traces (each division is 10 bars) for some cycles for the cylinder 1 (a), cylinder 2 (b&c) and cylinder 3 (d) at 2000x1700 mbar with 4 CAD of spark advance increase

It seems that the cylinder 2 shows a higher knocking tendency when compared to both cylinders 1 & 3 if we consider the pressure oscillations on the cycles plotted for the 3 cylinders in figure 3-4. However, it is much more interesting to plot the same in-cylinder pressures for the same cycles for the 3 cylinders as in figure 3-5

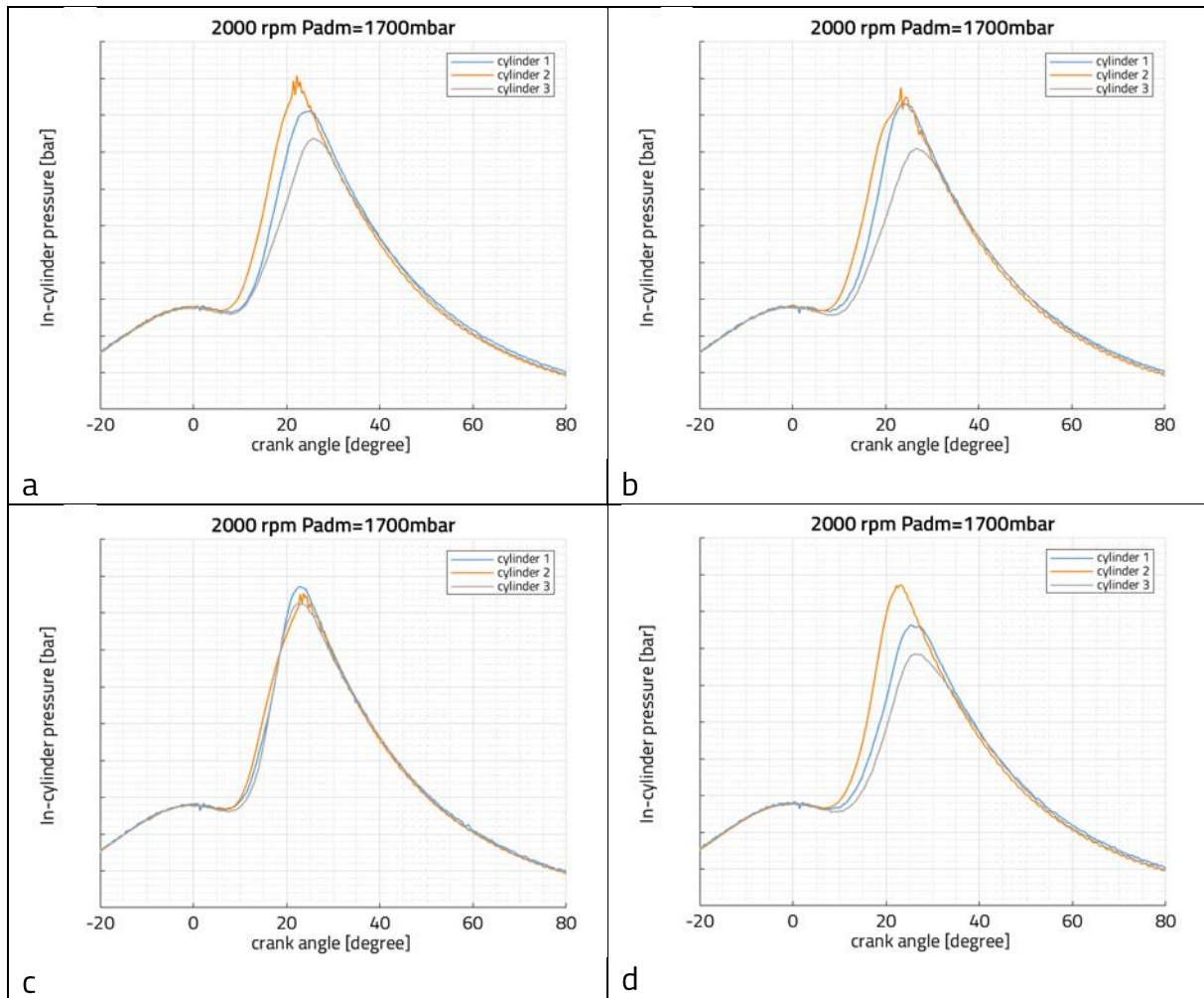


Figure 3-5: in-cylinder pressure traces (each division is 10 bars) for 4 cycles (a, b, c & d) for the cylinder 1, cylinder 2 and cylinder 3 at 2000x1700 mbar with 4 CAD of spark advance increase

In figure 3-5, the in-cylinder pressure was plotted for the 3 cylinders for the same cycle on the same graph and it can be observed that the cylinder 2 seems to have a higher tendency to knock if we consider the pressure oscillations. These plots remain some observations and it is necessary to consider all the cycle for all the cylinders to rule whether or not 1 of the 3 cylinders is more prone to knock. To do so, the knock index is plotted for the three cylinders. As it was seen earlier, the knock index takes into account all the cycles.

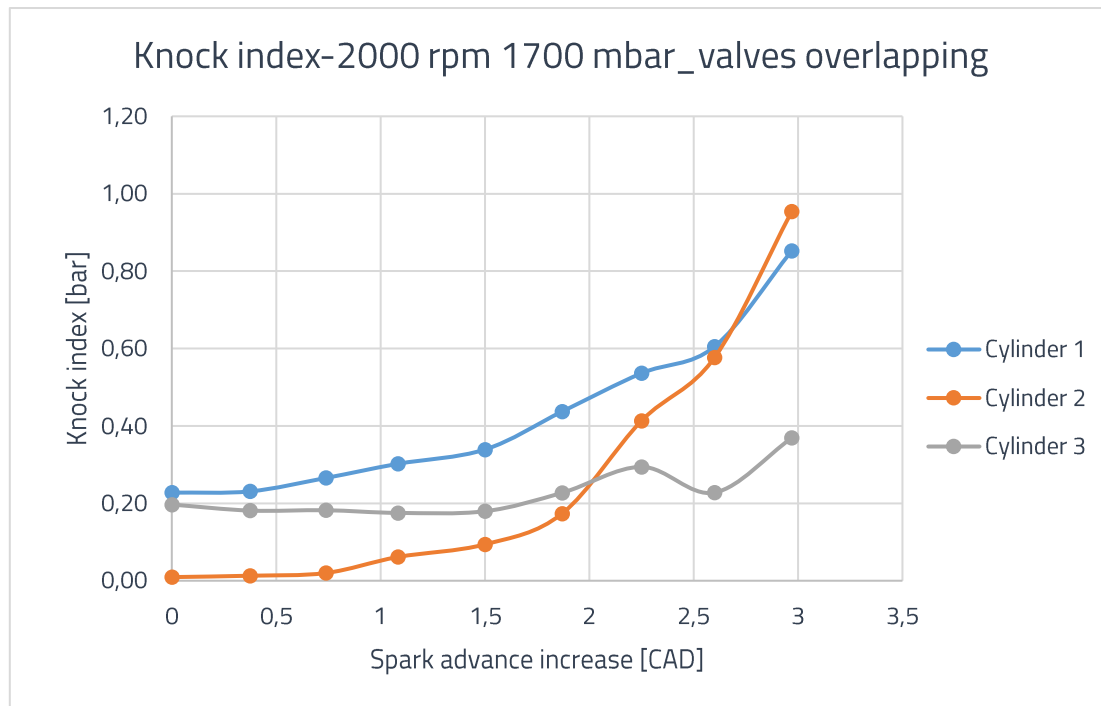


Figure 3-6: knock index versus spark advance increase for the three cylinders at 2000x1700 mbar

As it can be seen in the figure above, the cylinder 2 shows a higher knock index when the spark advance increase is at the maximum. However, at 0 spark advance increase, both cylinders 1 and 3 have KI equal to almost 0.2 and the cylinder 2 has a KI=0. The cylinder 2 is then selected as the most critical to knock between the three cylinders and that for the following reasons:

- The KI for the cylinder 3 does not evolve a lot with the spark advance increase. The cylinder 3 seems to be the less prone to knock in this engine. The KI starts to show a significant evolution after about 2.5 CAD of spark advance increase. At that value of spark advance increase, both KI of cylinders 1 and 2 are much higher. So the cylinder 3 is eliminated from the study. The same was observed on different operating points.
- A lot of noise was observed in the in-cylinder pressure trace for the cylinder 1. This noise is mainly due to the equipment setting. This noise is capable to show a false tendency of the engine to knock given that the knock index calculation is based on the filtered signal of this in-cylinder pressure. This noise is capable of causing a knock index of 0.2 at 0 spark advance increase.
- The KI values for the cylinder 2 show a clear tendency to increase starting from 0 as the spark advance is increased and it reached the highest value at the highest spark advance.

The cylinder 2 is thus a reliable cylinder to study the impact of knock limit on the engine behavior, and in a second stage to study the impact of engine control parameters such

intake air temperature, injection strategies and oil and water temperatures on knock apparition. In the following sections and chapters of this PhD thesis, the study will only be focused on the second cylinder as it is the first cylinder to knock and it should be used to help calibrate and dimension internal combustion engines.

The choice of the cylinder 2 as the most prone to knock can be understood if we look at the cylinder liners temperature for the three cylinders in figure 3-7

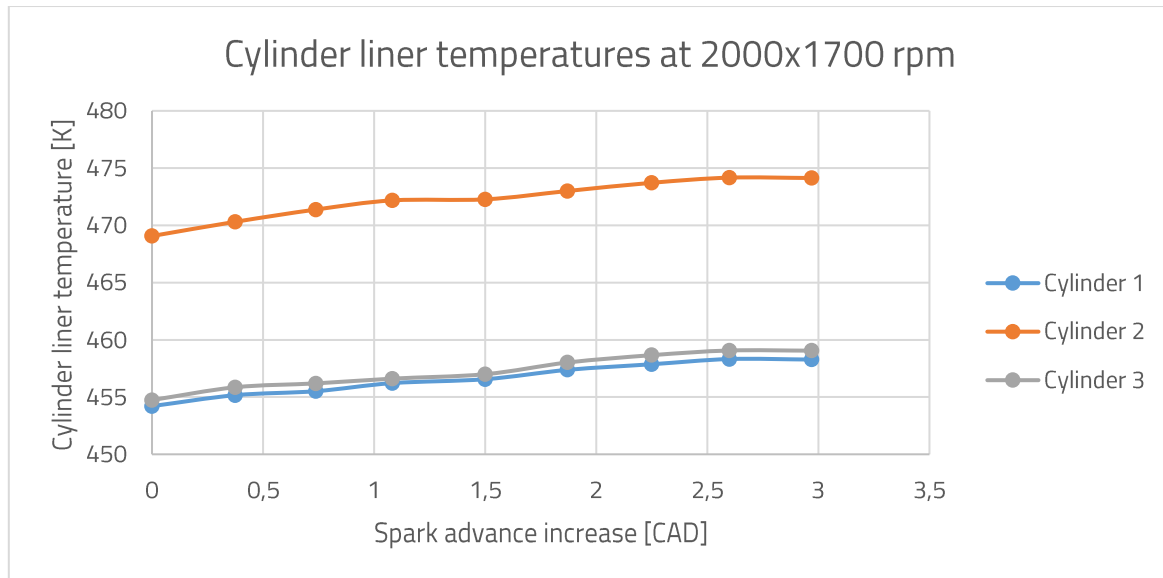


Figure 3-7: cylinder liner average temperatures for the three cylinders

This an averaged cylinder liner temperature over the whole surface as it can be seen in figure 3-8. The cylinder liner temperatures were calculated by GT Power using the finite element (FE)

$$T = \frac{\sum_{node=1}^n \frac{1}{\Delta t_{cycle}} \oint h_g(t) \cdot x_{surf}(t) \cdot A \cdot T_g(t) dt}{\sum_{node=1}^n \frac{1}{\Delta t_{cycle}} \oint h_g(t) \cdot x_{surf}(t) \cdot A dt}$$

$h_g(t)$ is the instantaneous gas-to-structure convective heat transfer coefficient [W/m²-K]

$x_{surf}(t)$ is the instantaneous fraction of surface area exposed to gas

A surface area of FE mesh node; combined with $x_{surf}(t)$ above gives surface area exposed to gas

$T_g(t)$ is instantaneous gas temperature [K]

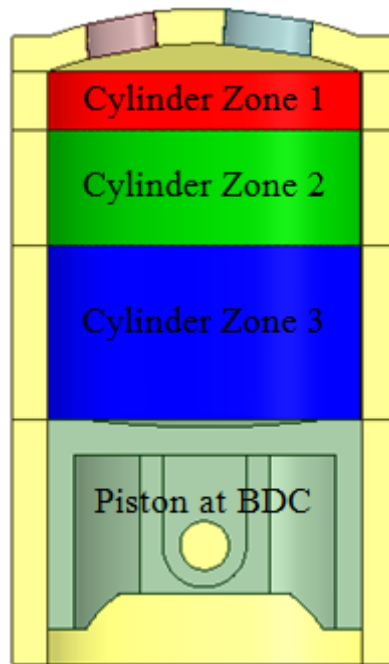


Figure 3-8: cylinder temperature zones

The calculation of the cylinder liner temperature are done on 3 separate zones (figure 3-8) and the values are averaged over the zones. It is clear that the cylinder liner temperature of the cylinder 2 is higher than that of the cylinder 1 and 3. The cylinder 2 has the less surface exposed to water coolant and less heat can thus be evacuated when compared to cylinder 1 and 3. The elevated surface temperature of cylinder 2 impact the end gas temperature and contributes to a shorter auto-ignition delay and thus a higher chance to knock.

It should be noted that the terms "knock apparition", "knock delay" and "knock advance" are directly related to knock index variation with spark advance increase.

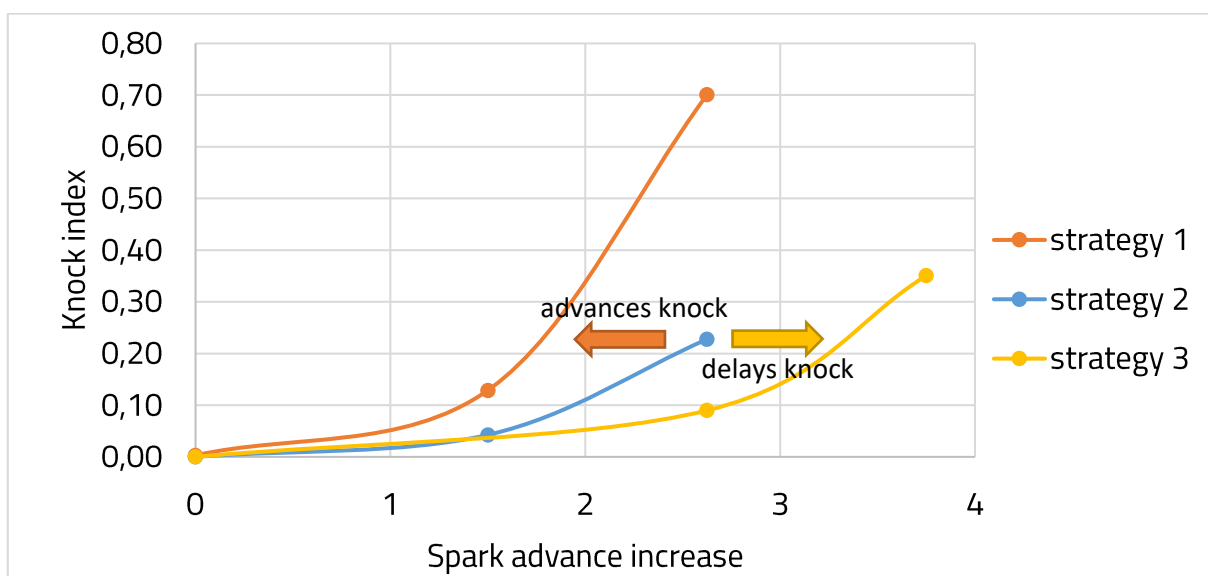


Figure 3-9: example of the knock index evolution with different strategies adopted

As seen in figure 3-9, if a certain strategy curve is on the right of another curve (for example strategy 3 on the right of strategy 2) , it means that former delays knock apparition since the spark advance should be further increased to reach a specific knock index of the latter. Subsequently, the latter advances the knock apparition when compared to the former. These terms are going to be used in all the sections of the present chapter.

3.3. Impact of Knock on engine behavior

3.3.1. Knock index evolution with valves timings sweeps

In this section, knock impact on the engine will be studied for the three operating points 1550x1500 mbar, 2000x1700 mbar and 2500x1700 mbar. The knock is induced by a simple increase of the spark advance. The specifications of the operating points are presented in the following table 3-3:

Engine Speed (rpm)	1550	2000	2500
Admission pressure (mbar)	1500	1700	1700
Admission temperature T2" (°C)	30	35	37
Coolant temperature (°C)	85	85	85
Oil temperature (°C)	90	90	90
Injection strategy	Single injection	Single injection	Single injection
SOI (CAD)	255	245	270
Calibrated spark advance (CAD)	-6.75	-6.75	-3
Valves timings	-overlapping -not overlapping	-overlapping -not overlapping	-overlapping -not overlapping

Table 3-3: Operating points specifications

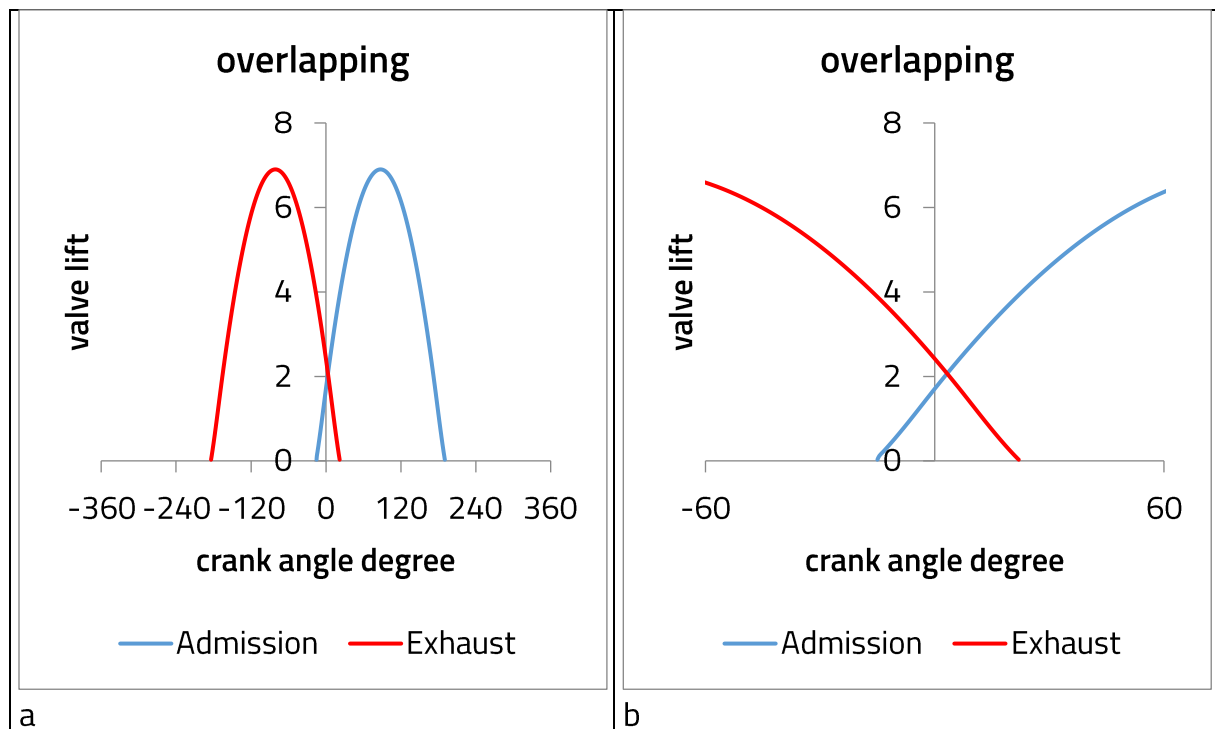


Figure 3-10: overlapping valves timing for 1550x1500 mbar (a) with a zoom on the overlap (b)

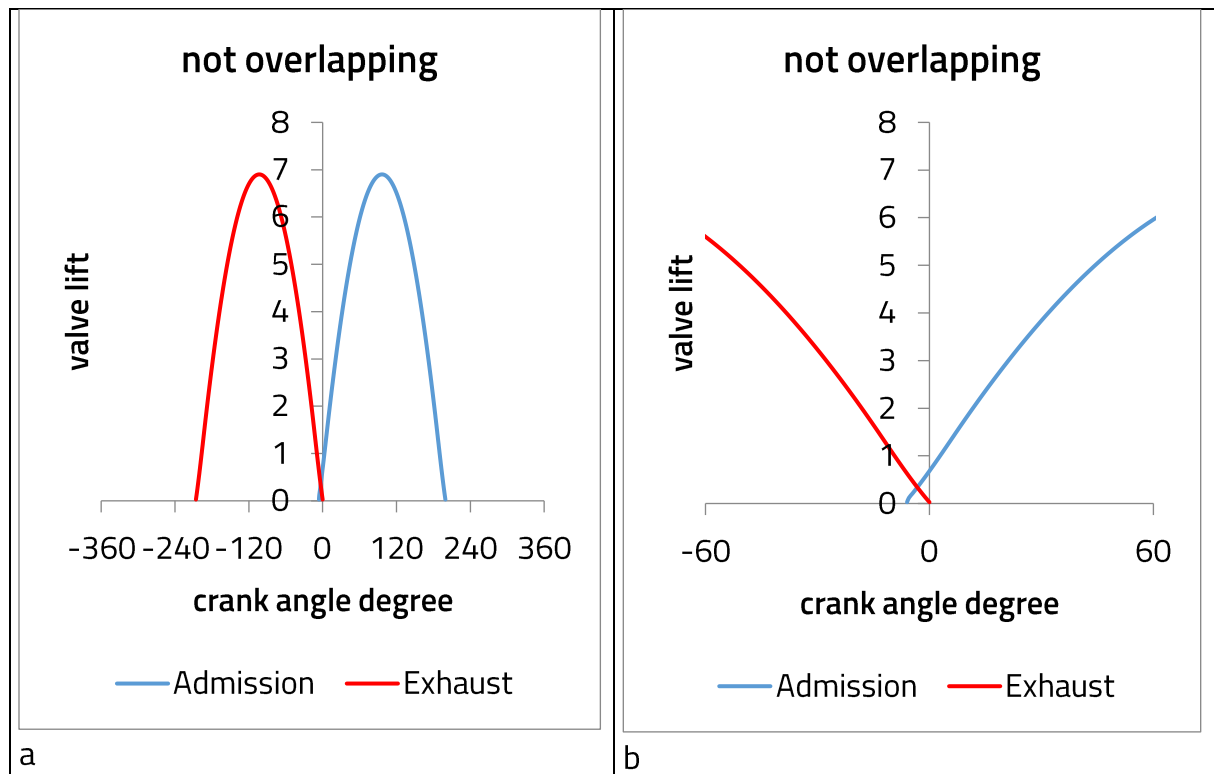


Figure 3-11: not overlapping valves timing for 1550x1500 mbar (a) with a zoom on the overlap (b)

For the three operating points, the coolant temperature was fixed at 85°C and the oil temperature at 90°C. The injection strategy was modified to a homogeneous injection for 1550 rpm and 2000 rpm. The reason behind that modification is to be able to use the experimental results of these tests to calibrate the knock model as the combustion model only works in homogeneous conditions. Valves timings were blocked at specific values. The Start Of Injection (SOI) is presented in terms of CAD advance with respect to the firing top dead center. As it can be 245, 255 and 270 CAD of SOI represent injections during the intake stroke which imply a homogeneous charge.

In this section, and as it was identified in chapter 2, valves timings are found to impact the combustion development, their values will be defined for 2 strategies as presented in figures 3-10 and 3-11

1. Overlapping strategy, which correspond to the baseline condition as defined by the internal control unit.
2. Not overlapping strategy where intake valves opening was delayed and exhaust valves closing was advanced to reduce as much as possible the valves overlap.

First, at 1550x1500 mbar, the knock index was plotted in function of spark advance increase as it can be seen in figure 3-12

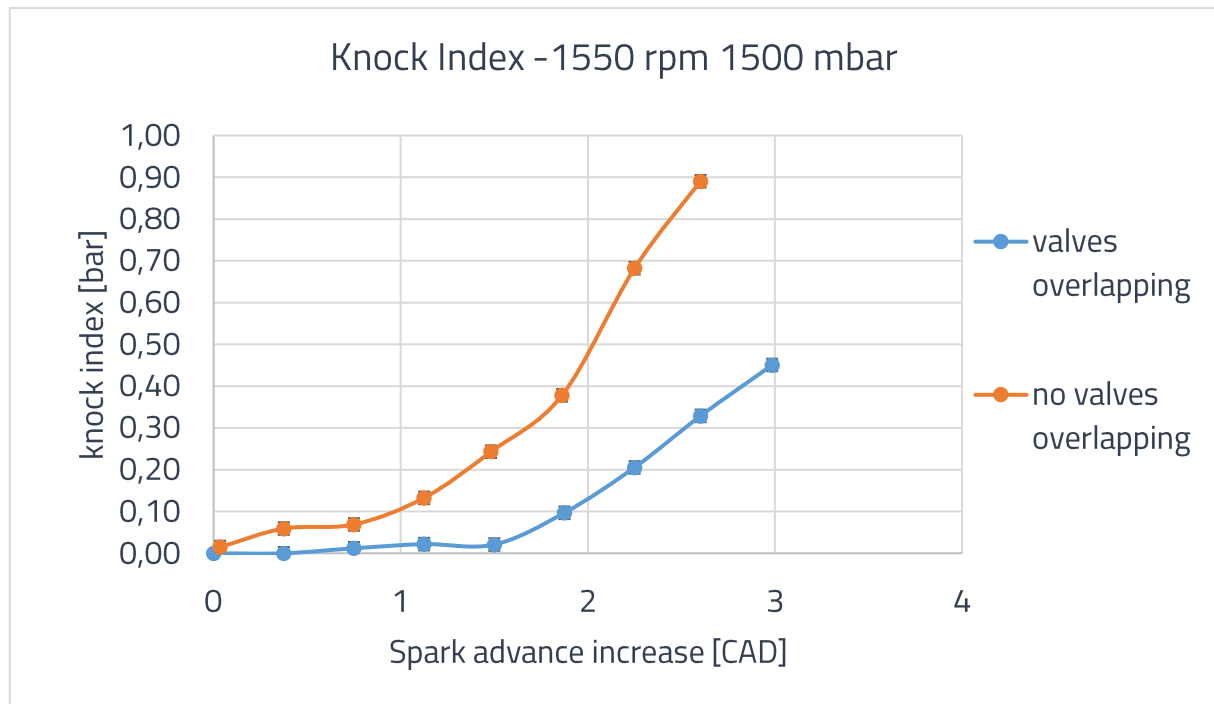


Figure 3-12: Knock index evolution with spark advance at 1550x1500 mbar

The curve of the knock index when the valves are overlapping is at the right of the curve when the valves are not overlapping. This indicates that when overlapping the valves, the knock is delayed: at a fixed knock index, the spark advance increase is higher for the case of overlapping valves. This means that the engine with valves overlapping can be operated at higher spark advance with a similar knock intensity of a non-overlapping valves case with a lower spark advance: the spark advance can be increased by almost 1 CAD for the overlapping case at KI=0.4 bar. In other terms, if we consider a fixed spark advance increase for both overlapping and not overlapping valves, for example 2CAD, the knock index for the overlapping valves is around 0.15 bar, while it is almost 0.5 bar for the non-overlapping valves case.

The reason behind this difference in the engine behavior under overlapping and not overlapping valves cases is the quantity of residuals confined within the cylinder at each cycle as it can be seen in the figure 3-13.

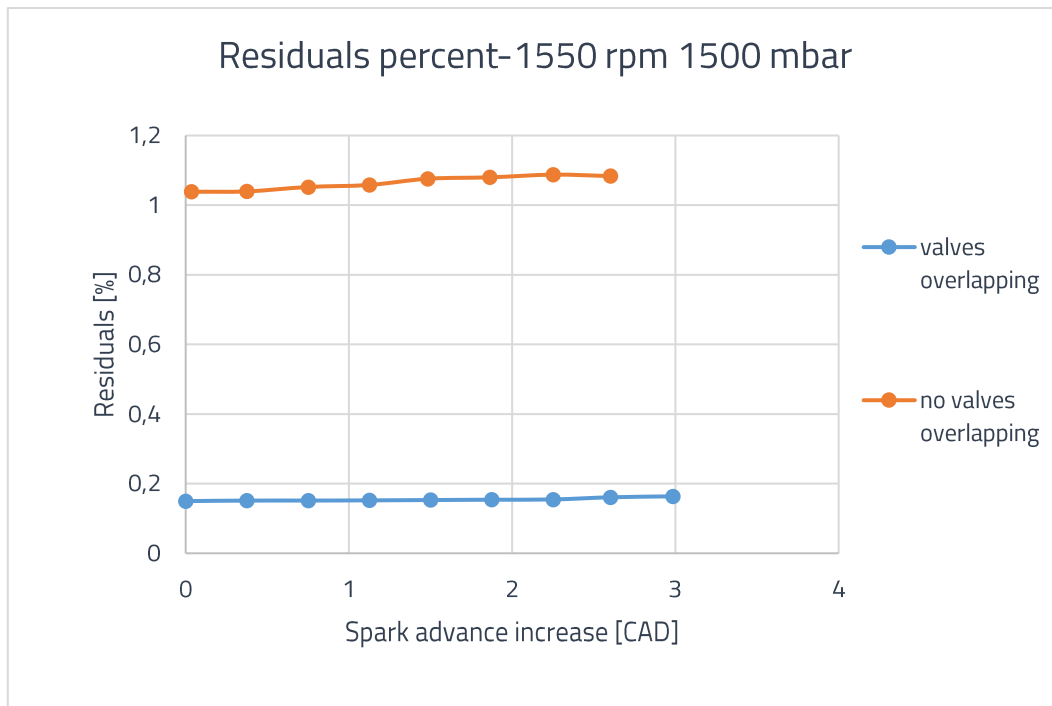


Figure 3-13: percentage of residuals confined inside the cylinder at 1550c1500 mbar

the residuals are calculated at the combustion start by the measured pressure analysis by GT Power. Valves overlap by around 37 CAD with intake valves opening before top dead center and exhaust valves closing after top dead center. This allows eliminating maximum quantity of hot residuals. Not overlapping valves was achieved by delaying intake valves opening and advancing exhaust valves closing. This increases the percentage of residuals confined inside the cylinder at each cycle. These hot residuals are mixed with the fresh air and fuel admitted in the following cycle and they contribute in increasing the end gas temperature as it can be seen in the figure 3-14.

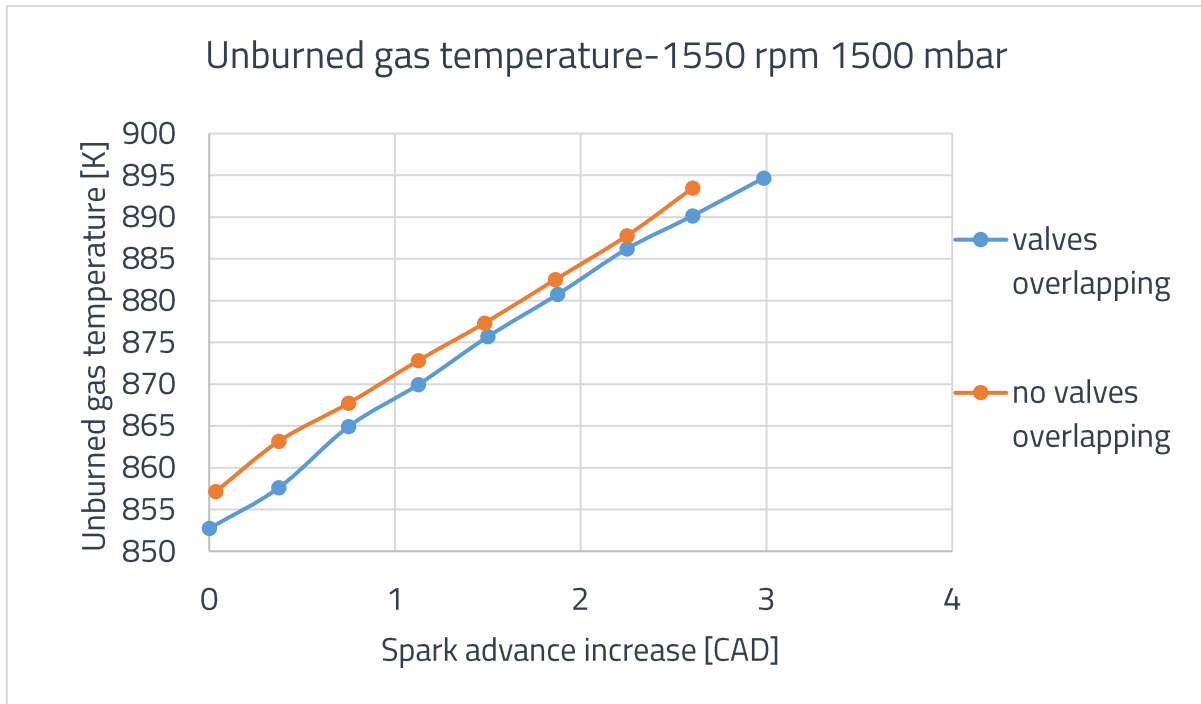


Figure 3-14: unburned gas temperature at 1550x1500 mbar

The end gas temperature of the unburned zone gas temperature increases as the quantity of residuals increases. It is also calculated by the model. The auto-ignition delay is thus shorter and the end gas mixture is more prone to knock in this case. On their behalf, Potteau et al. conducted experiments on a turbo-charged SI engine and tested cooled LP and HP EGR circuits. They observed that both LP and HP EGR reduced the in-cylinder temperature suppressing the knock and allowed the spark to be advanced. Both circuits also reduced the BSFC [42].

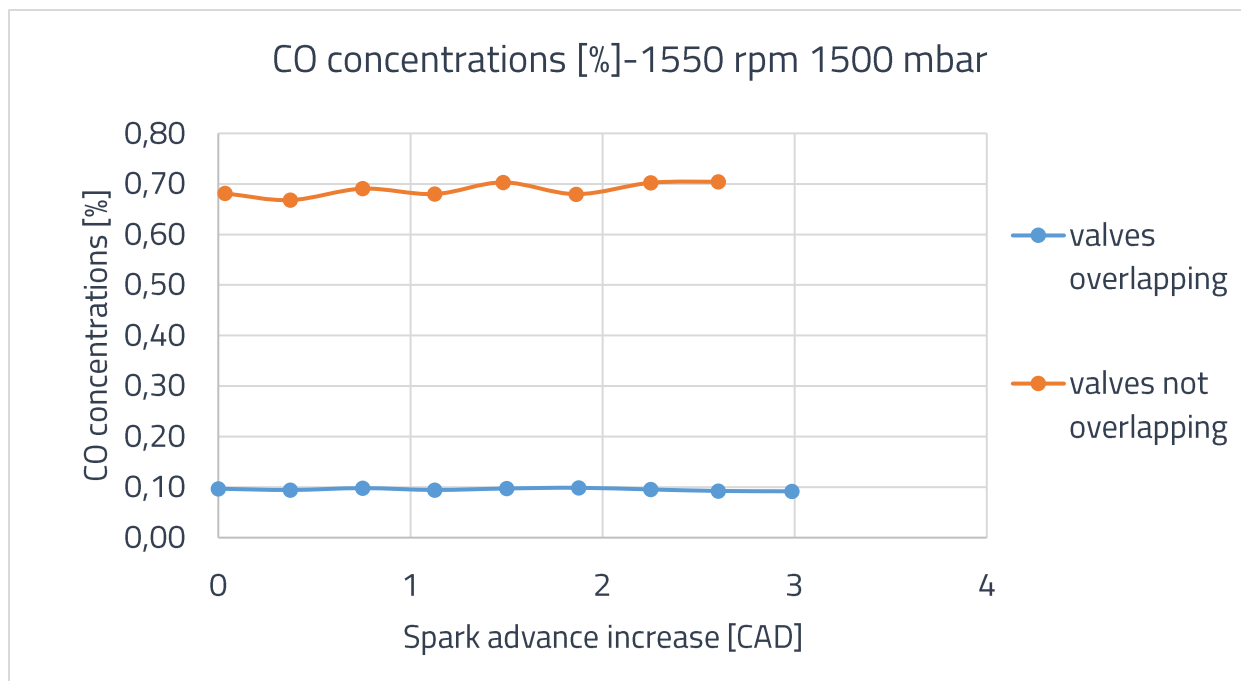


Figure 3-15: CO concentrations at 1550x1500 mbar

In figure 3-15, not overlapping valves degrades the combustion, deteriorates its efficiency and leads to increased CO concentrations in the exhaust. The CO concentrations are measured at the exhaust.

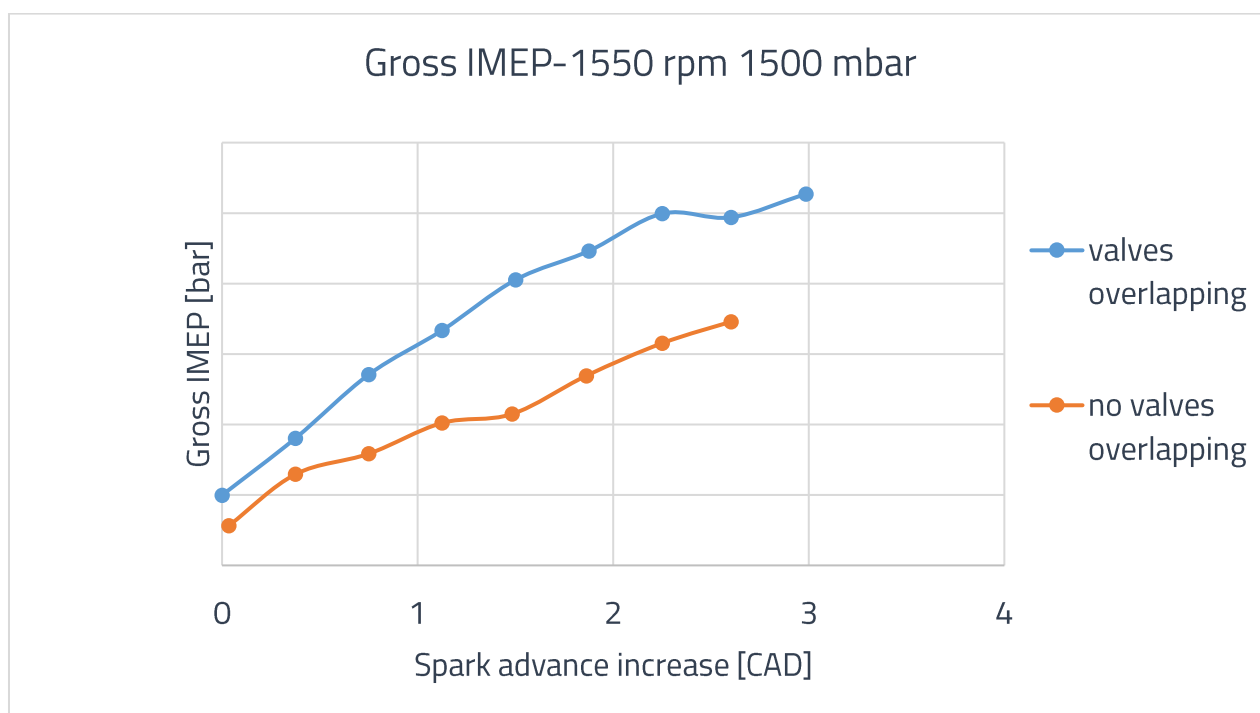


Figure 3-16: IMEP (each division is 0.2 bar) evolution with spark advance at 1550x1500 mbar

In figure 3-16, IMEP increases as the spark advance is increased. This means that the engine is still operating before the maximum break torque. In addition, changing the valves

settings from overlapping to not overlapping lower the engine air mass flow rate but the fuel flow rate remains constant.

As for 2000x1700 mbar, the same knocking behavior was also observed at 2000x1700 mbar as seen in figure 3-17.

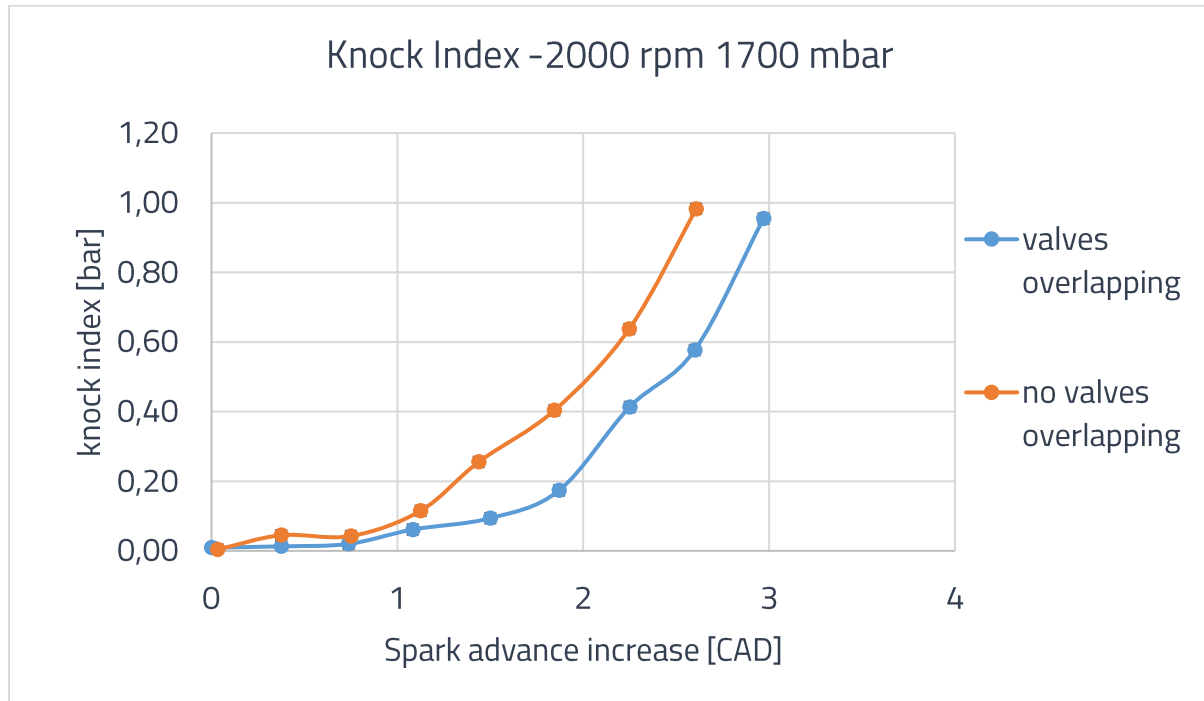


Figure 3-17: Knock index evolution with spark advance at 2000x1700 mbar

The knock apparition is also delayed with the valves overlapping as the residuals confined inside the cylinder decrease with the valves overlap as it can be seen in the figure 4-12. However, in the case of 2000 x 1700 mbar, the spark advance can be increased by around 0.5 CAD for the overlapping case when compared to the non-overlapping case at a constant knock index. This is due to the quantity of residuals confined when the valves do not overlap as observed in figure 3-18. In the case of 1550x1500 mbar, residuals are 5 times higher when the valves do not overlap, whereas at 2000x1700 mbar, residuals are almost doubled when the valves do not overlap. In fact, at 1550x1500 mbar, valves overlap for around 37 CAD and exhaust valves closes 22 CAD after top dead center, however for 2000x1700 mbar, valves overlap for 28 CAD and the exhaust valves closes 5 CAD after top dead center. The later the exhaust valves closing, the better the scavenging in the combustion chamber. This explains 0.6% at 2000 rpm and 0.2% at 1550 rpm.

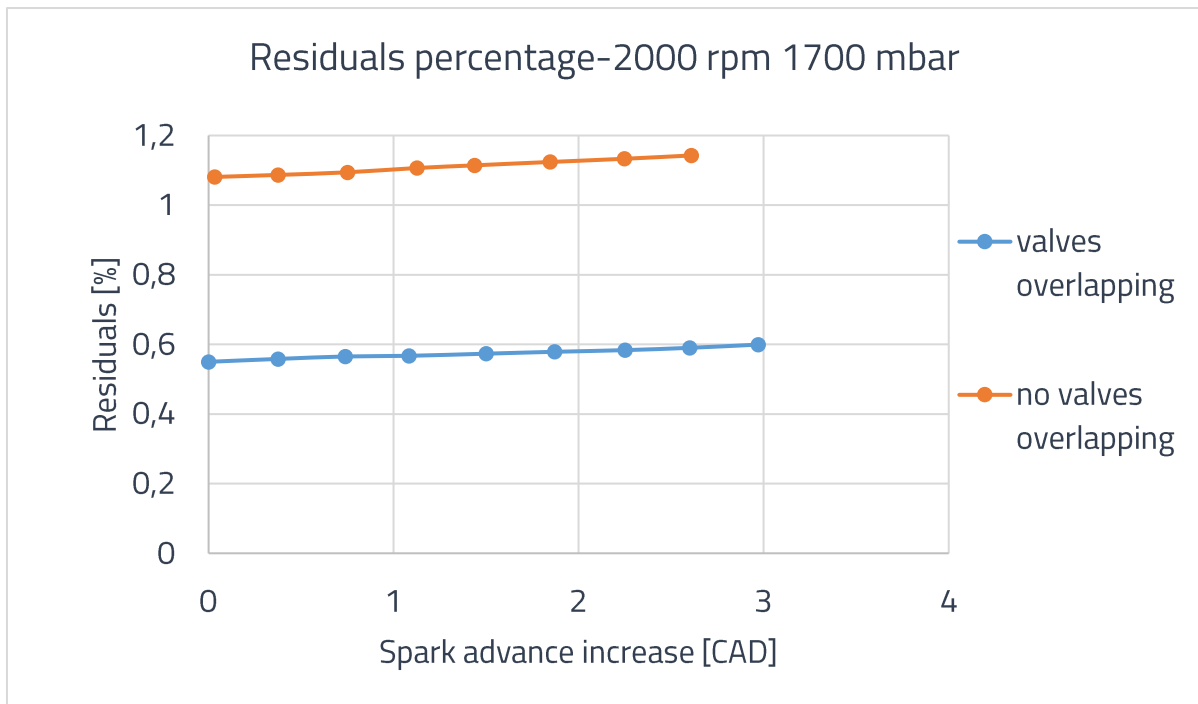


Figure 3-18: percentage of residuals confined inside the cylinder at 2000x1700 mbar

As engine speed increases, higher knock intensities are allowed without fearing engine failure. Knock intensities are directly related to pressure oscillations

Nevertheless, another effect was observed at 2500 rpm x 1700 mbar as it can be seen in figure 3-19. Overlapping the valves advances the apparition of the knock when compared to non-overlapping valves.

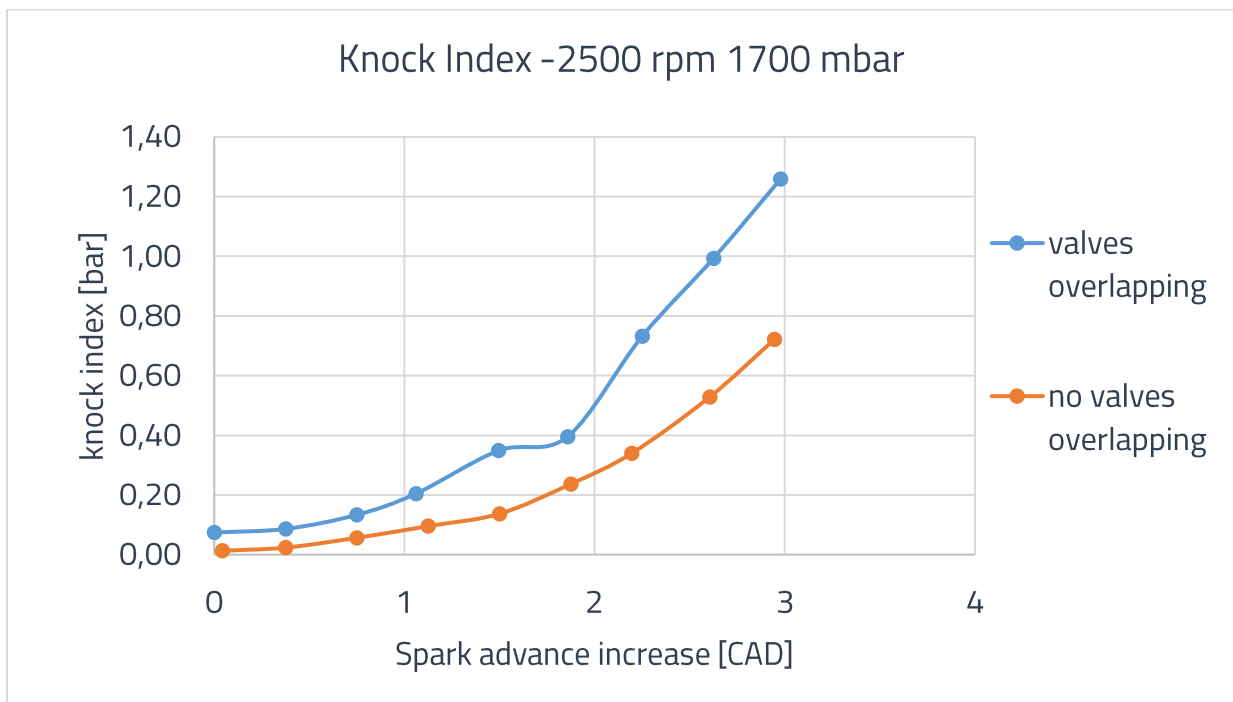


Figure 3-19: Knock index evolution with spark advance at 2500x1700 mbar

At 2500 x1700 mbar valves overlap by 10 CAD with intake valves opening before top dead center and exhaust valves closing at top dead center. Not overlapping the valves was achieved by delaying intake valves opening only, the quantity of air mass confined inside the cylinder was thus reduced as it can be seen in the figure 3-20, this can be seen as a load decrease. As air mass decreases and fuel mass decreases at constant fuel-to-air equivalence ratio, knock apparition is thus delayed and more spark advance can thus be achieved at constant knock index: spark advance can be increased by almost 0.75 CAD for the non-overlapping case for KI=0.8.

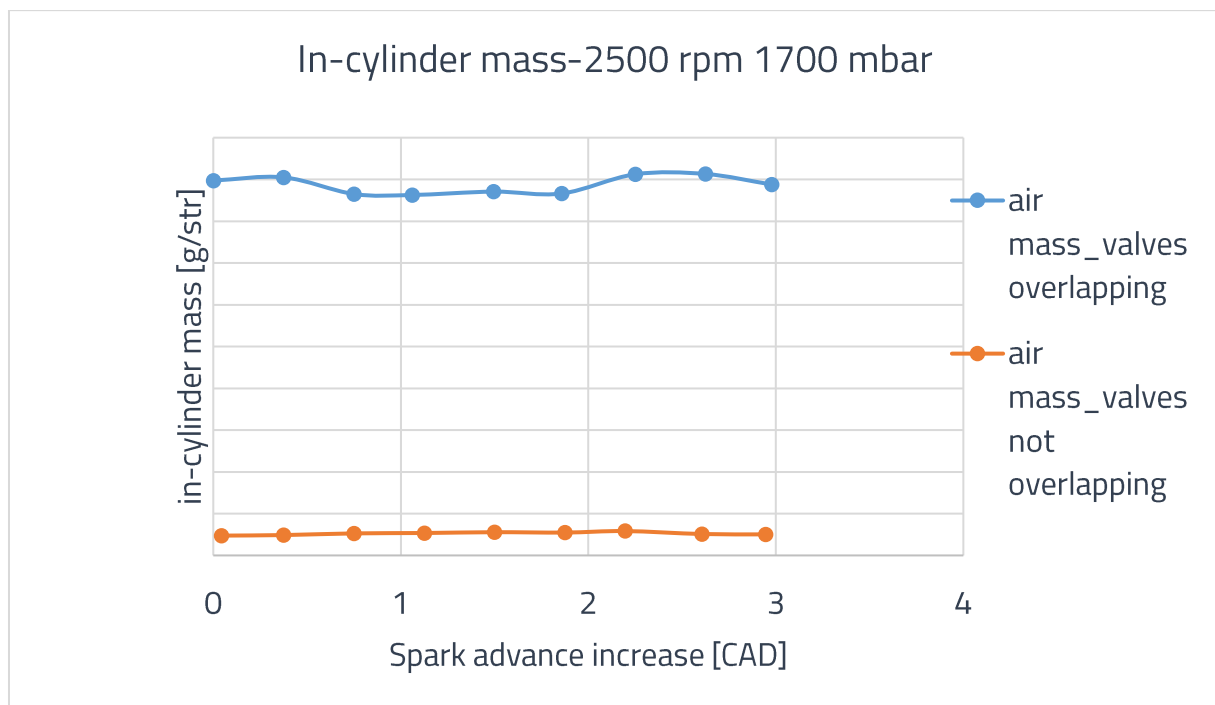


Figure 3-20: in-cylinder mass (each division is 0.005 g/str) at 2500x1700 mbar

As it can be seen, the air mass for the overlapping valves was around 0.755 g/stroke while in the not overlapping case it is about 0.71 g/stroke. This decrease in air mass can be seen as a load decrease and knock apparition is delayed with load decrease. Teodosio et al. studied the influence of EIVC, LIVC varying the lift on fuel consumption and knock tendency. They found out that both LIVC and EIVC improve BSFC when compared to full lift by 1.9% and 2.4% respectively and this was due to knock mitigation capacity and the advanced combustion phasing and reduced over fueling that was allowed on the engine with the modified valves strategies [106]

3.3.2. Conclusion of knock impact on engine behavior

The impact of knock apparition with a gradual increase of the spark advance on the three operating points considered in this PhD thesis is summarized as the following:

A similar behavior of the engine performance and knock apparition was observed on 1550x1500 mbar and 2000x1700 mbar where valves overlap delays knock apparition as the residuals quantity is reduced and the ignition delay of the end-gas is thus longer.

The opposite effect is observed at 2500x1700 mbar. Not overlapping the valves delays knock apparition as the mass of confined air is reduced and this phenomena is regarded as a load decrease and consequently knock delay.

For the three operating points, the engine is running below the maximum break torque region since with the spark advance increase, the engine performance is enhanced

3.4. Impact of injection strategies on knock occurrence

In this section, the impact of injection strategies on knock occurrence will be characterized for the three operating points 1550x1500 mbar, 2000x1700 mbar and 2500x1700 mbar. Several factors interact in the injection strategy:

1. Number of injections
2. The injection timings
3. The quantity of injected fuel, or in other terms, the ratio of the injected fuel for each injection.

On the engine bench, 4 different strategies were adopted in order to couple all of the previously mentioned factors:

1. Single injection to study the effect of injection timing during the intake stroke on knock occurrence
2. Double injection strategy where both injections happen during the compression stroke to study the effect of the injection timing during the compression stroke on knock occurrence
3. Double injection, the first one during the intake stroke and the second one during the compression stroke. The injection timings and the total quantity of injected fuel are fixed but the ratio of the injected fuel was modified. The objective is to study the effect of the ratio of injected fuel on knock occurrence.
4. Triple injection, the first one during the intake stroke and the others during the compression stroke. The injection timings and the total quantity of injected fuel are fixed but the ratio of the injected fuel was modified. The objective is to study the effect of the ratio of injected fuel on knock occurrence in the case of a triple injection.

In the third and fourth strategies, the injection timings of the first 2 injections are the same. This means that in the case of a triple injection, the third injection is an additional one on the first two.

For each operating point and for each injection strategy, 3 values of spark advances were swept:

1. 0 spark advance increase: which means that the injection strategy was tested with the calibrated spark timing for each operating point. The calibrated spark timing is maintained constant for all the study and for all the control parameters in this PhD thesis.
2. Maximum spark advance increase: on the engine bench the spark advance was increased by steps of 0.375 CAD until an alarm was triggered indicating that the engine approaches a failure phase if the spark timing is further advanced. The alarm is triggered on the bench when the Maximum Amplitude of the Pressure Oscillation

exceeds the maximum allowed threshold more than 3 cycles within 10 seconds. This configuration is advised by the engine constructor.

3. An intermediate value of spark advance between the 0 and the maximum spark advance

The objective of 3 spark timing for each strategy is to be able to plot a variation of the knock index with respect to the spark advance and to be able to compare different strategies (different curves). The number of spark timings was limited to 3 unlike in the previous section because a lot of tests were performed. Plotting the variation of the knock index in function of the spark advance increase is so important to compare the different injection strategies since the maximum spark advance increase is not the same for all of the strategies and thus a simple comparison between knock index values would be meaningless.

3.4.1. Impact of injection timing during intake stroke on knock occurrence

The injection timing was swept during the intake stroke to assess its impact on knock occurrence. The injection timings are presented in terms of injection advance with respect to firing top dead center, in other terms a start of injection SOI=300 CAD refers to 300 CAD before top dead center. They can be observed in figure 3-21 along with the valves lift. In this set of experiments, the quantity of injected fuel is maintained constant as well as the equivalence ratio.

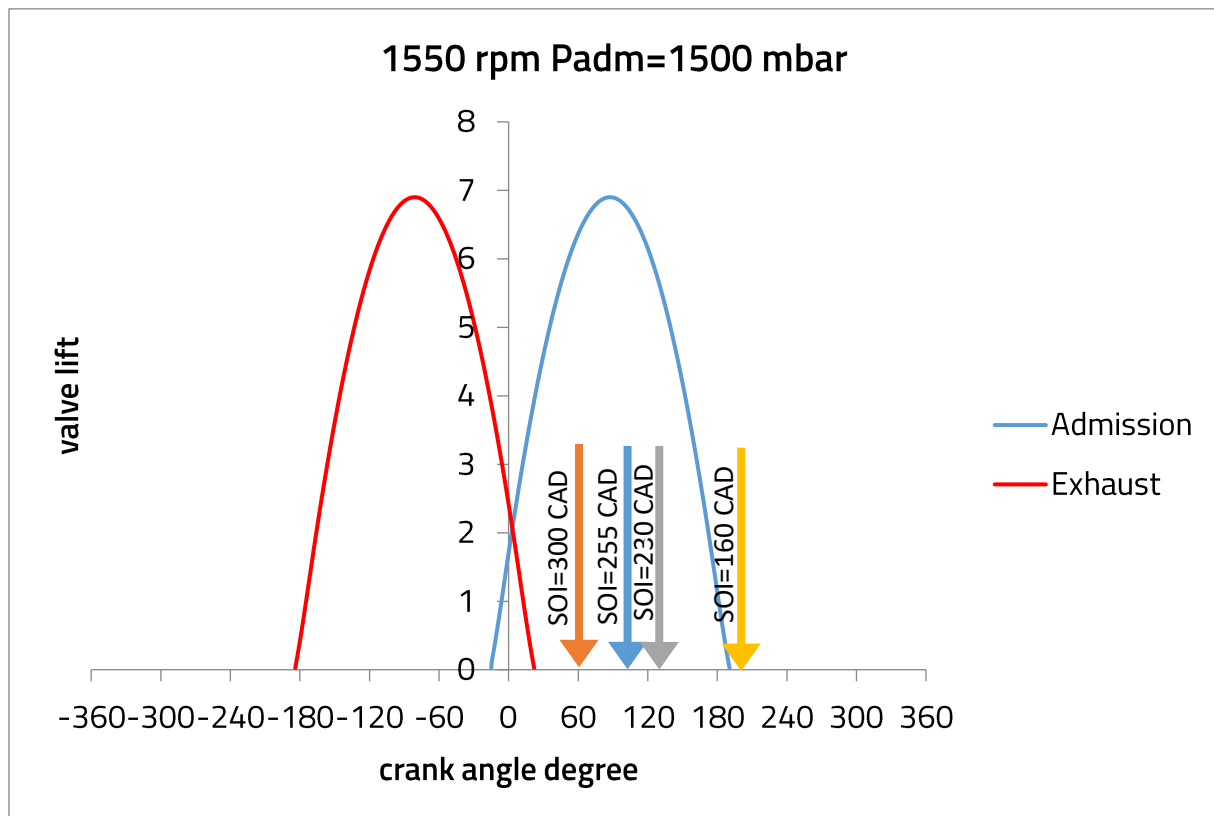


Figure 3-21: valves timings and injection timings for the single injection strategie at 1550x1500 mbar

The intake stroke is considered between the opening of the intake valves and closing of the intake valves, SOI=160 CAD is thus considered in the intake stroke since the valves close at around 150 CAD before the firing top dead center.

At 1550x1500 mbar, the earliest injection timing lead to the highest the tendency to knock as it can be seen in figure 3-22 except for SOI=255 CAD and the latest injection timing lead to the lowest tendency to knock.

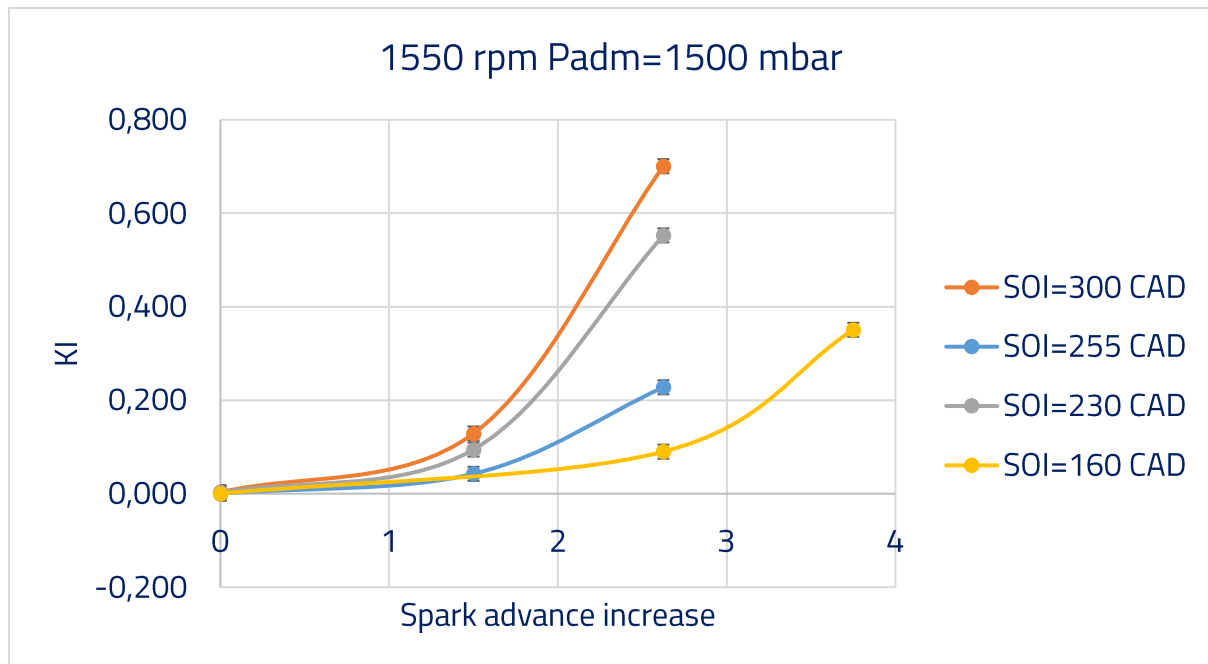


Figure 3-22: Knock index evolution with injection timing sweep during the intake stroke at 1550x1500 mbar

In fact, advancing the injection during the intake stroke leads to a better homogenization of the fresh charge; the mixture is rapidly consumed after the spark discharge leading to a faster burn and a higher-pressure rise as it can be seen in figure 3-23. This increase the end gas pressure leading to a shorter ignition delay and a higher tendency to knock. The knock apparition is then delayed as the injection timing is delayed but it is accompanied by a degraded performance since the torque decreases from 165 N.m to 160 N.m as the injection timing is delayed from SOI=300CAD to SOI=160CAD with 0 spark advance decrease.

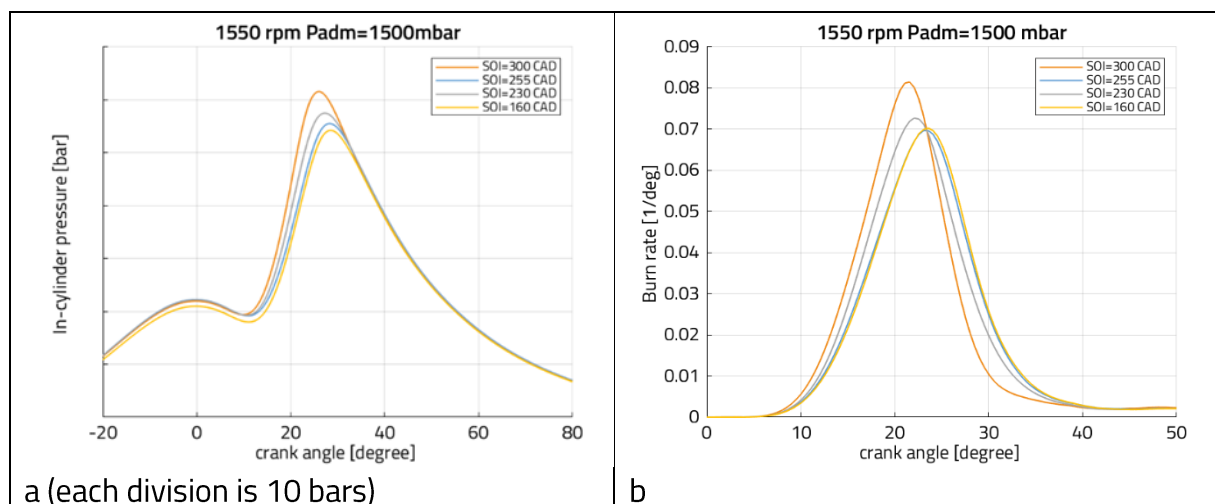


Figure 3-23: in-cylinder pressure (a) and burn rate (b) evolution with injection timing sweep during the intake stroke at 1550x1500 mbar and at 0 spark advance increase

However, in the case of 1550x1500 mbar, SOI=255 CAD seem to present a sort of trade-off between performance loss and knock delaying. SOI=255 CAD can be regarded as an

optimum injection timing since it delays knock more than SOI=230 CAD reproducing a similar torque of 163 N.m. For SOI=230 CAD, the burn rate is faster than SOI=255 CAD and the pressure rise inside the cylinder compresses the end-gas more than SOI=255 CAD and leads to its auto-ignition earlier than SOI=255 CAD. For the upcoming study on the injection strategy, SOI=255 CAD will be maintained when an injection in the intake stroke is to be considered.

The effect of charge cooling due to late injection can be observed on the in-cylinder trace at SOI=160 CAD in figure 3-23 (a). The evaporation of the fuel leads to charge cooling which consequently reduces the pressure the end of the compression stroke. This phenomenon is only observed at SOI=160 CAD.

The same behavior of the knock index evolution is also be observed at 2000x1700 mbar:

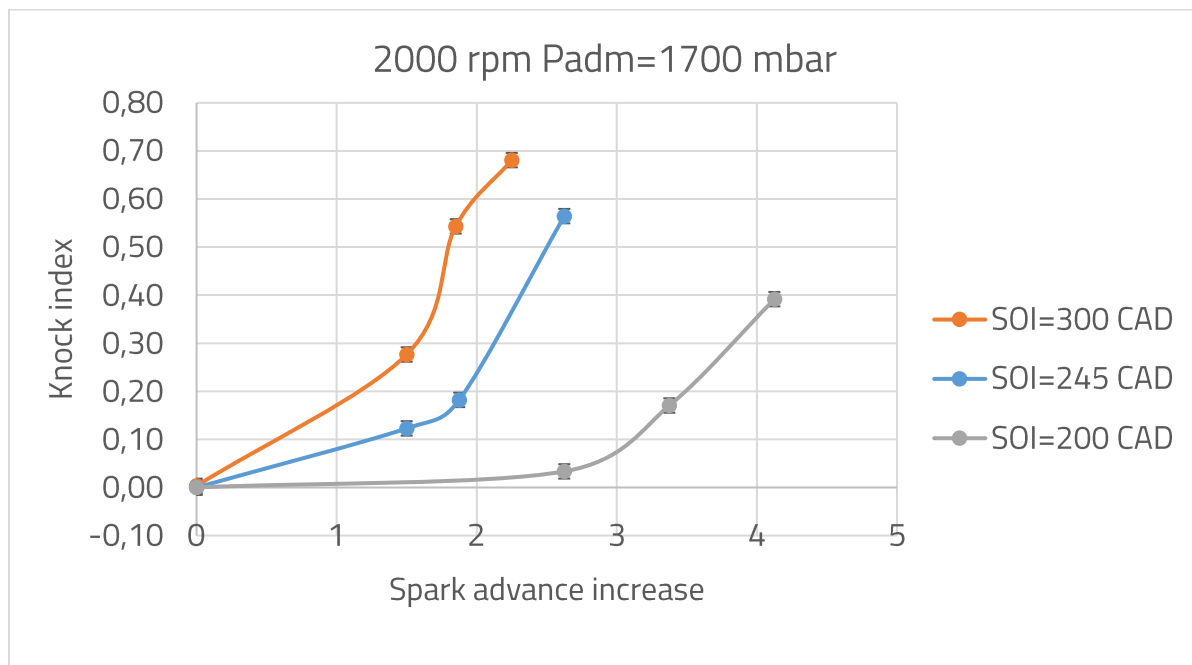


Figure 3-24: Knock index evolution with injection timing sweep during the intake stroke at 2000x1700 mbar

At 2000x1700 mbar, the same behavior was also observed, knock apparition was delayed as the injection timing is delayed as it can be seen in figure 3-24

At 2500x1700 mbar:

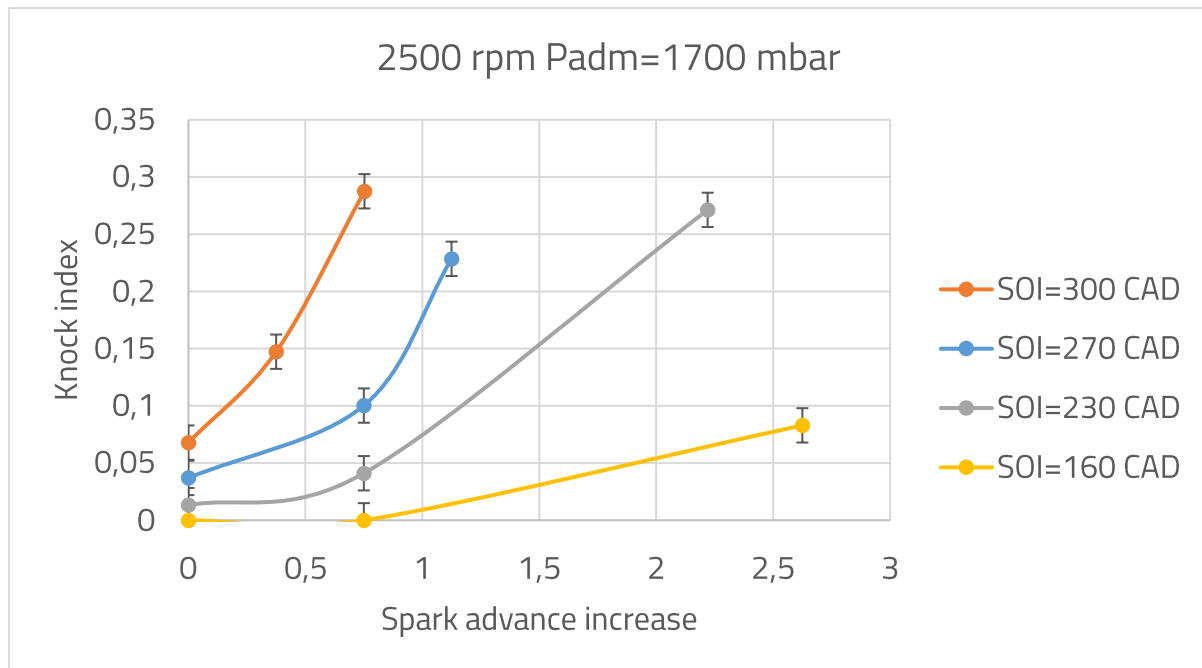


Figure 3-25: Knock index evolution with injection timing sweep during the intake stroke at 2500x1700 mbar

For the operating point 2500x1700 mbar as in figure 3-25, even the delay in the injection timing highly reduced the knock apparition, the loss in engine performance was much more pronounced than the 1550x1500 mbar. As start of injection was delayed from SOI=300 CAD till SOI=160 CAD, the torque decreased from 188 N.m till 170 N.m which is almost 10% while at 1550x1500 rpm, this torque loss was around 3%. In fact, the objective of maintaining the injected fuel quantity constant was not met at 2500x1700 mbar and SOI=160 CAD and it was accompanied by lower end-of compression pressure due to charge cooling which explains the torque loss. These results are in accordance with those observed by Singh et al. [107]: in a single injection, the knock index is lower when the injection timing is retarded. But this leads to a decreased IMEP. The intake pressure had to be increased in order to prevent the IMEP deterioration, but it was compensated by a higher CoV of IMEP.

3.4.2. Impact of injection timing during compression stroke on knock occurrence

The injection timing will be studied this time in the compression stroke while also splitting the quantity of fuel into 2 injections with the similar injected fuel ratio of 50% of the total mass each.

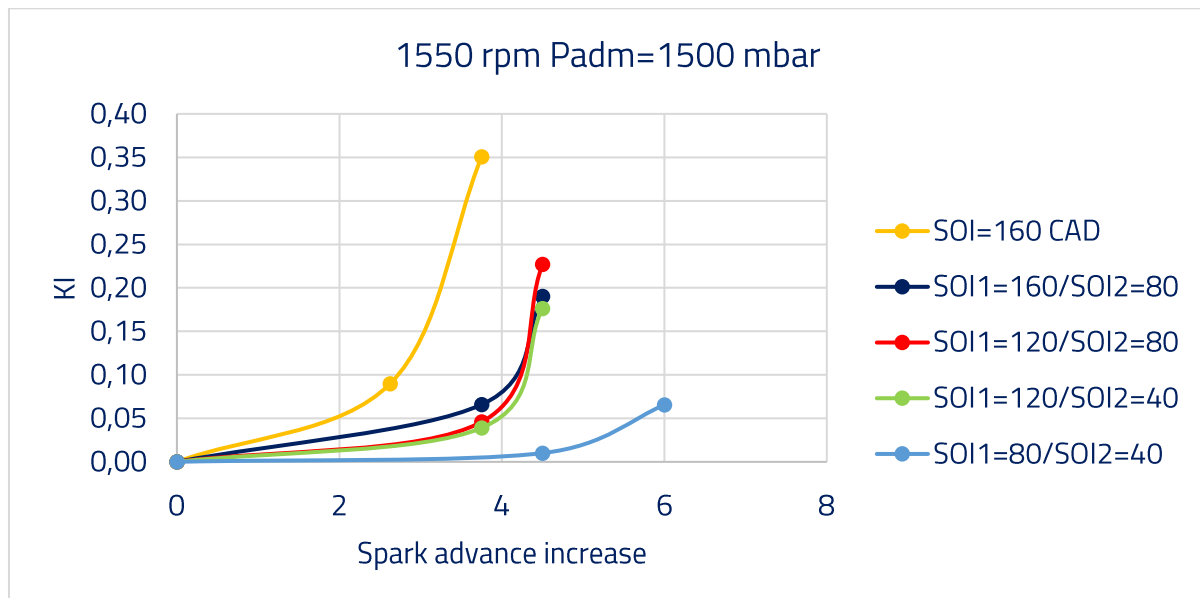


Figure 3-26: Knock index evolution with injection timing sweep during the compression stroke at 1550x1500 mbar

As it can be seen in figure 3-26, all of the injection in the compression stroke delays the knock apparition when compared to injection in the intake stroke. Injections during the compression stratifies the mixture as lean regions can be observed near the wall and rich regions are observed near the spark plug with an overall global equivalence ratio equal for all the cases.

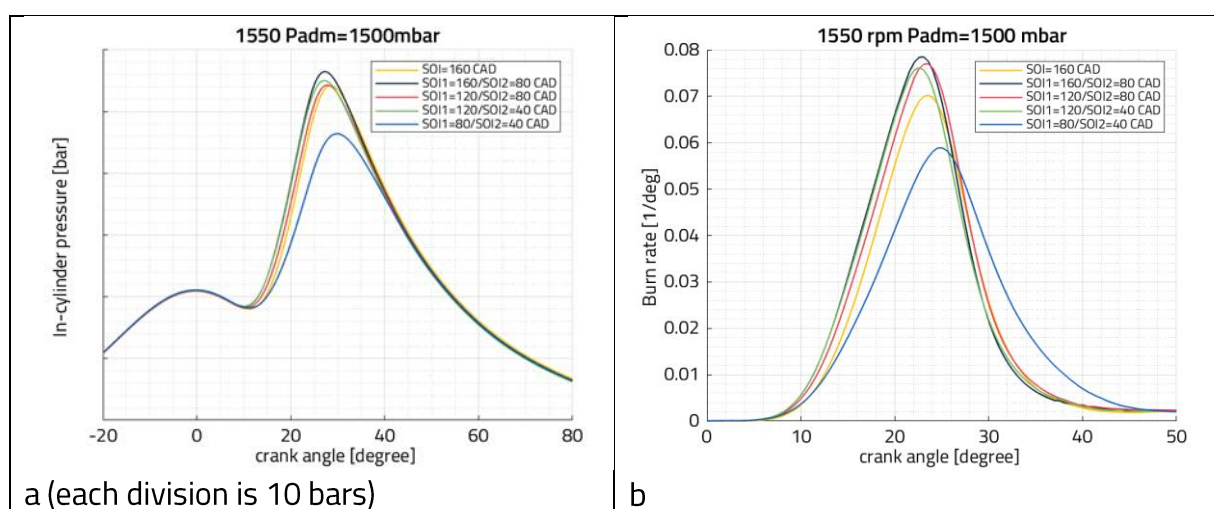


Figure 3-27: in-cylinder pressure (a) and burn rate (b) evolution with injection timing sweep during the compression stroke at 1550x1500 mbar and at 0 spark advance increase

The spark induced flame speed is thus increased consuming the mixture faster than auto-ignition delay of the end-gas whose duration is further increased due to a leaner composition. The later the injection, the faster the spark-induced flame speed and the knock apparition is thus further delayed. This applies for the first three injection timings during the compression where no differences were observed on the knock apparition between them. This can be seen on the in-cylinder pressure traces and burn rate in figure 3-26. The burn rate in the case of a single injection at $SOI=160$ CAD is slower than the double injections at $SOI1=160$ CAD/ $SOI2=80$ CAD, $SOI1=120$ CAD/ $SOI2=80$ CAD and $SOI1=120$ CAD/ $SOI2=40$ CAD. Moreover, the spark timing can be advanced a lot in the case of a double injection (up to 6 CAD) with a very small apparition of knock at $SOI1=80$ CAD/ $SOI2=40$ CAD. This is due to the decreased combustion burn rate where the late injection and charge cooling effect degraded the flammability of the mixture. The combustion developed later when compared to the other injections timings. The combustion reaches a lower peak and compresses the end-gas less than in the earlier injections. This extends the auto-ignition delay of the end-gas.

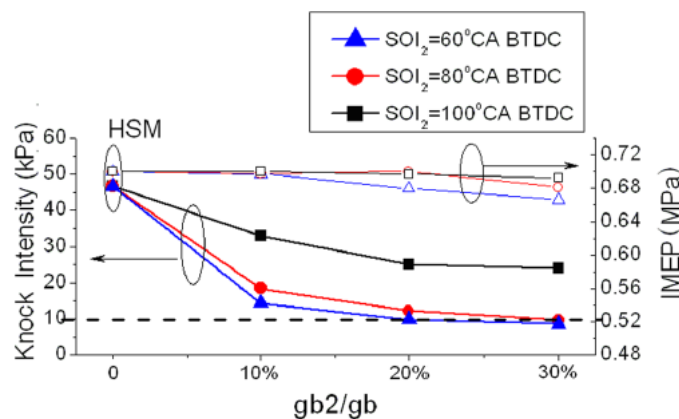


Figure 3-28: knock intensity for homogeneous stoichiometric mixture (HSM) and stratified mixture as studied by Bai et al. [57]

Similar results were observed by Bai et al. as it can be seen in figure 3-28: stratified stoichiometric mixtures suppressed the knock significantly better than homogeneous stoichiometric mixtures due to the lean zone near the walls and rich zones near the spark plug which offers better control over the flame speed [57].

3.4.3. Impact of injected fuel ratio in a double injection on knock occurrence

In this section, the effect of injected fuel ratio will be studied in a double injection strategy. To do so the injection timings were fixed. These tests were also performed at fixed injected quantity and equivalence ratio.

For the operating point 1550x1500 mbar, the first injection is set at SOI1=255 CAD in the intake stroke and the second injection at SOI2=120 CAD in the compression stroke. The injection ratio are presented in terms of percentages of the total injected fuel mass. In figure 3-29, the injections timings are presented in the same graph the valves lift.

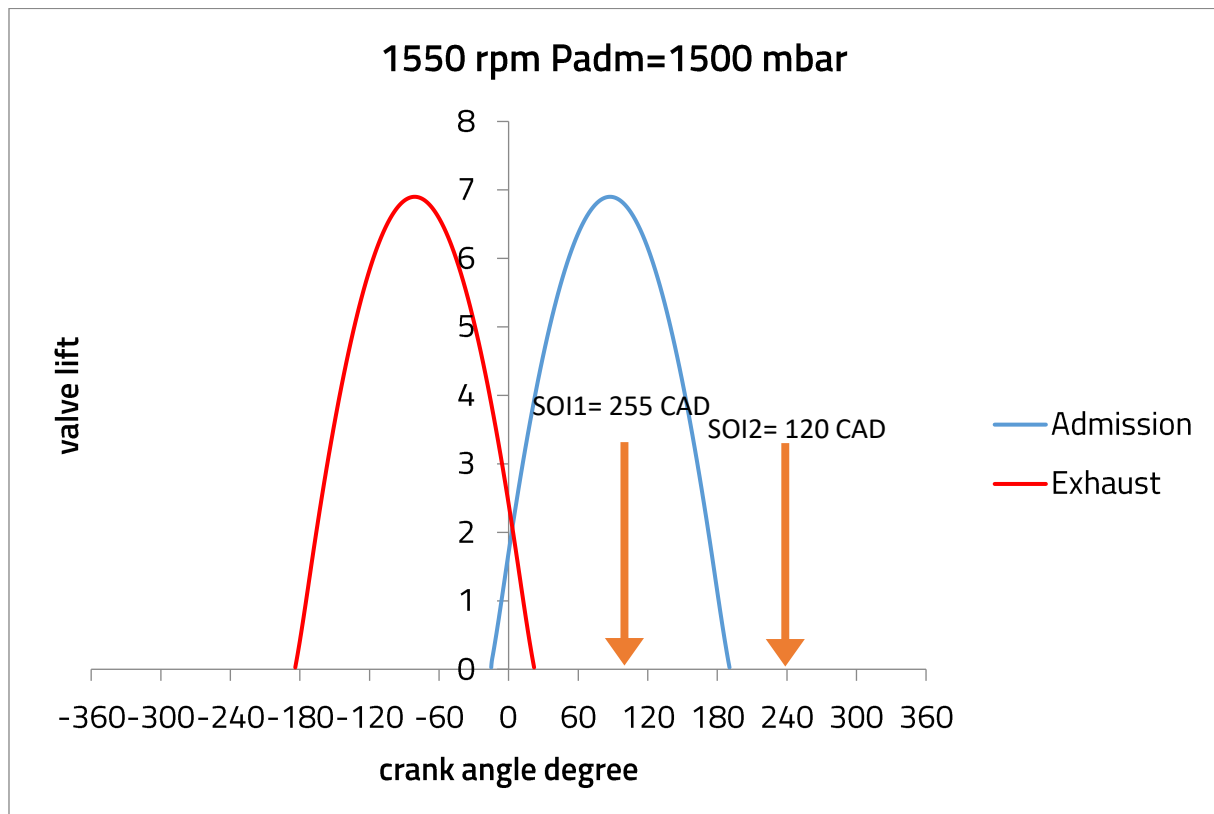


Figure 3-29: valves timings and injection timings for the double injection strategy at 1550x1500 mbar

3 settings were tested:

1. M1=50% and M2=50% with M1 and M2 referring the first and second injections ratios.
2. M1=66% and M2=34%
3. M1=34% and M2= 66%

The knock index in function of the spark advance increase are plotted for the three settings on the same graph.

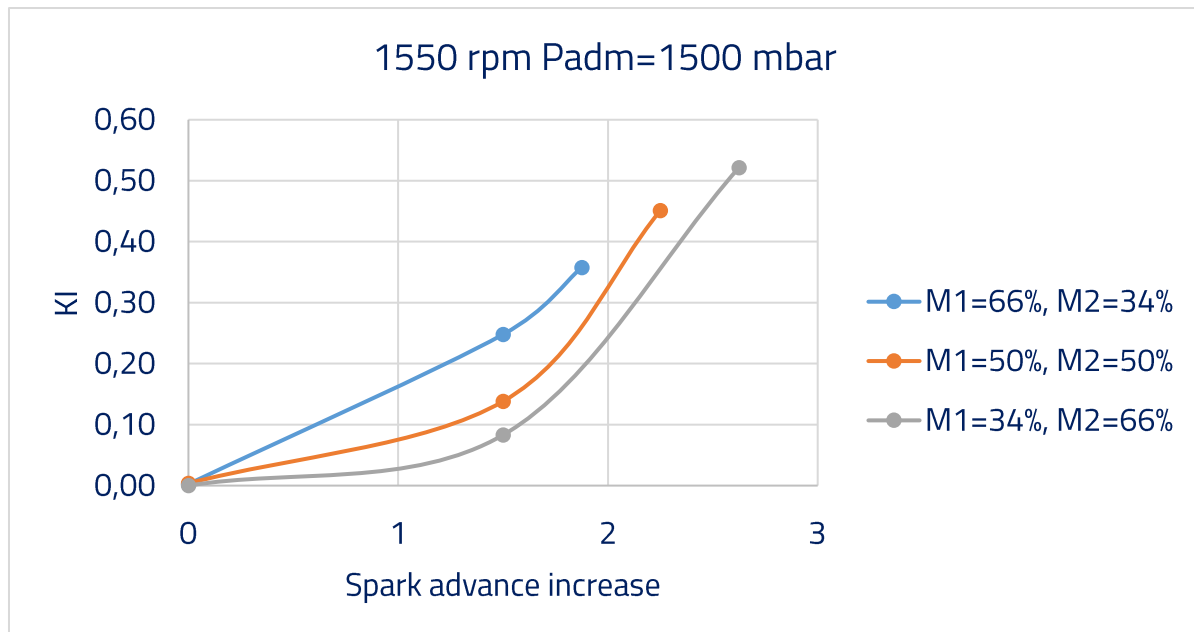


Figure 3-30: Knock index evolution with injection ratios sweep in a double injection strategy at 1550x1500 mbar

As it can be seen, the quantity of injected fuel in each injection affect the combustion development and consequently the knock apparition. Knock is delayed as the quantity in the second injection is increased. These results are compatible with those of the previous section. In the previous section, it was demonstrated that injections in the compression stroke enhance the charge stratification. In this section, increasing the quantity of fuel in the second injection accelerates the flame speed when compared to lesser fuel quantity in the second injection. The enhanced spark-induced flame consumes the end-gas faster than its auto-ignition delay which reduces knock apparition.

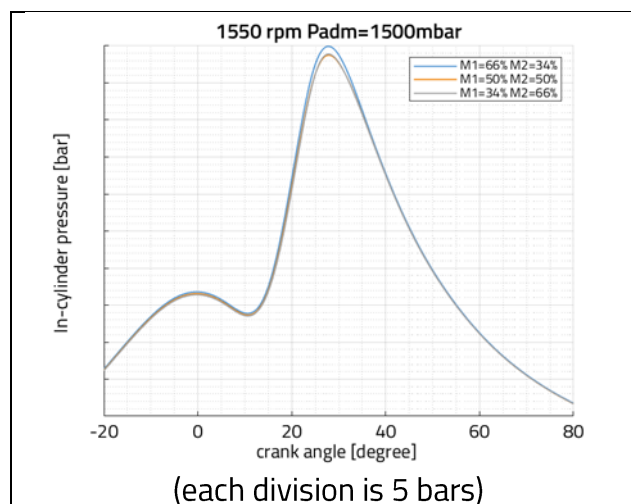


Figure 3-31: in-cylinder pressure evolution with injected fuel ratio sweep in a double injection at 1550x1500 mbar and at 0 spark advance increase

This behavior was also observed on the 2000x1700 mbar. The first injection is set at SOI1=245 CAD in the intake stroke and the second injection at SOI2=80 CAD in the compression stroke.

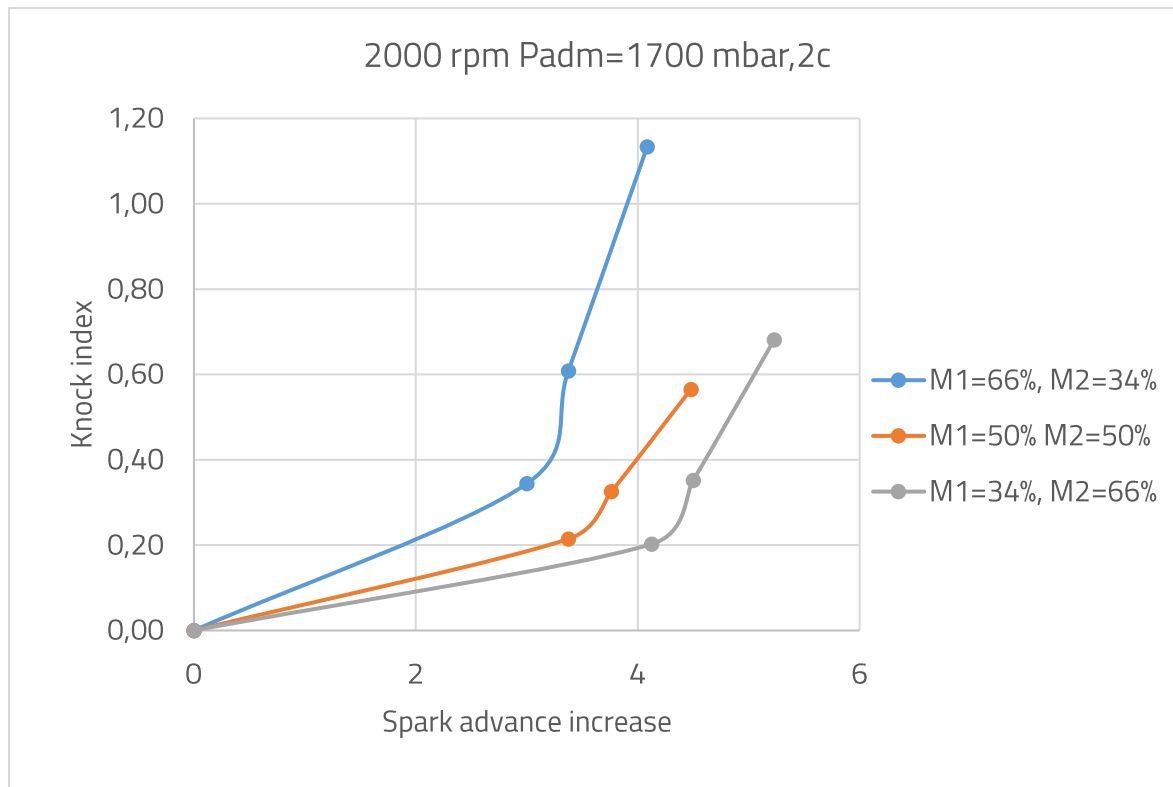


Figure 3-32: Knock index evolution with injection ratios sweep in a double injection strategy at 2000x1700 mbar

Splitting the injections into two is demonstrated to be beneficial on the knock apparition. However, it is always accompanied by a performance loss. For 1550x1500 mbar, the break torque for the single injection in the intake stroke was around 163 N.m and it drops to below 160 N.m in a double injection. For 2000x1700 mbar, the break torque for the single injection in the intake stroke was around 185 N.m and it drops to below 180 N.m in a double injection. Nevertheless, the ratio of injected fuel also affect the performance in the case of a double injection. For 2000x1700 mbar, the torque drops from 180 N.m for M1=66%, M2=34% to 177 N.m for M1=50%, M2=50% and to 173 N.m for M1=34%, M2=66% . The higher the quantity in the first injection, the higher the break torque.

3.4.4. Impact of injected fuel ratio in a triple injection on knock occurrence

In this section, another injection is added in the compression stroke to further analyze the effect of splitting the injection and the ratio of injected fuel in each one on the knock margin.

At 1550x1500 mbar operating point, the triple injection strategy was performed in a way to split the second injection in the double injection strategy into two injections in the compression stroke according to the following. SOI1=255 CAD (intake stroke), SOI2=120 CAD (compression stroke) and SOI3= 40 CAD (compression stroke) as it can be seen in figure 3-33.

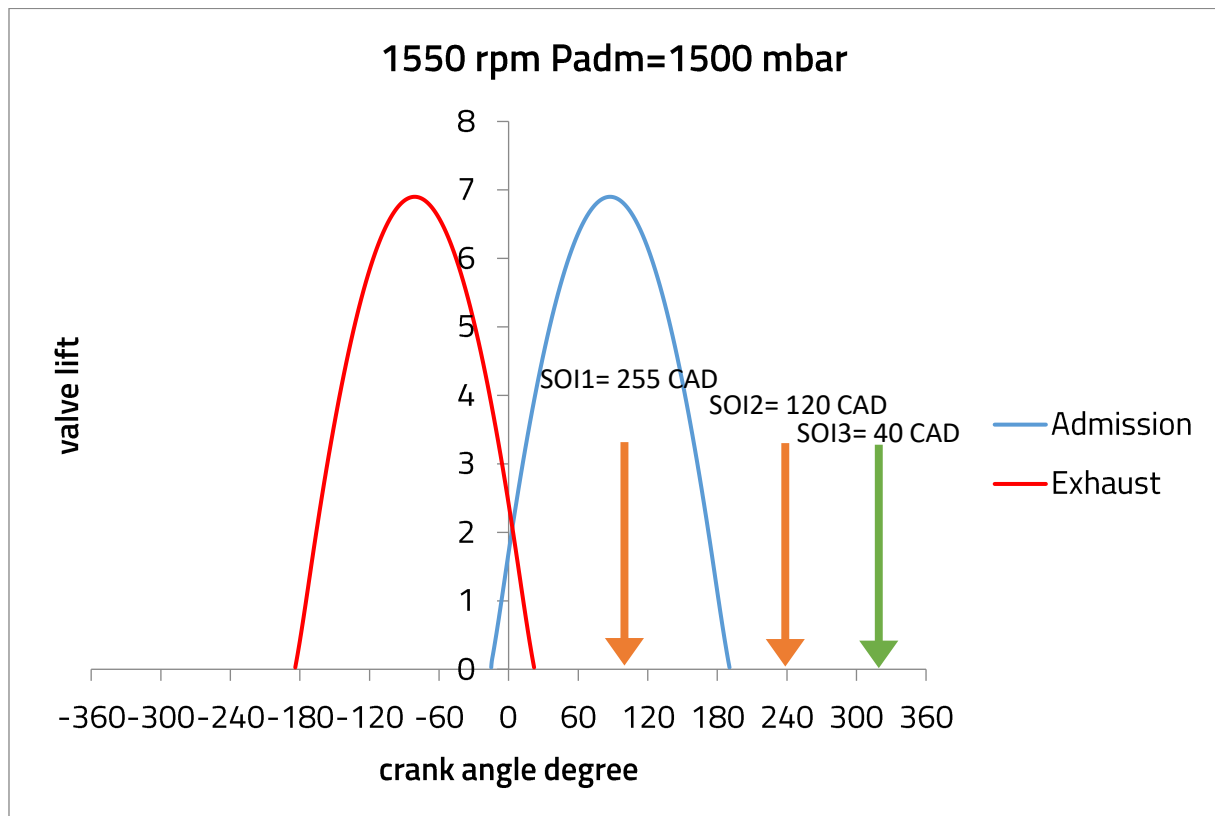


Figure 3-33: valves timings and injection timings for the triple injection strategy at 1550x1500 mbar

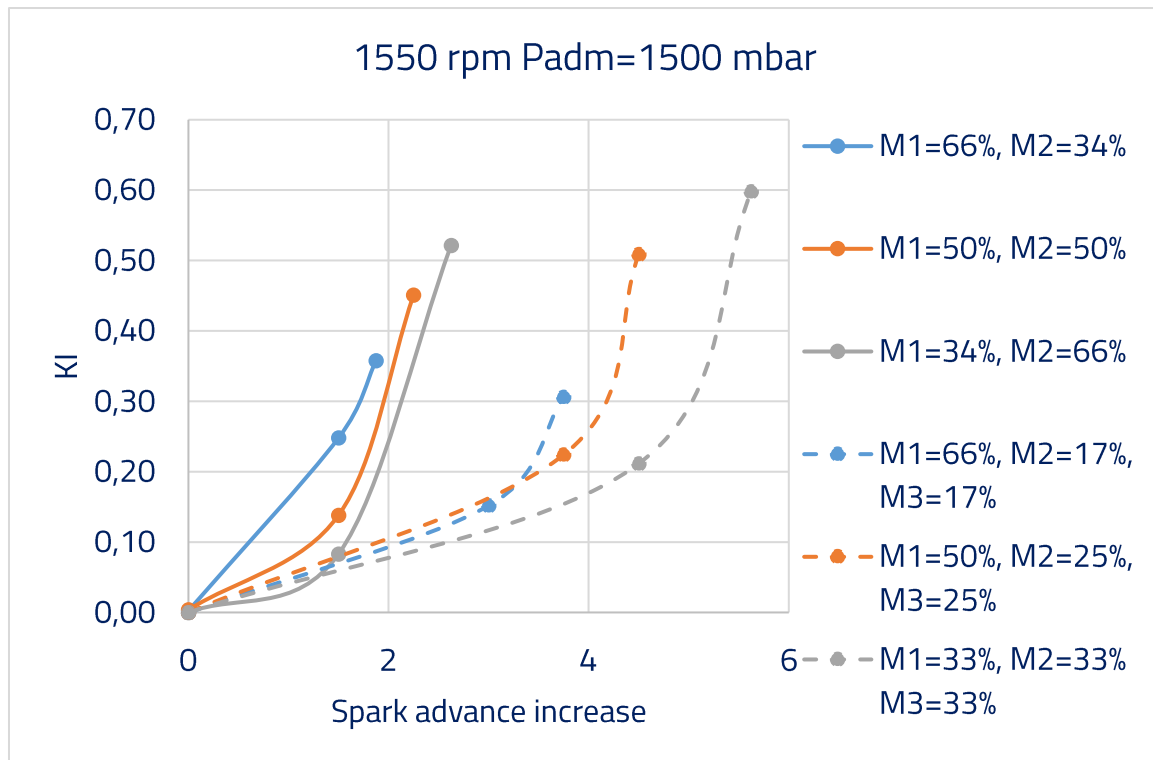


Figure 3-34: Knock index evolution with injection ratios sweep in a triple injection strategy at 1550x1500 mbar

It is clear that triple injection further delays the knock apparition when compared to double injection. As it was observed in section 3.4.2, injections in the compression stroke contribute to enhanced spark-induced flames that consumes the end-gas before it auto-ignites. The quantity of fuel injected in the first injection is still controlling the knock behavior in the same manner as the previous section. Blue curves (solid and dashed lines) refer to the highest ratio of injected fuel in the intake stroke and they are the more susceptible to knock in both double and triple injections. Gray curves (both solid and dashed lines) refer to the lowest ratio of injected fuel in the intake stroke and they both have the highest knock margin in both double and triple injection. For the same injected fuel ratio, in the intake stroke, the triple injection strategies delays knock apparition more than the double injection. The late third injection increases the spark-induced flame and the burn rate and consumes the end-gas faster than its auto-ignition. The spark-induced combustion in a double injection is faster than its equivalent in the triple injection, the peak pressure obtained is higher and this compresses more the end-gas, shortens its auto-ignition delay and advances a little bit knock apparition.

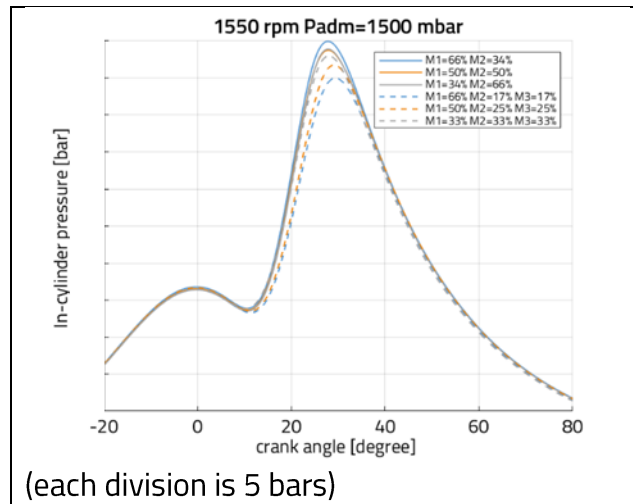


Figure 3-35: in-cylinder pressure evolution with injected fuel ratio sweep in a double and triple injection strategies at 1550x1500 mbar and at 0 spark advance increase

At 2000x1700 mbar, the triple injection strategy was performed in a way to split the second injection in the double injection strategy into two injections in the compression stroke but this time while interposing an earlier injection in the compression stroke as observed in figure 3-36.

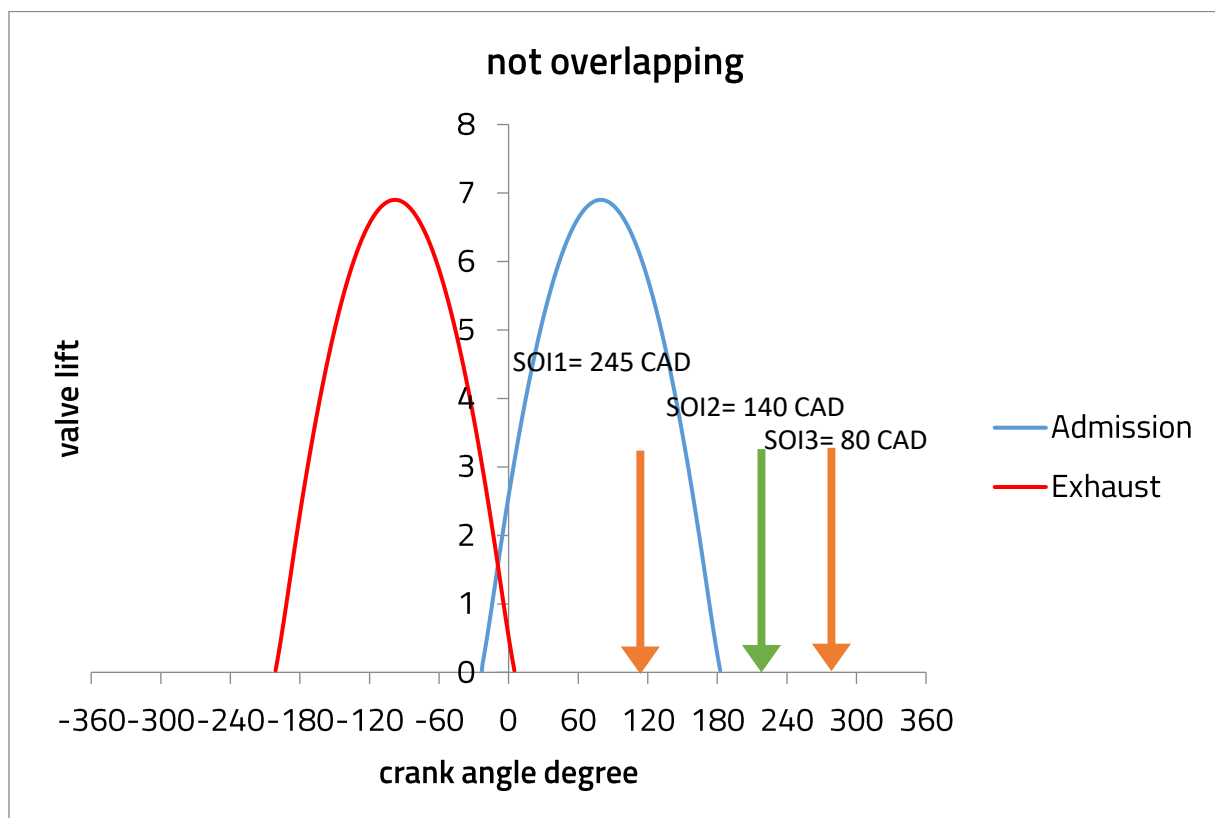


Figure 3-36: valves timings and injection timings for the double injection strategy at 2000x1700 mbar

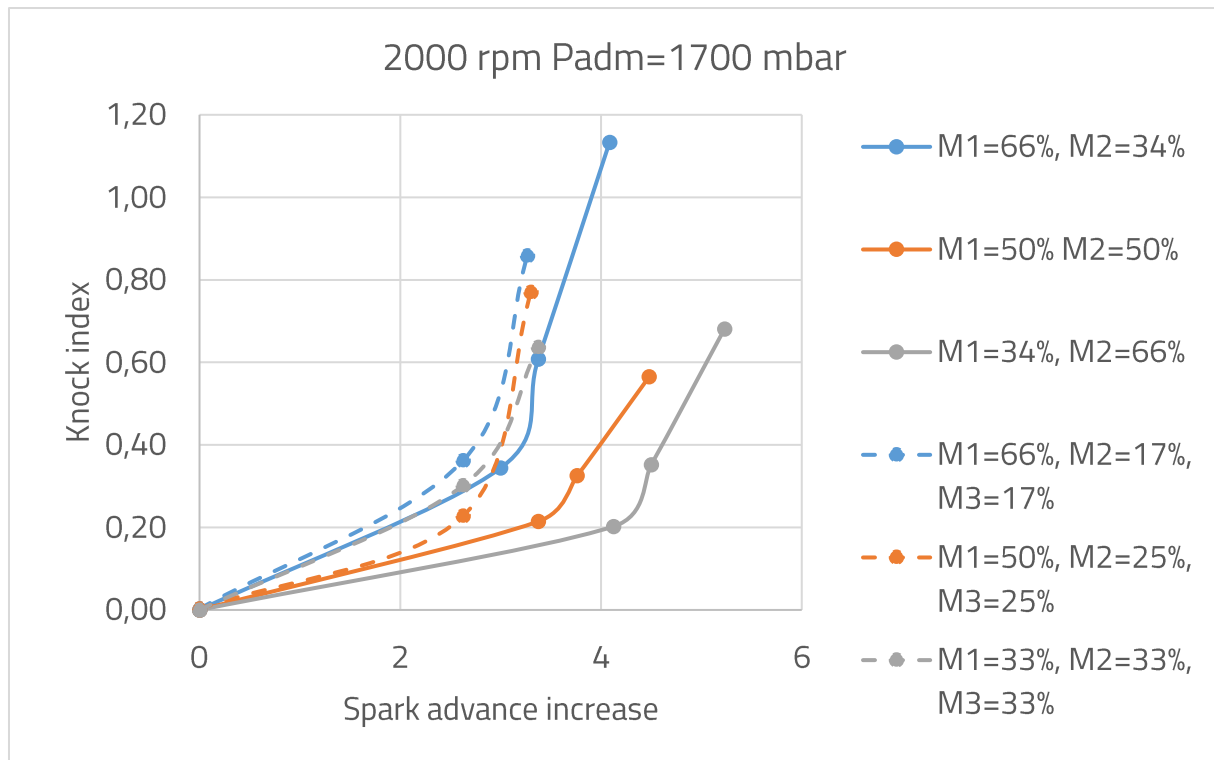


Figure 3-37: Knock index evolution with injection ratios sweep in a triple injection strategy at 2000x1700 mbar

As it was expected, interposing an earlier third injection increases the knock apparition since a lesser fuel quantity is injected in the latest injection. If double and triple injections are compared separately, the strategies with the higher injected ratio in the intake stroke are more susceptible to knock and the strategies with higher injected ratio in the last injection are the less prone to knock. Curves are plotted in the same order of knock probability for both set of double and triple injections. These results are compatible with all of the previous results in sections 3.4.1 and 3.4.2 and 3.4.3. However and in contradiction to the results obtained earlier in section 3.4.3, interposing a third injection degraded the knock margin when compared to double injection. In fact, this third injection, as it arrived earlier in the cycle, reduced the ratio of the latest injection, reducing the stratification of the mixture caused by the last injection, reducing the auto-ignition delay of the end-gas making it more susceptible to knock.

3.4.5. Conclusion of injection law strategies impact on knock occurrence

For the injection timing in the intake stroke, a similar behavior of the engine performance and knock apparition was observed across all the engine speeds considered. The knock apparition is delayed as the injection timing is delayed. Delaying injection timing degrades the engine performance in the case of a single injection in the intake stroke. A trade-off at SOI=255 CAD between knock apparition and engine performance was observed for 1550x1500 mbar.

For the injection timings in the compression stroke: Injections in the compression stroke delay the knock apparition when compared to injections in the intake stroke. Injections in the compression stroke stratifies the mixture, with a rich zone near the spark plug and lean zone near the walls. This increases the spark-induced flame speed which consumes the end gas before it auto-ignites. However with a very late injection in the compression stroke, knock apparition is further delayed but for a different reason. It is due to the decreased combustion burn rate where the late injection and charge cooling effect degraded the flammability of the mixture. The combustion developed later when compared to the earlier injections timings.

As for the injected fuel ratios in a double injection, a similar behavior is observed on both the 1550x1500 mbar and 2000x1700 mbar operating points. Fuel injected in the second injection stratifies the mixture, creates lean zone near the walls and richer zones near the spark slug. Knock is delayed as the quantity in the second injection is increased

Regarding the injected fuel ratios in a triple injection: Triple injection strategy clearly delays knock apparition when the quantity of injected fuel are well distributed. The intake stroke injection is the main injection responsible of the engine performance enhancement. The latest compression stroke injection is the one responsible of knock apparition enhancement. These two injections affect the engine behavior in a opposite way. A trade-off is obtained by interposing a third injection in a way to maintain engine torque and a knock margin. For 1550x1500 mbar, splitting the second injection of the double injection strategy into two injections in the compression stroke delays knock apparition whereas for 2000x1700 mbar, interposing a third injection earlier in the compression stroke increases the knock apparition.

3.5. Impact of intake air temperature on knock occurrence

The auto-ignition delay of the end-gas depends on the temperature of the fresh gases. It is thus important to study the impact of that temperature on knock occurrence. In this section, the effect of intake air temperatures on knock apparition will be studied on the three operating points 1550x1500 mbar, 2000x1700 mbar and 2500x1700 mbar.

3.5.1. Knock index evolution with intake air temperature sweeps.

Intake air temperature were swept between 25°C and 45°C with a 10°C step and for two cases of valves settings: overlapping and not overlapping. Same as for the injection law strategies, for each temperature setting and for each operating point, 3 values of spark advances were swept.

For 1550x1500 mbar, the evolution of knock index in function of spark advance increase for the overlapping setting is presented in figure 3-38:

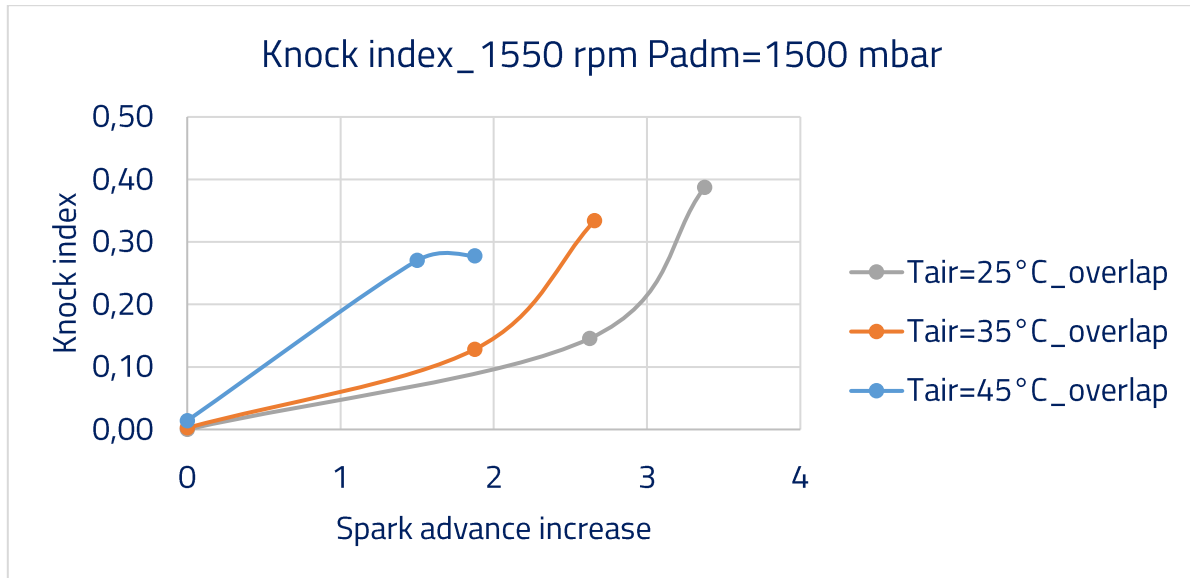


Figure 3-38: knock index evolution with spark advance increase for intake air temperatures sweep at 1550x1500 mbar

As the inlet air temperature was reduced, the knock apparition is delayed. In figure 3-38, we can observe that 0.75 CAD can be gained on the spark timing by a 10°C decrease of the intake air temperature. These values can be observed at a fixed knock index value on the curves above. This means that on the knock margin, the spark timing can be advanced by 0.75 CAD if a decrease of 10°C of intake air temperature was achieved. This is due to lower end-gas temperature and its increased auto-ignition delay. This can be observed on the maximum unburned gas temperature (or the end gas) as it can be seen in the figure 3-39. This maximum unburned gas temperature is calculated by GT Power in the unburned zone.

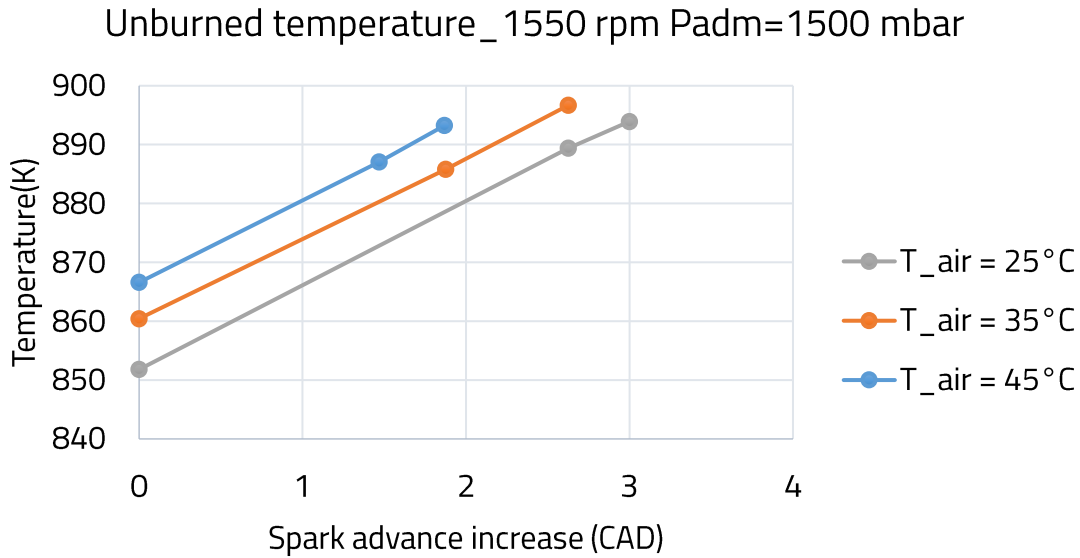


Figure 3-39: maximum unburned zone temperature

As the inlet air temperature is reduced, the fresh mixture temperature is gradually reduced inside the cylinder. The temperature of the mixture inside the cylinder is almost 15°C cooler when the inlet air temperature is reduced from 45°C to 25°C. In the figure above the evolution of the unburned gas temperature is presented. This temperature is increased as spark advance is increased. This is due to the compression of the end-gas by the spark-induced flame which is more pronounced.

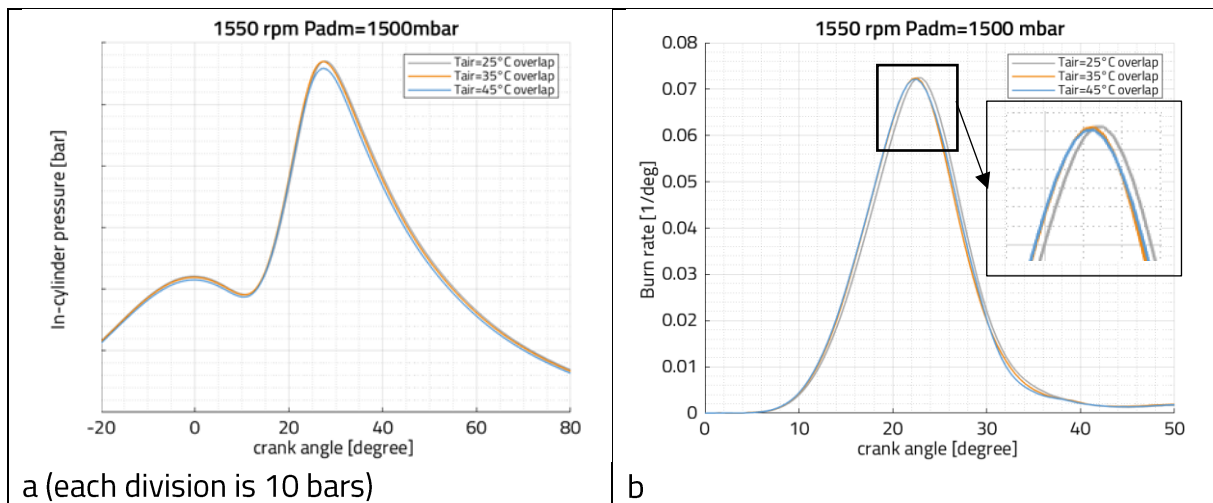


Figure 3-40: in-cylinder pressure (a) and burn rate (b) evolution with intake air temperature sweeps at 1550x1500 mbar overlapping and at 0 spark advance increase

As for the combustion development as in figure 3-40, decreasing the intake air temperature decreases a little bit the burn rate. This is only visible when the air temperature is decreased to 25°C.

The no-overlap case also follows the same trend. But when we see both cases together, the overlap and no-overlap case, the knock index is higher for the same spark advance in

no-overlap case when compared to the overlap case. In other words, the no-overlap case is more prone to knock and spark can be advanced more for the overlap case to fall on the same knock index.

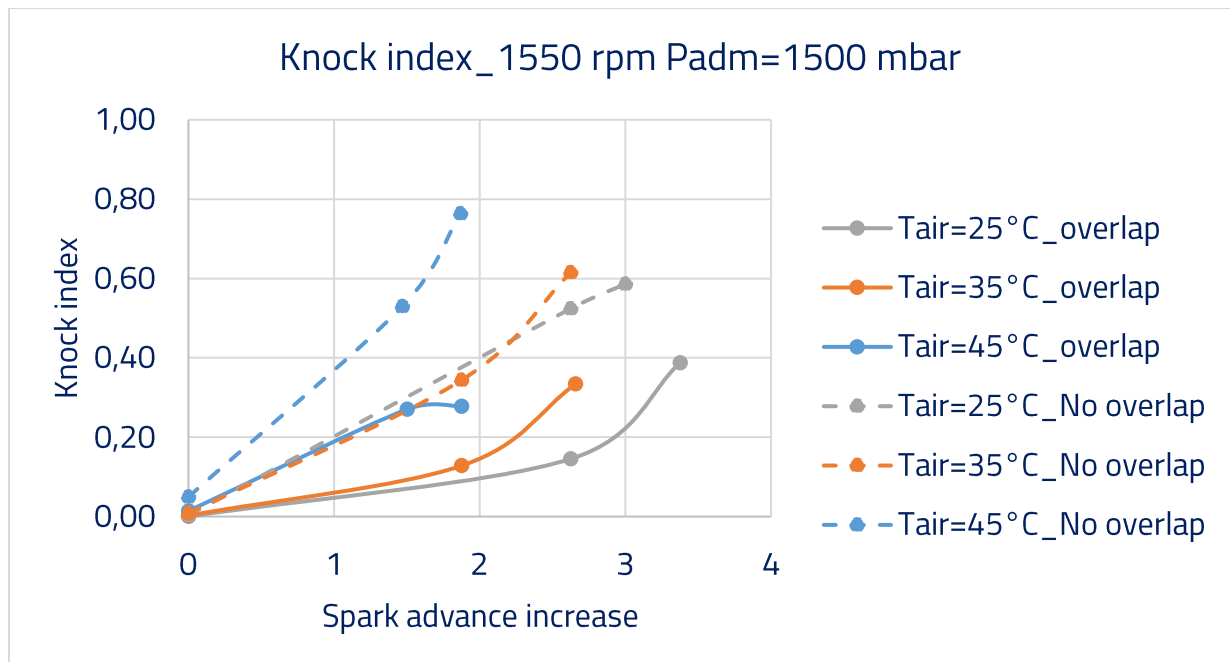


Figure 3-4 1: knock index evolution with spark advance increase for intake air temperatures sweep at 1550x1500 mbar for both overlapping and not overlapping settings

As it can be seen, the knock apparition for the intake temperature at 25°C without overlap is similar to the knock apparition for the intake air temperature at 45°C with overlap. In fact, this is due to burned gases trapped inside the cylinder as it was identified for this operating point. Overlapping valves increases the scavenging and clears the combustion chamber from residuals, however, not overlapping valves, increases the quantity of hot residuals which in turn increases the end gas temperature. The result identified here is that a margin of 20°C of the intake temperature can be achieved by overlapping the valves.

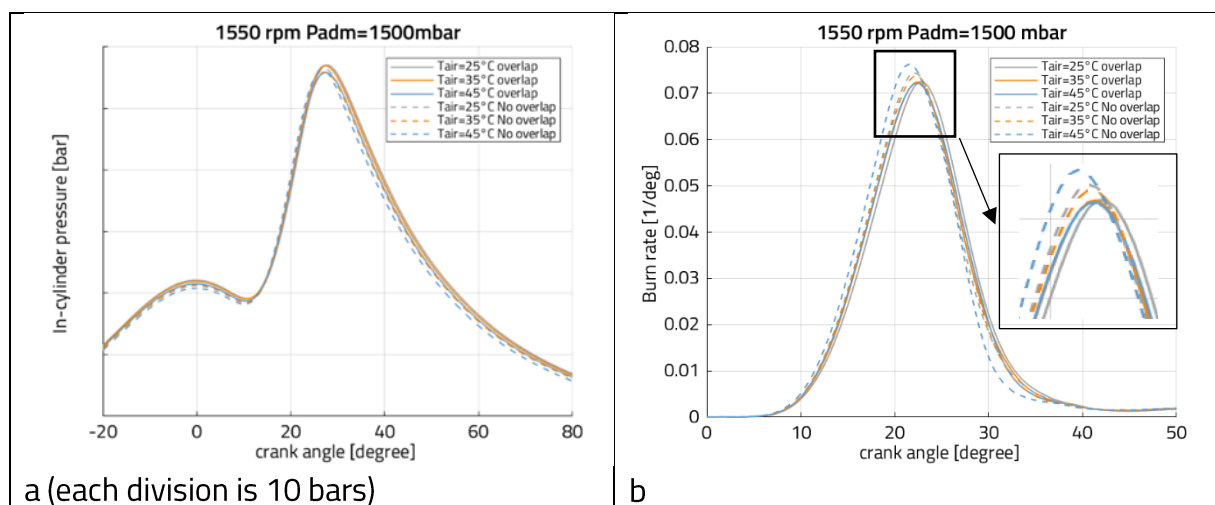


Figure 3-42: in-cylinder pressure (a) and burn rate (b) evolution with intake air temperature sweeps at 1550x1500 mbar and at 0 spark advance increase

Intake air temperature affect both the combustion development and the knock apparition.. Since the temperature inside the cylinder is lower, the flame propagates slowly inside the cylinder. Chen et al. [108] studied the effect of flame speed on knock. By using a swirl control valve, the turbulence inside the cylinder was modified. The higher turbulence resulted in high-speed flame propagation and thereby advancing the auto-ignition.

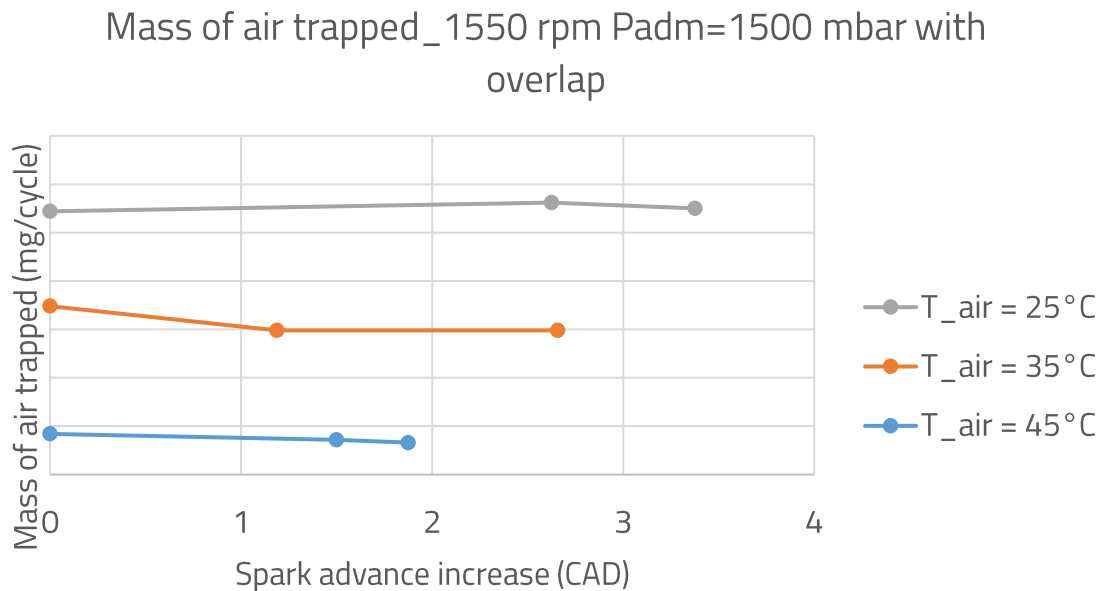


Figure 3-43: Mass of air trapped (each division is 5 mg/cycle) at 1550x1500 mbar with overlap

The reduction of inlet air temperature increases the density of the air. The increase in density results in increase in the mass of trapped inside the cylinder as in figure 3-43. Hence, the volumetric efficiency of the cylinder is increased. This led to some significant gains in the engine performance.

2 phenomena can be observed when increasing the intake air temperature:

- Increase the burn the rate of the combustion due to the higher mixture temperature.
- Decrease the burn rate of the combustion due to the reduced mass of air trapped

The increased burn rate could either accelerates the flame speed to consume the end gas before its auto-ignition or increase the in-cylinder pressure and help to compress more the end-gas reducing by that its auto-ignition delay and advancing knock apparition.

In the case of our study, increasing the intake air temperature increased the burn rates for both overlapping and non-overlapping settings as observed in figure 3-42. And this increase in burn rate increased the in-cylinder pressure, compressed the end-gas and advanced knock occurrence except for the no-overlap case when the air temperature increased from 25°C to 35°C. In that case, the increased burn rate and its effect of advancing knock apparition was compensated by the reduced air mass trap and its effect

on delaying knock apparition and the same behavior on knock apparition was observed in this case.

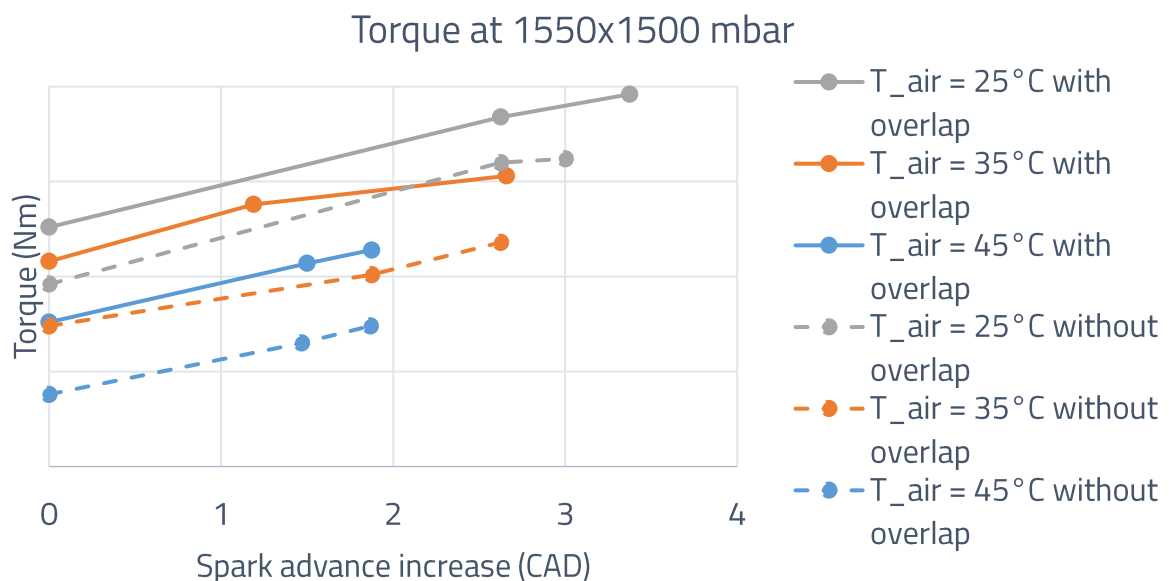


Figure 3-44: torque (each division is 5 N.m) at 1550x1500 mbar

From the figure 3-44, we can see that the torque is increasing when the inlet air temperature is reduced. This is due to increase in the mass trapped. When we compare overlap with no-overlap case, the overlap case has higher torque than the non-overlap case.

Hirooka et al. [109] showed that there is a spark timing at which maximum break torque can be achieved called MBT timing. There is also a spark timing beyond which any further advances in the spark timing will lead to knock. This spark timing is called KLSA. We have to always try to reach the MBT before we reach KLSA so that we can extract maximum torque from the combustion event. This can be done delaying the knock. More we delay the knock; spark can be advanced more to reach MBT. In case of no-overlap case, since the knock cannot be delayed due to high in-cylinder temperatures. Hence, the amount of spark that can be advanced is restricted. So, KLSA is reached before MBT which results in lesser torque when compared to overlap case.

As for the 2000x1700 mbar operating the same behavior was observed regarding the knock apparition with both overlapping and not overlapping conditions, however an opposite effect was observed at 2500x1700 mbar as it can be seen in the following figure 3-45

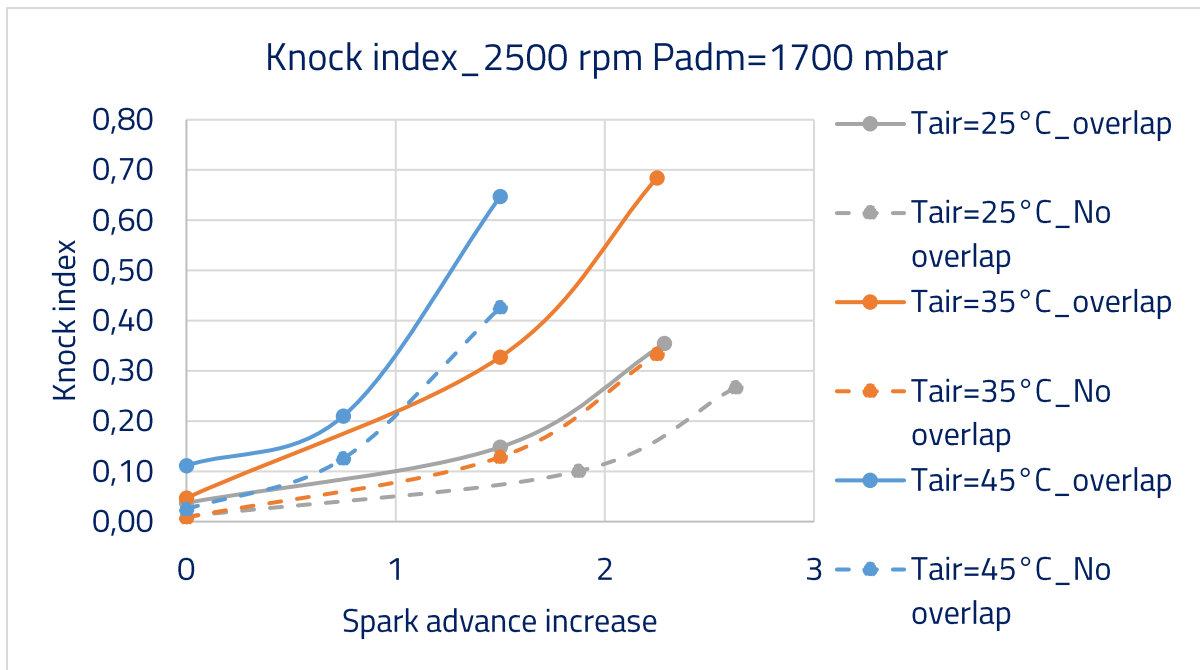


Figure 3-45: knock index evolution with spark advance increase for intake air temperatures sweep at 2500x1700 mbar for both overlapping and not overlapping settings

For 2500x1700 mbar operating point, not overlapping the valves delayed knock apparition as the in-cylinder mass confined inside the chamber was reduced. Reducing that confined is regarded as a load decrease: the combustion burn rate induced by the spark plug is slower, end gas is less compressed by the spark-induced flame which extends the auto-ignition delay and retards knock apparition when compared to overlapping settings as observed in figure 3-46.

Decreasing the intake temperature by 10°C leads to a gain in knock margin of almost 0.75 CAD of spark timing in the overlapping case and around 1 CAD in the no-overlapping case

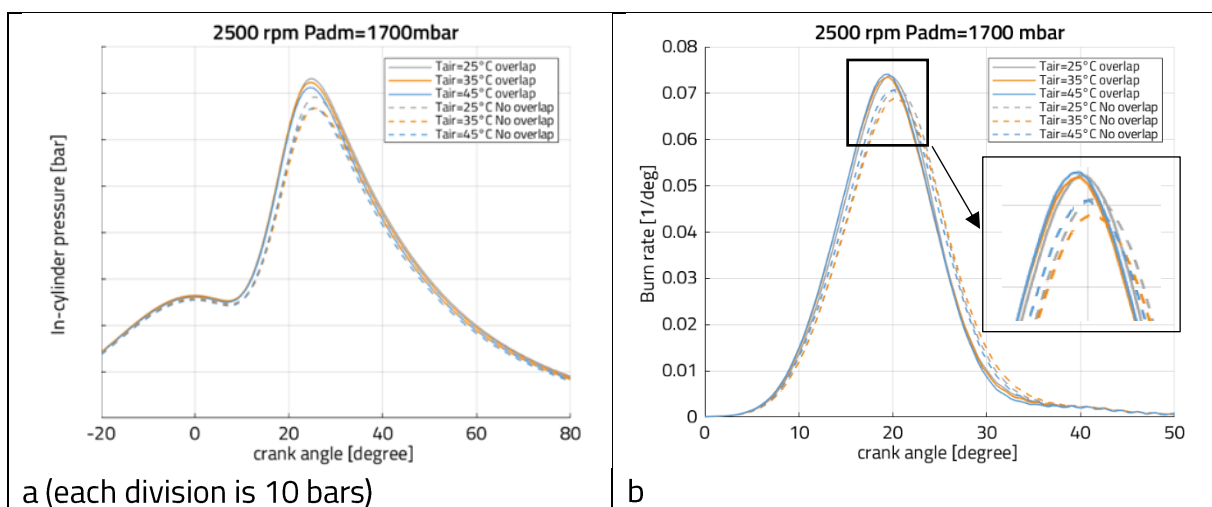


Figure 3-46: in-cylinder pressure (a) and burn rate (b) evolution with intake air temperature sweeps at 2500x1700 mbar and at 0 spark advance increase

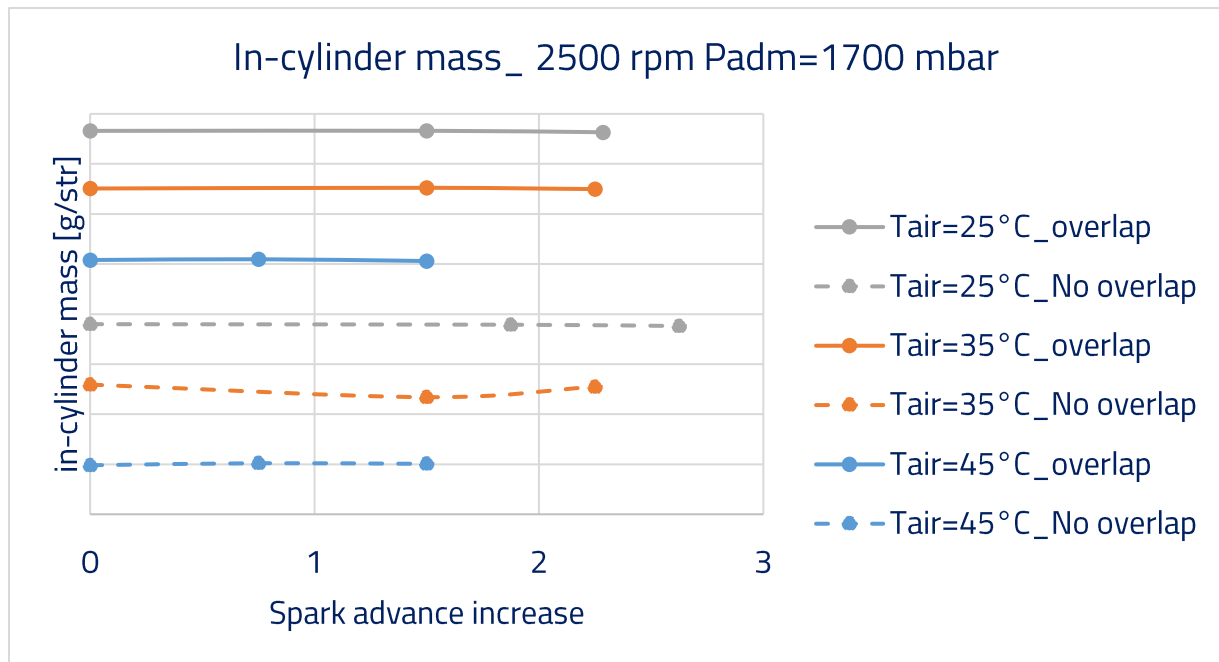


Figure 3-47: in-cylinder air mass (each division is 0.01 g/str) for intake air temperatures sweep at 2500x1700 mbar for both overlapping and not overlapping settings

In the figure 3-47, confined air mass is always lower for not overlapping case when compared to overlapping case at constant air temperature. And as intake temperature is increased, the confined air mass decreased as the air density decreases. In order to eliminate the effect of air mass variation with intake temperature, the same experiments were repeated at 35°C and 25°C with varying the admission pressure in a way to fall on the same air mass of 45°C setting according to figure 3-48.

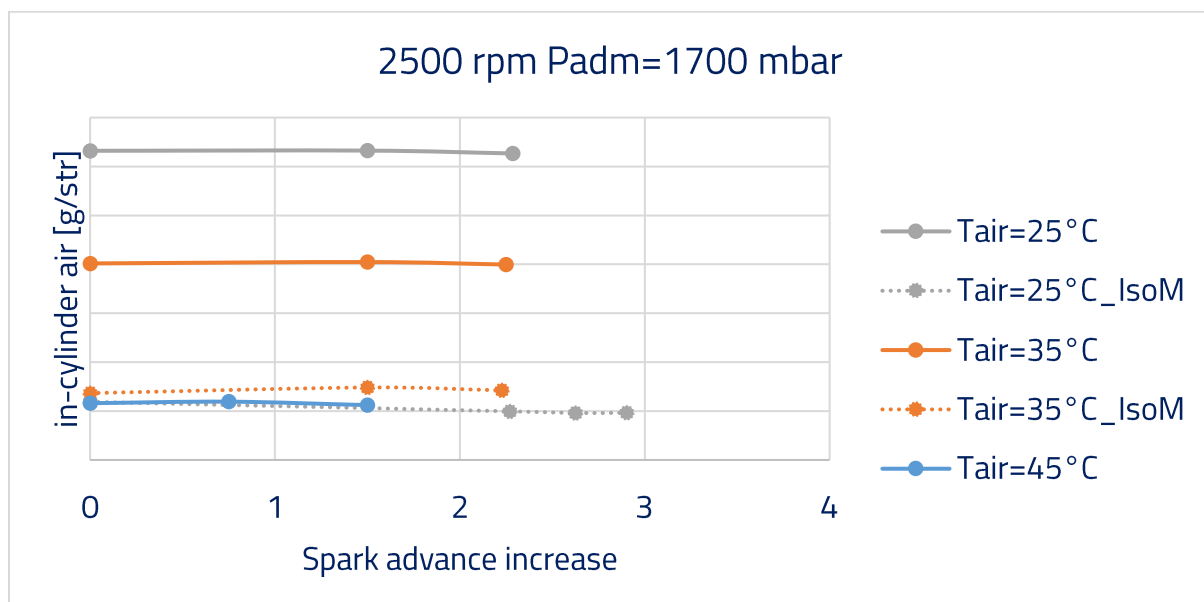


Figure 3-48: in-cylinder air mass (each division is 0.005 g/str) for intake air temperatures sweep at 2500x1700 mbar for iso mass settings

The resulting evolution of the knock index is presented in figure 3-49

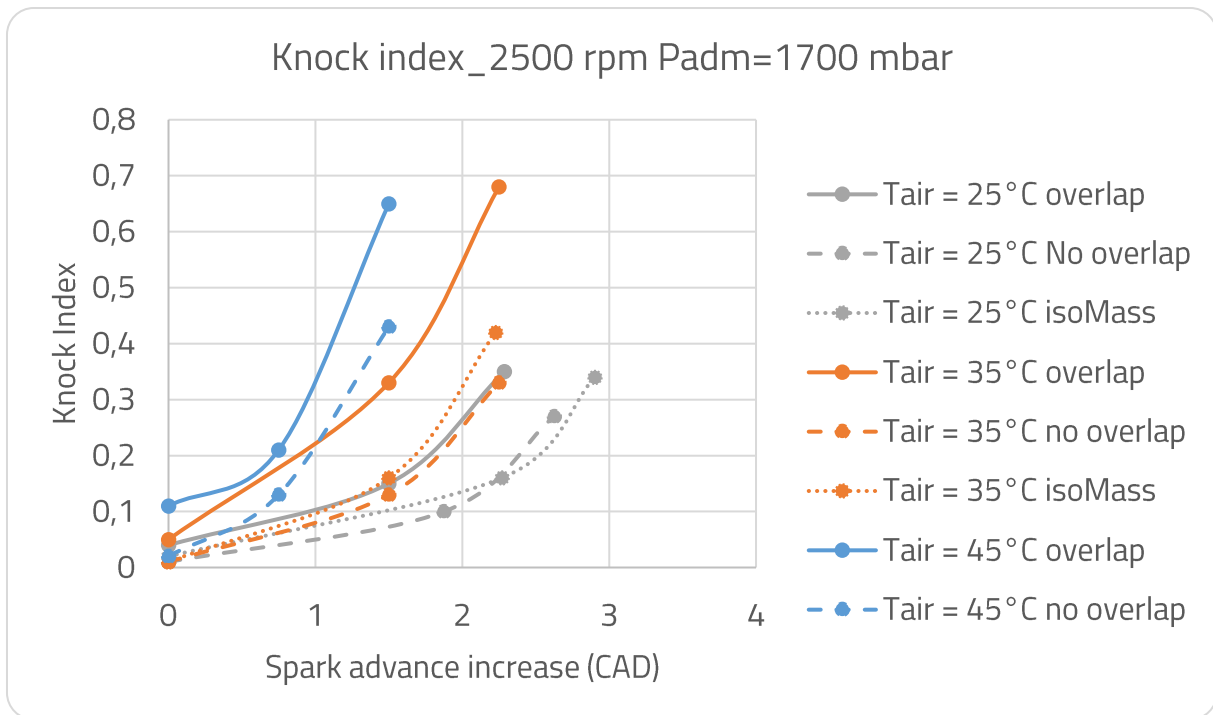


Figure 3-49: knock index evolution with spark advance increase for intake air temperatures sweep at 2500x1700 mbar for both overlapping and not overlapping and iso mass settings

Admission pressure at 25°C and 35°C were reduced to 1645 mbar and 1675 mbar respectively to fall on the same air mass as 45°C. Isomass cases were performed with overlapping valves. The impact of constant air mass is clear as the effect of intake temperature was put into evidence: as intake temperature is reduced the end-gas temperature is also reduced extending its auto-ignition delay and delaying knock apparition. In this cases, combustion development and the spark flame are no longer influenced by the intake temperature decrease. It can be seen that falling on the same air mass is similar to not overlapping the valves as in both cases, confined air mass is being reduced.

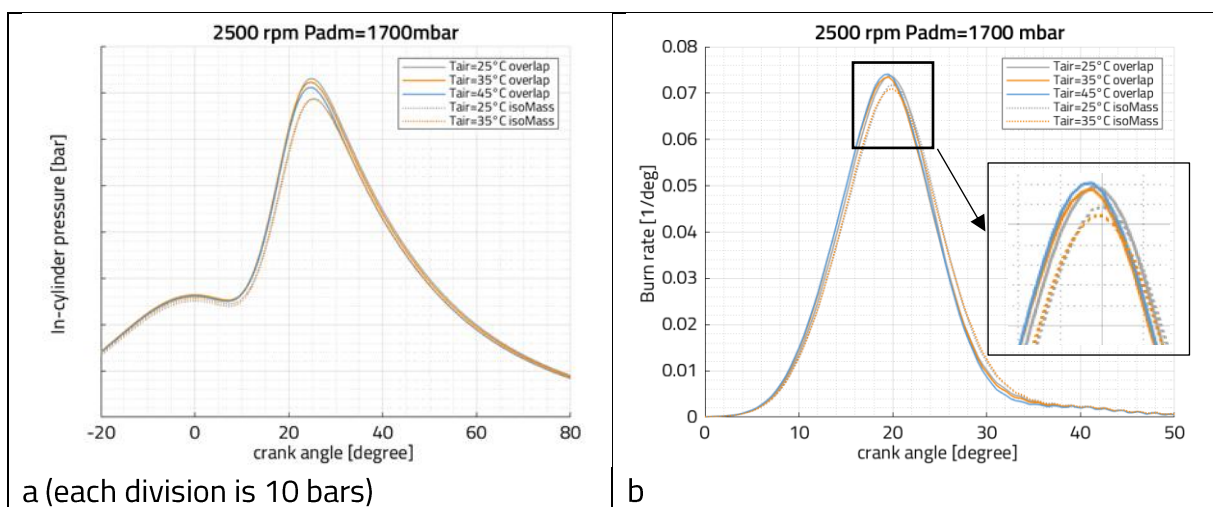


Figure 3-50: in-cylinder pressure (a) and burn rate (b) evolution with intake air temperature sweeps at 2500x1700 mbar and at 0 spark advance increase for both overlap and isomass settings

3.5.2. Conclusion of intake air temperature impact on knock occurrence

2 phenomena were observed when increasing the intake air temperature:

1. Increase the burn rate of the combustion due to the higher mixture temperature.
2. Decrease the burn rate of the combustion due to the reduced mass of air trapped

Across all the operating points, increasing the intake air temperature increase the knock apparition. This is due to the increased burn rate which increases the in-cylinder temperature and compresses the end-gas reducing by that its auto-ignition delay and advancing knock apparition. One exception was observed in the no-overlap case when the air temperature increased from 25°C to 35°C where the effect were compensated and knock index remained the same.

On the knock margin and on average, 0.75 CAD of spark timing can be achieved by a 10°C decrease of intake air temperature.

1550x1500 mbar and 2000x1700 mbar have a similar behavior when it comes to overlapping and not overlapping valves cases. In fact, overlapping valves delays knock apparition when compared to not overlapping valves. On these operating points, residuals are confined inside the cylinder when valves do not overlap which increase the end-gas temperature and shortens auto-ignition delay and increases the knock occurrence. The opposite effect is observed on 2500x1700 mbar as overlapping increases the confined air mass inside the cylinder when compared to no-overlap setting, increasing engine load and thus knock apparition

3.6. Impact of coolant and lubricant oil temperatures on knock occurrence

In the preliminary combustion campaign, it was put into evidence that coolant and oil temperatures affect combustion development. Two opposing effects were identified: as cylinder walls get colder, the burn rate is either faster if the in-cylinder mass is increased due to higher density, or the burn rate is slower as the initiation of the combustion is affected by cold surroundings. In this section, the effect of coolant and oil temperatures on knock apparition will be studied on the three operating points 1550x1500 mbar, 2000x1700 mbar and 2500x1700 mbar.

3.6.1. Knock index evolution with coolant and oil temperatures sweep

For each coolant and oil temperatures setting and for each operating points, 3 values of spark advances were swept in the same manner as the injection strategy and intake air temperature

For the 1550x1500 mbar, the coolant and oil temperatures sweep are presented in table 3-4

Tadm	Padm	T coolant	T oil	setting
°C	mb	°C	°C	
30	1500	85	90	1
		85	60	2
		60	60	3
		60	40	4
		40	40	5

Table 3-4: coolant and oil temperatures sweep at 1550x1500 mbar

5 different coolant and oil temperatures settings were tested with coolant temperature going from 85°C to 40°C and oil temperatures going from 90° till 40°C. knock index evolution with spark increase are plotted on the same graph for all of the 5 settings in figure 3-51

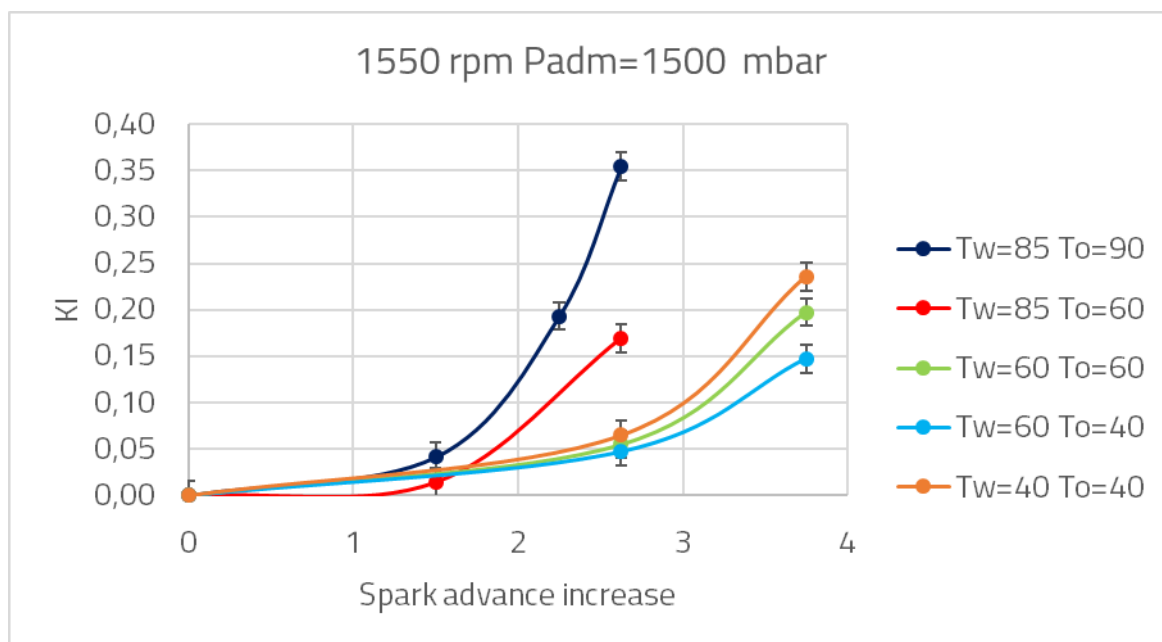


Figure 3-51: knock index evolution with spark advance increase for coolant and oil temperatures sweep at 1550x1500 mbar

The highest coolant and oil temperatures setting (Tw=85°C, To=90°C) is the most prone to knock when compared to other settings. End-gas is closer to cylinder walls and colder walls increases the heat transfer which decrease the end-gas temperature and increases its auto-ignition delay. As it can be seen, the end-gas temperature is only affected by coolant

temperature. The knock apparition is thus a competition between the spark-induced flame and end-gas auto-ignition. When coolant temperature was decreased to 60°C, the increase in auto-ignition delay wins over the increase of in-cylinder mass thus the Tw=60°C, To=60°C setting wins over the Tw=85°C, To=60°C setting. The opposite effect is observed for the coldest setting (Tw=40°C, To=40°C), colder walls increase the burn rate of the spark-induced combustion, even though the end-gas temperature is decreased, its auto-ignition is advanced due to a faster compression by the spark-induced flame in that case which increases the knock apparition when compared to both Tw=60°C, To=60°C and Tw=60°C, To=40°C settings as seen in figure 3-52. In these experiments, 1.5 CAD of spark timing are achieved on the knock margin with a coolant decrease of 25°C from 85°C to 60°C

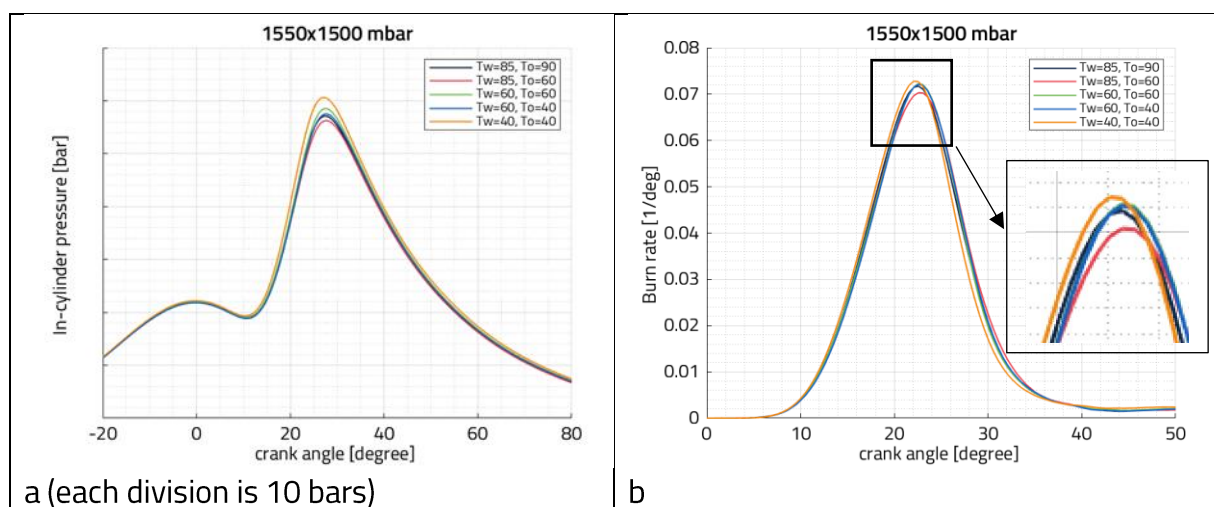


Figure 3-52: in-cylinder pressure (a) and burn rates (b) of the 5 settings of coolant and oil temperatures at 0 spark advance increase for 1550x1500 mbar

The same experiment was also performed at 2000x1700 mbar and 2500x1700 mbar.

At 2500x1700 mbar, the coolant and oil temperatures sweep are presented in table 3-5.

Tadm	Padm	T coolant	T oil	setting
°C	mb	°C	°C	
37	1700	85	90	1
		85	60	2
		60	60	3
		60	40	4
		40	40	5

Table 3-5: coolant and oil temperatures sweep at 2500x1700 mbar

5 different coolant and oil temperatures settings were tested with coolant temperature going from 85°C to 40°C and oil temperatures going from 90° till 40°C. Knock index evolution with spark increase are plotted on the same graph for all of the 5 settings in figure 3-53

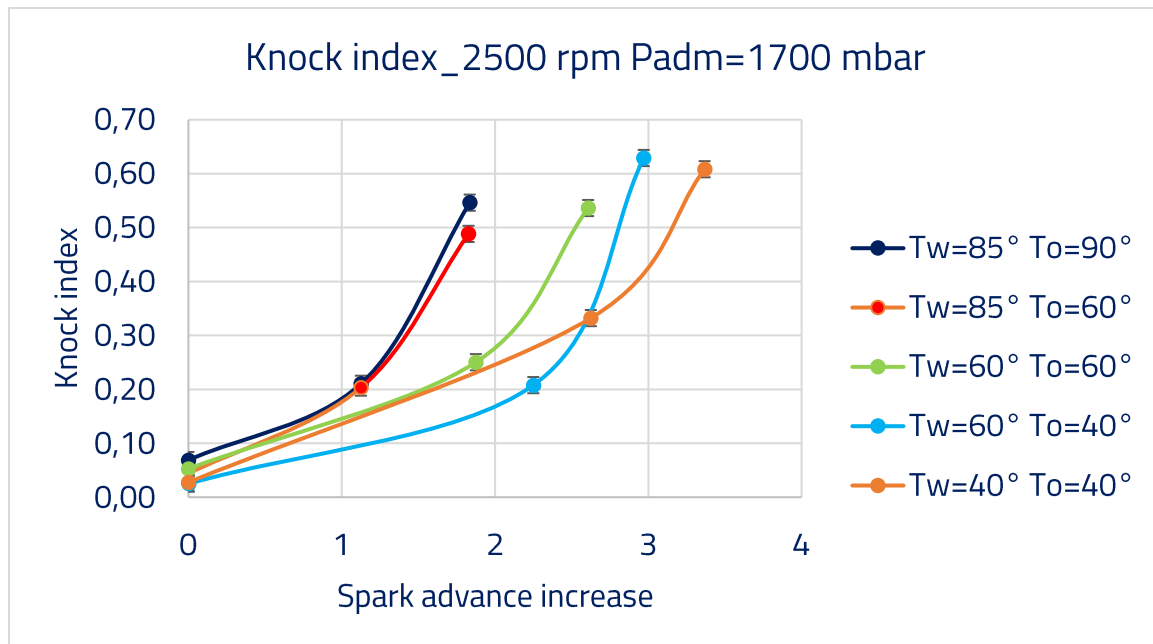


Figure 3-53: knock index evolution with spark advance increase for coolant and oil temperatures sweep at 2500x1700 mbar

The same results as for 1550x1500 mbar are obtained for 2500x1700 mbar. Decreasing coolant temperature from 85°C to 60°C delayed knock apparition so setting 3 delayed knock when compared to setting 2. Decreasing coolant temperature from 60°C to 40°C also delayed knock apparition even though it might seem the opposite in the intermediate spark advance increase: setting 5 delays knock when compared to setting 4. Oil temperature decrease had a smaller influence than 1550x1500 mbar especially when it was decreased from 90°C to 60°C: setting 1 and 2 show a similar behavior on knock apparition, however, it is much more pronounced between setting 3 and 4. At 2500x1700 mbar, 1 CAD of spark timing is achieved on the knock margin with a coolant decrease of 25°C from 85°C to 60°C

In order to eliminate the effect of cold walls on in-cylinder mass, the same settings of coolant and oil temperatures were performed but this while maintaining the in-cylinder mass constant. To do so, the admission pressure was modified to fall on the same in-cylinder mass as it can be seen in table 3-6:

T adm	P adm	T coolant	T oil	setting
°C	mb	°C	°C	
37	1700	85	90	1
	1695	85	60	2
	1670	60	60	3
	1670	60	40	4
	1640	40	40	5

Table 3-6: coolant and oil temperatures sweep at 2500x1700 mbar while maintaining the in-cylinder mass constant

As it was observed in the preliminary study, coolant temperature decrease only affected the in-cylinder mass as the admission pressure had to be decreased in order to maintain the in-cylinder mass constant. When the oil temperature was decreased at constant coolant temperature, the admission pressure had not to be decreased to fall on the same in-cylinder mass.

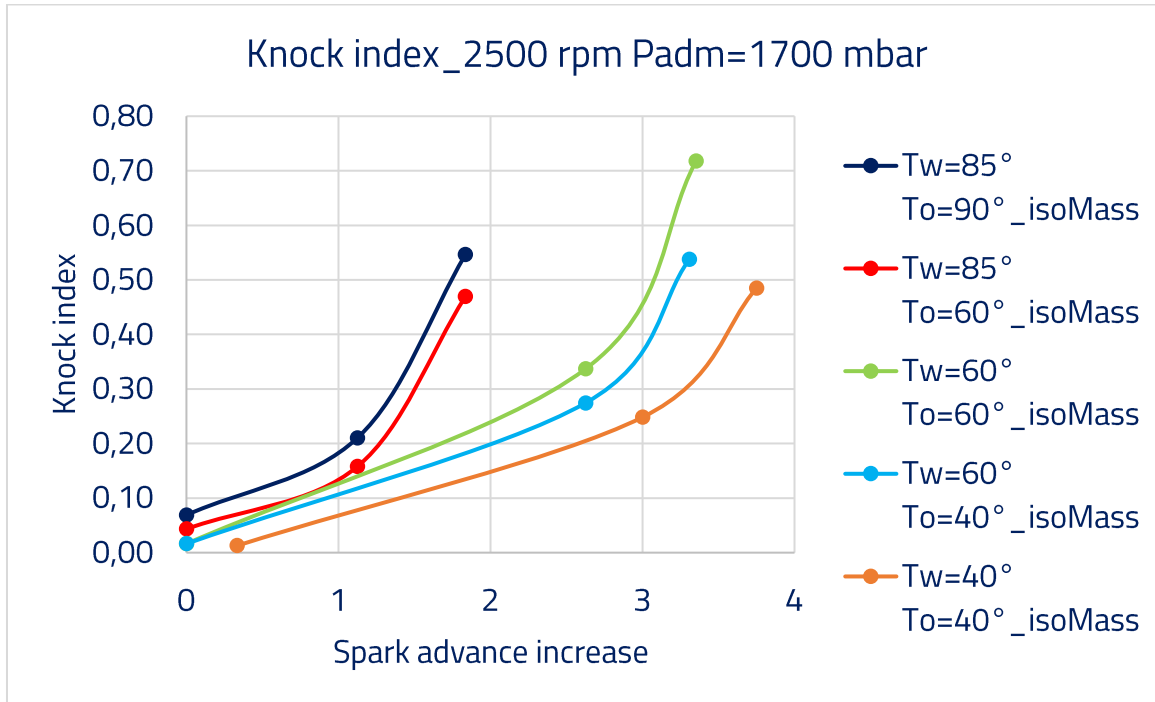


Figure 3-54: knock index evolution with spark advance increase for coolant and oil temperatures sweep at iso mass conditions at 2500x1700 mbar

The effect of cold wall is clearly put into evidence in that case: decreasing coolant temperature was compensated by a decrease in admission pressure and the combustion development is thus identical as it can be seen in figure 3-54. In that case, knock apparition is only influenced by end gas temperature that gets colder which increases its ignition delays and retards knock apparition. This is observed between settings 2 & 3 and settings 4&5. Oil temperature had a little or no effect on in-cylinder mass, it only slowed down the burn rate and the same effects on knock apparition are observed as in figure 3-55.

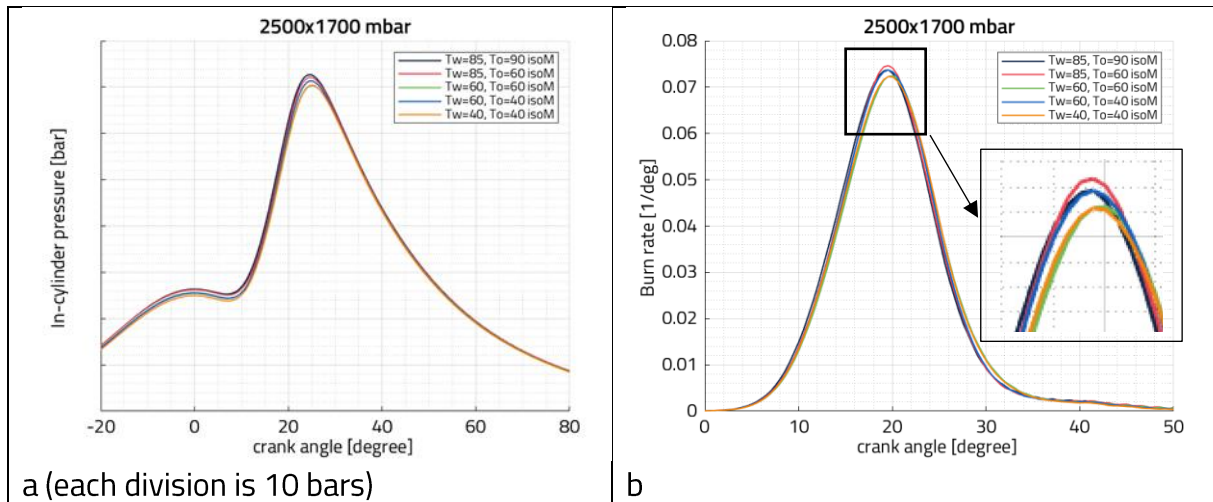


Figure 3-55: n-cylinder pressure (a) and burn rates (b) of the 5 settings of coolant and oil temperatures at 0 spark advance increase for 2500x1700 mbar

With in-cylinder mass maintained constant, combustion development is identical between settings 2&3 and settings 4&5. These results are compatible with those observed by Cho et al. as they separated head and the liner coolant effect and they achieved 0.2, 0.12 and 0.11 CAD of ignition timing advance per coolant unit decrease of simultaneous cooling, head cooling and liner cooling respectively at 1500 rpm [110].

3.6.2. Conclusion of coolant and oil temperatures impact on knock occurrence

Two opposing effects are observed when coolant temperature is decreased:

1. The air mass trapped inside the cylinder increases which subsequently increase the burn rate
2. The burn rate decreases due to colder wall temperatures

Two opposing effect are observed when the burn rate increases:

1. The spark-induced flame speed increases which subsequently consumes the end mixtures before it auto-ignites and thus knock is delayed.
2. The in-cylinder pressure rises higher and compresses and heats more the end-gas and reduces its auto-ignition delay and thus knock is advanced.

In our study, the same behavior was observed on the operating points, decreasing coolant temperature led to faster burn rate which consumed the end-gas before its auto-ignition and delayed knock apparition. One exception was observed at 1550x1500 rpm when coolant temperature decreased from 60° to 40° C, the faster burn increased the in-cylinder pressure, compressed the end-gas, reduced its auto-ignition delay and advanced knock.

Decreasing oil temperatures did not affect the combustion development nor the knock occurrence as the coolant temperature sweep.

3.7. Conclusion on the experimental results

The various parametric studies carried out have highlighted the complexity of the knocking phenomenon. A variation of a control parameter often has opposite effects on the occurrence of knock, such as increasing the spark-induced flame speed (favorable to repelling the knock) but also a reduction in the time required for the auto-ignition of the fresh mixture. The occurrence of knocking is also highly dependent on wall temperatures.

Modeling the onset of knock should therefore be able to predict these various phenomena with sufficient precision.

Les différentes études paramétriques menées ont mis en exergue la complexité du phénomène de cliquetis. Une variation d'un paramètre de contrôle a souvent des effets opposés sur l'apparition du cliquetis, comme par exemple l'augmentation de la vitesse de flamme (plutôt favorable à repousser le cliquetis) mais aussi une réduction du temps nécessaire pour l'auto-inflammation du mélange frais. L'apparition du cliquetis est par ailleurs fortement dépendante des températures de parois.

La modélisation de l'apparition du cliquetis devra donc être en mesure de prédire avec suffisamment de précision ces différents phénomènes.

4. Knock modeling and simulations

The fourth chapter deals with the modeling of the onset of the knock in the context of a OD-1D modeling of a complete engine intended to be used in the pre-calibration or even calibration of the powertrain phases.

First, a bibliographical review of the main phenomenological models of knock is carried out. It highlights the often succinct description of the calibration methodology of the models presented. In addition, it leads to the choice of two models to be tested and compared.

In a third section, the model considered to be the most predictive is tested more exhaustively and compared to the results of the test campaign presented in the previous chapter, in terms of critical spark advance and knock index.

Le quatrième chapitre porte sur la modélisation de l'apparition du cliquetis dans le cadre d'une modélisation OD-1D d'un moteur complet destinée à être utilisée en phases de pré-calibration voire de calibration de la chaîne de traction.

Tout d'abord, une revue bibliographique des principaux modèles phénoménologiques de cliquetis est menée. Elle met en évidence la description souvent succincte de la méthodologie de calibration des modèles présentés. Par ailleurs, elle conduit au choix de deux modèles pour être testés et comparés.

Dans une troisième section, le modèle jugé le plus prédictif est testé de manière plus exhaustive et confronté aux résultats de la campagne d'essais présentée au chapitre précédent, en termes d'avance à l'allumage critique et d'indice de cliquetis.

4.1. Review of knock models

Auto ignition of a gaseous mixture of fuel and air occurs when the chemical energy released by the reactions as thermal energy is larger than the thermal energy lost to the surroundings by heat transfer. Hence, the temperature of the mixture increases rapidly due to the exponential temperature dependence of the rates of the chemical reactions involved. According to Heywood[21], the state at which such spontaneous ignition occurs is often characterized by the self-ignition temperature and the resulting self-accelerating event where the gas pressure and temperature increase rapidly is termed a thermal explosion.

Phenomenological engine cycle simulation has proven its worth to be a powerful tool in both optimizing conceptual design and reducing calibration efforts in the development of spark-ignition engines. Either way, a large number of variables including both design and operation parameters must be optimized to minimize fuel consumption and maximize efficiency and output power. If their effects on knock were not taken into account at full throttle (WOT), optimization based on cycle simulation leads to unacceptable and even misleading errors. Consequently, a predictive knock model in engine simulation is essential[111].

The most accepted theory of knock is the autoignition of the end gas. In the literature, knock models based on the end-gas autoignition are divided into three categories:

- Detailed chemical kinetic mechanisms
- Simplified chemical kinetic mechanism
- Phenomenological models based on the Arrhenius expression

Detailed chemical kinetic mechanisms are generally associated with zero-dimensional or quasi-dimensional combustion models. With advances in computer technology, recent simulations of detailed chemical kinetics coupled with three-dimensional computational fluid dynamics (3-D CFD) have appeared to study knock combustion. Changes in local thermodynamic states, including pressure, temperature, and velocity, as well as species concentrations, could be assessed and knock onset locations could be predicted with detailed chemical reactions and 3D CFD simulation. However, a detailed chemical kinetic mechanism of gasoline substitutes typically includes hundreds of species and thousands of elemental reactions which increases the computational cost and restricts its application when coupled with 3D CFD calculations. Efforts have also been made on the use of simplified chemical kinetics. For example, Shu et al. incorporated a reduced chemical reaction mechanism and the pressure wave equation into a 3D CFD code. Their calculations indicated that high-frequency pressure oscillations can characterize the knock onset and quantify its intensity accurately [101]. However, even with the reduced mechanism, the mesh sizes, and time step in 3D-CFD calculations must be small enough to simulate the pressure wave and analyze the knock characteristics, resulting in a very computational cost.

Such a cost does not apply to the optimization of several variables and objects [111] [112] [113]

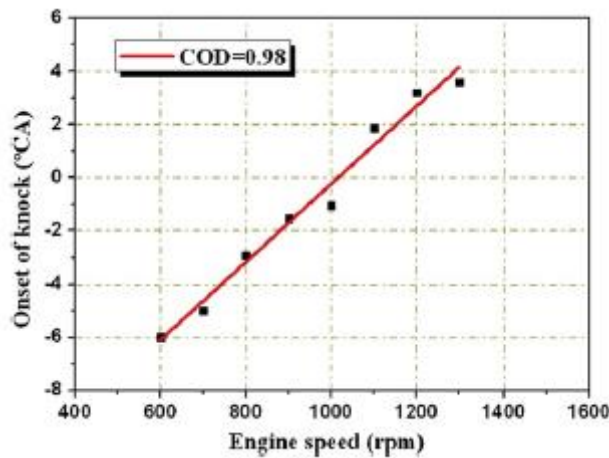


Figure 4-1: the correlation between knock onset and engine speed according to Shu et al.[101]

As for the phenomenological models, they involve a one-step reaction instead of detailed (or reduced) chemical kinetics. These models are described by the Arrhenius equation of the ignition delay τ :

$$\tau = C_1 \cdot P^{-C_2} \cdot e^{\frac{C_3}{T}}$$

P and T are respectively the pressure and the temperature of the end gas, C_1 , C_2 and C_3 are calibrating coefficients. According to Livengood and Wu, the auto-ignition of end gas (or knock onset) is defined as the moment when the concentration $[X]$ of certain species X , reaches a critical concentration $[X]_c$. Assuming that the reaction rate does not change with time during a fixed state process, the averaged production rate of X during the induction period is written as [68]:

$$\frac{d[X]}{dt} = \frac{[X]_c}{\tau}$$

In the case of spark-ignition 4 stroke engines, a predictable knock model, also known as the Livengood-WU integral can be obtained by simply integrating the equation from the intake valve closing to the knock onset.

$$1 = \int_{t_0}^{t_{knock}} \left(\frac{1}{\tau} \right) dt$$

Where t_0 refers to the start of calculation (IVC) and t_{knock} to the time of the knock onset. Thus, knock occurs when the integral is equal to 1.

These phenomenological models are widely used in knock prediction in engine simulation due to their simplicity and their low computational cost. The best known is the Douaud & Eyzat correlation defined as the following[114]:

$$\tau = C_1 \cdot \left(\frac{ON}{100}\right)^{C_2} \cdot P^{-C_3} \cdot e^{\frac{C_4}{T}}$$

Here ON is the octane number and, $C_1 = 17.69$, $C_2 = 3.402$, $C_3 = 1.7$ and $C_4 = 3800$

The Douaud&Eyzat model has been employed by many researchers without any modification such as Mittal et al. [115], Kasseris et al[116]. and Kim et al[117]. Kasseris et al. adapted the correlation of Douaud for use with higher ethanol content in fuel blends by adjusting the octane number in calibrating the C_2 coefficient. Kim et al. evaluated three different knock calculation methods and found that the ignition delay approach calibrated by Douaud was as accurate as the other and is less computationally expensive.

Other researchers recalibrated the coefficients in the Douaud& Eyzat approach [118], [119], [120],[121], [122], [123]. However Elmqvist did not take the octane number contribution into account. [124]

Douaud & Eyzat correlation does not account for the EGR and the fuel-to-air equivalence ratio, thus it could be less accurate when simulating engine cycles with EGR and fuel enrichment. Some researchers included these parameters in their correlation as they not only have a thermal effect on the knock onset but also a chemical effect on the apparition of knock. Soylu included the propane ratio and equivalence ratio in his correlation but he disregarded the EGR [125].

In the following, a summary of different works achieved on the ignition delay knock integral based correlation is presented.

Authors	Model correction
Douaud [114] Mittal [115] Kasseris [116] Kim [117]	$\tau = 17.68 \left(\frac{ON}{100}\right)^{3.402} \cdot P^{-1.7} \cdot e^{\frac{3800}{T}}$
Wayne[118][119]	$\tau = 0.389 \left(\frac{ON}{100}\right)^{7.202} \cdot P^{-1.15} \cdot e^{\frac{5200}{T}}$
Worret [120]	$\tau = 0.0187 \left(\frac{RON}{100}\right)^{3.402} \cdot P^{-1.7} \cdot e^{\frac{3800}{T}}$
Elmqvist [124]	$\tau = 0.021 \cdot P^{-1.7} \cdot e^{\frac{3800}{T}}$
Burluka [121]	$\tau = 0.01869 \left(\frac{ON}{100}\right)^{3.4017} \cdot P^{-1.7} \cdot e^{\frac{3800}{T}}$
Syolu [125]	$\tau = 0.985 \cdot P^{-0.887} \cdot e^{\frac{f(\phi,PR)}{T}}$

Table 4- 1: summary of the some models and their correlation

Syed et al. involved the dilution effect explicitly in their correlations [126]

$$\tau = C_1 \cdot (1 + X_d)^{C_2} \cdot P^{-C_3} \cdot e^{\frac{C_4}{T}}$$

and Hoepke et al. involved the EGR explicitly in their correlations [46]

$$\tau = 8.49 \cdot 10^{-5} \cdot (1 - X_{EGR})^{0.8881} \cdot P^{-1.343} \cdot e^{\frac{5266}{T}}$$

Vancoillie et al. included both the dilution factor X_d and the equivalence ratio φ explicitly in their correlation. [127]

$$\tau = C_1 \cdot \varphi^{C_2} (1 + X_d)^{C_3} \cdot P^{-C_4} \cdot e^{\frac{C_5}{T}}$$

C_1, C_2 depend on the temperature range and C_3, C_4, C_5 are polynomial functions

The kinetics fit model is based on the reduced chemical kinetic model for internal combustion engine combustion simulations developed by Ra et al. [128]:

The induction time is defined by the following expression for Kinetics Fit model is:

$$\tau_j = M_1 a_i \left(\frac{ON}{100} \right)^{b_i} [Fuel]^{c_i} [O_2]^{d_i} [Diluent]^{e_i} e^{\left(\frac{f_i}{M_2 T} \right)} \quad j = 1, 2 \text{ and } h$$

M_1 and M_2 are the knock induction time multiplier and the activation energy multiplier respectively. ON is the fuel octane number, $[Fuel]$, $[O_2]$ and $[Diluent]$ are concentrations expressed in mol/m³. The diluent concentration is the sum of the N_2 , CO_2 and H_2O concentrations. a_i to f_i are models constants whose values are displayed in table 4-2

i	a	b	C	d	e	f
1	4.445E-7	3.613	-0.64	-0.564	0.3978	12920
2	11941.423	3.613	-0.64	-1.4596	0.4867	-1957
3	8.905E-7	0	-0.25	-0.547	0	16856

Table 4-2: values of the Kinetics Fit model constant

The Kinetics Fit model take into account the NTC regime and the overall knock induction time is thus calculated by:

$$\frac{1}{\tau} = \frac{1}{\tau_1 + \tau_2} + \frac{1}{\tau_h}$$

In fact, experimentally, the temperature of the end gas in an engine can only be estimated by measuring the velocity of propagation of sound. However, it can be calculated using the thermodynamic equations but inaccurate results could be obtained due to uncertainties in the end gas volume and large heat transfer effects. As it was seen, auto ignition is widely modeled in the function of pressure, temperature, and time using the Livengood-Wu (LW)

integral [68]. The equation represented by Livengood-Wu has restrictive assumptions and doesn't work properly with complex fuel chemistry and with the fuels that depend on the temperature due to cool flame or what we call Negative Temperature Coefficient (NTC).

In the NTC regimes, there are three stages: low, intermediate, and high-temperature range as it can be seen in figure 4-2. For the low and high temperatures, the ignition delay is shortened as the temperature increases. For the intermediate stage which is known as the NTC region, the opposite effect is observed and the ignition delay decreases as the temperature increases.

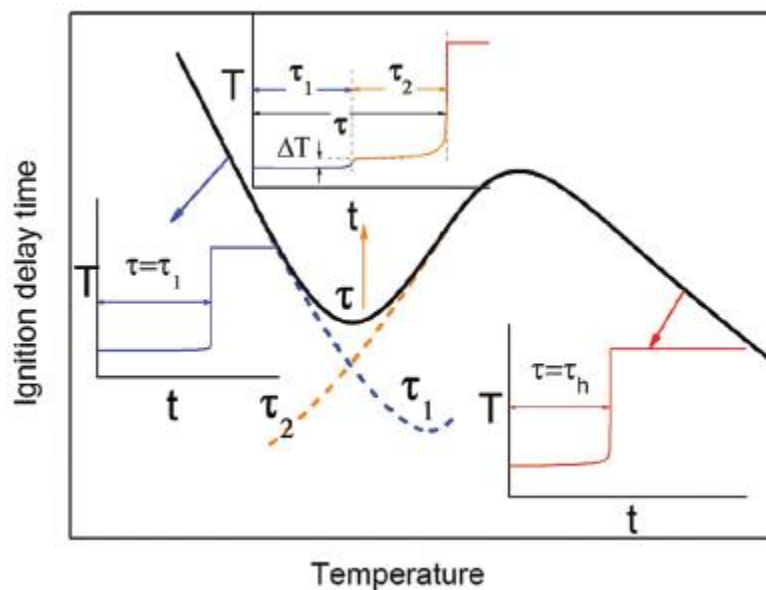


Figure 4-2: schematic showing the NTC behavior and typical temperature histories of low-temperature, NTC and high-temperature auto-ignition regimes [129]

The reason behind this limitation of the LW integral is that there's a change in the chemistry of the mixture and the temperature after the first stage. The 2 stage NTC region splits the L-W integral into two integrals and the ignition delay time is calculated for the first and the second stage. The reason for that is that the mixtures thermodynamic state defined by the temperature and the pressure changes after the first stage and therefore a new ignition delay time should be calculated using the new temperatures and pressures [130]. The entire auto ignition process in the NTC regime proceeds into two stages: low-temperature chemistry involving large oxygenated species and medium to high chemistry involving small species. The ignition time depends on the pressure and the equivalence ratio. The higher the pressure or the equivalence ratio, the higher the temperature difference between the 2 NTC regions [129]. The plateau length of a hot spot and its temperature gradient affect the auto ignition possibility. The steeper the temperature gradient, the larger the plateau region should be to cause detonation [131]

In figure 4-3, in the case of a relatively low initial temperature, autoignition of the mixture occurs in a two-stage behavior. After an induction period $t = \tau_1$, the auto-ignition process reaches a first ignition delay shorter than $\tau = \tau_1 + \tau_2$. At this instant $t = \tau_1$, the chemical activity in the air-fuel mixture produces a pale blue cool flame [132]. This cool flame is characterized by a small consumption of the air-fuel mixture and a small temperature ΔT increase that generally does not exceed 200K [132] [133]. Afterwards, the reactions are accelerated for $t > \tau_1$ by heat added to the reacting system and the generated species. This cool flame is thus followed by a second stage of auto-ignition at $t = \tau_1 + \tau_2$ that corresponds to the highly exothermic main auto-ignition [134]

Moreover, in the case of a relatively high initial temperature, autoignition occurs in a single-stage after a delay $t = \tau_h$. The high-temperature chemistry drives the reaction system [129] [131] [135]

The overall knock induction time is thus calculated by:

$$\frac{1}{\tau} = \frac{1}{\tau_1 + \tau_2} + \frac{1}{\tau_h}$$

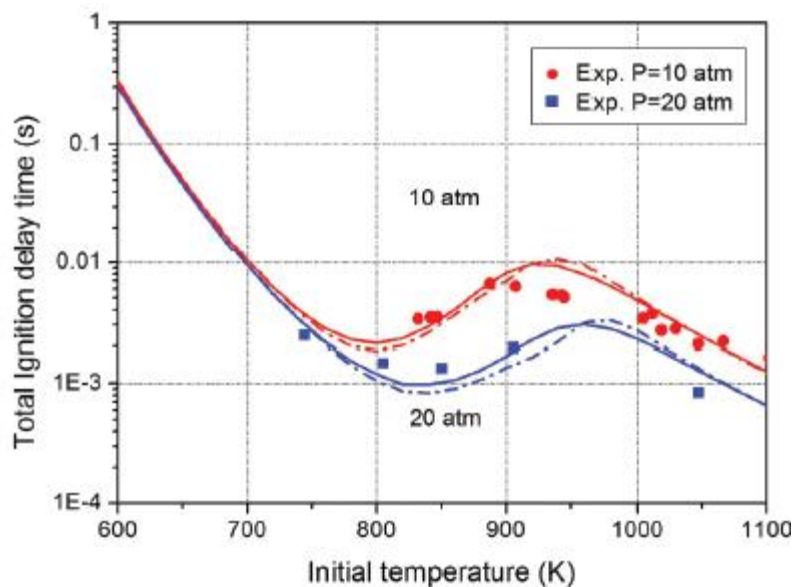


Figure 4-3: Comparison between detailed chemical kinetic calculations (line) and combined global expressions (dash-dot) for the ignition delays of stoichiometric n-heptane/air mixture under 10 (red) and 20 (blue) atm [129]

As it can be seen in figure 4-3, a good agreement between the global expression and detailed kinetics are obtained for the entire ignition delay throughout both stages [129]. In this figure, we can see that the NTC region ($750\text{K} < T < 950\text{K}$) results from the two stage ignition process, and corresponds to a transition between low- and high-temperature

Auto-ignitions types are identified using two non-dimensional numbers: the non-dimensional time ε which is the ratio of the acoustic time to the excitation time and the non-dimensional gradient of temperature ξ [136].

$$\varepsilon = \frac{r_0/a}{\tau_e}$$

$$\xi = \frac{a}{u_a}$$

Where r_0/a is the residence time of the pressure wave travelling at the sound speed a in the hot spot of of initial radius r_0 and τ_e rate to go from 5% to the maximum heat release by auto-ignition, u_a hotspot propagation velocity [136]

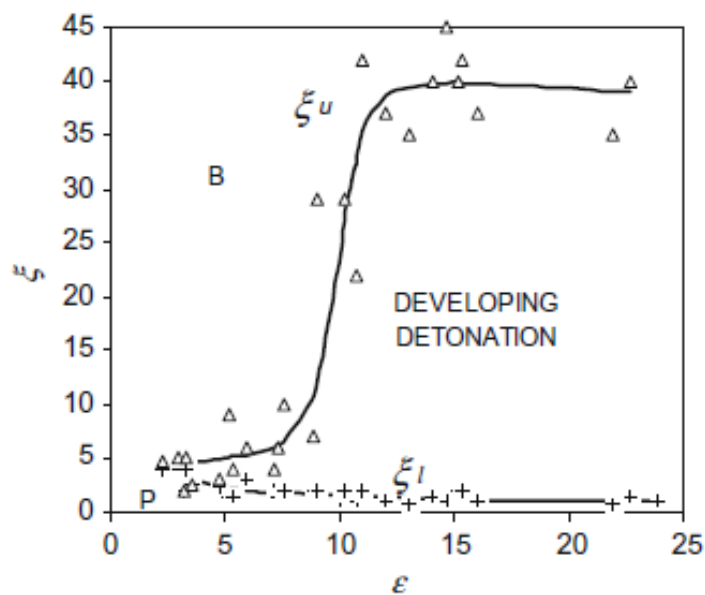


Figure 4-4: Developing detonation peninsula on plot of ξ against ε [28][137]

The detonation development regime caused by the concentration non-uniformity is similar to the one caused by the temperature gradient. The ignition delay time decreases with the increase of the equivalence ratio. When the reaction front speed u_a is close to the local speed of sound a , the chemical reaction and pressure wave are coupled and therefore reach the Chapman-Jouguet detonation speed and cause detonation. Detonation development is characterized by 2 parameters: The non-dimensional time ε and the non-dimensional gradient of equivalence ratio ξ . A third parameter $\eta = \xi\varepsilon$ is added which represents the ratio of the heat release rate and the speed of the reaction front propagation. For a small value of η , there's no detonation and there's a critical value η_c which leads to detonation [138].

Because of species and thermal diffusion, a developing detonation is not restricted to the critical value of $\xi = 1$. In fact, depending on the reactivity, a wider range of initial conditions

can lead to a developing detonation and as it can be seen in figure 4-4. Thus, an upper limit ξ_u and a lower limit ξ_l are defined to categorize the different auto-ignition modes [28] [136] [139] [140]

1. $\xi_u < \xi$ subsonic deflagrative auto-ignition
2. $\xi_l < \xi < \xi_u$ developing detonation
3. $0 < \xi < \xi_l$ supersonic deflagrative auto-ignition
4. $\xi = 0$ thermal explosion

4.2. Knock modeling and calibrations

In the literature, knock modeling calibration is generally based on the prediction of the crank angle at knock onset [46] [119] [120] [124]. The crank angle at knock is referred to the start of the pressure rise in the pressure trace or in other terms the start of the pressure oscillation [121]. The constants in the ignition delay correlation are tuned to match the crank angle at knock onset.

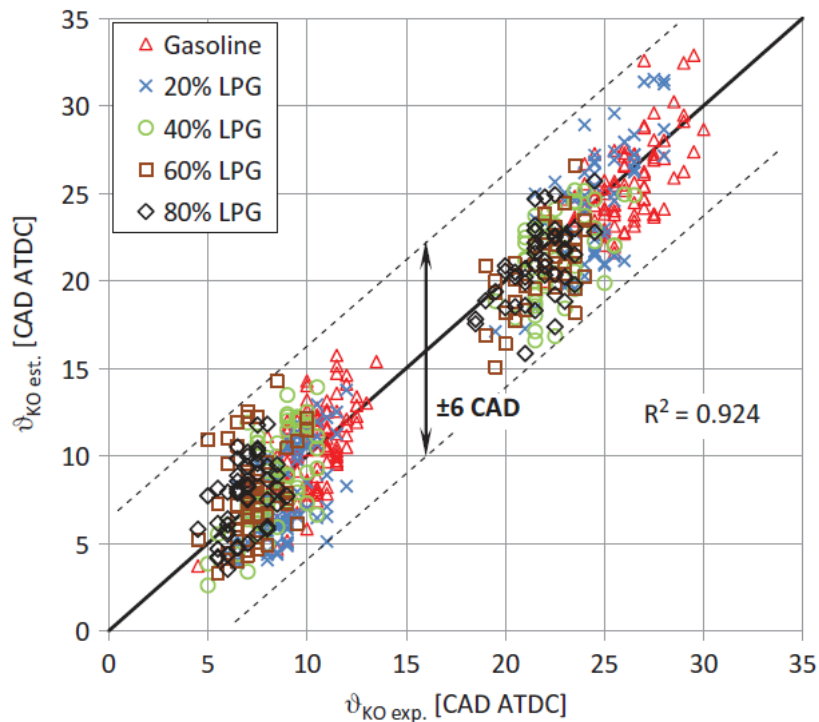


Figure 4-5: Comparison between estimated and experimental knock onset crank angles by Beccari et al. [141]

In the work of Beccari et al. [141], they used sets of experimental data to predict knock occurrence in engines of different types (aspirated or supercharged) and with different geometries and with different liquefied petroleum gas mixture. They found out that the auto-ignition time of the Liquefied petroleum gas-gasoline mixtures linearly depends on the liquefied petroleum gas mass fraction as it can be seen in figure 4-5. Their model predicts the knock onset crank angle with a maximum error of 6 CAD and a mean absolute error of just 1.82 CAD.

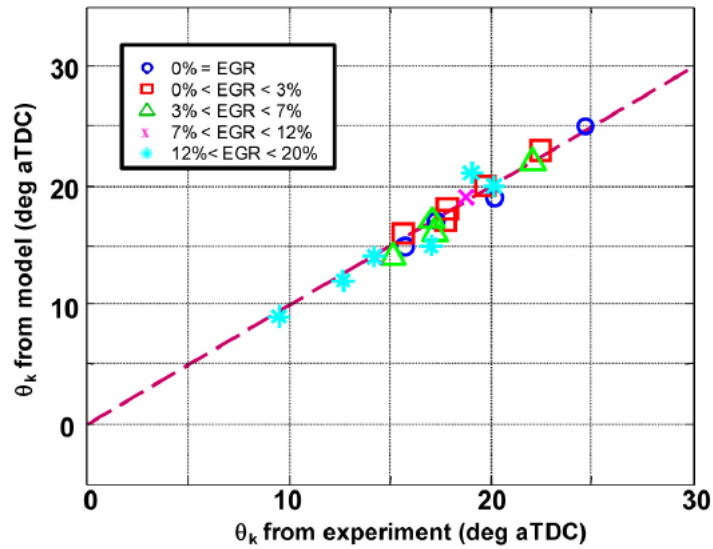


Figure 4-6: predicted vs experimental crank angle at knock onset [46]

Hoepke et al. [46] improved their ignition delay correlation and included the EGR to predict the crank angle at knock onset as it can be seen in figure 4-6. Their results were accurate by 2 CAD

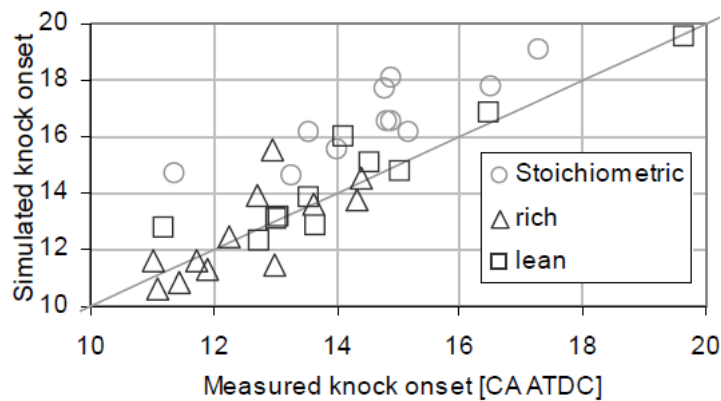


Figure 4-7: Measured versus simulated knock angle for 3000 rpm and Stoichiometric, rich and lean conditions [124]

Elmqvist et al. [124] empirical knock model can predict knock onset by approximately two crank angle degrees of error as it can be seen in figure 4-7. They concluded that their results are good due to the difficulty in measuring knock onset.

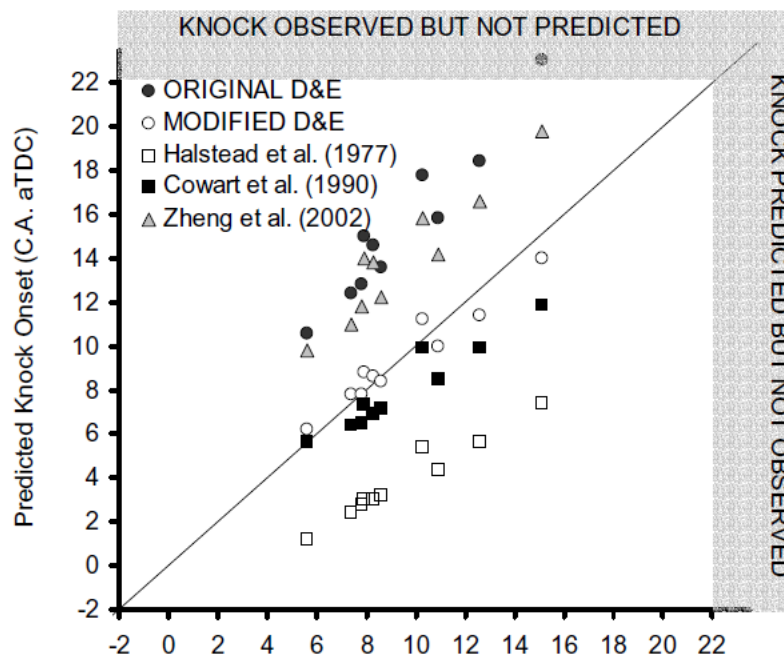


Figure 4-8: Experimental knock onset vs. predicted knock onset time for different predictive knock models [121]

In figure 4-8, predicted vs experimental knock onset crank angle are compared for 4 different knock models (Douaud & Eyzat, Halstead, Cowart and Zheng). The best fit is obtained using the routine of Cowart et al. and modified Douaud&Eyzat with prediction within 2 CAD followed by the original Douaud&Eyzat and Zheng, that gave onset results later than experiments within 4 to 6 CAD. The Halstead model gave early predictions by 5 to 8 CAD.

These correlations proposed in the literature, are all interesting and they offered some acceptable results. In the frame of this PhD thesis, 2 of them are first picked to be tested: the Douaud&Eyzat and the Kinetics Fit models. Douaud & Eyzat is also chosen to be tested since it has been widely utilized and it is interesting to calibrate it on the complete engine model and to test its knock prediction capacities. Kinetics Fit is an interesting knock since it takes the NTC regime into account and it could provide more accurate results on a complete engine model.

In the following parts of the section, a simple calibration of knock models will be presented based on the prediction of crank angle at knock onset for both Kinetics Fit and Douaud&Eyzat. In the second part of this section, a Kinetics Fit knock model will be modified and improvement on the prediction capacity will be proposed. The results are going to be presented for all overlapping and not overlapping cases at 1550x1500 mbar, 2000x1700 mbar and 2500x1700 mbar.

4.2.1. Calibration procedure of knock models based on the crank angle at knock onset

Two calibration multipliers are defined in any phenomenological knock model. They are both in the ignition delay as it can be seen in the following equation.

$$\tau = M_1 C_1 \cdot P^{-C_2} \cdot e^{\frac{C_3}{M_2 T}}$$

- M1: Multiplier to the induction time. Multiplier values less than 1 cause the predicted knock timing to be advanced. Values greater than 1 cause the predicted knock timing to be retarded.
- M2: Multiplier to the inverse of the activation energy. Multiplier values greater than 1 cause the predicted knock timing to be advanced. Values less than 1 cause the predicted knock timing to be retarded. This multiplier is very sensitive to knock prediction and a care should be taken when it is calibrated.

As it was stated before, knock occurs when the inductance integral is equal to 1 according to the following equation.

$$1 = \int_{t_0}^{t_{knock}} \left(\frac{1}{\tau} \right) dt = \int_{t_0}^{t_{knock}} \left(\frac{1}{M_1 C_1 \cdot P^{-C_2} \cdot e^{\frac{C_3}{M_2 T}}} \right) dt$$

This inductance equation can easily be transformed from time to crank angular as it can be seen on the kinetics fit by implementing the engine speed:

$$I(\alpha) = \frac{1}{6 (RPM)} \int_{\alpha_0}^{\alpha} \left(\frac{1}{M_1 C_1 \cdot P^{-C_2} \cdot e^{\frac{C_3}{M_2 T}}} \right) d\alpha$$

$I(\alpha)$ is the induction time integral expressed in crank angle degrees, α is the crank angle, α_0 is the crank angle at the start of the cycle, P and T are respectively the pressure and the temperature of the end gas, C_1 , C_2 and C_3 are calibrating coefficients

The operation of the knock model is thus simplified and two results can be obtained.

1. If during the cycle, the inductance integral reaches 1, the operating point is considered a knocking point and the crank angle at which the integral reaches 1 is selected and it is denoted by "crank angle at knock onset"
2. If by the end of the cycle, the inductance integral never reaches 1, the operating point is considered a non-knocking point as the thermodynamic conditions of the end gas do not allow an auto-ignition process.

To start, Douaud&Eyzat knock model and KineticsFit model were calibrated. The objective of the calibration is to find a single set of multipliers that predicts the crank angle at knock

onset for all the operating points that were implemented in this PhD thesis. To recall, the operating points that were used:

1. 1550x1500 mbar with 9 values of spark advances in the overlapping case and 8 values of spark advances in the non-overlapping case.
2. 2000x1700 mbar with 9 values of spark advances in the overlapping case and 8 values of spark advances in the non-overlapping case.
3. 2500x1700 mbar with 9 values of spark advances in the overlapping case and 9 values of spark advances in the non-overlapping case

This makes a total of 52 operating points.

In order to fit it into the complete engine model, the knock models multipliers were calibrated on 12 of 52 operating points. The genetic algorithm was used and the objective is to optimize the aforementioned multipliers in order to match crank angle at knock onset between the experimental values and the predicted values.

The 12 operating points used for calibration represent the last four spark advances increase of each of the overlapping cases of 1550x1500 mbar, 2000x1700 mbar and 2500x1700 mbar. The other 40 points were used to validate the model. In the table 4-3 calibration points are framed in blue and validation points are framed in orange. The objective of picking the last four spark advances increase is to enhance to capacity of the model to predict the crank angle at knock onset on the highly knocking points regarded as the most critical to knock. The calibration points were used across the three engine speeds and loads used in this PhD thesis in order to get a predictive knock model able to predict knock apparition across all low to mid-engine speed and high load region of the engine performance map which is the more prone to knock in an internal combustion engine.

	Spark advance increase [CAD]								
	0	0.375	0.75	1.125	1.5	1.875	2.25	2.625	3
1550x 1500 overlapping	✓	✓	✓	✓	✓	✓	✓	✓	✓
1550x 1500 not overlapping	✓	✓	✓	✓	✓	✓	✓	✓	✗
2000x 1700 overlapping	✓	✓	✓	✓	✓	✓	✓	✓	✓
2000x 1700 not overlapping	✓	✓	✓	✓	✓	✓	✓	✓	✗
2500x 1700 overlapping	✓	✓	✓	✓	✓	✓	✓	✓	✓
2500x 1700 not overlapping	✓	✓	✓	✓	✓	✓	✓	✓	✓

Table 4-3: overview of the operating points with the different spark advances increase used for calibration in blue frames and the spark advances increase used for validation in orange frames

Using the genetic algorithm, each knock model was provided experimental crank angle at knock onset values for the 12 operating points marked in the blue frame in the table above and the optimizer runs to provide one set of multipliers that best predicts the crank angle at knock onset in the model. The criteria to pick the best set of multipliers is by calculating the summation of the differences between the experimental and the predicted values for each of the 12 cases. The experimental crank angle at knock onset is defined by the angle at which the oscillation of in-cylinder pressure starts as it can be seen in the figure 4-5. The resulting multipliers values obtained at the end of the calibration procedure for both models are presented in table 4-4.

	Douaud & Eyzat	Kinetics Fit
Multiplier 1	1.914035	2.9609828
Multiplier 2	0.96304244	1.0974842

Table 4-4: multipliers values obtained for both Douaud&Eyzat and Kinetics Fit models at the end of the calibration procedure

The differences between the obtained values of each multiplier for both models is directly linked to the definition of the inductance integral for the models. To recall the definitions, the Douaud&Eyzat inductance is:

$$1 = \int_{t_0}^{t_{knock}} \left(\frac{1}{\tau} \right) dt = \int_{t_0}^{t_{knock}} \left(\frac{1}{M_1 17.68 \left(\frac{ON}{100} \right)^{3.402} \cdot P^{-1.7} \cdot e^{\frac{3800}{M_2 T}}} \right) dt$$

And the Kinetics Fit inductance is:

$$1 = \int_{t_0}^{t_{knock}} \left(\frac{1}{\tau} \right) dt = \int_{t_0}^{t_{knock}} \left(\frac{1}{M_1 a_i \left(\frac{ON}{100} \right)^{b_i} [Fuel]^{c_i} [O_2]^{d_i} [Diluent]^{e_i} e^{\left(\frac{f_i}{M_2 T} \right)}} \right) dt$$

The differences lie within the equivalence ratio and the diluent integration in the Kinetics Fit and the values of the constants in each model. In order to predict for example a fixed t_{knock} which can easily be transformed into a crank angle value, the multipliers values must be different in each model.

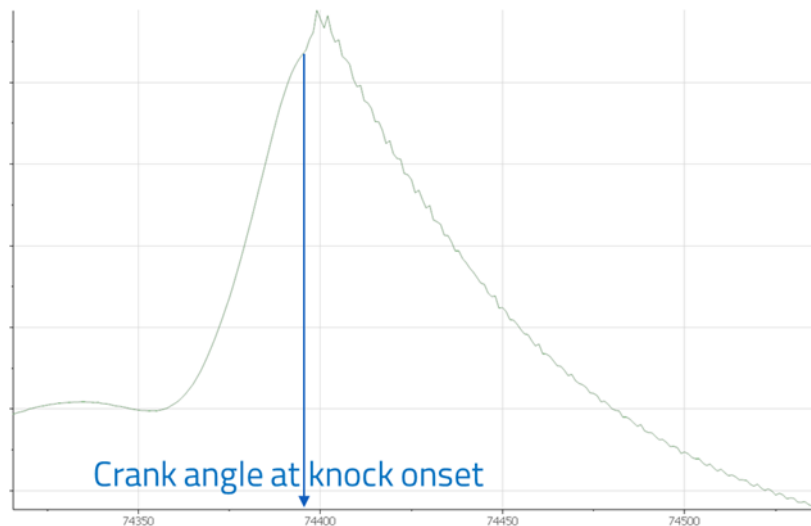


Figure 4-9: experimental crank angle at knock onset

The figure 4-9 presents the in-cylinder pressure trace of a single cycle. For each operating point and for each spark advance, the crank angle at knock onset is calculated for all of the knocking cycles (cycles whose MAPO values exceed the threshold of 0.6 bar) and the values are averaged over the number of knocking cycles.

$$C_{ko} = \frac{\sum_{i=1}^{N_k} C_{koi}}{N_k}$$

C_{koi} is the crank angle at knock onset for knocking cycles

N_k is the total number of knocking cycles.

An example is presented for 2000x1700 mbar in figures 4-10 and 4-11

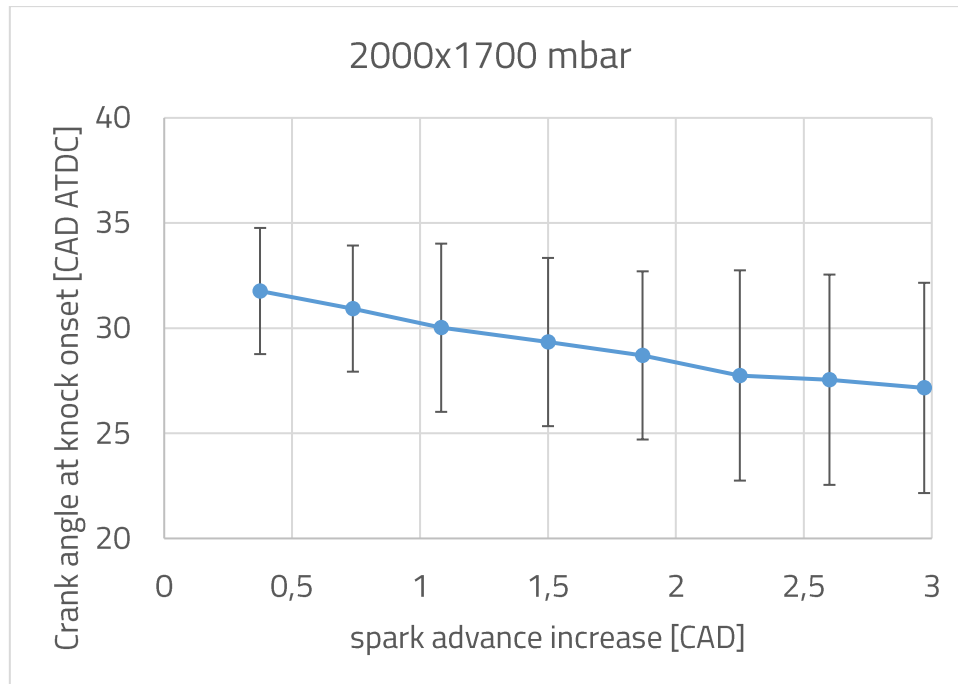


Figure 4-10: crank angle at knock onset variation with spark advance increase

The crank angle at knock onset decrease with the increasing spark advance. In the figure 4-10, these values represent an averaged value over all the knocking cycles for every spark advance. As it can be seen, these values tend to fluctuate more as the spark advance increases. In other terms, at 1.5 CAD of spark advance increase, the crank angle at knock onset of the different cycles varies between -4 CAD and 4 CAD around the average. AT 3 CAD of spark advance increase, the crank angle at knock onset of the different cycles varies between -5 and 5 CAD around the average.

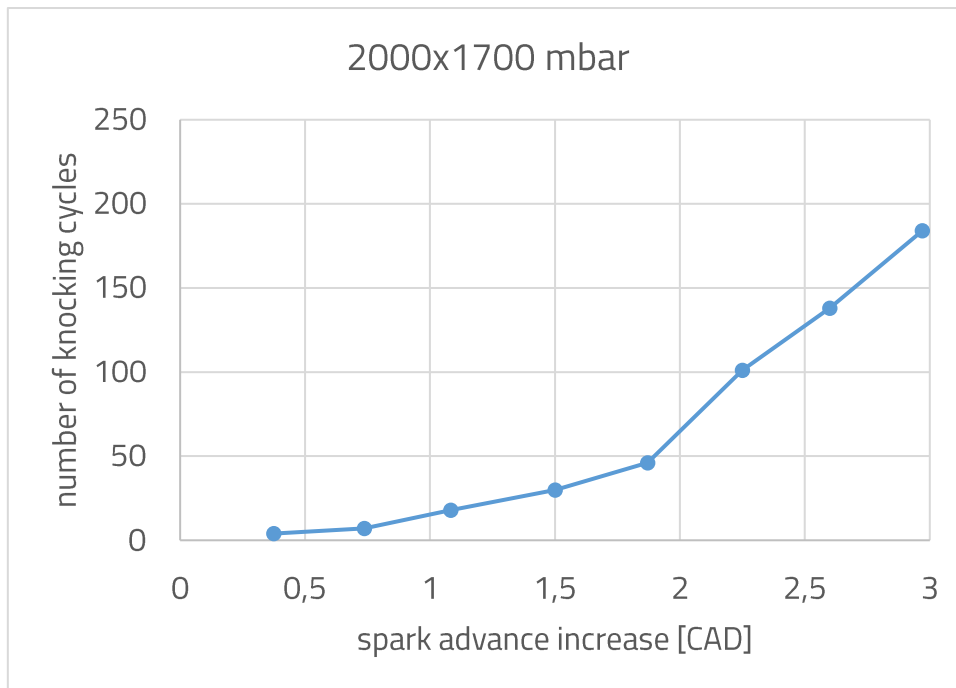


Figure 4-11: number of knocking cycles evolution with spark advance increase

As it can be seen in figure 4-11, the number of knocking cycles increases with the increasing spark advance. At 1.5 CAD of spark advance increase, only 30 out of 250 recorded cycles knock (20%), however, at 3 CAD of spark advance increase, 184 cycles out of 250 knock (74%).

The results for Douaud&Eyzat and Kinetics Fit knock models are presented below for all of the calibration points (overlapping settings at 1550x1500 mbar, 2000x1700mbar and 2500x1700 mbar) and validation points (the no overlapping settings) in figures 4-12 , 4-13. In these figures, predicted vs experimental crank angle at knock onset are plotted on the same graph for the different spark advances.

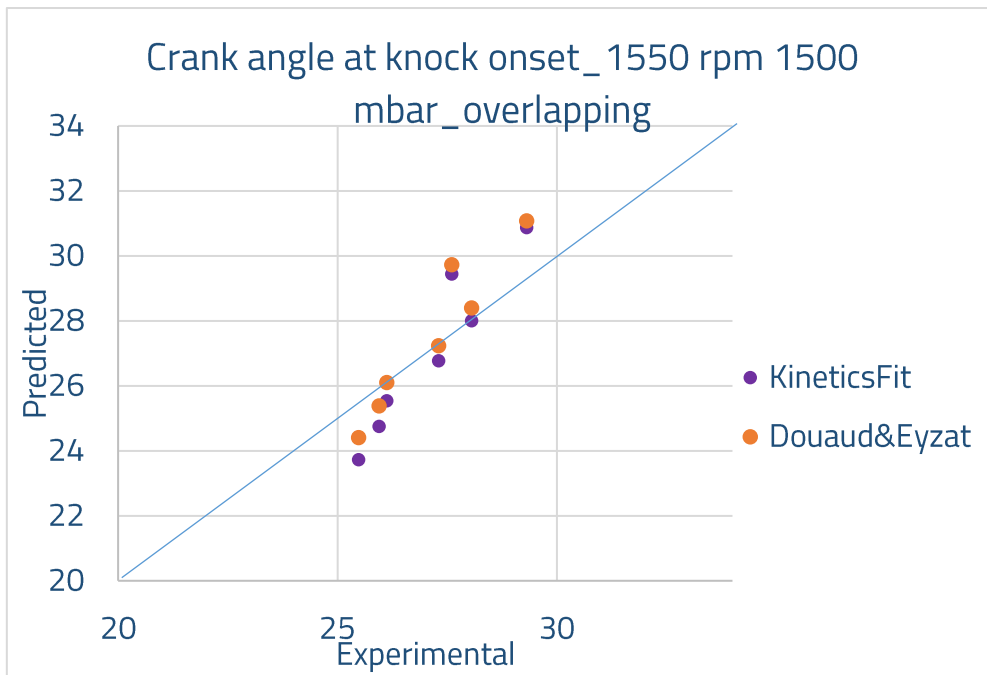


Figure 4-12: experimental vs predicted crank angle at knock onset for 1550x1500 mbar overlapping case for the different spark advances (calibration points)

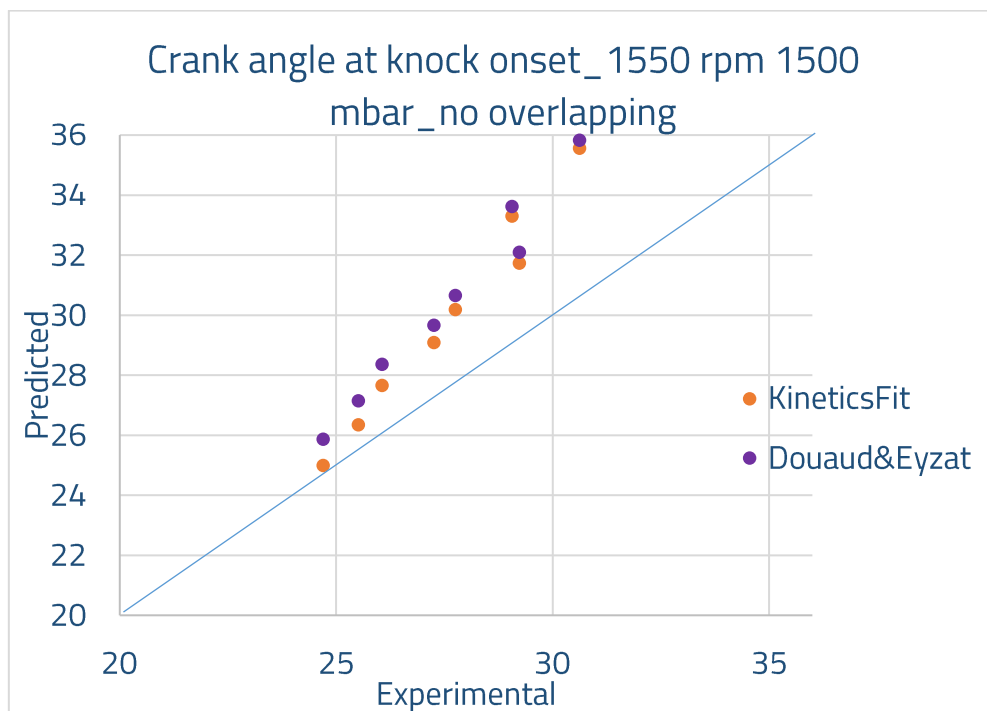


Figure 4-13: experimental vs predicted crank angle at knock onset for 1550x1500 mbar not overlapping case for the different spark advances (validation points)

KineticsFit and Douaud&Eyzat predict well crank angle at knock onset for calibration and validation operating points at 1550x1500 mbar, however they seem to underestimate a little bit knock onset during the cycle in the validation cases since experimental crank angle

at knock onset is lower than the predicted which means that knock apparition is predicted later in the cycle than the experiments. Moreover, both KineticsFit and Douaud&Eyzat knock models overestimates the knock occurrence during the cycle a little bit for the highest spark advance increases in the calibration cases and underestimates the knock apparition for the lowest spark advances decreases. Nevertheless, both of these models detect knock occurrence for all of the operating points including those with 0 spark advance increase which are knock-free operating points and knock shouldn't be predicted as it can be seen in figure 4-14.

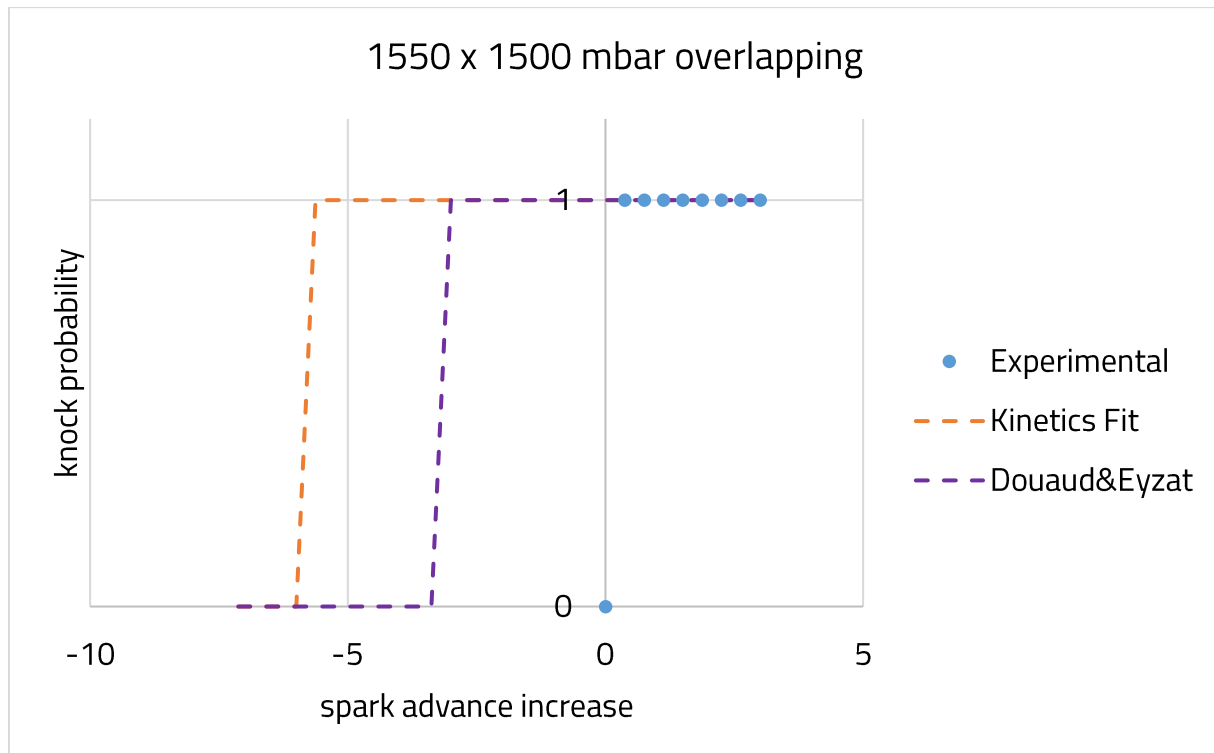


Figure 4-14: knock probability for 1550x1500 mbar

This “knock probability” parameter works in binary and it returns “0” when the operating point is considered knock-free and “1” when the operating point is a knocking point. It is also based on the inductance integral. If this integral reaches 1 before the end of the cycle, the operating point is considered a knocking point and the knock probability takes the values of 1. In the opposite case, knock probability is 0. In figure 4-14, knock probability is plotted for experiments and both Kinetics Fit and Douaud&Eyzat models. As it can be seen, experimentally at 1550x1500 mbar, knock occurs beyond 0.375 CAD of spark advance increase. At 0 spark advance increase, knock does not occur experimentally. However, both of the models predict knock occurrence with up to 6 degree of spark timing earlier than experiments.

The same behavior is observed for calibration and validation points for 2000x1700 mbar and 2500x1700 mbar. Both knock models Douaud&Eyzat and Kinetics Fit predict knock with up to 6 degrees of spark timing earlier than the experiments. This means that the calibration procedure based on the crank angle at knock onset, are not accurate enough to differentiate between a knocking operating and a non-knocking operating and to rule whether operating conditions might lead to knock or not. This calibration procedure lead to predict well crank angle at knock onset values but it does not provide a model to be used for the virtual calibration of the engine.

This has lead the modeling in this PhD thesis to be converted into enhancing the capacity of the engine model by the knock model to separate knocking points from non-knocking points. Since both models present some similar and inaccurate results on knock probability, the rest of the study will be focused on one them. The KineticsFit model will be used in this PhD thesis since it accounts for the diluents and the equivalence ratio for the prediction of knock and these 2 parameters are interesting to be included especially when the resulting model sensitivity will be tested on engine control parameters sweep.

4.2.2. Implementation of knock detection on a Kinetics Fit model

In this section, Kinetics Fit model will be improved to integrate a new capacity to separate knocking points from non-knocking points. To do so the “knock probability” K_p parameter will be integrated within calibration procedure.

As it was demonstrated previously Kinetics Fit has a tendency to overestimate knock in a way to predict its occurrence even on non-knocking operating points. To counter this overestimation, a new optimization function is defined to include the knock probability is the calibration targets of the multipliers. To do so, 3 operating points at 1550x1500 mbar, 2000x1700 mbar and 2500x1700 mbar with 0 CAD of spark advance increase were picked to run the optimizer and it was requested to target “0” as knock probability.

Moreover and to increase the accuracy of the knock prediction and the crank angle at knock onset, 9 more operating points with higher spark advance increase were picked from 1550x1500 mbar, 2000x1700 mbar and 2500x1700 mbar and it was requested from the optimizer to target the experimental crank angle at knock onset on these operating points as it can be seen in table 4-5.

	Spark advance increase [CAD]								
	0	0.375	0.75	1.125	1.5	1.875	2.25	2.625	3
1550x 1500 overlapping	✓	✓	✓	✓	✓	✓	✓	✓	✓
2000x 1700 overlapping	✓	✓	✓	✓	✓	✓	✓	✓	✓
2500x 1700 overlapping	✓	✓	✓	✓	✓	✓	✓	✓	✓

Table 4-5: overview of the operating points with the different spark advances increase used for calibration in blue frames

The following function is thus defined and integrated in the model:

$$f = \frac{\sum_{i=1}^N (C_{ko,i} - C_{ko,target})^2}{N_{ti}} + \frac{\sum_{j=1}^N (K_{p,j} - K_{p,target})^2}{N_{tj}} = f_1 + f_2$$

$C_{ko,i}$ is the predicted crank angle at knock onset and $C_{ko,target}$ is the target value which is the experimental value. It should be noted that C_{ko} are only calculated to the knocking operating points. The knock free points are not considered in the calculation of that function. $K_{p,j}$ is the predicted knock probability and the $K_{p,target}$ is the target value. Since crank angle degree (which are between 20 and 30 CAD) and knock probabilities restricted to 0 & 1 are of different order of magnitude, a normalizing term was introduced to both

parts of the function to equally consider knock probability and the crank angle at knock onset for the model.

In this function both “knock probability” and the crank angle at knock onset are taken into account to improve knock prediction capacities of the Kinetics Fit model.

This functions calculate the differences between predicted and experimental values for both “knock probability” and “crank angle at knock onset” for the 12 operating points that were displayed in table 4-5 inside the blue frame. The experimental values are presented in table 4-6.

	Spark advance increase [CAD]	0.00	1.50	2.25	3.00
1550x 1500 overlapping	Knock probability	0	1	1	1
	Crank angle at knock onset [CAD]	X	28.0	26.0	25.0
2000x 1700 overlapping	Knock probability	0	1	1	1
	Crank angle at knock onset [CAD]	X	29.3	27.7	27.0
2500x 1700 overlapping	Knock probability	0	1	1	1
	Crank angle at knock onset [CAD]	X	25	24.8	24

Table 4-6: experimental “knock probability” and “crank angle on knock onset” values

The objective of using this function is to obtain multipliers at the end of the optimization process for a knock model which is more accurate and that can be used for virtual calibration of spark timing and to ensure that knock constraints are still met when evaluating changes to engine control parameters.

The optimizer objective is to minimize this function using the aforementioned multipliers. When this function is minimized, it means that “knock probability” is enhanced as the model will be able to attribute “0” for knock probability for non-knocking operating points. On the other hand, the crank angle at knock onset which indicates the time at which knock occurs is also improved when this function is minimized. In other terms, the multipliers that will be selected are those which minimize the most this objective function.

To minimize this function, a genetic algorithm was chosen. It runs several sets of multipliers and calculates the resulting value of the function at the end of each simulation. The optimizer uses 10 generations and 15 population as advised by the software to compute multipliers values which makes a total of 150 designs. The set of multipliers which reduces the most the objective function is selected and they are provided to the Kinetics Fit knock model implemented in the SITurb combustion model within the complete engine model.

The resulting optimization designs are presented in figure 4-15.

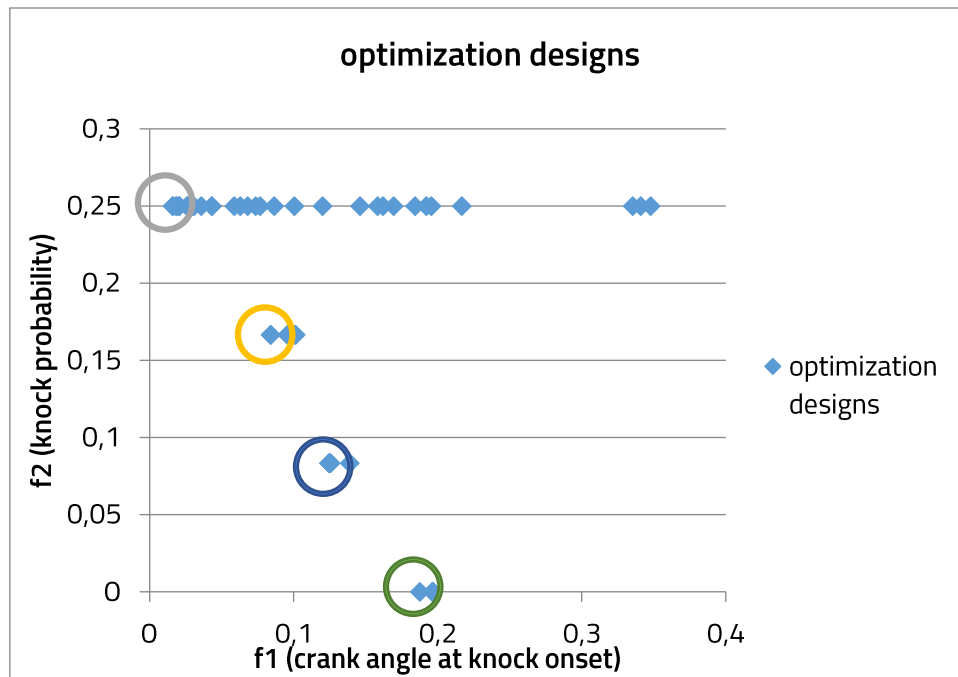


Figure 4-15: optimization designs obtained at the end of the calibration procedure

In figure 4-15, f_1 and f_2 functions values of the various designs generated by the genetic algorithm are plotted on the same graph. 4 designs denoted by v2.1, v2.2, v2.3, v2.4 minimizes the most the function according to the following table 4-7.

	f_1	f_2	f
v2.1	0,01581555	0,25	0,26581555
v2.2	0,08386666	0,16666667	0,25053333
v2.3	0,12465641	0,08333333	0,20798974
v2.4	0,19627317	0	0,19627317

Table 4-7: functions values of the best designs

From v2.1 to v2.4, the design are less accurate at the level of crank angle at knock onset predictions and more accurate at the level of knock probability.

The results of the knock probability and the crank angle at knock onset of these design are presented in the following figures.

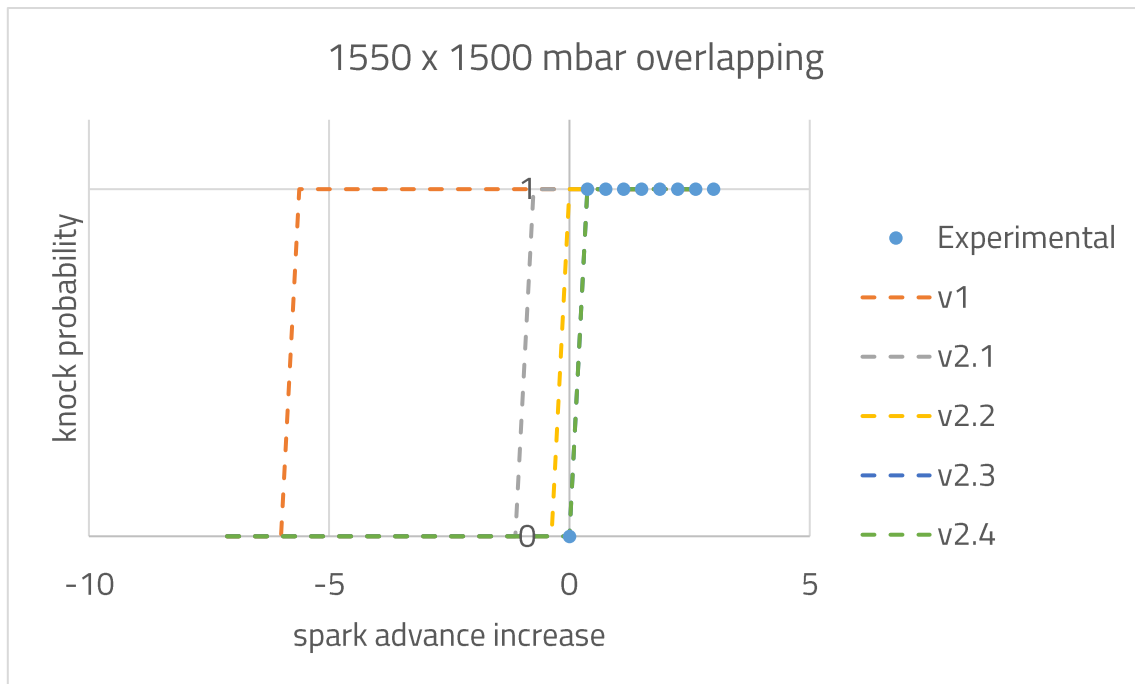


Figure 4-16: knock probability for the various design obtained on the new calibration procedure at 1550x1500 mbar overlapping (calibration points)

As it can be seen in figure 4-16, knock probability predictions in enhanced with the new calibration procedure. All of the design v2.1 to v2.4 predict knock probability within [-1, 0] degree of spark timing margin when compared to experiments. Both design v2.3 and v2.4 reproduced the experiments on 1550x1500 mbar overlapping. Crank angle knock onset predictions are presented in figure 4-17.

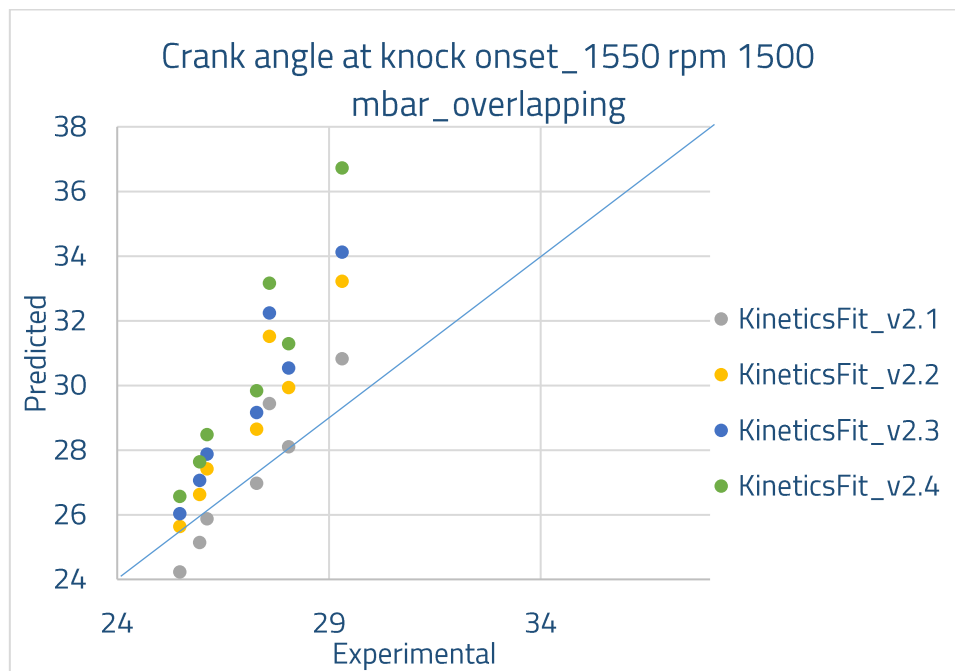


Figure 4-17: crank at knock onset for the various design obtained on the new calibration procedure at 1550x1500 mbar overlapping (calibration points)

As it can be seen in figure 4-17, the designs v2.1 to v2.4 provided crank angle at knock onset predictions that fall within the [-5,5] CAD range which is the range of the cycle-by-cycle variations obtained on the experimental crank angle at knock onset values. As it was stated earlier, v2.1 presented the most accurate predictions when compared to the rest of the designs. As for the validation points at 1550x1500 mbar:

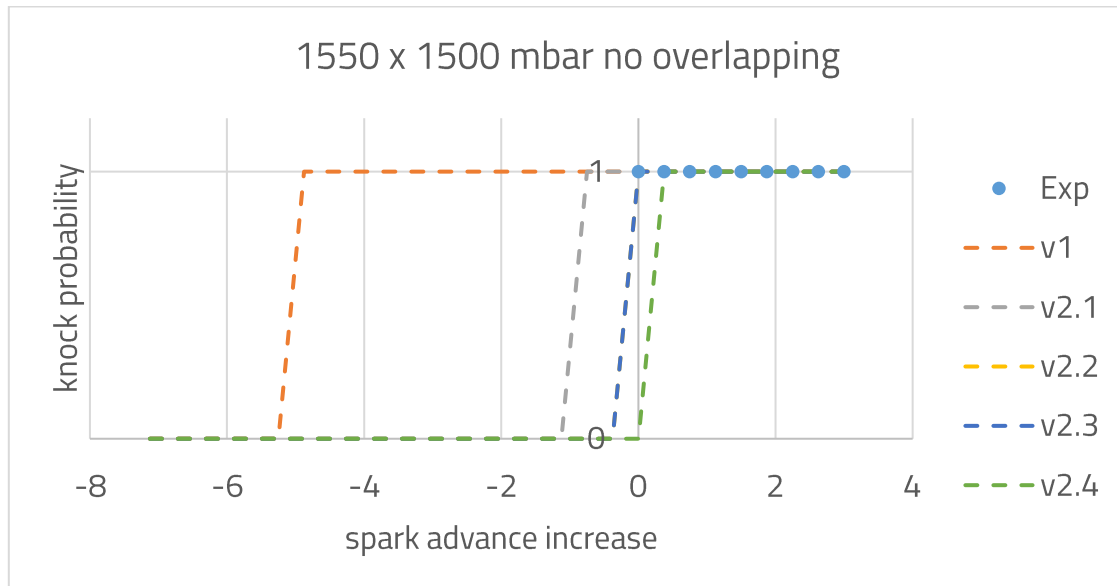


Figure 4-18: knock probability for the various design obtained on the new calibration procedure at 1550x1500 mbar no overlapping (validation points)

The knock probability is also improved for the validation points at 1550x1500 mbar as it can be seen in figure 4-18 since all the design from v2.1 to v2.4 predict knock probability within [-0.75, 0.375] CAD of spark timing margin. The v1 calibration predicted knock probability 5 degree of spark timing earlier than experiments.

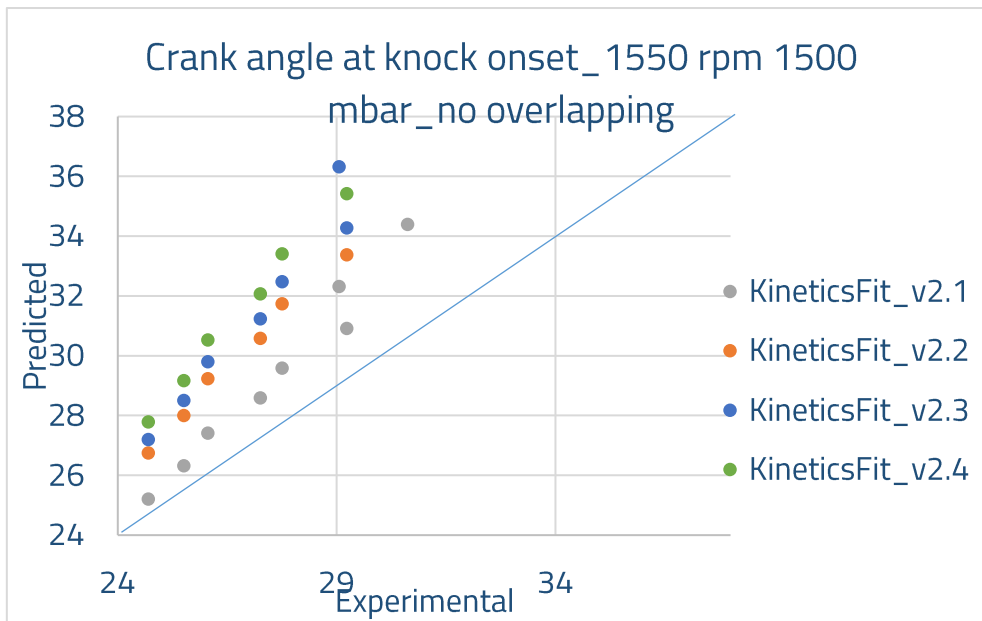


Figure 4-19: crank at knock onset for the various design obtained on the new calibration procedure at 1550x1500 mbar no overlapping (validation points)

As it can be seen in figure 4-19, the designs v2.1 to v2.4 provided crank angle at knock onset predictions that fall within the [-5,5] CAD range which is the range of the cycle-by-cycle variations obtained on the experimental crank angle at knock onset values.

The same behavior is also observed on the 2000x1700 mbar and 2500x1700 mbar for both calibration and validation points for the prediction of knock probability and crank angle at knock onset as it can be seen in the following figures 4-20 to 4-23.

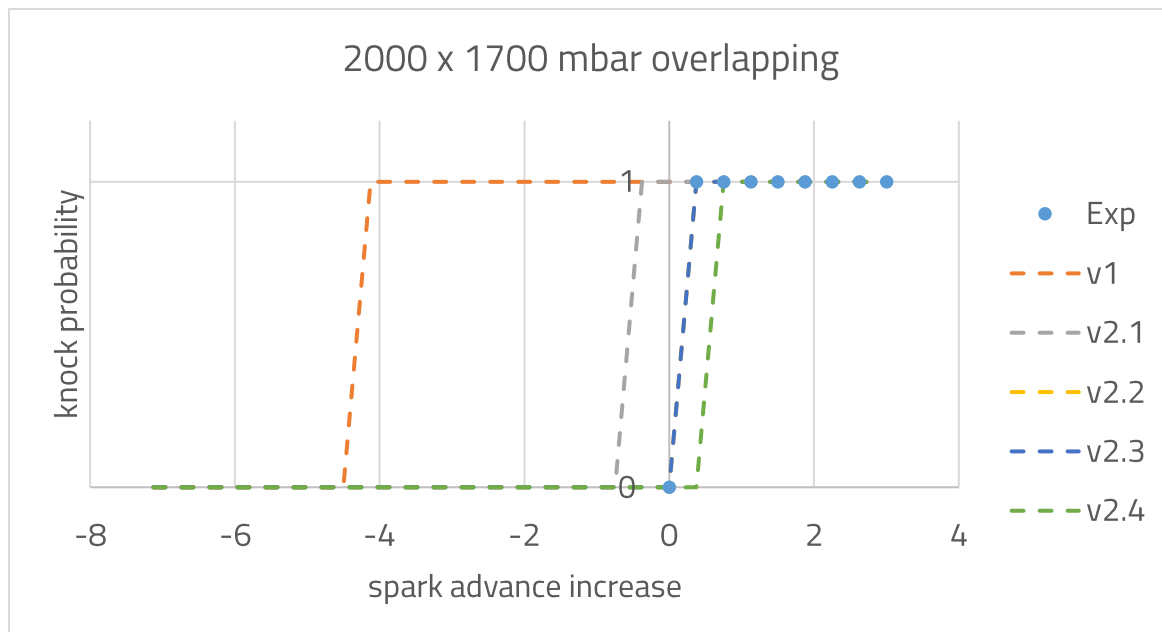


Figure 4-20: knock probability for the various design obtained on the new calibration procedure at 2000x1700 mbar overlapping (calibration points)

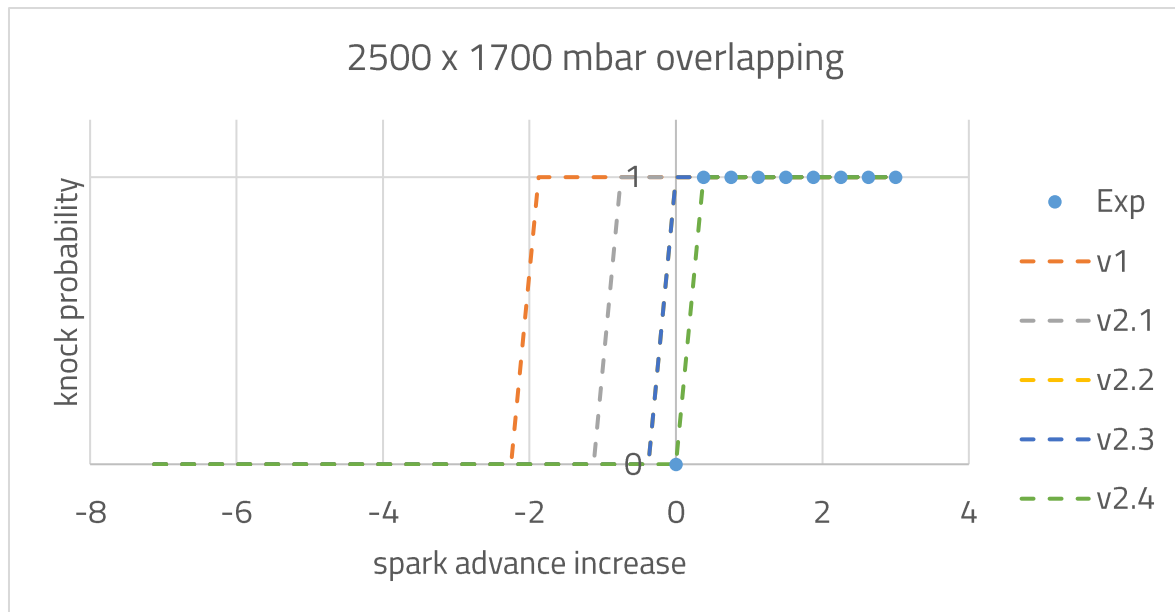


Figure 4-21: knock probability for the various design obtained on the new calibration procedure at 2500x1700 mbar overlapping (calibration points)

The new calibration procedure improves the knock probability at 2000x1700mbar and 2500x1700 for calibration points and validation points. At 2000x1700 mbar, knock probability is predicted within [-0.375, 0.75] CAD of spark timing margin and within [-0.75, 0.375] CAD for 2500x1700 mbar. As it can be seen in figure 4-20 and 4-21, the new calibration improvement is less pronounced at 2500x1700 mbar (from -2 CAD of spark timing difference to [-0.75, 0.375]CAD) than 2000x1700 mbar (from -4 CAD of spark timing difference to [-0.375, 0.75] CAD) since the v1 calibration shows better predictions on 2500x1700 mbar than 2000x1700 mbar.

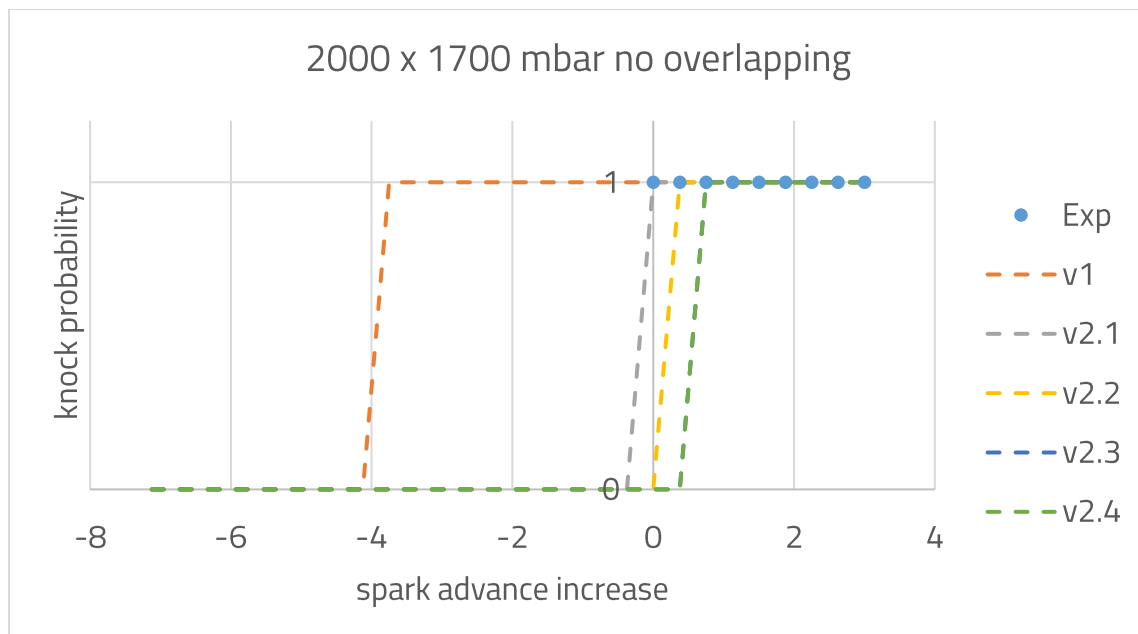


Figure 4-22: knock probability for the various design obtained on the new calibration procedure at 2000x1700 mbar no overlapping (validation points)

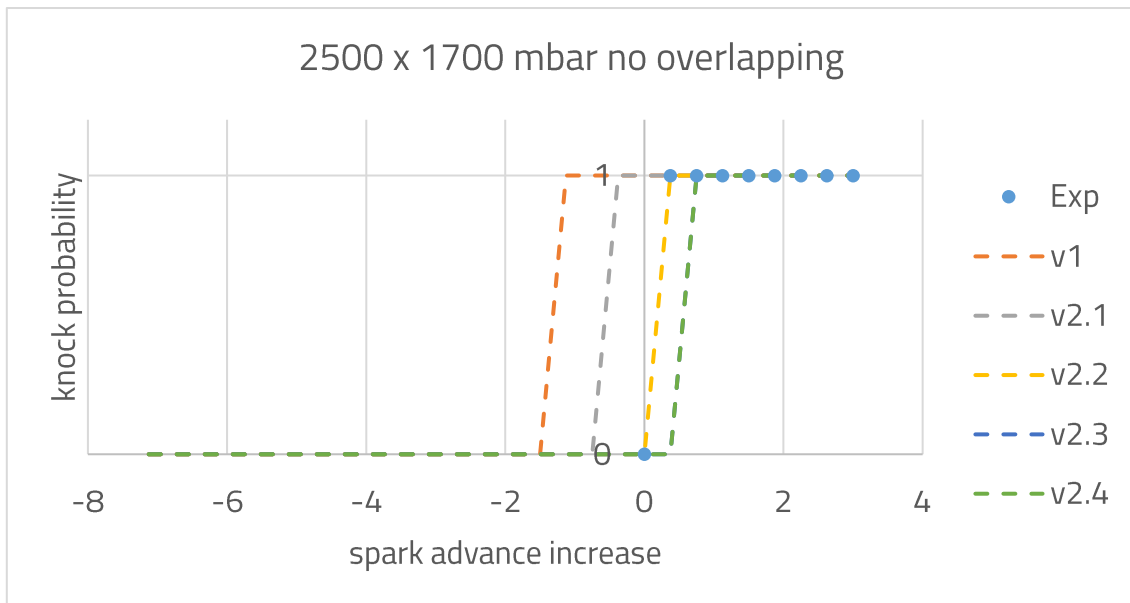


Figure 4-23: knock probability for the various design obtained on the new calibration procedure at 2500x1700 mbar no overlapping (validation points)

To conclude, the new calibration method improved the knock probability predictions and even though it compromised the crank angle at knock onset predictions, the obtained values fall within the cycle-by-cycle variation range for all of the calibration and validation points.

Out the 4 designs v2.1, v2.2, v2.3 and v2.4, the design v2.4 the one that minimizes the most the function f and the set of multipliers M1&M2 provided by that design will be later on used for the rest of the analysis of the simulation results and to test the sensitivity of the model on the variation of the engine control parameters.

4.3. Simulation results on complete engine model

In this section, the improved Kinetics Fit model is implemented in calibrated SITurb combustion model within the complete engine model and some simulations were run. These simulations include the valves timings variations, the injection strategies, the intake air temperature and the coolant and oil temperatures as they were performed on the engine test bench. The objectives of these simulations is to test the sensitivity of the model on the effect of control parameter sweep on the knock occurrence.

In this section, knock probability of the model is presented as well as the predicted knock index. It should be noted that the knock index calculations in the model is different than the knock index calculations in the experimental results.

In fact, the experimental knock index was calculated based on the in-cylinder pressure oscillations, the maximum amplitude of pressure oscillation (MAPO) was averaged over all the cycles to compute the knock index. In the simulations run, the pressure oscillations cannot be simulated and thus a similar computation of the knock index is not possible. On the other hand, the knock index in the numerical results was calculated according to the following equation.

$$KI_{sim} = 100 \cdot u(\alpha) \cdot \frac{V_{TDC}}{V(\alpha)} \cdot e^{\left(\frac{-6000}{T(\alpha)}\right)} \cdot \max\left(0, 1 - (1 - \varphi(\alpha))^2\right) \cdot I_{ave}(\alpha)$$

KI_{sim} is the simulated knock index, α is the crank angle, $u(\alpha)$ is the percentage of cylinder mass unburned, V_{TDC} is the cylinder volume at top dead center, $V(\alpha)$ is the cylinder volume, $T(\alpha)$ is the bulk unburned gas temperature in K, φ is the equivalence ratio of the unburned zone, I_{ave} is the induction time integral averaged over all end gas zones.

This simulation knock index cannot either be utilized on the experimental results as the exact calculation unburned gas temperature in function of the crank angle degree as well as the computation of the equivalence ratio of the unburned zone are not feasible.

For these reasons, the comparison between the experimental and the predicted results of the knock index will be restricted to the qualitative comparison as the quantitative comparison is not significant and does not provide useful information since the calculation methods are different.

Both the experimental and the predicted knock index are plotted on the same graph for the considered operating points in order to perform a qualitative comparison.

4.3.1. Knock model sensitivity of valves timings on knock prediction

The knock model sensitivity of valves timings was tested. Simulations were run on 1550x1500 mbar, 2000x1700 mbar and 2500x1700 mbar on both overlapping and not overlapping cases. Knock index are plotted on the same graph.

For the 1550x1500 mbar.

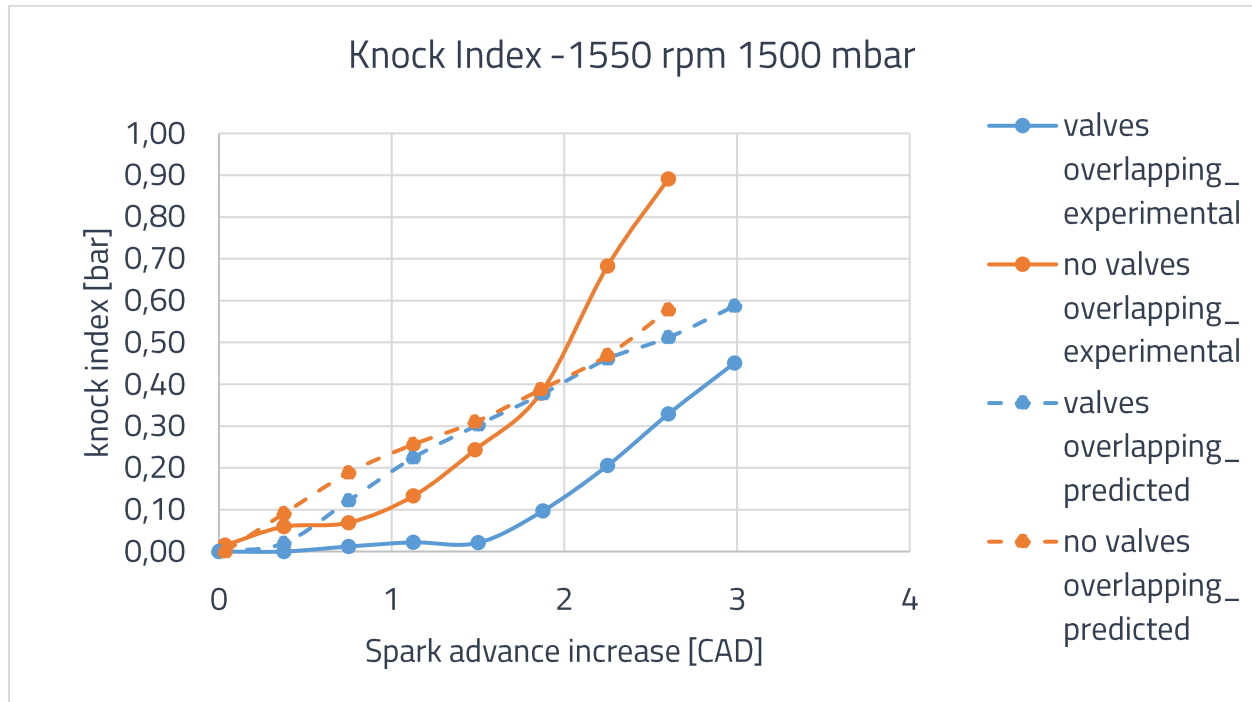


Figure 4-24: experimental vs predicted knock index for both overlapping and not overlapping case at 1550x1500 mbar

Tiny differences can be observed between the prediction of the overlapping and not overlapping cases. Experimentally, 1CAD of spark timing on the knock margin can be achieved by overlapping the valves (calculated at knock index KI=0.4). In the simulations, these results could not be reproduced

For 2000x1700 mbar:

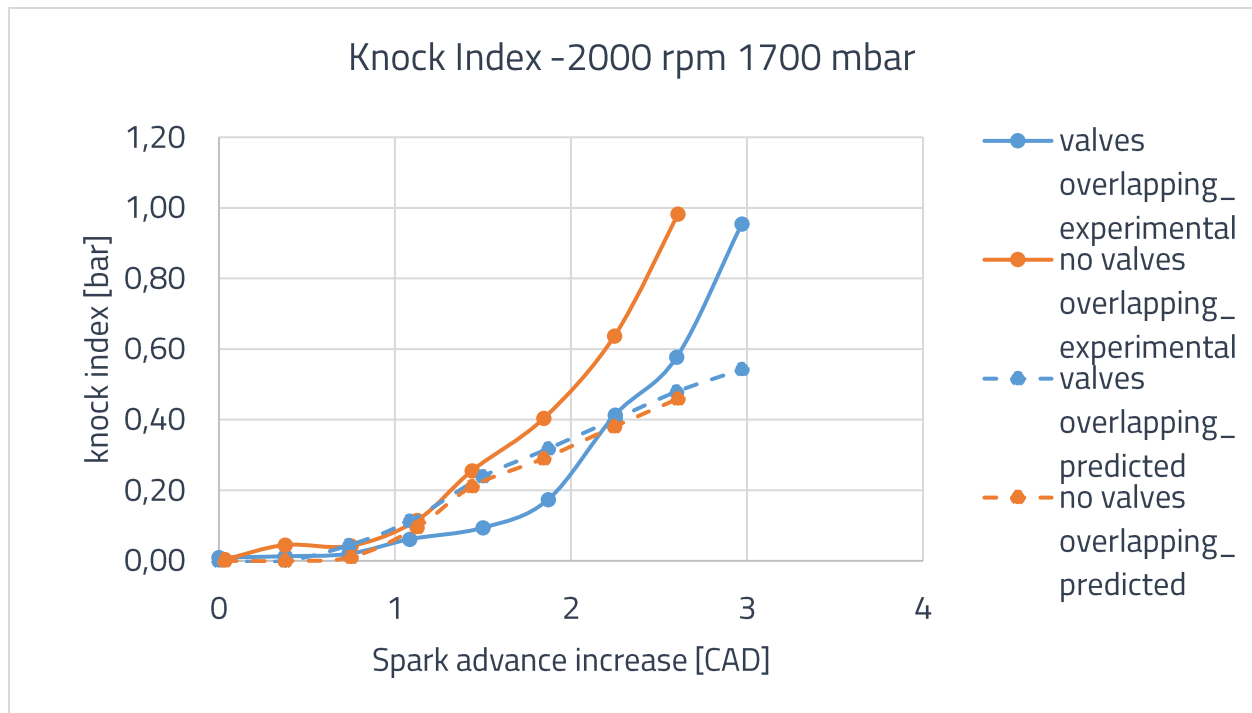


Figure 4-25: experimental vs predicted knock index for both overlapping and not overlapping case at 2000x1700 mbar

As it can be seen on the figures 4-24 and 4-25, the experimental knock index present a quadratic function of the spark advance increase. The knock index increase in a polynomial relationship as the spark advance increases. However, this numerical knock index has sort of a linear relationship with the spark advance increase. This can be seen on both 1550x1500 mbar and the 2000x1700 mbar graphs.

In addition, on these operating points, the Kinetics Fit model does not predict significant differences on the knock index between the overlapping and the non-overlapping cases. The Kinetics Fit is not sensitive to valves timings when they modify the residuals concentrations on the operating points.

As for the 2500x1700 mbar:

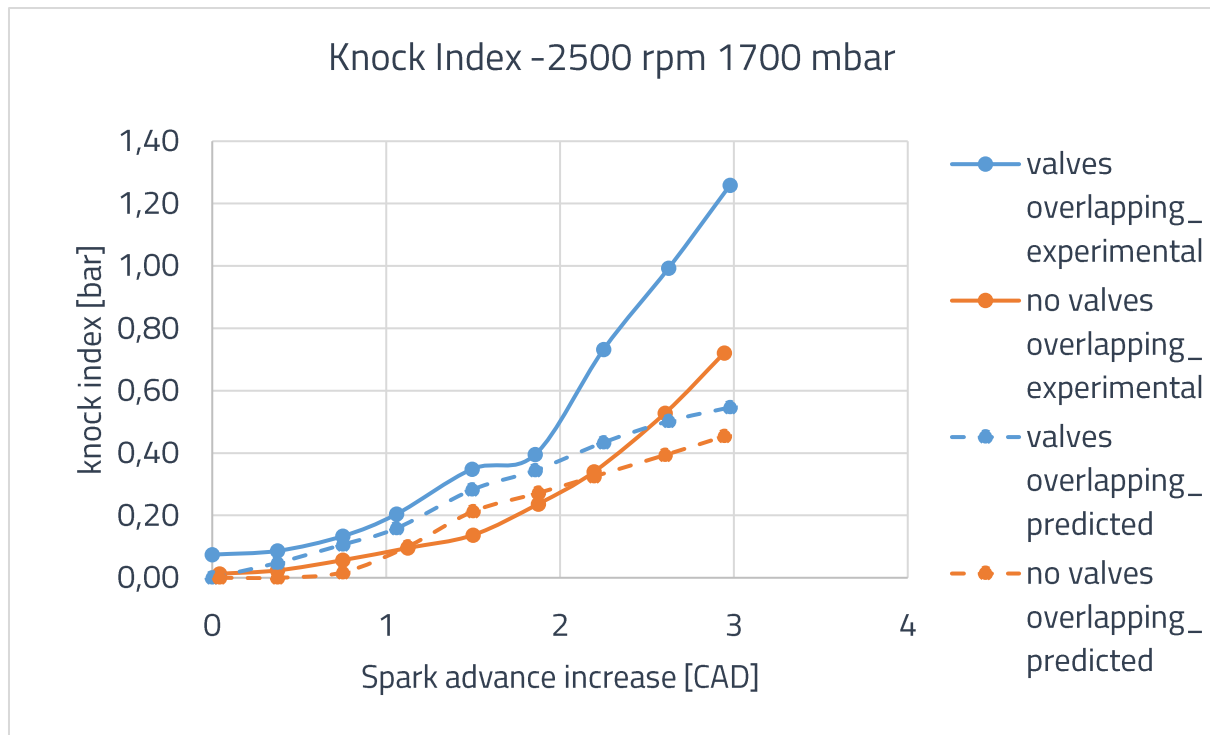


Figure 4-26: experimental vs predicted knock index for both overlapping and not overlapping case at 2500x1700 mbar

On the 2500x1700 mbar operating point, the effect of valves timings can be observed using Kinetics Fit. In fact, varying valves timings on that operating point affect the confined mass and subsequently the load. The overlapping case predicts a little more knock than the not overlapping cases. This is compatible with the experimental results.

4.3.2. Knock model sensitivity of injection strategies on knock prediction.

The knock model sensitivity to injection strategies variations is presented in this section. The sensitivity of the single injection is only presented since the combustion model is only supposed to perform under homogeneous charge. It should be recalled that knock index computations are different in the case of the simulations and the in the case of the experimental results.

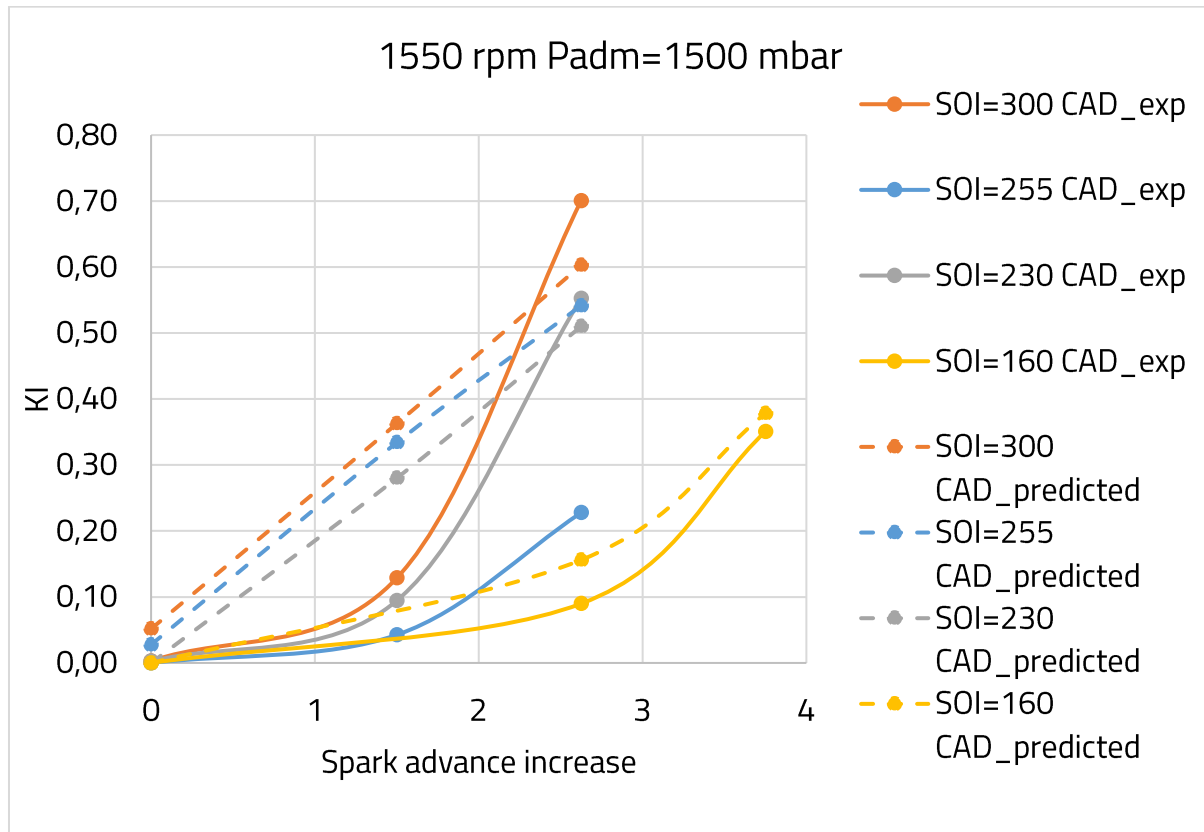


Figure 4-27: experimental vs predicted knock index for the injection timing of a single injection for 1550x1500 mbar

As it was previously mentioned, the knock index evolution is linear in the case of the simulations results. As it can be seen, the knock model is sensitive to the injection timing. The earlier the injection, the higher the knock intensity. It should be noted that for the first three injection timing, the knock intensities are close however for SOI=160 CAD, knock intensity prediction is way less than the three others. The model is sensitive to the charge cooling, and it delays knock apparition as the injection timing is delayed. This sensitivity is more pronounced in the latest injection timing as it appears in the piston movement from bottom to top dead center before the intake valve closing. The model overestimates knock delay when compared to the experimental results. For example at spark advance increase of 2.6 CAD, the model predicts for SOI=160 CAD almost 5 times less knock intensity than SOI=255 CAD whereas in the experimental results the knock intensity is almost half for SOI=160 CAD when compared to SO=255 CAD. However, one difference can also be observed, in the experiments, knock intensity is higher for SOI=230 CAD than SOI=255 CAD.

This was not observed in the simulations results as charge cooling is observed as injection timing is delayed.

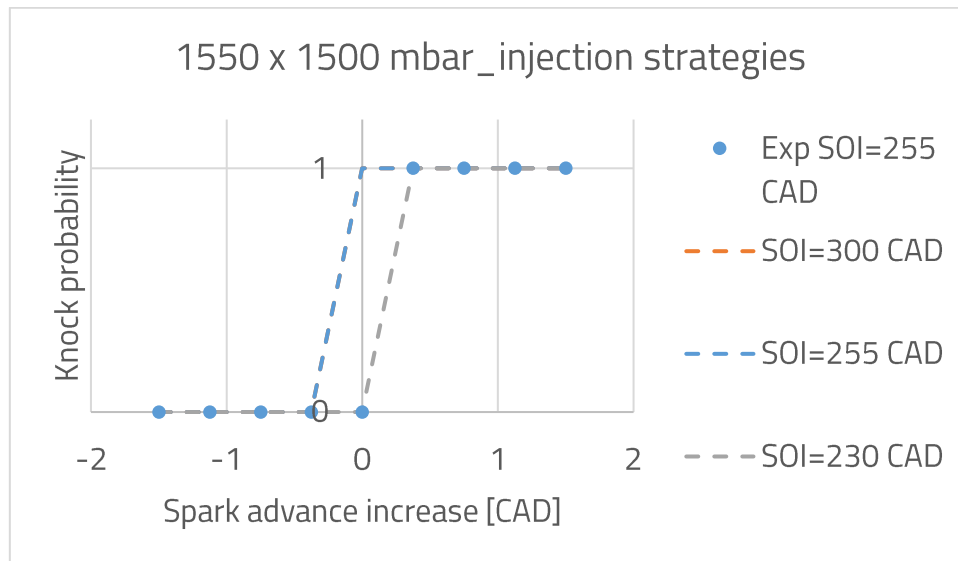


Figure 4-28: knock probability predictions for single injection strategy at 1550x1500 mbar

Regarding knock probability and as it can be observed in figure 4-28, the model predicts knock apparition with 0.375 CAD of spark timing earlier than experiments which is in accordance with the capacity of the model. It is sensitive when start of injection is retarded to SOI=230 CAD where it predicts knock apparition later than both SOI=255 CAD and 300 CAD. As for 2000x1700 mbar:

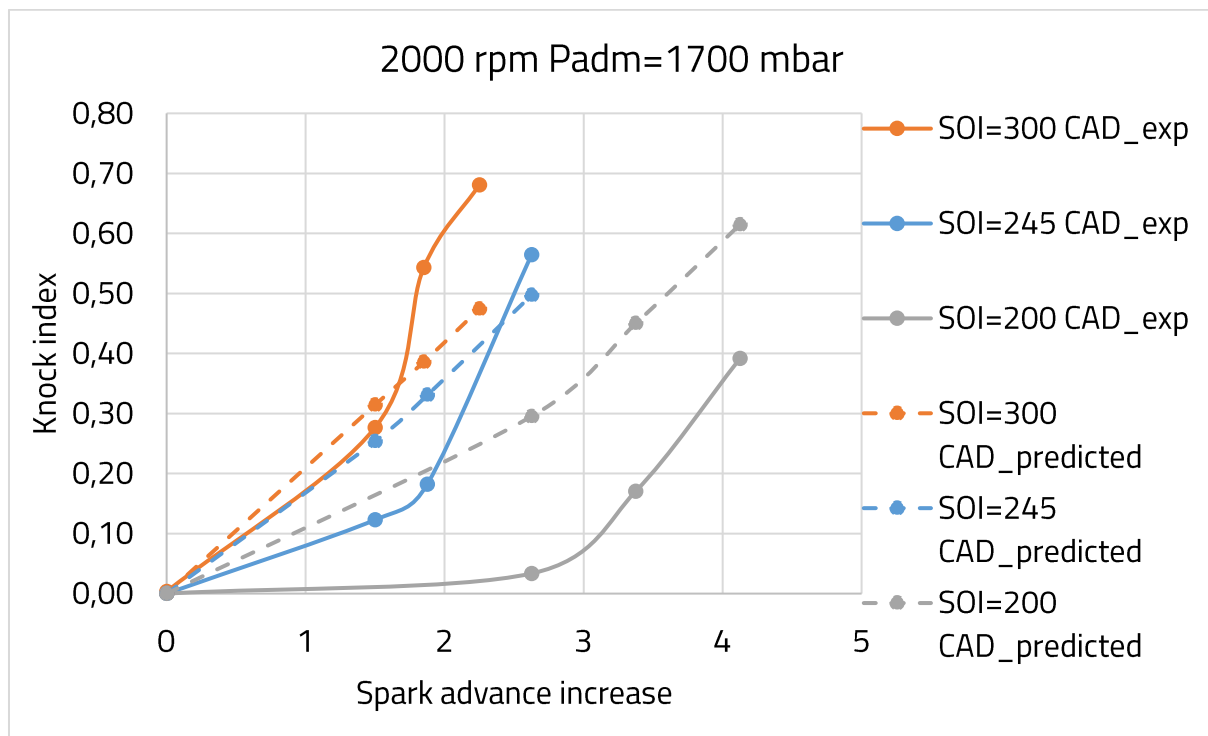


Figure 4-29: experimental vs predicted knock index for the injection timing of a single injection for 2000x1700mbar

The same can be concluded for 2000x1700 mbar regarding the knock intensities and the injection timing. Experimentally 1.875 CAD of knock margin are achieved when the start of injection is retarded by 45 CAD from 245 CAD to 200 CAD (obtained at KI=0.4). Numerically, only 1 CAD of knock margin is achieved in the same condition.

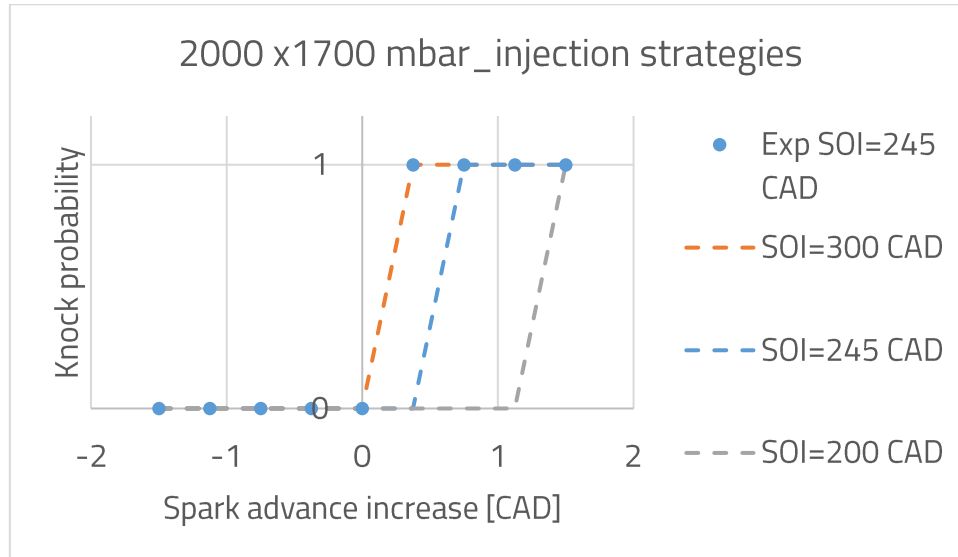


Figure 4-30: knock probability predictions for single injection strategy at 2000x1700 mbar

At 2000x1700 mbar, for SOI=245 CAD, the prediction of knock probability is 0.375 CAD of spark timing later than experiments and the model is sensitive to injection timing sweeps

4.3.3. Knock model sensitivity of intake air temperature on knock prediction

The model sensitivity to intake air temperatures are presented in figure 4-31

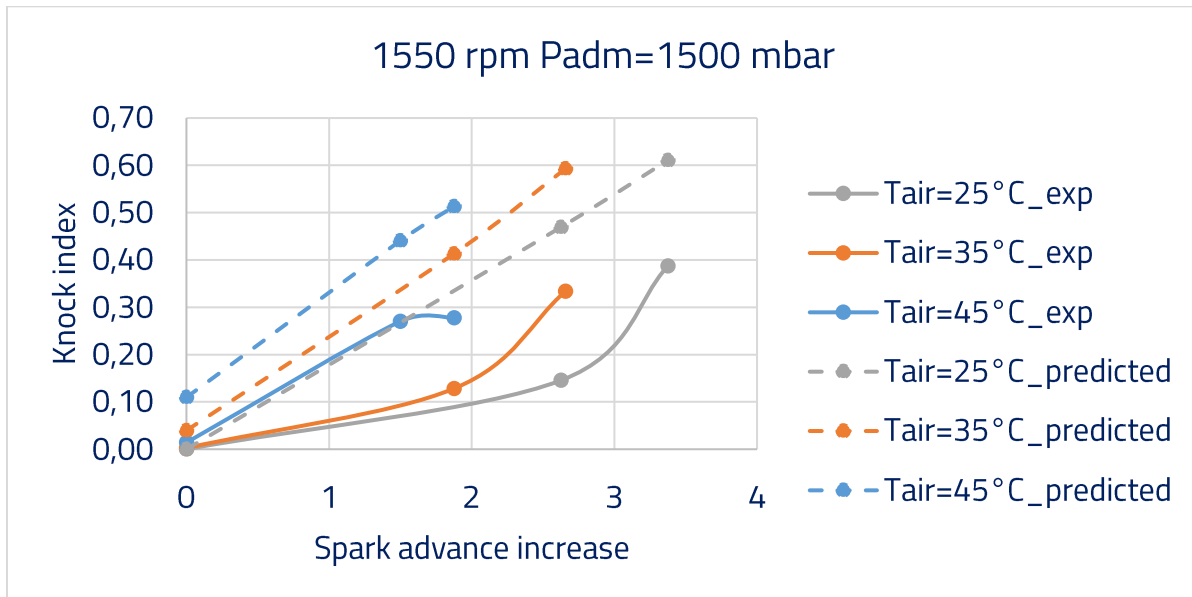


Figure 4-31: experimental vs predicted knock index for intake air temperatures variations for 1550x1500 mbar

As it can be seen in the figure 4-31, the knock model is sensitive to the intake air temperature. In fact, the intake air temperature impacts the end-gas temperature: lower intake air temperature increase the ignition delay of the end-gas which delays knock apparition. This is observed on the predicted curves in figure 4-32 where the intake air temperature at 25°C delays knock more than 35°C and 45°C respectively.

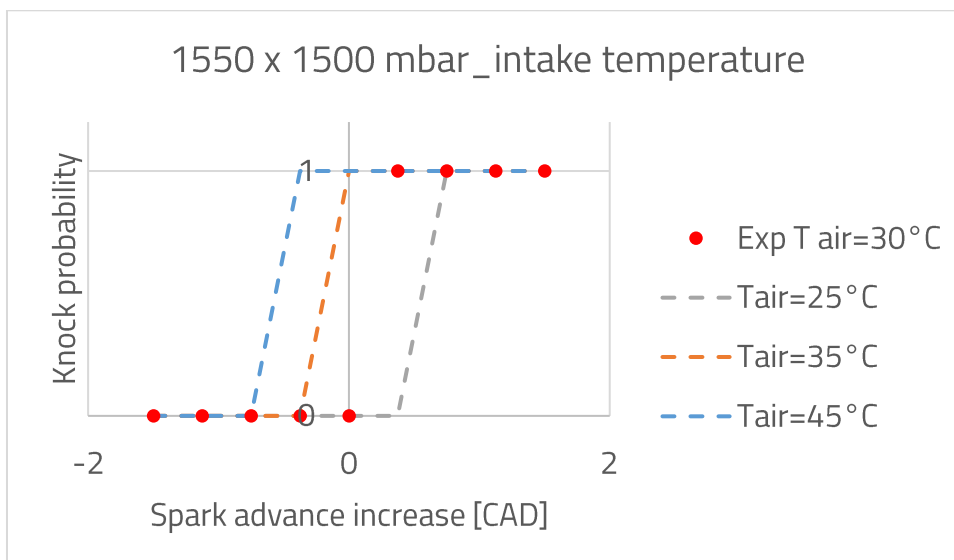


Figure 4-32: knock probability predictions for intake air temperature sweeps at 1550x1500 mbar

Regarding knock probability in figure 4-32, the simulations results are compared to the only experimental results performed at a wide range of spark advances which is at 30°C. The

knock predicts knock probability as a function of the intake temperature. The model delays the knock probability by 0.375 CAD of spark timing for every 5°C decrease of intake air temperature between 35°C and 25°C and by 0.375 CAD of spark timing between for 10°C decrease between 45°C and 35°C.

Regarding the iso mass conditions, the impact of the intake air temperature at 2500x1700 conditions is presented in figure 4-33

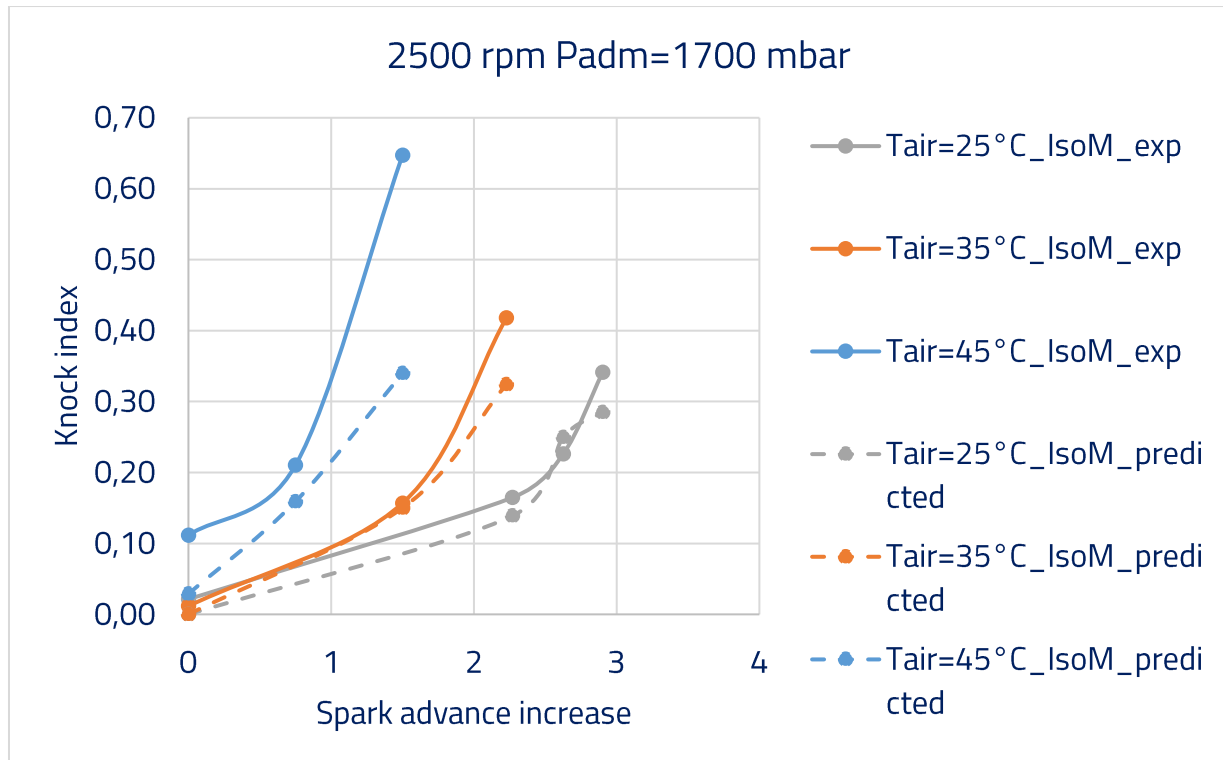


Figure 4-33: experimental vs predicted knock index for intake air temperatures variations at iso mass for 2500x1700 mbar

Iso mass conditions increase the differences in knock index between the various intake temperatures. In fact, when decreasing the intake temperature from 45°C to 25°C, the end-gas temperature is reduced which contributes to knock delay. In addition, the admission pressure was also reduced in order to fall on the same in-cylinder mass. These two previously mentioned factors contribute to knock delay at lower intake temperatures when compared to higher intake temperatures.

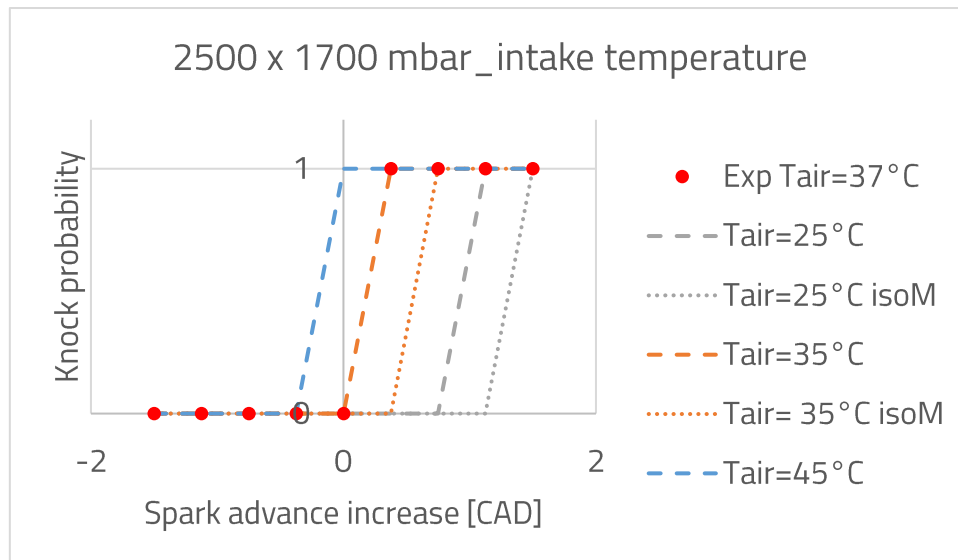


Figure 4-34: knock probability predictions for intake air temperature sweeps at 2500x1700 mbar

Regarding the knock probability, the model delays the knock probability by 0.75 CAD of spark timing for every 10°C decrease of intake air temperature between 35°C and 25°C and by 0.375 CAD of spark timing between for 10°C decrease between 45°C and 35°C . The model is also sensitive to the iso-mass effect. However isomass was achieved by reducing the intake pressure, the model is also sensitive to these variations as less mass is trapped and the knock probability is delayed.

4.3.4. Knock model sensitivity of coolant and oil temperature on knock prediction

The model sensitivity to coolant and oil temperatures are presented in figure 4-35

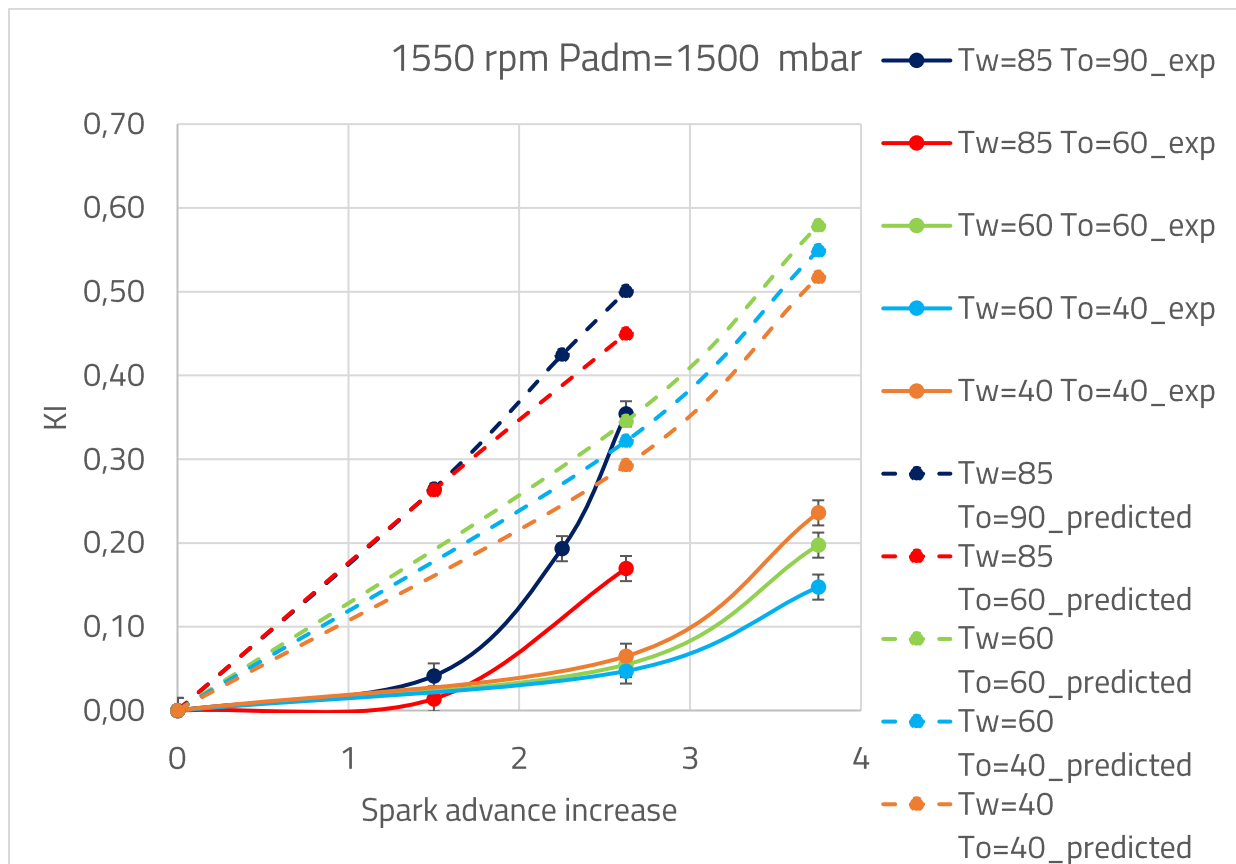


Figure 4-35: experimental vs predicted knock index for coolant and oil temperatures variations for 1550x1500 mbar

The knock prediction in the cases of coolant and oil temperatures sweep are a little bit than the experimental. In the model, variations of the coolant and oil temperatures affected the cylinders walls temperatures which impacted the end-gas temperature. As it can be seen in figure 4-35, as coolant or oil temperature decrease, the knock is delayed. In the experiments, this was not always the case: in fact, when the coolant temperature decreased from 60°C to 40°C, the spark-induced flame speed was increased due to the increased in-cylinder mass, which compressed the end-gas and contributed to a faster auto-ignition when compared to coolant temperature at 60°C. This advanced knock apparition at coolant temperature at 40°C when compared to 60°C.

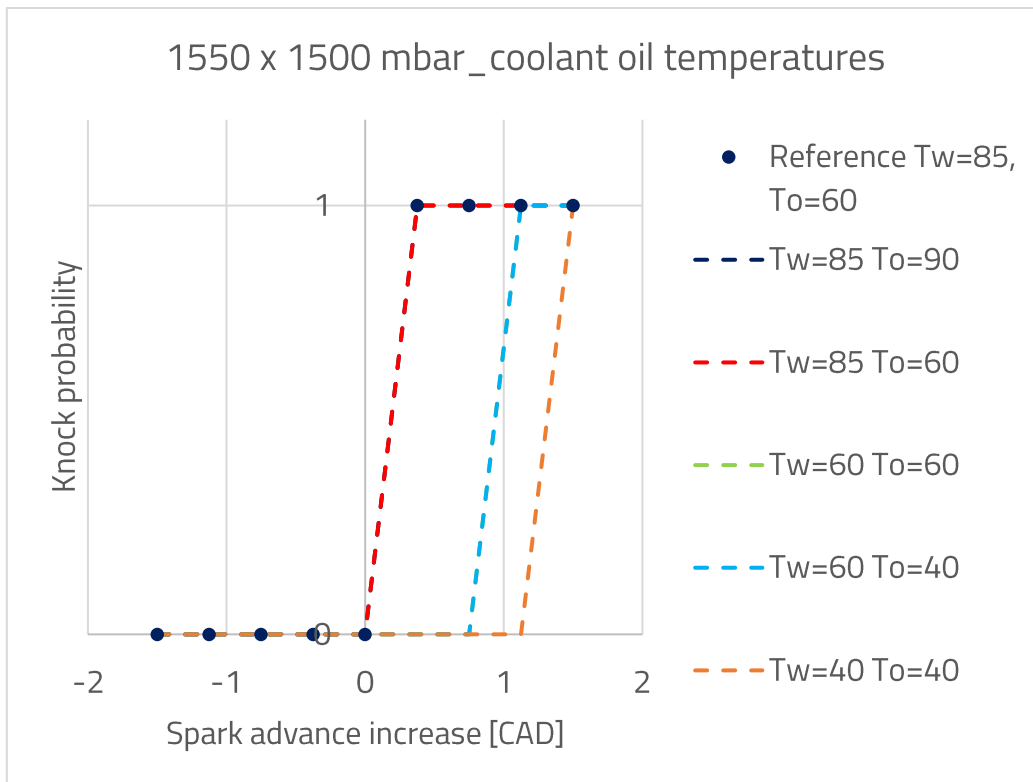


Figure 4-36: knock probability predictions for coolant and oil temperature sweeps at 1550x1500 mbar

The model is sensitive to coolant and oil temperatures variations when they were reduced below 60°C.

4.4. Sensitivity study for perspectives

4.4.1. Impact of heat transfer coefficient

The heat transfer model influences the trapped air mass inside the cylinder and this parameter represent an important impact on the knock occurrence. In this section a sensitivity study is carried out on the heat transfer coefficient (CHT) applied to the complete engine model and its behavior on the knock apparition is going to be studied.

Une heat transfer multiplier is applied to the Woschni heat transfer model in the engine model. In the model used in chapter 4, the CHT coefficient was set to 1.35.

The CHT heat transfer multiplier was modified and its influence on the air mass trapped is presented in figure 4-37

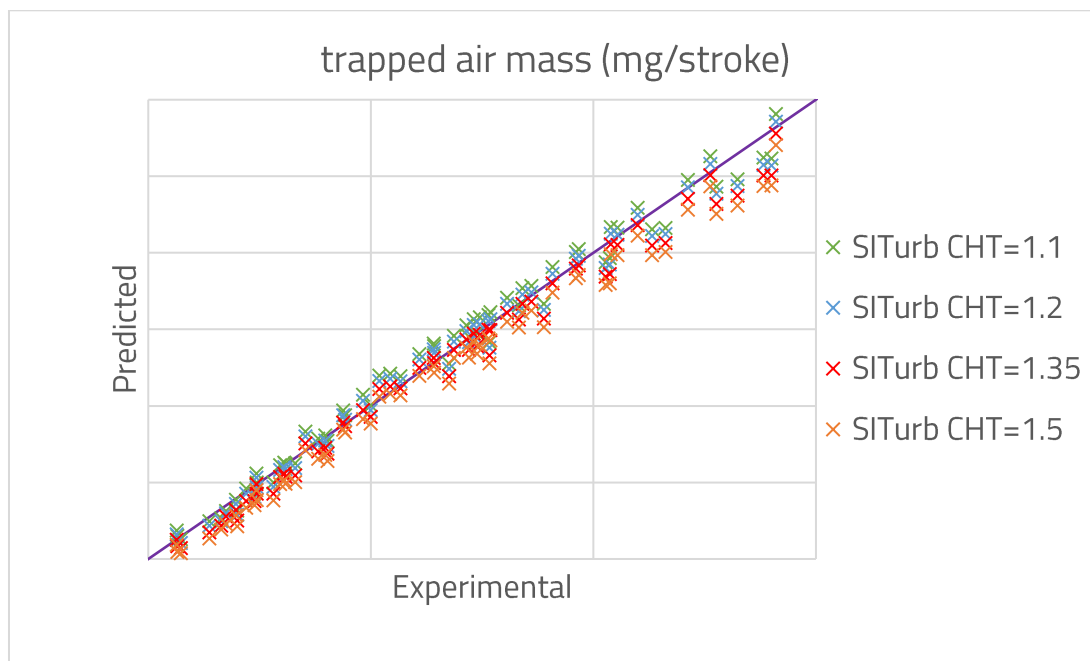


Figure 4-37: experimental (each division is 200 mg/stroke) vs predicted (each division is 100 mg/stroke) air mass trapped in function of the heat transfer multiplier

As it can be seen in figure 4-37, increasing the heat transfer multiplier decreases the predicted air mass trapped inside the cylinder

In the following figures, the predicted in-cylinder and burn rate on from some operating points from the performance maps are plotted again with a sweep of the heat transfer multiplier.

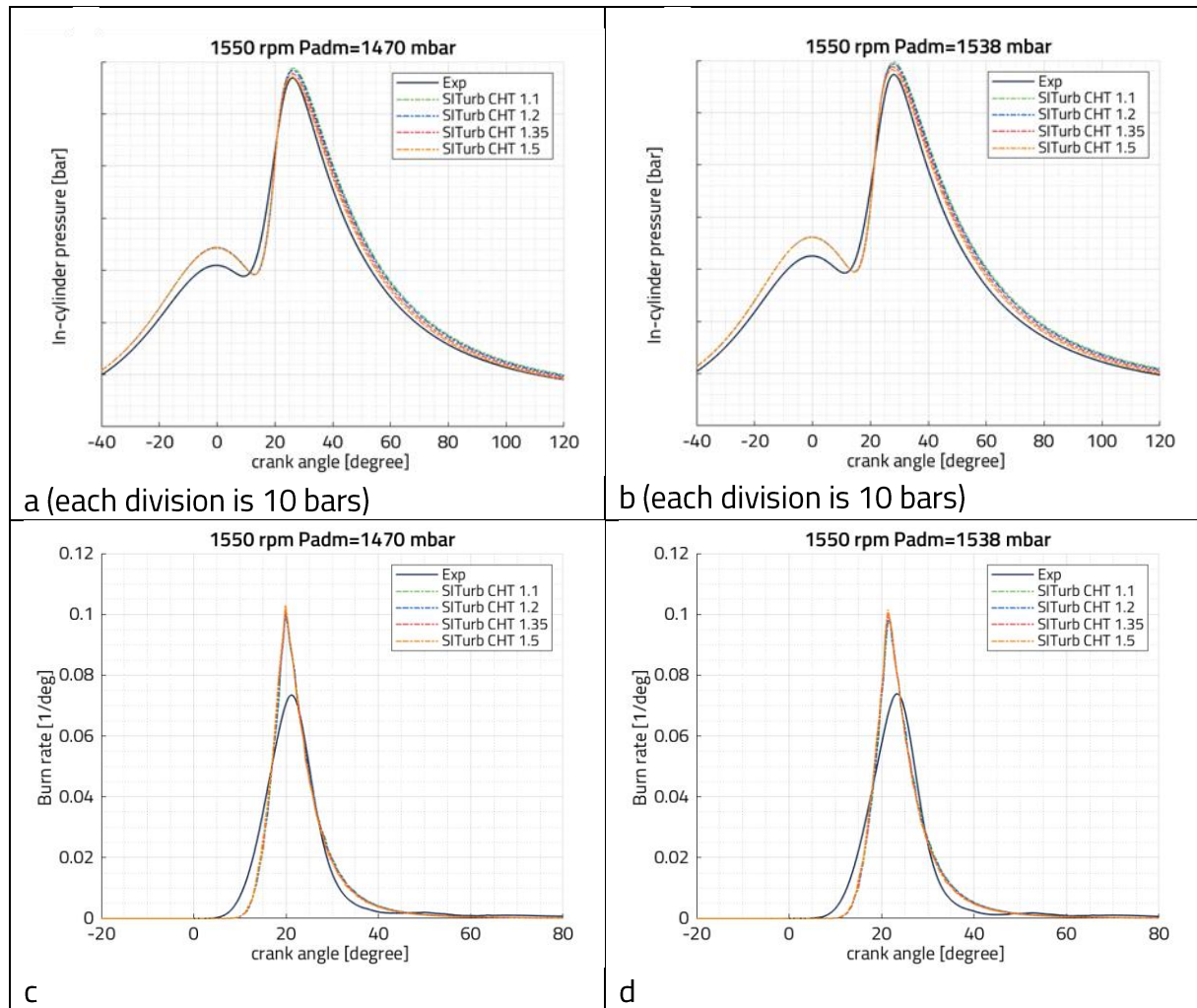
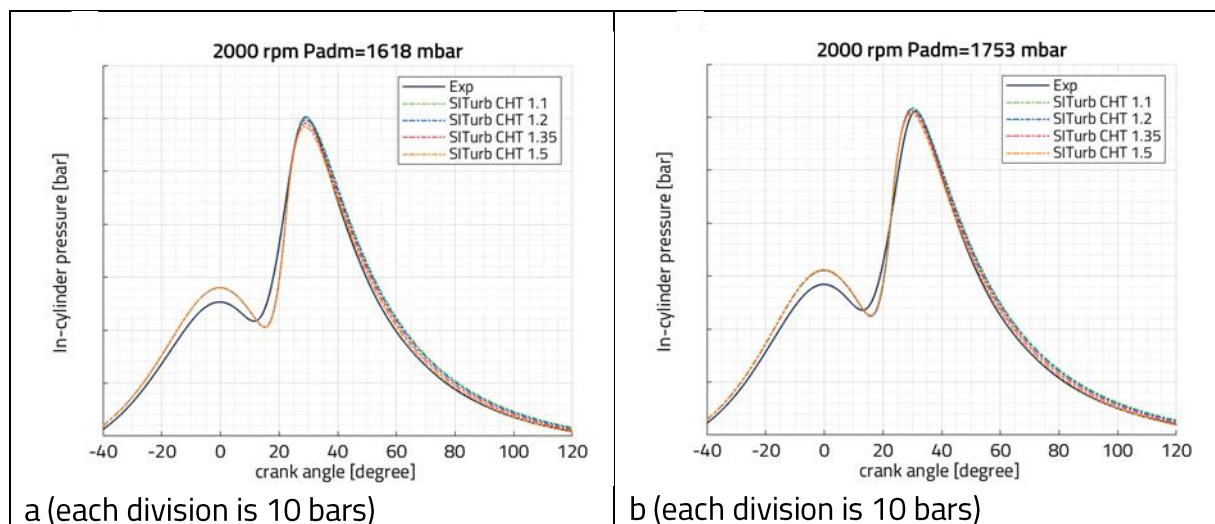


Figure 4-38: experimental vs SI-Turb prediction of in-cylinder pressures (a&b) and burn rates (c&d) for 2 operating points at 1550 rpm with the sensitivity of heat transfer multiplier



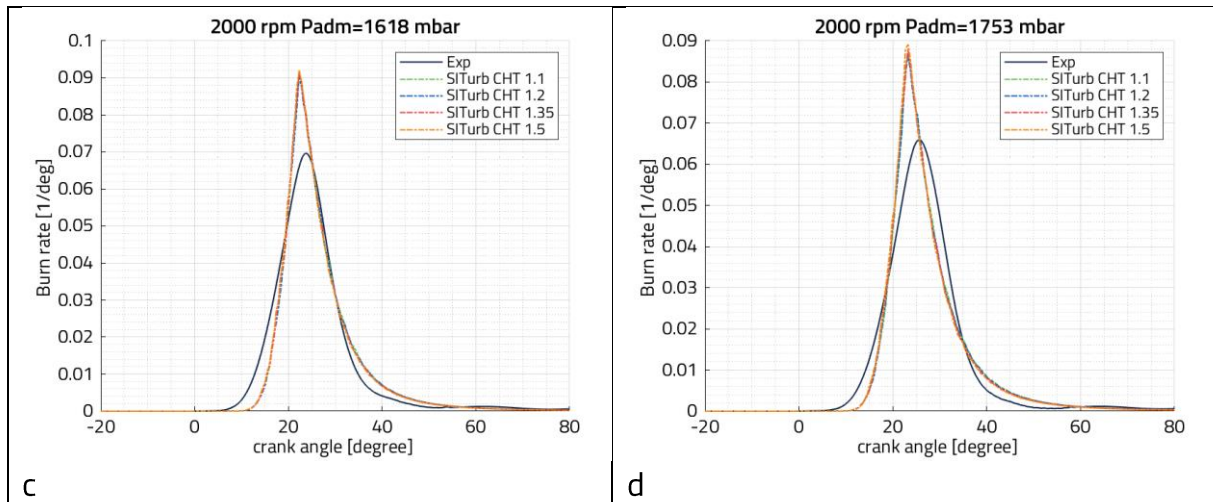


Figure 4-39: experimental vs SiTurb prediction of in-cylinder pressures (a&b) and burn rates (c&d) for 2 operating points at 2000 rpm with the sensitivity of heat transfer multiplier

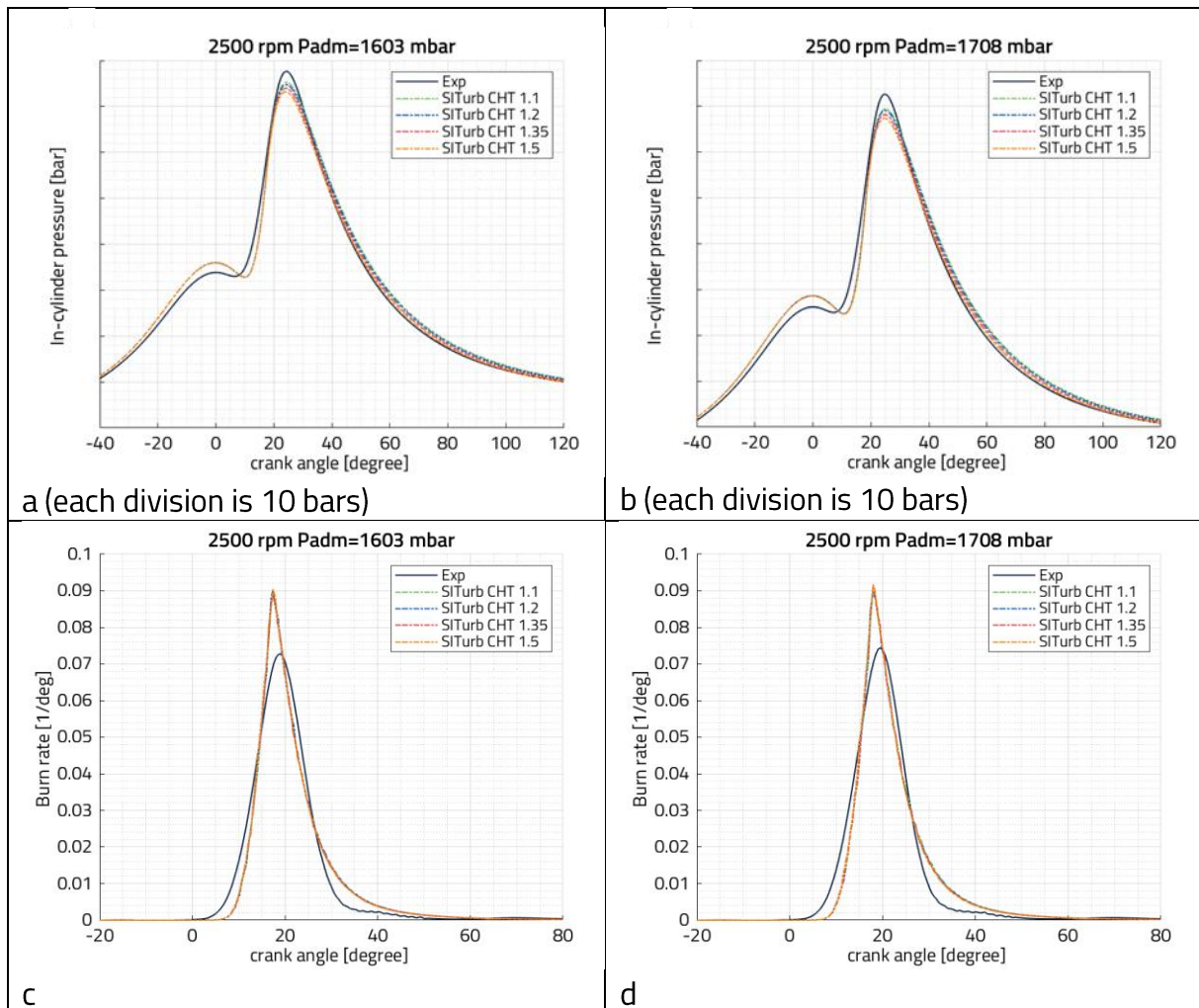


Figure 4-40: experimental vs SiTurb prediction of in-cylinder pressures (a&b) and burn rates (c&d) for 2 operating points at 2500 rpm with the sensitivity of heat transfer multiplier

The sweep of the heat transfer multiplier does not affect the end of compression pressure but it did affect the combustion development. In all of the cases, if the multiplier value increases the in-cylinder peak pressure decreases without any effect on the burn rate. The burn rate is unchanged with the multiplier sweep and only the air mass trapped was affected. The heat transfer model can thus affect the knock model as it affect the air mass trapped and consequently knock apparition could either be delayed or advanced.

In the following figures 4-41 and 4-42, the knock probability are plotted for 1550x1500 mbar for both overlapping and no overlapping conditions.

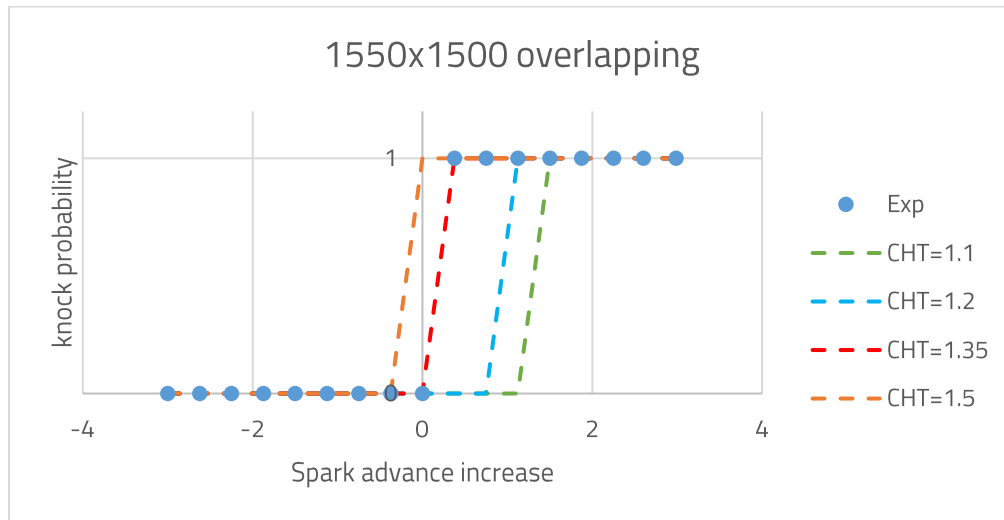


Figure 4-41: knock probability predictions with 1550x1500 overlapping with heat transfer multiplier sweep

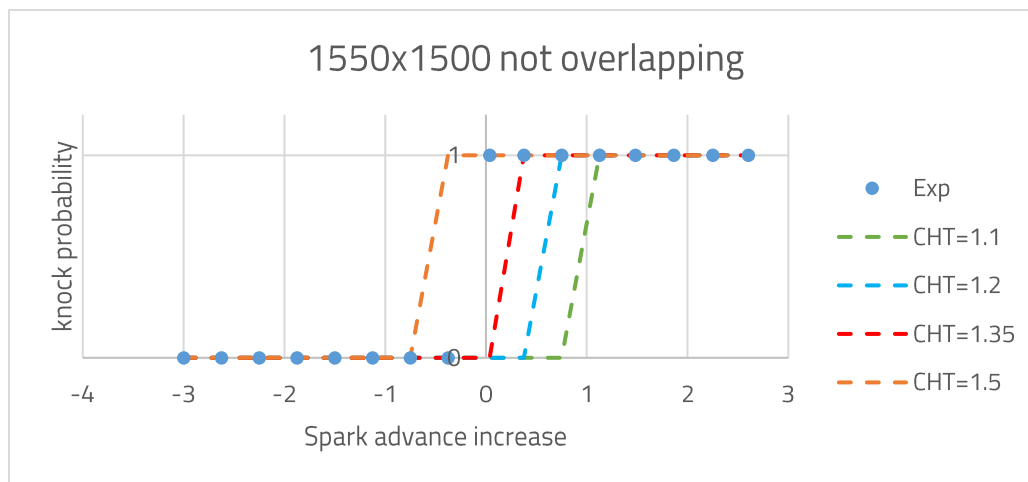


Figure 4-42: knock probability predictions with 1550x1500 no overlapping with heat transfer multiplier sweep

As it was observed on the in-cylinder pressure traces, the heat transfer multiplier affected the combustion development and consequently knock apparition. The knock probability was delayed as the coefficient is increased and was advanced when the coefficient is decreased. This corresponds to higher pressure peak when the coefficient decreases which compresses more the end-gas, reducing its auto-ignition delay and advancing its knock apparition.

4.4.2. Impact of the burn rate

As it was seen, the burn rate which is influenced by the combustion model plays a huge role in the in-cylinder pressure development which consequently can affect knock occurrence. In this sensitivity study, the experimental burn rate will be imposed to the complete engine model. The effect on knock occurrence will then be studied.

For 1550x1500 mbar and overlapping conditions:

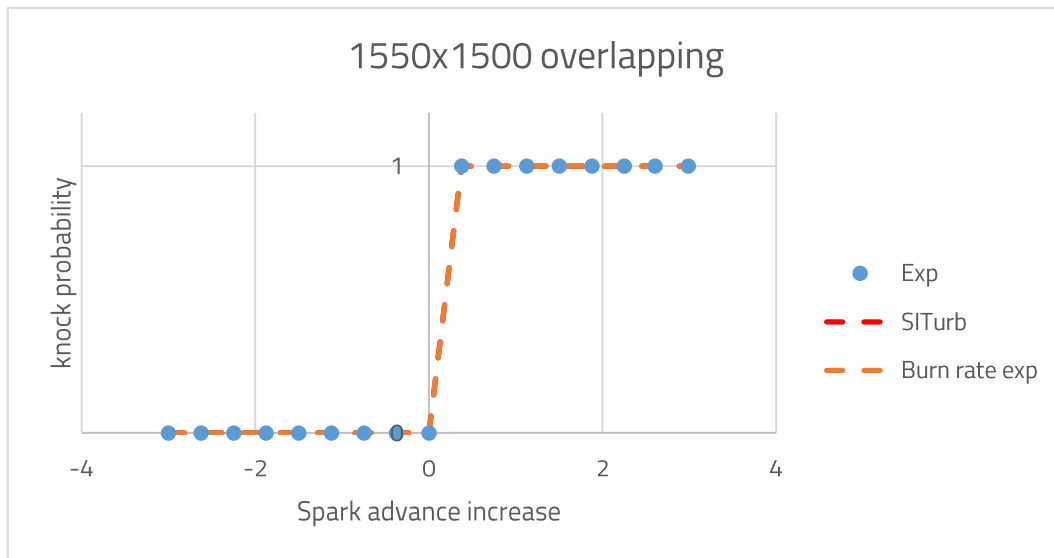


Figure 4-43: knock probability predictions at 1550x1500 overlapping with both SITurb and experimental burn rate imposed

As it can be seen in figure 4-43, imposing the burn rate did not affect the knock probability predictions at 1550x1500 mbar as it was accurately predicted by SITurb. For the crank angle at knock onset:

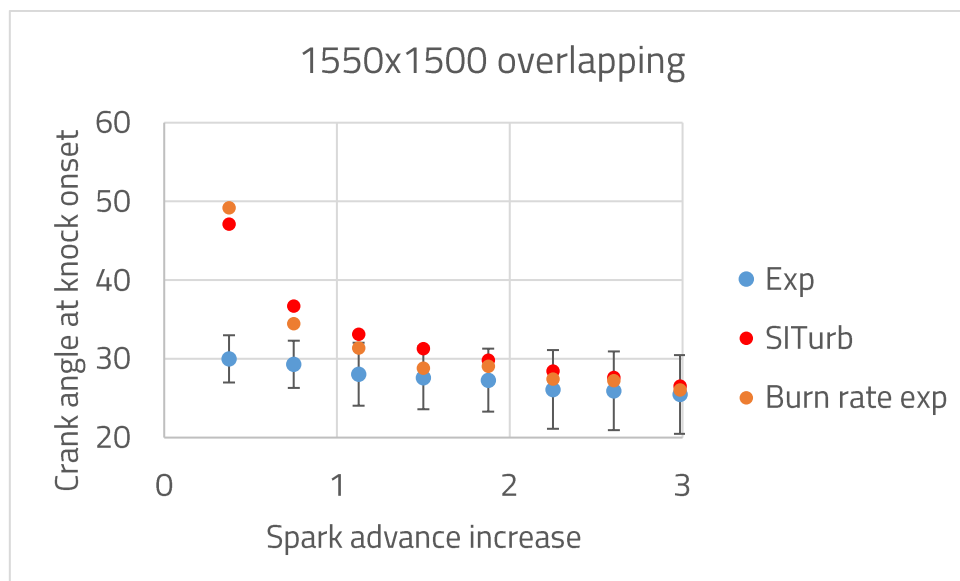


Figure 4-44: crank angle at knock onset predictions at 1550x1500 overlapping with both SITurb and experimental burn rate imposed

In figure 4-44, imposing the experimental burn rate improves a little bit the prediction of the crank angle at knock onset. However, and beyond 1 CAD of spark advance increase, both SITurb and experimental burn rate predict that crank angle within the cycle-by-cycle experimental range of that angle.

For the no overlapping conditions:

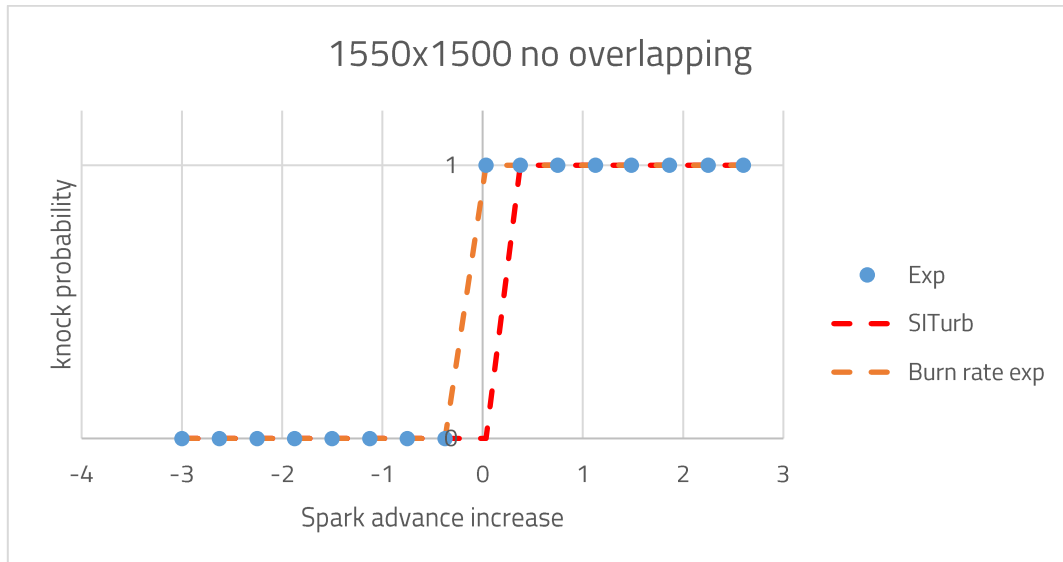


Figure 4-45: knock probability predictions at 1550x1500 no overlapping with both SITurb and experimental burn rate imposed

In the no-overlapping setting, imposing the burn rate predicts the knock probability with a 0.375 CAD of spark timing more accurately than the SITurb matching by that the experimental conditions as it can be seen in figure 4-45.

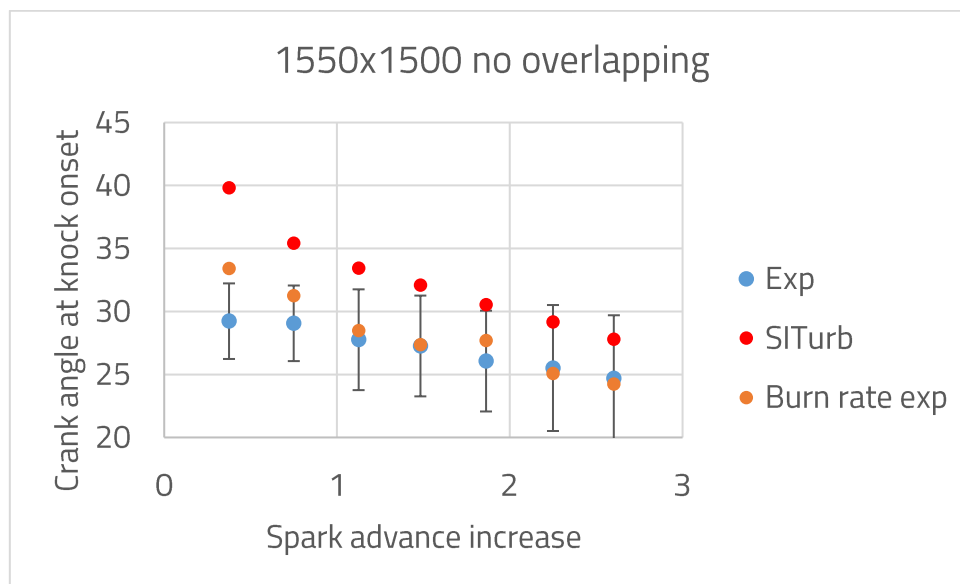


Figure 4-46: crank angle at knock onset predictions at 1550x1500 no overlapping with both SITurb and experimental burn rate imposed

Similarly as the overlapping settings, the experimental burn rate improves a little bit the crank angle at knock onset predictions. Moreover, and beyond 1.5 CAD of spark advance increase, both SITurb and experimental burn rate predict that crank angle within the cycle-by-cycle experimental range of that angle.

4.5. Conclusion of knock modeling and simulations

The "Kinetics Fit" model was chosen to estimate the onset of knocking. A first attempt of calibration aimed at finding the experimental crankshaft angle at knock onset. Calibrated, this model is not able to discriminate with good precision the engine conditions (in particular the level of spark timing) for which there may or may not be knocking cycles. Also, a second calibration procedure has been proposed that significantly improves knock detection, or in other words critical spark advance.

Then, sensitivity studies were performed using the full engine model including this knock model. Various engine control parameters were tested. For each change in the value of one of the control parameters, a variation of the spark advance was made so as to achieve the knocking combustions. The complete model compared to the results of the experiments shows a fairly good correlation between calculations and experiments in terms of the occurrence of the knock.

Le modèle « Kinetics Fit » a été retenu pour tenter d'estimer l'apparition du cliquetis. Une première tentative de calibration visant à retrouver l'angle vilebrequin expérimental d'apparition du cliquetis a tout d'abord été mise en œuvre. Ainsi calibré, ce modèle n'est pas capable de discriminer avec une bonne précision les conditions moteur (notamment niveau d'avance à l'allumage) pour lesquelles il y a ou non apparition de cycles cliquetants. Aussi, une deuxième procédure de calibration a été proposée et permet d'améliorer sensiblement la détection de cliquetis, ou autrement dit l'avance à l'allumage critique.

Ensuite, des études de sensibilité ont été réalisées en utilisant le modèle complet du moteur incluant ce modèle de cliquetis. Différents paramètres de contrôle moteur ont été testés. Pour chaque changement de valeur d'un des paramètres de contrôle, une variation d'avance à l'allumage a été réalisée de manière à atteindre le cliquetis. Le modèle complet confronté aux résultats de l'expérience montre une assez bonne adéquation calculs-expériences en termes d'apparition du cliquetis.

5. Conclusions and Perspectives

The work presented in this thesis consisted in first establishing a large database of tests to characterize, on a 3-cylinder turbocharged automobile spark-ignition internal combustion engine, the impact of the various control parameters on the occurrence of knock, and also on the physical parameters of influence such as the air filling, the equivalence ratio of the trapped mixture, the wall temperatures, the combustion rate, or the residual gas rate. The controlled parameters studied are: spark advance, air-to-fuel equivalence, coolant and oil temperatures, valves timing (intake and exhaust), intake temperature, the law of injection (number, quantities, and phasing of injections during the cycle). The main contributions of the experimental campaign can be summarized as follows:

- The variation of the valve timing has a different impact on the occurrence of knock depending on the operating point: for 1550x1500 mbar and 2000x1700 mbar, the valve overlap delays the occurrence of the knock because the quantity of residuals is reduced and the ignition delay of fresh gas is therefore longer. Whereas for 2500x1700 mbar, the fact of not overlapping the valves delays the onset of knock because the trapped air mass is reduced and this phenomenon is considered as a decrease in load and therefore a delay in knock.
- The onset of the knocking is delayed as long as the injection timing is delayed for a single injection in the admission stroke.
- The injections in the compression stroke delay the onset of the knock when compared to the injections in the intake stroke.
- The increase in the temperature of the intake air increases the occurrence of knock. On the knock margin and on average, 0.75 CAD of spark timing can be achieved by a 10 ° C decrease in intake air temperature.
- The decrease in coolant temperature led to a faster burning rate which consumed the fresh gas before it auto-ignited and delayed the onset of knocking.

Secondly, a complete procedure for modeling the onset of knocking combustion on a turbocharged spark-ignition engine was proposed. A complete model of the study engine was developed in the GT-Power environment. The semi-predictive combustion model used is the SI-Turb model, for which a calibration procedure has been implemented. It allows you to find the main characteristics such as the CA50, the combustion time, the maximum in-cylinder pressure, or the IMEP over the entire engine operating range. Regarding the specific knocking model, the "Kinetics Fit" model was chosen and an original calibration methodology was developed. This consists, not only in finding the experimental crankshaft angle at knock onset, but also in introducing a new objective in the calibration to separate with good precision the engine conditions (in particular the level of spark timing) for which there may or may not be knocking cycles.

The calibrated model significantly improves knock detection, or in other words critical spark timing. Overall, the complete model compared to the results of the experiments shows a fairly good match between calculations and experiments in terms of the occurrence of the knock. In more detail, the main conclusions are listed below:

- The Kinetics Fit phenomenological knock model has shown acceptable results in predicting knock, particularly at the level of the crankshaft angle at the onset of knock.
- The knock index appears to have a linear relationship with the increase in spark advance in the Kinetics Fit model. In the experimental results, the knock index is a quadratic function of the increase in spark advance.
- When the valve timings were changed in 1550x1500 mbar and 2000x1700 mbar, the knock index does not show significant differences between overlapping and non-overlapping cases. However, these valve timing effects were observed on the 2500 x 1700 mbar because they involved a variation in cylinder load and therefore a variation in knock prediction.
- The effect of injection timing on the onset of knocking can be observed by the Kinetics Fit. The results are compatible with the experiments: the model delays the onset of the knock when the injection timing is delayed.
- The effect of intake air temperature can be observed by the knock model. The results obtained by the model are consistent with the experiments: the occurrence of the knocking combustion increases with the temperature of the intake air.
- The knock model is less sensitive to changes in coolant and oil temperature than the sweep of other control parameters. It delays the onset of knocking when the coolant temperature is too low.

In addition, a sensitivity study to the knocking model input data was carried out, in particular on the level of heat losses and on the calculation of the heat release rate.

The work presented in this thesis brings several **perspectives**:

From an **experimental** point of view:

- The experimental study carried out in this work has shown that physical phenomena are inter-correlated. It could be interesting to try to study the separate influence of each of the phenomena (examples: study of the residuals independently of the temperature of the enclosed gases or of the wall temperatures, study of the residuals at fixed levels of turbulence at the end of the intake stroke)
- In addition, a detailed analysis of the impact of cycle-to-cycle dispersions on the occurrence of knock could be carried out, based in particular on individual cylinder pressure readings.

From a numerical point of view:

- As a first step, in order to be able to compare the results of the experiments with the simulation results, it would be good to define a common indicator for the intensity of the knock. For example, by modeling cycle-to-cycle dispersions, it would then be possible to define a probability of the knocking cycles.
- For better sensitivity of the control parameters, the knock model can also be calibrated using a wider choice of operating points with a sweep of one or more engine control parameters.
- The occurrence of knocking combustion being particularly dependent on the level of stratification in the combustion chamber, an interesting development would consist in having phenomenological models of combustion and auto-ignition taking into account the level of stratification.
- Similarly, it would be relevant to improve the modeling of heat transfers to the walls, so as to better estimate the temperatures of the fresh gases and their auto-ignition.

Le travail présenté dans ce mémoire a consisté à établir dans un premier temps une large base de données d'essais pour caractériser, sur un moteur 3 cylindres automobile suralimenté à allumage commandé, l'impact des différents paramètres de contrôle sur l'apparition de cliquetis, mais également sur les paramètres physiques d'influence tels que le remplissage en air, la richesse du mélange enfermé, les températures de parois, le taux de combustion, ou encore le taux de gaz résiduels. Les paramètres de contrôlé étudiés sont : l'avance à l'allumage, la richesse, les températures de liquide de refroidissement et d'huile, le calage de la distribution (admission et échappement), la température d'admission, la loi d'injection directe de carburant (nombre, quantités, et phasages des injections au cours du cycle). Les principaux apports de la campagne expérimentale peuvent être résumés comme suit :

- La variation du calage des soupapes impacte différemment l'apparition du cliquetis selon le point de fonctionnement : pour les points 1550 tr/min / 1500 mbar et 2000 tr/min / 1700 mbar, le croisement des soupapes retarde l'apparition du cliquetis car la quantité de résidus est réduite et le délai d'allumage du gaz frais est donc plus long. Alors que pour le point 2500tr/min / 1700 mbar, le fait de décroiser les soupapes retarde l'apparition du cliquetis car la masse d'air enfermée est réduite, ce qui équivaut à une diminution de charge.
- L'apparition du cliquetis est repoussée lorsque l'injection est retardée pour une injection simple en admission.
- Les injections dans la phase de compression retardent l'apparition du cliquetis par rapport aux injections dans la course d'admission.
- L'augmentation de la température de l'air d'admission augmente l'apparition de cliquetis, conduisant en moyenne à une réduction de 0,75 °V d'avance à l'allumage pour une augmentation de 10 °C.
- La diminution de la température du liquide de refroidissement conduit à une vitesse de flamme plus élevée, ce qui conduit à une retardation de l'apparition du cliquetis.

Dans un deuxième temps, une procédure complète de modélisation de l'apparition du cliquetis sur un moteur à allumage commandé suralimenté a été proposée. Un modèle complet du moteur de l'étude a été développée dans l'environnement GT-Power. Le modèle semi-prédictif pour la combustion utilisé est le modèle SI-Turb, pour lequel une procédure de calibration a été mise en place. Il permet de retrouver les principales caractéristiques telles que le CA50, la durée de combustion, la pression maximale dans le cylindre, ou la PMI sur l'ensemble du champ de fonctionnement moteur. S'agissant du modèle spécifique de cliquetis, le modèle « Kinetics Fit » a été retenu et une méthodologie de calibration originale a été développée. Celle-ci consiste, non pas uniquement à retrouver l'angle vilebrequin expérimental d'apparition du cliquetis, mais également à introduire un nouvel objectif dans la calibration pour discriminer avec une bonne précision les conditions moteur (notamment niveau d'avance à l'allumage) pour lesquelles il y a ou non apparition de cycles cliquetants.

Le modèle ainsi calibré permet d'améliorer sensiblement la détection de cliquetis, ou autrement dit l'avance à l'allumage critique. Globalement, le modèle complet confronté aux résultats de l'expérience montre une assez bonne adéquation calculs-expériences en termes d'apparition du cliquetis. Plus en détails, les principales conclusions sont listées ci-après :

- Le modèle phénoménologique de cliquetis Kinetics Fit a montré des résultats acceptables pour prédire le cliquetis, en particulier au niveau de l'angle de vilebrequin au début du cliquetis.
- L'indice de cliquetis semble avoir une relation linéaire avec l'augmentation de l'avance à l'allumage dans le modèle Kinetics Fit. Dans les résultats expérimentaux, l'indice de cliquetis est une fonction quadratique de l'augmentation de l'avance à l'allumage.
- Lorsque les calages des soupapes ont été modifiés sur les points 1550x1500 mbar et 2000x1700 mbar, l'indice de cliquetis ne montre pas de différences significatives entre les cas croisés et non croisés. Cependant, ces effets de synchronisation des soupapes ont été observés sur les 2500 x 1700 mbar car ils impliquaient une variation de charge dans le cylindre et donc une variation de prédiction de cliquetis.
- L'effet du temps d'injection sur l'apparition du cliquetis peut être observé par le Kinetics Fit. Les résultats sont compatibles avec les expériences : le modèle retarde l'apparition du cliquetis quand le temps d'injection est retardé.
- L'effet de la température de l'air d'admission peut être observé par le modèle de cliquetis. Les résultats obtenus par le modèle sont compatibles avec les expériences : l'apparition du cliquetis augmente avec la température de l'air d'admission.
- Le modèle de cliquetis est moins sensible aux variations de température du liquide de refroidissement et de l'huile que le balayage des autres paramètres de contrôle. Il retarde l'apparition du cliquetis lorsque la température du liquide de refroidissement est fortement réduite.

En outre, une étude de sensibilité aux données d'entrée du modèle de cliquetis a été menée, en particulier sur le niveau de pertes aux parois et sur le calcul du taux de dégagement de chaleur.

Le travail présenté dans ce mémoire amène plusieurs **perspectives** :

D'un point de vue **expérimental** :

- L'étude expérimentale menée dans ce travail a montré que les phénomènes physiques sont inter-corrélés. Il pourrait être intéressant de tenter d'étudier l'influence séparée de chacun des phénomènes (exemples : étude des résiduels indépendamment de la température des gaz enfermés ou des températures de parois, étude des résiduels à iso niveau de turbulence en fin d'admission,)
- Par ailleurs, une analyse détaillée sur l'impact des dispersions cycle à cycle sur l'apparition du cliquetis pourrait être menée, sur la base notamment des relevés individuels de pression cylindre.

D'un point de vue numérique :

- *Dans un premier temps, de manière à pouvoir comparer résultats de l'expériences avec les résultats de simulation, il serait bien de définir un indicateur commun pour l'ampleur du cliquetis. Par exemple, en modélisant les dispersions cycle à cycle, il serait alors possible de définir une probabilité d'apparition du cliquetis.*
- *Pour une meilleure sensibilité des paramètres de contrôle, le modèle de cliquetis peut également être réglé sur un plus large choix de points de fonctionnement avec un balayage d'un ou plusieurs paramètres de contrôle du moteur.*
- *L'apparition du cliquetis étant notamment dépendante du niveau de stratification de richesse dans la chambre de combustion, une évolution intéressante consisterait à disposer de modèles phénoménologiques de combustion et d'auto-inflammation prenant en compte le niveau de stratification.*
- *De même, il serait pertinent d'améliorer la modélisation des transferts aux parois, de manière à mieux estimer les températures des gaz frais et leur auto-inflammation.*

References

- [1] S. Demesoukas, "0D/1D combustion modeling for the combustion systems optimization of spark ignition engines," Université d'Orléans, 2015.
- [2] T. Poinso and D. Veynante, *theoretical and numerical combustion 3rd edition*, 3rd ed. 2012.
- [3] J. Jarosinski, "The thickness of laminar flames," *Combustion and Flame*, vol. 56, no. 3, pp. 337–342, Jun. 1984, doi: 10.1016/0010-2180(84)90067-1.
- [4] Y. B. Zeldovich, *Theory of combustion and detonation gases*. Academy of Moscow, 1944.
- [5] R. J. BLINT, "The Relationship of the Laminar Flame Width to Flame Speed," *Combustion Science and Technology*, vol. 49, no. 1–2, pp. 79–92, Sep. 1986, doi: 10.1080/00102208608923903.
- [6] C. Endouard, "Etude expérimentale de la dynamique des flammes de prémélange iso-octane/air en expansion laminaire et turbulente fortement diluées," p. 201.
- [7] B. Karlovitz and D. W. Denniston, "STUDIES ON TURBULENT FLAMES A. Flame Propagation Across Velocity Gradients," p. 8.
- [8] G. H. Markstein, *Non-steady flame propagation*. Oxford: Pergaman Press, 1964.
- [9] F. A. Williams, "A review of some theoretical considerations of turbulent flame structure," *Agard conf. Proceeding*, 1975.
- [10] M. Matalon and B. J. Matkowsky, "Flames as gasdynamic discontinuities," *Journal of Fluid Mechanics*, vol. 124, no. 1, p. 239, Nov. 1982, doi: 10.1017/S0022112082002481.
- [11] F. Halter, T. Tahtouh, and C. Mounaïm-Rousselle, "Nonlinear effects of stretch on the flame front propagation," *Combustion and Flame*, vol. 157, no. 10, pp. 1825–1832, Oct. 2010, doi: 10.1016/j.combustflame.2010.05.013.
- [12] P. Clavin, "Dynamic behavior of premixed flame fronts in laminar and turbulent flows," *Progress in Energy and Combustion Science*, vol. 11, no. 1, pp. 1–59, Jan. 1985, doi: 10.1016/0360-1285(85)90012-7.
- [13] P. G. Aleiferis, J. Serras-Pereira, and D. Richardson, "Characterisation of flame development with ethanol, butanol, iso-octane, gasoline and methane in a direct-injection spark-ignition engine," *Fuel*, vol. 109, pp. 256–278, Jul. 2013, doi: 10.1016/j.fuel.2012.12.088.
- [14] O. Cadot, "Introduction à la turbulence, cours de l'ENSTA-ParisTech 2A," p. 85.
- [15] N. Peters, "Laminar flamelet concepts in turbulent combustion," *Symposium (International) on Combustion*, vol. 21, no. 1, pp. 1231–1250, Jan. 1988, doi: 10.1016/S0082-0784(88)80355-2.
- [16] N. Peters, "The turbulent burning velocity for large-scale and small-scale turbulence," *Journal of Fluid Mechanics*, vol. 384, pp. 107–132, Apr. 1999, doi: 10.1017/S0022112098004212.
- [17] G. Damkohler, "EINFLISSE DER STROMUNG, DIF'FUSION LTND DES WARMEBERGANGES AUF DIE LEISTUNG VON REAKTIONSOFFEN.," p. 17.
- [18] R. Borghi, "On the Structure and Morphology of Turbulent Premixed Flames," in *Recent Advances in the Aerospace Sciences*, C. Casci and C. Bruno, Eds. Boston, MA: Springer US, 1985, pp. 117–138. doi: 10.1007/978-1-4684-4298-4_7.
- [19] M. A. Hossain, "DESIGN OF A HIGH INTENSITY TURBULENT COMBUSTION SYSTEM," p. 165.
- [20] V. De Bellis, F. Bozza, and D. Tufano, "A Comparison Between Two Phenomenological Combustion Models Applied to Different SI Engines," presented at the International Powertrains, Fuels & Lubricants Meeting, Oct. 2017. doi: 10.4271/2017-01-2184.
- [21] J. Heywood, *Internal combustion engines fundamentals*, McGraw-Hill.

- [22] Z. Wang, H. Liu, and R. D. Reitz, "Knocking combustion in spark-ignition engines," *Progress in Energy and Combustion Science*, vol. 61, pp. 78–112, Jul. 2017, doi: 10.1016/j.pecs.2017.03.004.
- [23] G. T. Kalghatgi, D. Bradley, J. Andrae, and A. J. Harrison, "The nature of 'superknock' and its origins in SI engines," p. 14.
- [24] E. Winklhofer, A. Hirsch, P. Kapus, M. Kortschak, and H. Philipp, "TC GDI Engines at Very High Power Density — Irregular Combustion and Thermal Risk," Sep. 2009, pp. 2009-24-0056. doi: 10.4271/2009-24-0056.
- [25] M. Amann, T. Alger, and D. Mehta, "The Effect of EGR on Low-Speed Pre-Ignition in Boosted SI Engines," *SAE Int. J. Engines*, vol. 4, no. 1, pp. 235–245, Apr. 2011, doi: 10.4271/2011-01-0339.
- [26] Z. Wang *et al.*, "Relationship between super-knock and pre-ignition," *International Journal of Engine Research*, vol. 16, no. 2, pp. 166–180, Feb. 2015, doi: 10.1177/1468087414530388.
- [27] E. Chapman, R. S. Davis, W. Studzinski, and P. Geng, "Fuel Octane and Volatility Effects on the Stochastic Pre-Ignition Behavior of a 2.0L Gasoline Turbocharged DI Engine," *SAE Int. J. Fuels Lubr.*, vol. 7, no. 2, pp. 379–389, Apr. 2014, doi: 10.4271/2014-01-1226.
- [28] D. Bradley and G. T. Kalghatgi, "Influence of autoignition delay time characteristics of different fuels on pressure waves and knock in reciprocating engines," *Combustion and Flame*, vol. 156, no. 12, pp. 2307–2318, Dec. 2009, doi: 10.1016/j.combustflame.2009.08.003.
- [29] G. Bansal and H. G. Im, "Autoignition and front propagation in low temperature combustion engine environments," *Combustion and Flame*, vol. 158, no. 11, pp. 2105–2112, Nov. 2011, doi: 10.1016/j.combustflame.2011.03.019.
- [30] J.-M. Zaccardi, L. Duval, and A. Pagot, "Development of Specific Tools for Analysis and Quantification of Pre-ignition in a Boosted SI Engine," *SAE Int. J. Engines*, vol. 2, no. 1, pp. 1587–1600, Jun. 2009, doi: 10.4271/2009-01-1795.
- [31] C. Dahnz, K.-M. Han, U. Spicher, M. Magar, R. Schiessl, and U. Maas, "Investigations on Pre-Ignition in Highly Supercharged SI Engines," *SAE Int. J. Engines*, vol. 3, no. 1, pp. 214–224, Apr. 2010, doi: 10.4271/2010-01-0355.
- [32] Z. Wang, Y. Xu, and J. Wang, "Suppression of super-knock in TC-GDI engine using two-stage injection in intake stroke (TSII)," *Sci. China Technol. Sci.*, vol. 57, no. 1, pp. 80–85, Jan. 2014, doi: 10.1007/s11431-013-5374-3.
- [33] G. T. Kalghatgi, D. Bradley, J. Andrae, and A. J. Harrison, "The nature of 'superknock' and its origins in SI engines," p. 14.
- [34] N. Peters, B. Kerschgens, and G. Paczko, "Super-Knock Prediction Using a Refined Theory of Turbulence," *SAE Int. J. Engines*, vol. 6, no. 2, pp. 953–967, Apr. 2013, doi: 10.4271/2013-01-1109.
- [35] G. T. Kalghatgi, "Developments in internal combustion engines and implications for combustion science and future transport fuels," *Proceedings of the Combustion Institute*, vol. 35, no. 1, pp. 101–115, 2015, doi: 10.1016/j.proci.2014.10.002.
- [36] C. Dahnz and U. Spicher, "Irregular combustion in supercharged spark ignition engines – pre-ignition and other phenomena," *International Journal of Engine Research*, vol. 11, no. 6, pp. 485–498, Dec. 2010, doi: 10.1243/14680874JER609.
- [37] G. Lim, S. Lee, C. Park, Y. Choi, and C. Kim, "Effect of ignition timing retard strategy on NO_x reduction in hydrogen-compressed natural gas blend engine with increased compression ratio," *International Journal of Hydrogen Energy*, vol. 39, no. 5, pp. 2399–2408, Feb. 2014, doi: 10.1016/j.ijhydene.2013.11.131.

- [38] X. Zhen *et al.*, "The engine knock analysis – An overview," *Applied Energy*, vol. 92, pp. 628–636, Apr. 2012, doi: 10.1016/j.apenergy.2011.11.079.
- [39] M. Abu-Qudais, "GAS TEMPERATURE FOR KNOCK AND CONTROL IN SPARK IGNITION ENGINE," p. 10.
- [40] Y. Duchaussoy, A. Lefebvre, and R. Bonetto, "Dilution Interest on Turbocharged SI Engine Combustion," Mar. 2003, pp. 2003-01–0629. doi: 10.4271/2003-01-0629.
- [41] E. Singh and R. Dibble, "Effectiveness of Fuel Enrichment on Knock Suppression in a Gasoline Spark-Ignited Engine," Sep. 2018, pp. 2018-01–1665. doi: 10.4271/2018-01-1665.
- [42] S. Potteau, P. Lutz, S. Leroux, S. Moroz, and E. Tomas, "Cooled EGR for a Turbo SI Engine to Reduce Knocking and Fuel Consumption," Oct. 2007, pp. 2007-01–3978. doi: 10.4271/2007-01-3978.
- [43] L. Teodosio, V. De Bellis, and F. Bozza, "Fuel Economy Improvement and Knock Tendency Reduction of a Downsized Turbocharged Engine at Full Load Operations through a Low-Pressure EGR System," *SAE Int. J. Engines*, vol. 8, no. 4, pp. 1508–1519, Apr. 2015, doi: 10.4271/2015-01-1244.
- [44] Y. Qi, K. K. Srinivasan, S. R. Krishnan, H. Yang, and K. C. Midkiff, "Effect of hot exhaust gas recirculation on the performance and emissions of an advanced injection low pilot-ignited natural gas engine," *International Journal of Engine Research*, vol. 8, no. 3, pp. 289–303, Jun. 2007, doi: 10.1243/14680874JER02306.
- [45] K. Kumano and S. Yamaoka, "Analysis of Knocking Suppression Effect of Cooled EGR in Turbo-Charged Gasoline Engine," Apr. 2014, pp. 2014-01–1217. doi: 10.4271/2014-01-1217.
- [46] B. Hoepke, S. Jannsen, E. Kasseris, and W. K. Cheng, "EGR Effects on Boosted SI Engine Operation and Knock Integral Correlation," *SAE Int. J. Engines*, vol. 5, no. 2, pp. 547–559, Apr. 2012, doi: 10.4271/2012-01-0707.
- [47] D. Parsons, S. Akehurst, and C. Brace, "The potential of catalysed exhaust gas recirculation to improve high-load operation in spark ignition engines," *International Journal of Engine Research*, vol. 16, no. 4, pp. 592–605, Jun. 2015, doi: 10.1177/1468087414554628.
- [48] J. Su, M. Xu, T. Li, Y. Gao, and J. Wang, "Combined effects of cooled EGR and a higher geometric compression ratio on thermal efficiency improvement of a downsized boosted spark-ignition direct-injection engine," *Energy Conversion and Management*, vol. 78, pp. 65–73, Feb. 2014, doi: 10.1016/j.enconman.2013.10.041.
- [49] H. Wei, T. Zhu, G. Shu, L. Tan, and Y. Wang, "Gasoline engine exhaust gas recirculation – A review," *Applied Energy*, vol. 99, pp. 534–544, Nov. 2012, doi: 10.1016/j.apenergy.2012.05.011.
- [50] E. Galloni, G. Fontana, and R. Palmaccio, "Effects of exhaust gas recycle in a downsized gasoline engine," *Applied Energy*, vol. 105, pp. 99–107, May 2013, doi: 10.1016/j.apenergy.2012.12.046.
- [51] H. Xie, K. Xu, M. Wan, T. Chen, and H. Zhao, "Investigations into the influence of internal and external exhaust gas recirculation on the combustion stability in an optical gasoline spark ignition engine," *Proceedings of the Institution of Mechanical Engineers, Part D: Journal of Automobile Engineering*, vol. 229, no. 11, pp. 1514–1528, Sep. 2015, doi: 10.1177/0954407014565800.
- [52] S. Potteau, P. Lutz, S. Leroux, S. Moroz, and E. Tomas, "Cooled EGR for a Turbo SI Engine to Reduce Knocking and Fuel Consumption," Oct. 2007, pp. 2007-01–3978. doi: 10.4271/2007-01-3978.
- [53] L. Teodosio, V. De Bellis, and F. Bozza, "Fuel Economy Improvement and Knock Tendency Reduction of a Downsized Turbocharged Engine at Full Load Operations through a Low-

- Pressure EGR System," *SAE Int. J. Engines*, vol. 8, no. 4, pp. 1508–1519, Apr. 2015, doi: 10.4271/2015-01-1244.
- [54] K. Kumano and S. Yamaoka, "Analysis of Knocking Suppression Effect of Cooled EGR in Turbo-Charged Gasoline Engine," Apr. 2014, pp. 2014-01–1217. doi: 10.4271/2014-01-1217.
- [55] K. Yeom and C. Bae, "Stratified liquefied petroleum gas—dimethyl ether compression ignition engine combustion at various intake valve open timings," *International Journal of Engine Research*, vol. 11, no. 3, pp. 187–197, Jun. 2010, doi: 10.1243/14680874JER552.
- [56] Y. Li, H. Zhao, B. Leach, and T. Ma, "Development of a fuel stratification spark ignition engine," *Proceedings of the Institution of Mechanical Engineers, Part D: Journal of Automobile Engineering*, vol. 219, no. 7, pp. 923–934, Jul. 2005, doi: 10.1243/095440705X11220.
- [57] Y. Bai, J. Wang, Z. Wang, and S. Shuai, "Knocking Suppression by Stratified Stoichiometric Mixture With Two-Zone Homogeneity in a DISI Engine," *Journal of Engineering for Gas Turbines and Power*, vol. 135, no. 1, p. 012803, Jan. 2013, doi: 10.1115/1.4005113.
- [58] M. Costa, P. Sementa, U. Sorge, F. Catapano, G. Marseglia, and B. M. Vaglieco, "Split Injection in a GDI Engine Under Knock Conditions: An Experimental and Numerical Investigation," Sep. 2015, pp. 2015-24–2432. doi: 10.4271/2015-24-2432.
- [59] Z. Wang, H. Liu, Y. Long, J. Wang, and X. He, "Comparative study on alcohols–gasoline and gasoline–alcohols dual-fuel spark ignition (DFSI) combustion for high load extension and high fuel efficiency," *Energy*, vol. 82, pp. 395–405, Mar. 2015, doi: 10.1016/j.energy.2015.01.049.
- [60] Y. Li, H. Zhao, and T. Ma, "Stratification of fuel for better engine performance," *Fuel*, vol. 85, no. 4, pp. 465–473, Mar. 2006, doi: 10.1016/j.fuel.2005.08.005.
- [61] A. Mohammadi, M. Shioji, Y. Nakai, W. Ishikura, and E. Tabo, "Performance and combustion characteristics of a direct injection SI hydrogen engine," *International Journal of Hydrogen Energy*, vol. 32, no. 2, pp. 296–304, Feb. 2007, doi: 10.1016/j.ijhydene.2006.06.005.
- [62] Z. Wang, Y. Xu, and J. Wang, "Suppression of super-knock in TC-GDI engine using two-stage injection in intake stroke (TSII)," *Sci. China Technol. Sci.*, vol. 57, no. 1, pp. 80–85, Jan. 2014, doi: 10.1007/s11431-013-5374-3.
- [63] L. Zhou, A. Shao, J. Hua, H. Wei, and D. Feng, "Effect of Retarded Injection Timing on Knock Resistance and Cycle to Cycle Variation in Gasoline Direct Injection Engine," *Journal of Energy Resources Technology*, vol. 140, no. 7, p. 072202, Jul. 2018, doi: 10.1115/1.4039322.
- [64] E. Singh, K. Morganti, and R. Dibble, "Optimizing split fuel injection strategies to avoid pre-ignition and super-knock in turbocharged engines," *International Journal of Engine Research*, vol. 22, no. 1, pp. 199–221, Jan. 2021, doi: 10.1177/1468087419836591.
- [65] S. Luisi, V. Doria, A. Stroppiana, F. Mollo, and M. Mirzaeian, "Experimental Investigation on Early and Late Intake Valve Closures for Knock Mitigation through Miller Cycle in a Downsized Turbocharged Engine," Apr. 2015, pp. 2015-01–0760. doi: 10.4271/2015-01-0760.
- [66] H. Hirooka, S. Mori, and R. Shimizu, "Effects of High Turbulence Flow on Knock Characteristics," Mar. 2004, pp. 2004-01–0977. doi: 10.4271/2004-01-0977.
- [67] T. Ueda, T. Okumura, S. Sugiura, and S. Kojima, "Effects of Squish Area Shape on Knocking in a Four-Valve Spark Ignition Engine," May 1999, pp. 1999-01–1494. doi: 10.4271/1999-01-1494.
- [68] J. C. Livengood and P. C. Wu, "Correlation of autoignition phenomena in internal combustion engines and rapid compression machines," *Symposium (International) on Combustion*, vol. 5, no. 1, pp. 347–356, Jan. 1955, doi: 10.1016/S0082-0784(55)80047-1.
- [69] J. Harishchandra, K. Ravindra, B. Sachin, D. Centre, and M. Ltd, "Optimisation of Engine Cooling for Knock Suppression of Turbocharged Gasoline Engine.," p. 6.

- [70] M. Asif, K. Giles, A. Lewis, S. Akehurst, and N. Turner, "Influence of Coolant Temperature and Flow Rate, and Air Flow on Knock Performance of a Downsized, Highly Boosted, Direct-Injection Spark Ignition Engine," Mar. 2017, pp. 2017-01-0664. doi: 10.4271/2017-01-0664.
- [71] D. Takahashi, K. Nakata, and Y. Yoshihara, "Engine Thermal Control for Improving the Engine Thermal Efficiency and Anti-Knocking Quality," Apr. 2012, pp. 2012-01-0377. doi: 10.4271/2012-01-0377.
- [72] S. Cho, C. Song, S. Oh, K. Min, K.-P. Ha, and B.-S. Kim, "An Experimental Study on the Knock Mitigation Effect of Coolant and Thermal Boundary Temperatures in Spark Ignited Engines," Apr. 2018, pp. 2018-01-0213. doi: 10.4271/2018-01-0213.
- [73] S. Cho, C. Song, N. Kim, S. Oh, D. Han, and K. Min, "Influence of the wall temperatures of the combustion chamber and intake ports on the charge temperature and knock characteristics in a spark-ignited engine," *Applied Thermal Engineering*, vol. 182, p. 116000, Jan. 2021, doi: 10.1016/j.applthermaleng.2020.116000.
- [74] N. R. Abdullah, H. Ismail, Z. Michael, A. Ab. Rahim, and H. Sharudin, "EFFECTS OF AIR INTAKE TEMPERATURE ON THE FUEL CONSUMPTION AND EXHAUST EMISSIONS OF NATURAL ASPIRATED GASOLINE ENGINE," *Jurnal Teknologi*, vol. 76, no. 9, Sep. 2015, doi: 10.11113/jt.v76.5639.
- [75] L. Zhou, Y. Song, J. Hua, F. Liu, and H. Wei, "Effects of miller cycle strategies on combustion characteristics and knock resistance in a spark assisted compression ignition (SACI) engine," *Energy*, vol. 206, p. 118119, Sep. 2020, doi: 10.1016/j.energy.2020.118119.
- [76] H. Wei, A. Shao, J. Hua, L. Zhou, and D. Feng, "Effects of applying a Miller cycle with split injection on engine performance and knock resistance in a downsized gasoline engine," *Fuel*, vol. 214, pp. 98–107, Feb. 2018, doi: 10.1016/j.fuel.2017.11.006.
- [77] L. Zhou, K. Dong, J. Hua, H. Wei, R. Chen, and Y. Han, "Effects of applying EGR with split injection strategy on combustion performance and knock resistance in a spark assisted compression ignition (SACI) engine," *Applied Thermal Engineering*, vol. 145, pp. 98–109, Dec. 2018, doi: 10.1016/j.applthermaleng.2018.09.001.
- [78] Q. Liu *et al.*, "Comparative study on combustion and thermodynamics performance of gasoline direct injection (GDI) engine under cold start and warm-up NEDC," *Energy Conversion and Management*, vol. 181, pp. 663–673, Feb. 2019, doi: 10.1016/j.enconman.2018.12.043.
- [79] H. Liu, Z. Wang, and J. Wang, "Methanol-gasoline DFSI (dual-fuel spark ignition) combustion with dual-injection for engine knock suppression," *Energy*, vol. 73, pp. 686–693, Aug. 2014, doi: 10.1016/j.energy.2014.06.072.
- [80] Y. Zhuang, Y. Qian, and G. Hong, "The effect of ethanol direct injection on knock mitigation in a gasoline port injection engine," *Fuel*, vol. 210, pp. 187–197, Dec. 2017, doi: 10.1016/j.fuel.2017.08.060.
- [81] S. Zhu *et al.*, "A review of water injection applied on the internal combustion engine," *Energy Conversion and Management*, vol. 184, pp. 139–158, Mar. 2019, doi: 10.1016/j.enconman.2019.01.042.
- [82] F. Bozza, V. De Bellis, and L. Teodosio, "Potentials of cooled EGR and water injection for knock resistance and fuel consumption improvements of gasoline engines," *Applied Energy*, vol. 169, pp. 112–125, May 2016, doi: 10.1016/j.apenergy.2016.01.129.
- [83] W. G. Lovell, "Knocking Characteristics of Hydrocarbons," *Ind. Eng. Chem.*, vol. 40, no. 12, pp. 2388–2438, Dec. 1948, doi: 10.1021/ie50468a033.

- [84] D. C. Luff, T. Law, P. J. Shayler, and I. Pegg, "The Effect of Piston Cooling Jets on Diesel Engine Piston Temperatures, Emissions and Fuel Consumption," *SAE Int. J. Engines*, vol. 5, no. 3, pp. 1300–1311, Apr. 2012, doi: 10.4271/2012-01-1212.
- [85] M. Grill, T. Billinger, and M. Bargende, "Quasi-Dimensional Modeling of Spark Ignition Engine Combustion with Variable Valve Train," presented at the SAE 2006 World Congress & Exhibition, Apr. 2006. doi: 10.4271/2006-01-1107.
- [86] T. Hattrell, C. G. W. Sheppard, A. A. Burluka, J. Neumeister, and A. Cairns, "Burn Rate Implications of Alternative Knock Reduction Strategies for Turbocharged SI Engines," presented at the SAE 2006 World Congress & Exhibition, Apr. 2006. doi: 10.4271/2006-01-1110.
- [87] M. Metghalchi and J. C. Keck, "Laminar burning velocity of propane-air mixtures at high temperature and pressure," *Combustion and Flame*, vol. 38, pp. 143–154, Jan. 1980, doi: 10.1016/0010-2180(80)90046-2.
- [88] M. Metghalchi and J. C. Keck, "Burning velocities of mixtures of air with methanol, isooctane, and indolene at high pressure and temperature," *Combustion and Flame*, vol. 48, pp. 191–210, Jan. 1982, doi: 10.1016/0010-2180(82)90127-4.
- [89] A. Boiarciuc and A. Floch, "Evaluation of a 0D Phenomenological SI Combustion Model," presented at the SAE International Powertrains, Fuels and Lubricants Meeting, Aug. 2011. doi: 10.4271/2011-01-1894.
- [90] M. Rivas, P. Higelin, C. Caillol, O. Sename, E. Witrant, and V. Talon, "Validation and Application of a New 0D Flame/Wall Interaction Sub Model for SI Engines," *SAE International Journal of Engines*, vol. 5, no. 3, pp. 718–733, Aug. 2011, doi: 10.4271/2011-01-1893.
- [91] F.-A. Lafossas, O. Colin, F. Le Berr, and P. Menegazzi, "Application of a New 1D Combustion Model to Gasoline Transient Engine Operation," presented at the 2005 SAE Brasil Fuels & Lubricants Meeting, May 2005. doi: 10.4271/2005-01-2107.
- [92] T. Jaine, "Simulation zérodimensionnelle de la combustion dans un moteur Diesel à injection directe," University of Orleans, France, 2004.
- [93] T. Morel, C. I. Rackmil, R. Keribar, and M. J. Jennings, "Model for Heat Transfer and Combustion In Spark Ignited Engines and its Comparison with Experiments," presented at the SAE International Congress and Exposition, Feb. 1988. doi: 10.4271/880198.
- [94] S. D. Hires, R. J. Tabaczynski, and J. M. Novak, "The Prediction of Ignition Delay and Combustion Intervals for a Homogeneous Charge, Spark Ignition Engine," presented at the 1978 Automotive Engineering Congress and Exposition, Feb. 1978. doi: 10.4271/780232.
- [95] N. C. Blizzard and J. C. Keck, "Experimental and Theoretical Investigation of Turbulent Burning Model for Internal Combustion Engines," presented at the 1974 Automotive Engineering Congress and Exposition, Feb. 1974. doi: 10.4271/740191.
- [96] Gamma Technologies, "GT-Suite Engine performance application manual."
- [97] C. G. W. Sheppard, S. Tolegano, and R. Woolley, "On the Nature of Autoignition Leading to Knock in HCCI Engines," Oct. 2002, pp. 2002-01–2831. doi: 10.4271/2002-01-2831.
- [98] W. R. Leppard, "Individual-Cylinder Knock Occurrence and Intensity in Multicylinder Engines," p. 15.
- [99] K. M. Chun and J. B. Heywood, "Characterization of Knock In a Spark Ignition Engine," p. 16.
- [100] G. Benson, E. A. Fletcher, T. E. Murphy, and H. C. Scherrer, "Knock (Detonation) Control by Engine Combustion Chamber Shape," Feb. 1983, p. 830509. doi: 10.4271/830509.
- [101] G. Shu, J. Pan, and H. Wei, "Analysis of onset and severity of knock in SI engine based on in-cylinder pressure oscillations," *Applied Thermal Engineering*, vol. 51, no. 1–2, pp. 1297–1306, Mar. 2013, doi: 10.1016/j.applthermaleng.2012.11.039.

- [102] V. Arrigoni *et al.*, "Quantitative Systems for Measuring Knock," vol. 186, p. 9.
- [103] G. Breccq, J. Bellettre, and M. Tazerout, "A new indicator for knock detection in gas SI engines," *International Journal of Thermal Sciences*, vol. 42, no. 5, pp. 523–532, May 2003, doi: 10.1016/S1290-0729(02)00052-2.
- [104] C. Hudson, X. Gao, and R. Stone, "Knock measurement for fuel evaluation in spark ignition engines," *Fuel*, vol. 80, no. 3, pp. 395–407, Feb. 2001, doi: 10.1016/S0016-2361(00)00080-6.
- [105] G. Xiaofeng, R. Stone, C. Hudson, and I. Bradbury, "The Detection and Quantification of Knock in Spark Ignition Engines," Oct. 1993, p. 932759. doi: 10.4271/932759.
- [106] L. Teodosio, D. Pirrello, F. Berni, V. De Bellis, R. Lanzafame, and A. D'Adamo, "Impact of intake valve strategies on fuel consumption and knock tendency of a spark ignition engine," *Applied Energy*, vol. 216, pp. 91–104, Apr. 2018, doi: 10.1016/j.apenergy.2018.02.032.
- [107] E. Singh, K. Morganti, and R. Dibble, "Optimizing split fuel injection strategies to avoid pre-ignition and super-knock in turbocharged engines," *International Journal of Engine Research*, vol. 22, no. 1, pp. 199–221, Jan. 2021, doi: 10.1177/1468087419836591.
- [108] L. Chen, R. Zhang, H. Wei, and J. Pan, "Effect of flame speed on knocking characteristics for SI engine under critical knocking conditions," *Fuel*, vol. 282, p. 118846, Dec. 2020, doi: 10.1016/j.fuel.2020.118846.
- [109] H. Hirooka, S. Mori, and R. Shimizu, "Effects of High Turbulence Flow on Knock Characteristics," Mar. 2004, pp. 2004-01-0977. doi: 10.4271/2004-01-0977.
- [110] S. Cho, C. Song, S. Oh, K. Min, K.-P. Ha, and B.-S. Kim, "An Experimental Study on the Knock Mitigation Effect of Coolant and Thermal Boundary Temperatures in Spark Ignited Engines," Apr. 2018, pp. 2018-01-0213. doi: 10.4271/2018-01-0213.
- [111] L. Chen, T. Li, T. Yin, and B. Zheng, "A predictive model for knock onset in spark-ignition engines with cooled EGR," *Energy Conversion and Management*, vol. 87, pp. 946–955, Nov. 2014, doi: 10.1016/j.enconman.2014.08.002.
- [112] D. Linse, A. Kleemann, and C. Hasse, "Probability density function approach coupled with detailed chemical kinetics for the prediction of knock in turbocharged direct injection spark ignition engines," *Combustion and Flame*, vol. 161, no. 4, pp. 997–1014, Apr. 2014, doi: 10.1016/j.combustflame.2013.10.025.
- [113] X. Zhen, Y. Wang, and Y. Zhu, "Study of knock in a high compression ratio SI methanol engine using LES with detailed chemical kinetics," *Energy Conversion and Management*, vol. 75, pp. 523–531, Nov. 2013, doi: 10.1016/j.enconman.2013.07.001.
- [114] A. M. Douaud and P. Eyzat, "Four-Octane-Number Method for Predicting the Anti-Knock Behavior of Fuels and Engines," presented at the 1978 Automotive Engineering Congress and Exposition, Feb. 1978. doi: 10.4271/780080.
- [115] V. Mittal, B. M. Revier, and J. B. Heywood, "Phenomena that Determine Knock Onset in Spark-Ignition Engines," Jan. 2007, pp. 2007-01-0007. doi: 10.4271/2007-01-0007.
- [116] E. Kasseris and J. B. Heywood, "Charge Cooling Effects on Knock Limits in SI DI Engines Using Gasoline/Ethanol Blends: Part 2-Effective Octane Numbers," *SAE Int. J. Fuels Lubr.*, vol. 5, no. 2, pp. 844–854, Apr. 2012, doi: 10.4271/2012-01-1284.
- [117] K. S. Kim and J. Ghandhi, "Preliminary Results from a Simplified Approach to Modeling the Distribution of Engine Knock," Oct. 2012, pp. 2012-32-0004. doi: 10.4271/2012-32-0004.
- [118] W. S. Wayne, N. Clark, and C. Atkinson, "A Parametric Study of Knock Control Strategies for a Bi-Fuel Engine," Feb. 1998, p. 980895. doi: 10.4271/980895.
- [119] W. S. Wayne, N. Clark, and C. Atkinson, "Numerical Prediction of Knock in a Bi-Fuel Engine," Oct. 1998, p. 982533. doi: 10.4271/982533.

- [120] R. Worret, S. Bernhardt, F. Schwarz, and U. Spicher, "Application of Different Cylinder Pressure Based Knock Detection Methods in Spark Ignition Engines," May 2002, pp. 2002-01-1668. doi: 10.4271/2002-01-1668.
- [121] A. A. Burluka, K. Liu, C. G. W. Sheppard, A. J. Smallbone, and R. Woolley, "The Influence of Simulated Residual and NO Concentrations on Knock Onset for PRFs and Gasolines," Oct. 2004, pp. 2004-01-2998. doi: 10.4271/2004-01-2998.
- [122] A. Amer *et al.*, "Fuel Effects on Knock in a Highly Boosted Direct Injection Spark Ignition Engine," *SAE Int. J. Fuels Lubr.*, vol. 5, no. 3, pp. 1048-1065, Sep. 2012, doi: 10.4271/2012-01-1634.
- [123] D. Fuioreescu and B. Radu, "A Proposed Relation for Knock Auto-Ignition Induction Period Evaluation in a LPG Fueled SI Engine," May 2010, pp. 2010-01-1455. doi: 10.4271/2010-01-1455.
- [124] C. Elmqvist, F. Lindström, H.-E. Ångström, B. Grandin, and G. Kalghatgi, "Optimizing Engine Concepts by Using a Simple Model for Knock Prediction," Oct. 2003, pp. 2003-01-3123. doi: 10.4271/2003-01-3123.
- [125] S. Soyly, "Prediction of knock limited operating conditions of a natural gas engine," *Energy Conversion and Management*, vol. 46, no. 1, pp. 121-138, Jan. 2005, doi: 10.1016/j.enconman.2004.02.014.
- [126] I. Z. Syed, A. Mukherjee, and J. Naber, "Numerical Simulation of Autoignition of Gasoline-Ethanol/Air Mixtures under Different Conditions of Pressure, Temperature, Dilution, and Equivalence Ratio.," Apr. 2011, pp. 2011-01-0341. doi: 10.4271/2011-01-0341.
- [127] J. Vancoillie, L. Sileghem, and S. Verhelst, "Development and Validation of a Knock Prediction Model for Methanol-Fuelled SI Engines," Apr. 2013, pp. 2013-01-1312. doi: 10.4271/2013-01-1312.
- [128] Y. Ra and R. D. Reitz, "A reduced chemical kinetic model for IC engine combustion simulations with primary reference fuels," *Combustion and Flame*, vol. 155, no. 4, pp. 713-738, Dec. 2008, doi: 10.1016/j.combustflame.2008.05.002.
- [129] J. Pan, P. Zhao, C. K. Law, and H. Wei, "A predictive Livengood-Wu correlation for two-stage ignition," *International Journal of Engine Research*, vol. 17, no. 8, pp. 825-835, Oct. 2016, doi: 10.1177/1468087415619516.
- [130] J. J. Hernández, M. Lapuerta, and J. Sanz-Argent, "Autoignition prediction capability of the Livengood-Wu correlation applied to fuels of commercial interest," *International Journal of Engine Research*, vol. 15, no. 7, pp. 817-829, Oct. 2014, doi: 10.1177/1468087414521614.
- [131] M. D. Kurtz and J. D. Regele, "Acoustic timescale characterisation of a one-dimensional model hot spot," *Combustion Theory and Modelling* vol. 18, no. 4-5, pp. 532-551, Sep. 2014, doi: 10.1080/13647830.2014.934922.
- [132] M. Pöschl and T. Sattelmayer, "Influence of temperature inhomogeneities on knocking combustion," *Combustion and Flame*, vol. 153, no. 4, pp. 562-573, Jun. 2008, doi: 10.1016/j.combustflame.2007.11.009.
- [133] M. Ribaucour, R. Minetti, L. R. Sochet, H. J. Curran, W. J. Pitz, and C. K. Westbrook, "Ignition of isomers of pentane: An experimental and kinetic modeling study," *Proceedings of the Combustion Institute*, vol. 28, no. 2, pp. 1671-1678, Jan. 2000, doi: 10.1016/S0082-0784(00)80566-4.
- [134] M. Mehl, W. J. Pitz, C. K. Westbrook, and H. J. Curran, "Kinetic modeling of gasoline surrogate components and mixtures under engine conditions," *Proceedings of the Combustion Institute*, vol. 33, no. 1, pp. 193-200, 2011, doi: 10.1016/j.proci.2010.05.027.

- [135] C. K. Westbrook and F. L. Dryer, "Chemical kinetic modeling of hydrocarbon combustion," *Progress in Energy and Combustion Science*, vol. 10, no. 1, pp. 1–57, Jan. 1984, doi: 10.1016/0360-1285(84)90118-7.
- [136] J. Rudloff, J.-M. Zaccardi, S. Richard, and J. M. Anderlohr, "Analysis of pre-ignition in highly charged SI engines: Emphasis on the auto-ignition mode," *Proceedings of the Combustion Institute*, vol. 34, no. 2, pp. 2959–2967, Jan. 2013, doi: 10.1016/j.proci.2012.05.005.
- [137] D. Bradley, C. Morley, X. J. Gu, and D. R. Emerson, "Amplified Pressure Waves During Autoignition: Relevance to CAI Engines," Oct. 2002, pp. 2002-01–2868. doi: 10.4271/2002-01-2868.
- [138] C. Qi, P. Dai, H. Yu, and Z. Chen, "Different modes of reaction front propagation in n-heptane/air mixture with concentration non-uniformity," *Proceedings of the Combustion Institute*, vol. 36, no. 3, pp. 3633–3641, 2017, doi: 10.1016/j.proci.2016.06.086.
- [139] X. J. Gu, D. R. Emerson, and D. Bradley, "Modes of reaction front propagation from hot spots," *Combustion and Flame*, vol. 133, no. 1–2, pp. 63–74, Apr. 2003, doi: 10.1016/S0010-2180(02)00541-2.
- [140] P. Dai, Z. Chen, S. Chen, and Y. Ju, "Numerical experiments on reaction front propagation in n-heptane/air mixture with temperature gradient," *Proceedings of the Combustion Institute*, vol. 35, no. 3, pp. 3045–3052, 2015, doi: 10.1016/j.proci.2014.06.102.
- [141] S. Beccari, E. Pipitone, and G. Genchi, "Calibration of a Knock Prediction Model for the Combustion of Gasoline-LPG Mixtures in Spark Ignition Engines," *Combustion Science and Technology*, vol. 187, no. 5, pp. 721–738, May 2015, doi: 10.1080/00102202.2014.960925.

Titre : Caractérisation expérimentale et modélisation phénoménologique de l'apparition du cliquetis dans les moteurs à allumage commandé suralimentés

Mots clés : Combustion, cliquetis, modélisation, moteur automobile, paramètres de contrôle.

Résumé : Le cliquetis est l'un des principaux obstacles techniques à l'amélioration du rendement du moteur à allumage commandé et donc de l'ensemble de la chaîne de traction automobile dans le cadre de la réduction de la consommation de carburant et des émissions polluantes pour respecter les contraintes environnementales. Dans cette thèse, l'occurrence du cliquetis a été caractérisée expérimentalement sur un moteur à combustion interne trois cylindres suralimenté à injection directe installé sur un banc d'essais du laboratoire. L'apparition du cliquetis a ainsi été étudiée en faisant varier certains paramètres de contrôle du moteur tels que les lois d'injection, les calages des soupapes, la température de l'air d'admission, la température du liquide de refroidissement et la température de l'huile de lubrification.

D'un point de vue numérique, les outils de modélisation 0D-1D sont largement utilisés pour raccourcir les boucles de développement et évaluer les performances des moteurs. Quant aux modèles de cliquetis, ils sont généralement basés sur la théorie de l'auto-allumage des gaz frais et ils impliquent une réaction en une étape. Dans cette thèse, une nouvelle procédure de calibration a été proposée pour améliorer la modélisation du cliquetis sur un modèle de moteur complet. L'ensemble a été testé par confrontation aux mesures effectuées sur le banc d'essais et il permet de décrire les principaux phénomènes influençant l'apparition du cliquetis et de capturer l'influence des différents paramètres de contrôle du moteur sur le cliquetis. Implémenté dans le modèle complet, le modèle de cliquetis obtenu peut être utilisé pour assister la calibration numérique du moteur.

Title : Experimental characterization and phenomenological modeling of knock occurrence in turbocharged spark-ignition engines

Keywords : Combustion, knock, modeling, automotive engine, control parameters.

Abstract: Knock is one of the main technical obstacles to improving the efficiency of the engine and therefore of the entire powertrain in the context of reducing the fuel consumption and pollutant emissions to respect the environmental constraints. In this PhD thesis, knock occurrence was characterized on a turbocharged direct injection three cylinder internal combustion engine to assess the knock problems and to understand its behavior on an everyday-use vehicles confronted to real conditions. Knock occurrence was thus quantified by varying some of the engine control parameters such as the laws of injection, the valves timings, the intake air temperature, the coolant temperature and the lubricating oil temperature.

Numerically, 0D-1D modeling tools are widely employed to shorten the development loops and to evaluate the performance of the engines. As for knock models, they are usually based on the end-gas auto ignition theory and they involve a one-step reaction instead of detailed chemical kinetics. In this PhD thesis, a new calibration procedure was proposed to improve the modeling of knock apparition on a complete engine model. The obtained model was tested and it allows to describe the main physical and chemical phenomena influencing the occurrence of knock and to capture the influence of the various engine control parameters on the knock. Implemented on the complete model, the obtained knock model can be used to assist in the engine virtual calibration